Towards the Optimization of Fatigue Behaviour of 3D-printed Titanium Structures



Jieming S. Zhang

Supervisor: Prof. Alan C.F. Cocks
Prof. Roger C. Reed
Prof. Patrick S. Grant

Department of Materials
University of Oxford

This dissertation is submitted for the degree of
Doctor of Philosophy

The Queen's College

Submitted February 2024

Uneasy lies the head that wears a crown

— *William Shakespeare*

Acknowledgements

There are a number of people and organizations I am in debt to, for their relentless support and encouragement, I have embraced a continuum of time in the past three years at the University of Oxford.

First and foremost, I would like to thank Prof. Alan C.F. Cocks for sacrificing much of his retirement time on caring, inspiring, and pushing me through some of the most difficult times in my life. His academic expertise has guided me into the realm of solid mechanics and computational modeling. His enthusiasm and rigorousness in research have stimulated both my professional and personal development. His supervision has reinvented my personality and I owe him a debt that can never be compensated.

I am grateful to Prof. Roger C. Reed for granting me the opportunity to start this DPhil study. I will never forget many of our fruitful discussions and have always been motivated by his abundant vigour. I also need to thank my brother from another mother Prof. Yuanbo Tang who has persistently backed me up since when I was 15. His advice and life experience have lifted me up during many stressful times. I deeply appreciate the entire research group – Mrs. Karen Bamford, Dr. Satoshi Utada, Dr. Joseph N. Ghoussoub, Hirokazu Usuki, Prof. D. Graham McCartney, Celal Polatoğlu, Prof. Chinnapat Panwisawas, Dr. Sabin Sulzer, Ryo Sasaki, Dr. Yilun Gong – for their continuous friendship and support.

My gratitude also goes to Prof. Partick S. Grant for his guidance and mentorship. I have acquired a profound knowledge of leadership and project management through our productive discussions. Words cannot express my gratitude to Dr. Yun Deng for her

inexhaustible optimism and enthusiasm that have comforted me amidst my emotional nadir. I will always remember the times we spent together during the thesis writing. Special thanks to the great Dr. Andrew Lui for his camaraderie and knowledge of X-ray imaging. I have also benefited a lot from his patience and earnestness. I am thankful to many other pals in the Materials Department – Tongshan Liu, Justin Sy Limkaichong, Laura Lain Rodriguez, Dr. Kai Ling Ng, Ping-Yuan Lee, Dr. Botao Hao, Xiaohang Cai – for many incredible memories we share together.

I want to express my sincere gratitude to numerous wonderful sponsors and collaborators. I am obliged to Alloyed Ltd. and Innovate UK for funding this research. Thank you to the brilliant Dr. Enrique Alabort for setting up the foundation for this DPhil study and sharing many critical insights into industrial practice. A further thank you to Dr. Huifang Liu for enlightening my computational modeling skills and debugging my model day and night. I also owe Nicole Kuek a lot for refining experimental plans with me tirelessly.

My experience at CapitOx Consulting Group broadened the horizon of my DPhil study and I am immensely grateful to the committee members who have believed in my leadership. Thank you to Cherie Wong who has opened up my understanding of strategy consulting and advised me at every stage of my CapitOx journey. It was an honor to be part of this legendary society. Special thanks to Sophia Suganuma, Arda Battalgazi, Hongyin Pan, Nha Truc Dang, Jessica Luiz, and Can Uz for their amazing characters that have made this journey unforgettable.

I would never be able to reach this DPhil study without my time at Imperial College London. Thank you to Prof. Andrew Horsfield and Prof. David Dye for their inspiration to start off my research journey. Of course, thank you to Inés Díaz-Tejeiro Rodríguez, Haldrian Iriawan, Mirza Alesi Sjarif, Kaiqian Lu, Meryem Lamari, Fotios Tsitsos, Qian Cheng, and Wenli Zhou Chen for their enduring friendship during my DPhil.

Lastly, but most importantly, I would like to give my sincerest thank you to my parents, Li Wang and Dalei Zhang, for always pushing me to the best of my capabilities, and my grandparents, Yuzhi Liu and Mingzhi Wang, for your moral and emotional support in my life!

Preface

Research in this thesis has been prepared for publication as follows:

- Jieming S. Zhang, Yuanbo T. Tang, Ruining Jin, Andrew Lui, Patrick S. Grant, Enrique Alabort, Alan C.F. Cocks, Roger C. Reed *On the Size-dependent Fatigue Behaviour of Laser Powder Bed Fusion Ti-6Al-4V*, Additive Manufacturing, January 2024, Volume 79, doi: 10.1016/j.addma.2023.103922.

- Jieming S. Zhang, Yuanbo T. Tang, Yun Deng, Huifang Liu, Andrew Lui, Patrick S. Grant, Enrique Alabort, Roger C. Reed, Alan C.F. Cocks *Orientation Matters: Assessing the Cyclic Deformation Behaviour of Laser Powder Bed Fusion Ti-6Al-4V*, Additive Manufacturing, submitted.

- Jieming S. Zhang, Huifang Liu, Yuanbo T. Tang, Yun Deng, Nicole Kuek, Andrew Lui, Patrick S. Grant, Enrique Alabort, Roger C. Reed, Alan C.F. Cocks *Stochastic or Deterministic: Duality of Fatigue Behaviour of Metallic Lattice*, Acta Biomaterialia, submitted.

- Jieming S. Zhang, Yun Deng, Huifang Liu, Yuanbo T. Tang, Andrew Lui, Enrique Alabort, Patrick S. Grant, Alan C.F. Cocks, Roger C. Reed *Cyclic Deformation Behaviour of Metallic Metamaterial*, in preparation.

Abstract

Architected materials or metamaterials offer a new degree of flexibility to attain desirable material properties. With the aid of additive manufacturing (AM) techniques, the reliable fabrication of these materials steps into the realm of reality. However, architected materials often exhibit inferior fatigue resistance as a result of the high surface-to-volume ratio and stress localization within the structure. Most of the current research only assesses the fatigue properties of the constituent elements. It is unclear how best to correlate the knowledge of these elements with architected materials. Moreover, structural inhomogeneities such as surface roughness, geometrical inaccuracy, porosity, residual stresses, and heterogeneous microstructure are often induced by the AM processes but their influence on the fatigue behaviour of architected materials is still largely in debate. This research address these issues from a fundamental level *via* a combination of experimental efforts, numerical calculation, and finite element analysis (FEA). Ti-6Al-4V is selected as the parent material. First, the size and orientation dependency of the fatigue behaviour of the constituent elements is assessed, and surface roughness is found to be the pivotal factor governing the fatigue properties. Next, the cyclic deformation processes of stretching-dominated and bending-dominated

structures are unravelled. The fatigue failure mechanism is highly dependent on the unit cell type and design variables. Lastly, randomness is encoded into the lattice design to improve the defect tolerance of the structure. Design principles are derived to govern the consistent fatigue properties of architected materials. Overall, this thesis highlights the possibility of correlating the understanding of fatigue behaviour between monolithic and architected materials leading to the development of design protocols for fatigue-tolerant components.

Table of contents

Preface **ix**

List of tables **xvii**

Nomenclature **xix**

1 Introduction **1**
1.1 Metal additive manufacturing (AM) 1
1.2 Ti-6Al-4V alloy 4
1.3 Architected material 5
1.4 Aim of the research 8
1.5 Structure of the thesis 9

2 Literature Review **13**
2.1 Fatigue Behaviour of Monolithic Materials: Conventional Wisdom vs. Modern Insights 13
2.2 Fatigue Behaviour of Architected Materials 15
2.3 Contribution of Structural Inhomogeneity to the Fatigue Fracture Process 23
2.3.1 Surface Roughness 24
2.3.2 Geometrical Inaccuracy 27
2.3.3 Processing-induced Porosity 31
2.3.4 Residual Stress 33
2.3.5 Microstructure 36
2.4 Processing and Design Means of Improving Fatigue Behaviour 37
2.4.1 Customization of Processing Conditions 38
2.4.2 Post-processing 40
2.4.3 Design against Manufacturability 41
2.4.4 Mitigation of Stress Concentrations 43
2.5 Recent Advances on the Fatigue-tolerant Design 46

2.5.1 Conformal Lattice Design and Topology Optimization 46
2.5.2 Hierarchical and Functional Gradient Design 48
2.5.3 Applications of Machine Learning Algorithms and Data-driven Approaches 52
2.6 Summary 53
2.7 Conclusion remarks 54

3 On the Size-dependent Fatigue Behaviour of Laser Powder Bed Fusion Ti-6Al-4V 57
3.1 Introduction 57
3.2 Methods 59
3.2.1 Processing by Laser Powder Bed Fusion 60
3.2.2 Assessment of Static & Dynamic Mechanical Behaviour 61
3.2.3 Characterization by Electron Microscopy 61
3.2.4 X-ray Computed Tomography (XCT) 62
3.3 Results 63
3.3.1 Quasi-static Behaviour 63
3.3.2 Dynamic Behaviour in Fatigue 64
3.3.3 Microstructural characterization 66
3.3.4 Surface roughness 73
3.3.5 Processing-induced porosity 73
3.4 Discussion 78
3.4.1 Rationalization of the variation in tensile properties 78
3.4.2 Fatigue fracture behaviour 81
3.4.3 Rationalization of the variation in fatigue properties 88
3.5 Summary and Conclusions 91

4 Orientation Matters: Assessing the Cyclic Deformation Behaviour of Laser Powder Bed Fusion Ti-6Al-4V 93
4.1 Introduction 93
4.2 Experimental Methods 95
4.2.1 Design of Experimentation 95
4.2.2 Processing by Laser Powder Bed Fusion 96
4.2.3 Assessment of Static & Dynamic Mechanical Behaviour 97
4.2.4 Characterization by Electron Microscopy 97
4.2.5 X-ray Computed Tomography (XCT) 98
4.3 Experimental Results 101

4.3.1 Quasi-static Behaviour . . . 101
4.3.2 Dynamic Behaviour in Fatigue . . . 101
4.3.3 Microstructural Characterization . . . 102
4.3.4 Surface Roughness . . . 106
4.3.5 Processing-induced Porosity . . . 108
4.4 Discussion & Evaluation of Experimental Results . . . 111
4.4.1 Rationalization of the variation in tensile properties . . . 112
4.4.2 Fatigue fracture behaviour . . . 116
4.4.3 Rationalization of the variation in fatigue properties . . . 119
4.5 Orientation Effect on the Deformation Response of an Octet-truss Lattice Material . . . 124
4.5.1 Description of Finite Element Modelling . . . 126
4.5.2 Analysis of Elastic Response . . . 127
4.5.3 Analysis of Plastic Collapse . . . 130
4.5.4 Analysis of Failure under Cyclic Loading . . . 136
4.6 Summary and Conclusions . . . 138

5 Cyclic Deformation Behaviour of Metallic Metamaterial 141
5.1 Introduction . . . 141
5.2 Methods . . . 142
5.2.1 Design and Fabrication of Metamaterials . . . 142
5.2.2 Assessment of Static & Dynamic Mechanical Behaviour . . . 143
5.2.3 X-ray Computed Tomography (XCT) . . . 145
5.3 Results and Discussion . . . 146
5.3.1 Quasi-static Mechanical Behaviour . . . 146
5.3.2 Dynamic Behaviour in Fatigue . . . 148
5.3.3 Deformation Behaviour under Monotonic Loading . . . 149
5.3.4 Damage Evolution Process during Cyclic Loading . . . 149
5.3.5 Fatigue Fracture Behaviour . . . 150
5.4 Summary and Conclusions . . . 156

6 Stochastic or Deterministic: Duality of Fatigue Behaviour of Metallic Lattice 157
6.1 Introduction . . . 157
6.2 Methods . . . 159
6.2.1 Design and Manufacturing of the Lattices . . . 159
6.2.2 Assessment of Static & Dynamic Mechanical Behaviour . . . 161

6.2.3 X-ray Computed Tomography (XCT) . . . 162
6.2.4 Finite Element Modelling . . . 162
6.3 Results . . . 165
6.3.1 Quasi-static Mechanical Behaviour of the Voronoi Lattice . . . 165
6.3.2 Dynamic Behaviour in Fatigue . . . 166
6.3.3 Characterization of the Lattice Processability . . . 169
6.4 Discussion . . . 178
6.4.1 Duality of Fatigue Fracture Process . . . 178
6.4.2 Rationalization of the Role of Defects during Cyclic Loading . . 185
6.4.3 Damage Evolution during the Cyclic Deformation Process . . . 188
6.4.4 Analysis of Fatigue Failure Process . . . 190
6.5 Summary and Conclusions . . . 195

7 Conclusions and Future Work 197
7.1 Conclusion remarks . . . 197
7.2 Future Work . . . 200
7.2.1 Statistical Analysis of Fatigue Scatter . . . 200
7.2.2 Development of Fracture Mechanism Map . . . 201
7.2.3 Validation of Fatigue-tolerant Design . . . 202

List of figures 203

References 211

List of tables

3.1 A summary of dimensions of samples used in this study. 60
3.2 Processing parameters used for the manufacturing of tensile samples. . 61
3.3 A summary of the samples tested in this work. 63

4.1 Processing parameters used for the manufacturing of tensile samples. . 97
4.2 A summary of the samples tested in this work. 100
4.3 Materials properties used in finite element analysis. 127

5.1 A summary of the samples tested in this work. 154

6.1 Material properties of AM Ti-6Al-4V employed in the FEA model. . . . 163
6.2 A summary of the samples tested in this work. 164

Nomenclature

Acronyms / Abbreviations

3D	three dimensions
AM	additive manufacturing
BCC	Body-centred Cubic
CAD	computer-aided design
DMLS	direct metal laser sintering
EBM	electron beam melting
EBSD	electron backscatter diffraction
EOS	Electro Optical Systems
FCC	Face-centred Cubic
FEA	finite element analysis
FEG	field emission gun
HIP	hot-isostatic pressing
L-PBF	laser powder bed fusion
LED	light-emitting diode
ND	neutron diffraction
SEM	scanning electron microscopy
SLM	selective laser melting

TPMS	triply periodic minimal surface
V	Voronoi
XCT	X-ray computed tomography
XRD	X-ray diffraction

Chapter 1

Introduction

1.1 Metal additive manufacturing (AM)

Additive manufacturing (AM), or 3D printing, ignites a fundamental revolution in the production of metallic parts [1–3]. Through the consecutive addition of layers of material, its boundless design freedom at high geometrical precision commences a new pathway for the weight saving and structural functionalization of engineering components [4–6]. Such merits render the process particularly compatible with high-end industries, such as aerospace, aviation, biomedical, consumer electronics, automobile manufacturing, and energy generation [7–9]. Some examples of metallic components made by AM are shown in Figure 1.1.

The conceptualization of AM embarked in the 1980s with the development of stereolithography, a process that solidifies light-sensitive liquid polymer layer-by-layer using ultraviolet light [1, 16]. However, it was not until the 1990s, the first metal 3D

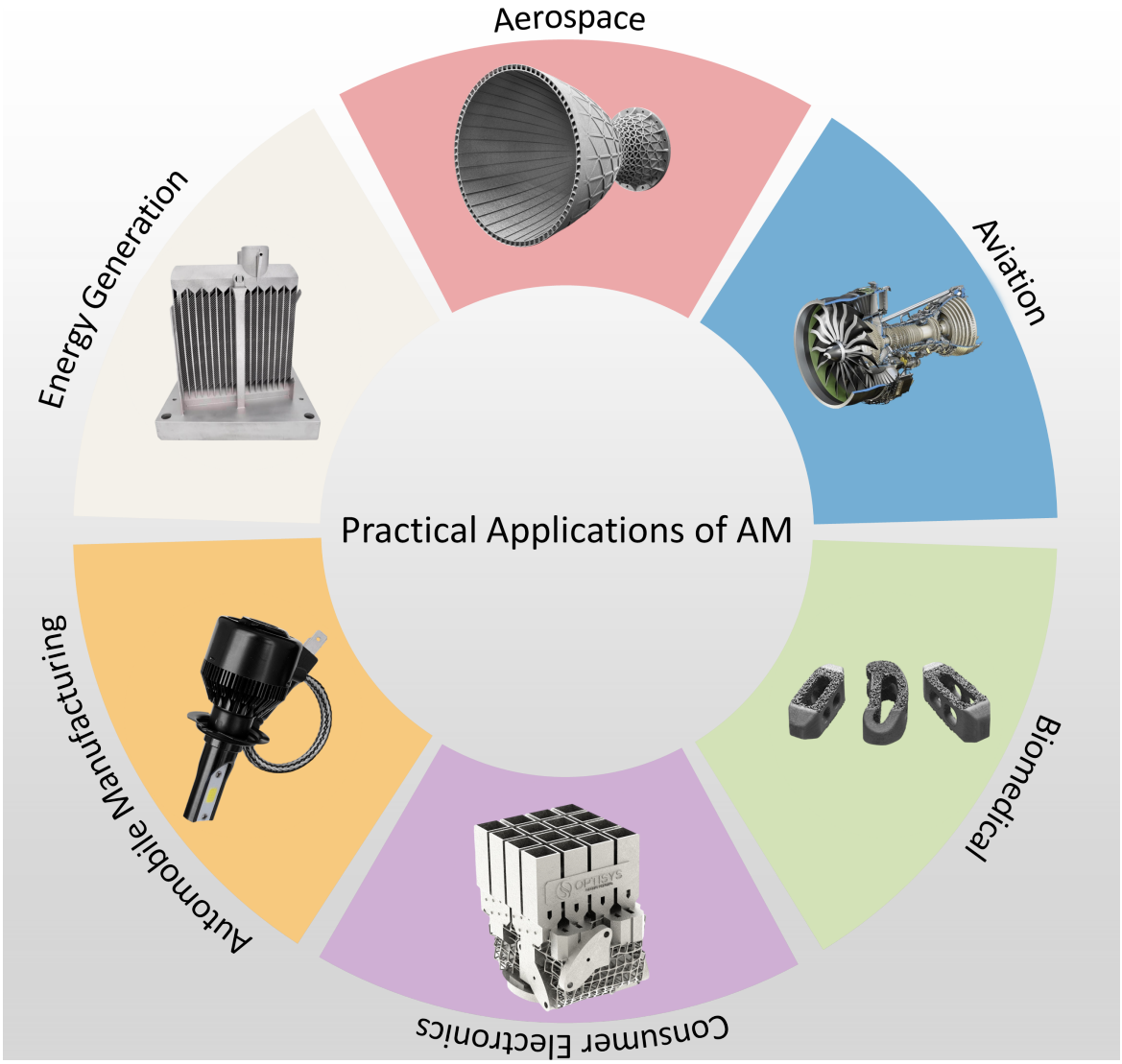


Fig. 1.1 Examples of metallic components made by AM including Alloyed rocket nozzle adapted from ref. [10], General Electric GE9X high-bypass turbofan adapted from ref. [11], Captiva TriboLOX-l titanium lumbar cage adapted from ref. [12], Optisys radio frequency antenna adapted from ref. [13], Alloyed automotive light-emitting diode (LED) headlight adapted from ref. [14], and Eplus3D heat exchanger adapted from ref. [15].

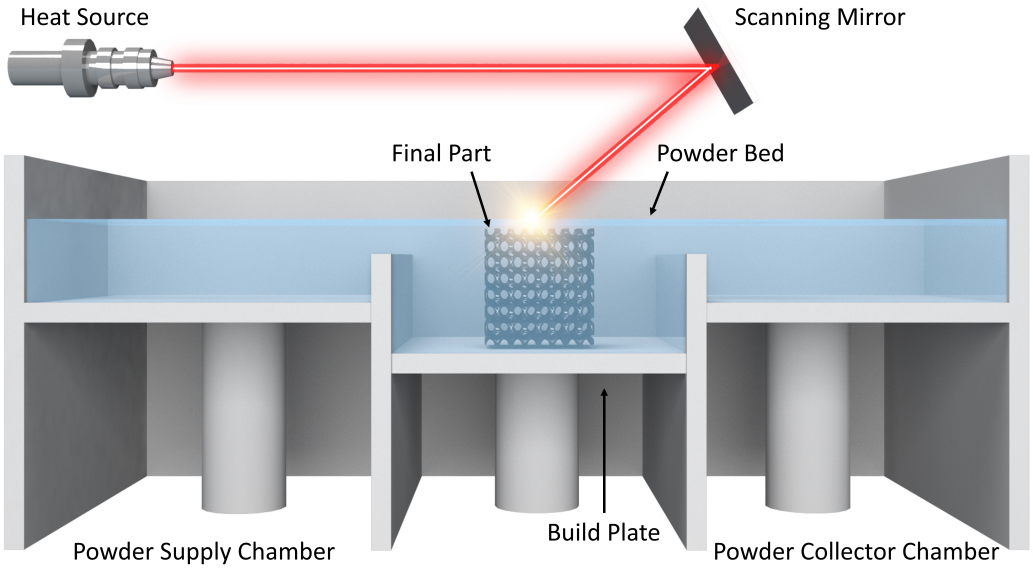


Fig. 1.2 A schematic illustration of the powder bed system.

printer was developed by Electro Optical Systems (EOS), termed the direct metal laser sintering (DMLS) technique [16]. Thereafter, there was an increasing capitalization of the metal AM technique leading to the development of laser powder bed fusion (L-PBF) – also known as selective laser melting (SLM) – and electron beam melting (EBM). These processes involve the ideally uniform deposition of powders into a relatively thin flat layer, followed by a heat source (laser or electron beam) that fuses the powder particles together in selective positions. The build plate is then lowered to enable the deposition of the next layer. The procedures iterate to the underlying layers until the final part is built. A schematic illustration of the powder bed system is shown in Figure 1.2.

Here, L-PBF is used, in which a laser beam serves as the heat source, for the production of all the specimens. Its advantages including improved surface quality and

higher resolution offer unparalleled competency to fabricate complex structures with thin features, such as architected materials [17, 18].

1.2 Ti-6Al-4V alloy

Ti-6Al-4V is an α+β titanium alloy (α = hexagonal close-packed, β = body-centred cubic) with superior specific strength, high fracture toughness, eminent fatigue endurance, and excellent corrosion resistance [19–21]. As the "workhorse" titanium alloy, Ti-6Al-4V takes up almost 50% of the global titanium market. The invention of Ti-6Al-4V originated in the 1950s and its first commercial adoption was for the production of the US military's U2 high-altitude reconnaissance plane [19, 22]. Since then, this alloy has emerged as a critical catalyst propelling the growth of the aerospace and aviation industry. Applications of Ti-6Al-4V alloy also extend beyond the aircraft. Structural components in the biomedical, energy generation, and automobile manufacturing sectors require outstanding mechanical properties and the ability to maintain structural integrity in a corrosive environment [21, 23, 24]. This has led to extensive integration of Ti-6Al-4V alloy into complex engineering systems including biomedical implants, energy extraction pipes, and motorcycle frames over the past half a century [25, 7, 26].

Despite the notable advantages Ti-6Al-4V offers, the production of the alloy requires careful thermomechanical processing owing to its low thermal conductivity [27], susceptibility to strain hardening [28, 29], and oxygen affinity [30]. Ti-6Al-4V alloy made by conventional manufacturing approaches such as forging, casting, and

rolling often requires subsequent machining to the final geometry, which results in high manufacturing expense, excessive material waste, and prolonged lead time [31]. AM is a promising avenue to address these issues because of its capability to print near-net shape parts [19, 2, 3]. Its geometrical freedom in design further broadens the versatility of Ti-6Al-4V alloy in many critical sectors.

L-PBF Ti-6Al-4V exhibits remarkable differences from the conventionally manufactured counterparts. During the solidification of the L-PBF process, the steep thermal gradients in the melt pool initially give rise to the formation of columnar β grains [19, 32]. Upon the rapid cooling (10^4 - 10^6 K/s) from above β transus temperature, β grains are decomposed into α' martensitic laths [19, 32]. Heat treatments are often applied to AM Ti-6Al-4V to relieve the residual stress coarsening the α' martensite into α laths [33, 34]. Moreover, the highly dynamic interaction between the heat source and the material induces many metallurgical defects including porosity and surface irregularity [19, 35]. A combination of these structural inhomogeneities governs the mechanical properties of L-PBF parts and hence forms the focus of this work.

1.3 Architected material

Over the bygone eras, material discoveries have been driven by the understanding of the processing-microstructure-property relationship [36–38]. The development of architected materials, also known as metamaterials, – structures with constituent elements in specific geometrical configurations – opens the door for integrating a

new degree of design freedom to attain macroscopic material properties beyond the scope of monolithic materials [39–41]. Yet, the manufacturing challenges arising from geometrical complexity have constrained the applications of these materials to mere academic speculations. The proliferation of the AM technique realizes the fabrication of architected materials with great precision and thus the geometries of these materials can be finely customized to unlock their exceptional properties [4, 5, 42].

Three classes of architected materials have been widely investigated: strut-based structures, and triply periodic minimal surface (TPMS) skeletal and sheet structures (see Figure 1.3) [43, 44]. Strut-based structures have nodes at the vertices or edges of the cell that are linked by strut members. These structures offer high porosity and ease of design, which allows the material distribution to be optimized [44, 45]. On the other hand, TPMS structures have a minimal surface area for a given boundary and can be packed together periodically in three dimensions (3D). The zero mean surface curvature of these topologies gives rise to high surface-area-to-volume ratios and nominal stress concentrations within the structures [44, 45].

In this work, we only focus on the strut-based lattices for the simplicity of topological optimization [46]. These lattices can be further categorized into two groups by analyzing the nodal connectivity: bending-dominated and stretching-dominated structures. The Maxwell stability criterion can serve as a necessary rather than sufficient condition for the classification of structures in 3D following: [44, 45, 47]

$$M = b - 3j + 6 \tag{1.1}$$

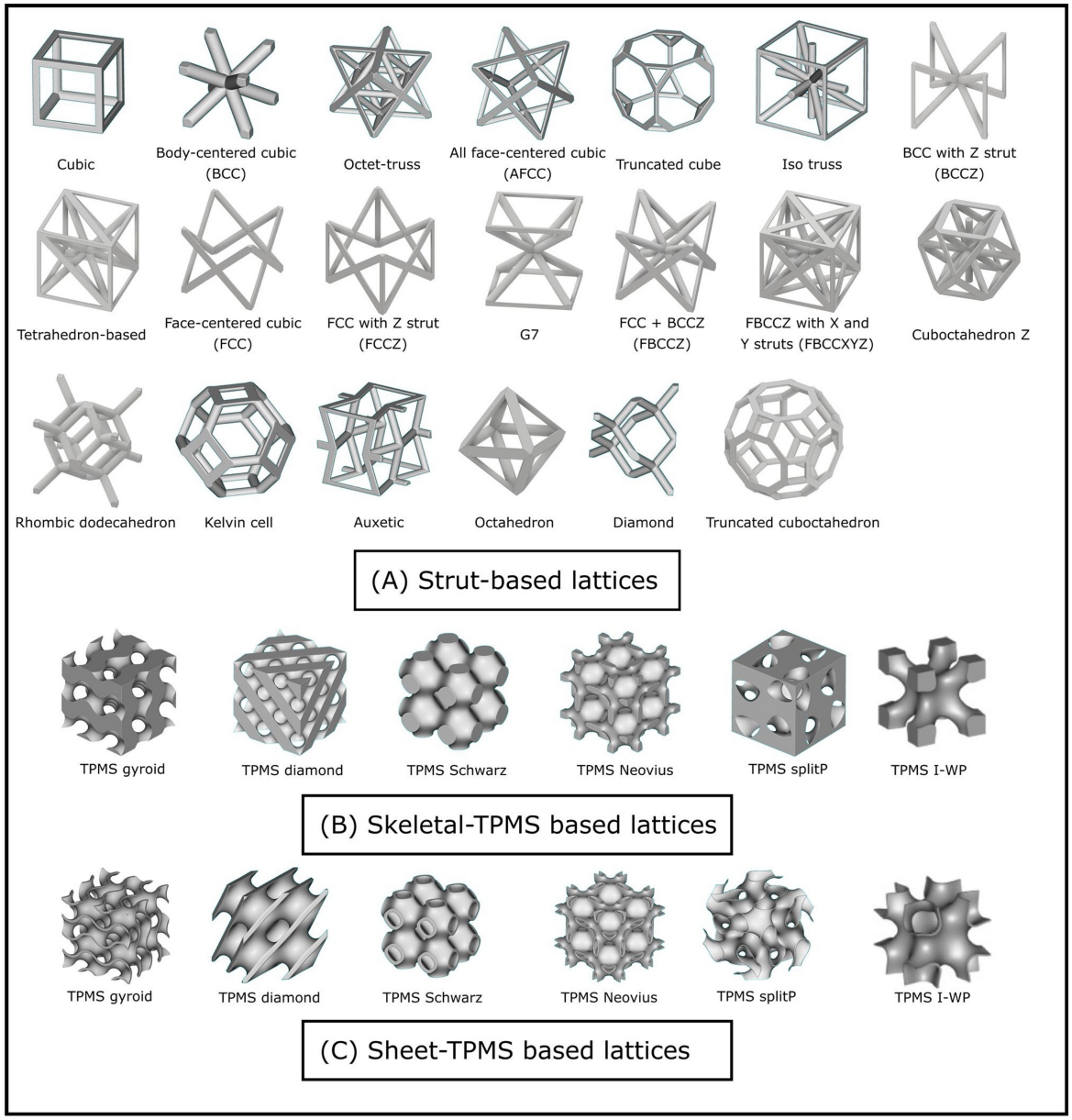


Fig. 1.3 Three classes of commonly used architected materials. Adapted from ref. [43].

where M is the Maxwell number, b is the number of struts, and j is the number of nodes. When $M < 0$, the number of struts is often insufficient to balance external forces without balancing the moments at nodes, which leads to the rotation of the struts about the nodes and the collapse of the structure by strut bending. Conversely, if $M \geq 0$, the axial tension and compression in struts likely equilibrate the external forces and the structures fail by strut stretching. The criterion can be used for a first-order assessment of the characteristics of the lattice structure [47]. Bending-dominated structures are more compliant whereas stretching-dominated structures are more structurally efficient [44, 45]. Both types of strut-based structures are assessed here to provide a holistic view of the geometrical design.

1.4 Aim of the research

Integrating AM and architected materials entails underlying challenges. The mechanical durability, especially the fatigue behaviour, of architected materials is significantly weaker than that of monolithic materials [44, 48, 49]. This limits the adoption of 3D-printed architected materials in many critical sectors [50, 51]. The porous structures reduce the effective loading area increasing the local stress concentrations, which facilitates the damage localization during cyclic loading. Yet, numerous efforts have been focusing on the fatigue behaviour of monolithic materials. The understanding of macroscopic behaviour between architected and monolithic materials requires further study. In addition, structural inhomogeneities such as microstructure, porosity, and

surface roughness are often induced by the AM process as described above [19, 35]. These irregularities act as stress concentrators leading to more susceptible fracture conditions for the structures. However, the synergistic effects of these attributes on the fatigue fracture process still remain in question. Moreover, is it feasible to engineer the lattice so that the influence of these inhomogeneities can be mitigated?

This work is initiated with the above in mind and aims to leverage a combination of experimentation and computational mechanics to unravel the cyclic deformation behaviour of 3D-printed Ti-6Al-4V structures and their constituent elements. First, we assess the size and orientation effects – two critical design parameters of architected materials – on the fatigue behaviour of the constituent elements. We then determine the implication of these effects on the deformation behaviour of architected materials. The fatigue fracture processes of architected materials are also interpreted. The results are rationalized to enlighten the design of fatigue-tolerant intricate components.

1.5 Structure of the thesis

Chapter 2 provides background and summary of the fatigue behaviour of 3D-printed architected materials and their constituent elements. It begins with the comparison of failure mechanisms between AM materials and conventionally manufactured counterparts. Then, an assessment of the cyclic deformation behaviour of architected materials is provided. This is followed by an overview of the structural inhomogeneities and how they contribute to the fatigue fracture process. Means of improving the fatigue

performance of 3D-printed lattices by processing are discussed. A review of various attempts to design against fatigue is made.

In Chapter 3, an unconventional size effect of the fatigue behaviour of L-PBF Ti-6Al-4V is identified and quantified. We consider two cylindrical samples: ∅ 1.3 mm and ∅ 2.0 mm. The larger specimen demonstrates superior fatigue life owing to the 50% lower surface roughness. Processing-induced porosity has been proven to be detrimental to fatigue performance even when the cracks are initiated from surface defects. The larger contribution of porosity to the failure process gives rise to higher fatigue scatter of the larger specimen. Microstructural differences between the two types of specimens have only a minimal influence on the variation in fatigue properties. Nevertheless, we show some evidence that the coarser microstructure of the larger specimen promotes a stronger defect tolerance and induces more corrugated crack paths hindering fatigue crack growth.

Chapter 4 investigates the orientation dependency of the fatigue behaviour of L-PBF Ti-6Al-4V. We design and fabricate specimens in seven build orientations relative to the build plate. The 75° specimen shows the optimal fatigue life owing to the superior surface quality and the marginal fraction of grains near-parallel to the loading direction. When the specimens are printed at 30° or below, all the cracks are initiated from the downward-facing surface owing to the poor surface quality. Beyond 45°, defects on the otherward-facing surface begin to serve as the initiation sites since the distribution of defects becomes more homogeneous across the sample surface. The larger contribution of porosity to the failure process governs the highest scatter in fatigue life of the 75°

specimen whereas the variation in the crack initiation sites gives rise to the large difference in fatigue life of the 45° specimen. Analytical calculation indicates the fatigue strength of a stretch-dominated metallic lattice can be improved by 51% at 10^6 cycles by optimizing the build orientation. This highlights the significance of build orientation in the design of mechanically durable components.

In Chapter 5, we assess the cyclic deformation behaviour of two periodic cellular structures: face-centred cubic (FCC) and body-centred cubic (BCC). Three specimens for each topology are considered. The stretching-dominated FCC structures present the formation of shear bands during the fatigue damage process, which is consistent with the deformation mode under monotonic loading. On the other hand, the bending-dominated BCC structures primarily show shear band failure during cyclic loading but progressive failure during quasi-static tests. At high applied stresses, progressive failure of the BCC structure is also observed when the strut thickness-to-length ratios are small.

Chapter 6 reveals a Janus-like deformation behaviour of metallic lattices during cyclic loading. We print five Voronoi (V) structures with a range of strut thicknesses and cell number densities. When the strut thickness is 200 μm or above, the fatigue failure process is deterministic. As the strut thickness reduces to 150 μm, the initial strut failure occurs randomly provoking inconsistent fatigue properties. The two distinct deformation modes originate from the processing limit of L-PBF. The fatigue scatter can also be reduced as the number of cells per unit volume increases. These findings broaden our understanding of the fatigue fracture process of architected

materials and confirm encoding randomness into lattice design could improve tolerance to processing-induced defects.

In Chapter 7, the key summary and conclusion of this research are outlined. Suggestions for the design and development of fatigue-tolerant architected materials are made.

Chapter 2

Literature Review

2.1 Fatigue Behaviour of Monolithic Materials: Conventional Wisdom vs. Modern Insights

Fatigue is one of the most common failure mechanisms in many engineering systems [52–54]. The peculiarity of the damage process is that metallic parts are subject to cyclic loading at stress levels well below the ultimate strength provoking fracture in the material. Structural failures can take place following millions or even billions of cycles, compromising the durability of the engineering components [55, 56].

The fatigue failure process is often characterized by three stages [55]. In the first stage, the repeated loading induces the glide of crystalline defects, which leads to the initiation of cracks along the crystallographic planes with the maximum shear stresses. In the second stage, once the crack size reaches a certain threshold, the cracks start to

propagate in a plane perpendicular to the applied load. Eventually, the crack growth leads to the final fracture of the material.

Characterization of fatigue failure involves the evaluation of fatigue life in terms of stress-life (S-N) or strain-life (ϵ-N) approaches. The value is highly dependent on the applied stress or strain during the test. When the stresses associated with the failure are low, material deformations are largely elastic, and crack initiation takes up the majority of the fatigue life; the number of cycles to failure under high cycle fatigue is often assessed by the stress-based approach. Conversely, under low cycle fatigue, materials undergo substantial plastic deformation. The fatigue failure is mostly governed by the crack propagation process. The strain-based approach is usually used to characterize the fatigue life in this case. The focus of this work is on the fatigue behaviour in the high cycle regime owing to the common loading conditions in practice.

The high cycle fatigue properties of AM Ti-6Al-4V have been widely reported in the literature [19, 57, 58]. The fatigue performance in the high cycle regime is often described by the fatigue limit or fatigue strength – the threshold stress before crack propagation starts [59]. Figure 2.1 provides some data available in the literature in comparison with that for conventionally manufactured counterparts. AM Ti-6Al-4V demonstrates at least two to three times lower fatigue strength than those prepared by forging or wrought, which confirms fatigue is one of the overarching concerns of AM materials. Since crack initiation is the dominant stage in high cycle fatigue, the fatigue strength of AM materials is highly sensitive to the presence of manufacturing defects. Existing research suggests there are four factors primarily facilitating the initiation

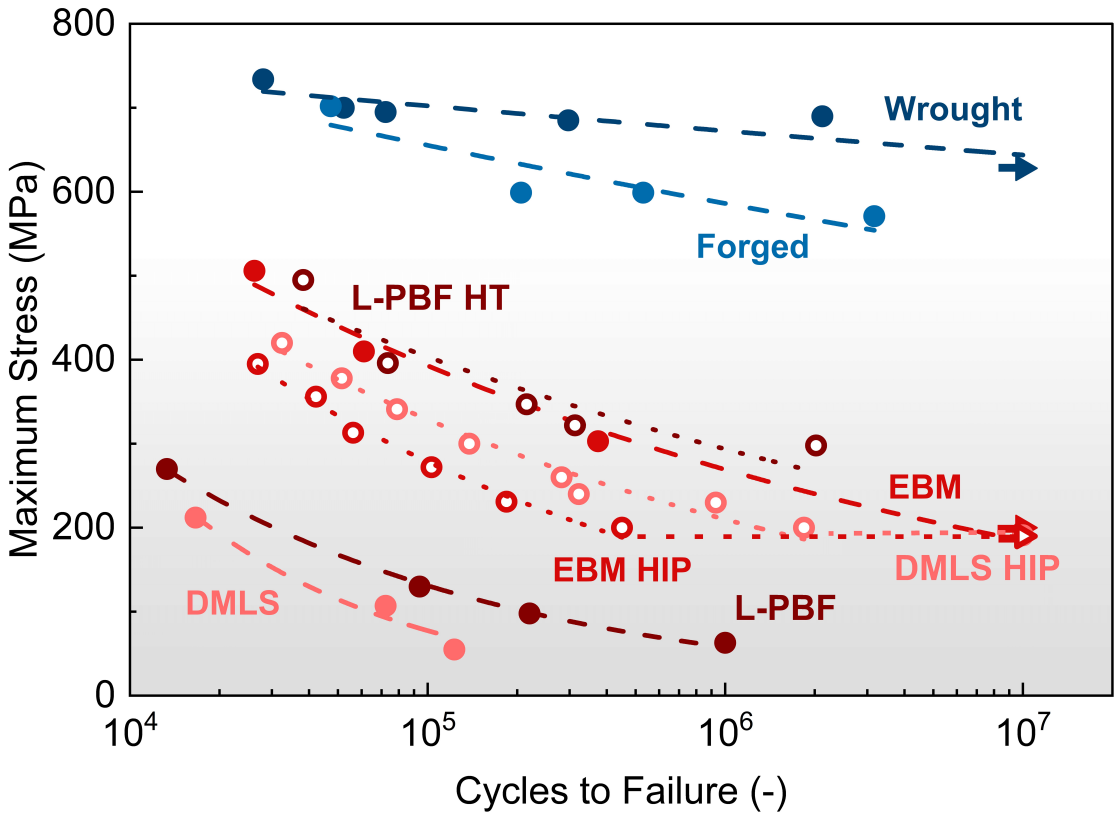


Fig. 2.1 Maximum applied stress vs. cycles to failure for AM Ti-6Al-4V against conventionally manufactured counterparts. Data provided includes Ti-6Al-4V prepared by L-PBF [61], L-PBF and then heat treatment (HT) [62], EBM [63], EBM and then hot isostatic pressing (HIP) [64], DMLS [65], DMLS and then HIP [64], forging [66], and wrought [65].

process: surface quality, porosity, residual stress, and microstructure [19, 60, 54]. The influence of these factors on the fatigue behaviour of AM materials will be discussed in Sec. 2.3.

2.2 Fatigue Behaviour of Architected Materials

Much fewer reports of the fatigue properties have been found on architected materials than on monolithic materials. Despite the lack of testing standards, uniaxial

compression-compression configuration has been adopted in most of the previous work owing to the simplicity in experimentation [49, 67, 48, 68, 69]. Specimen geometry is often designed following the International Standard ISO 13,314 – the rule of thumb for the quasi-static mechanical testing of porous and cellular metals. The linear dimensions of the specimen must be no less than 10 times the average cell size in order to minimize the influence of the specimen edge. Solid plates can be added to the top and bottom of the specimen to provide a better alignment between specimen surfaces and compression plates.

The majority of the compression fatigue tests of architected materials in the literature were performed at a load ratio of R=0.1. Hence, the usual practice of fatigue assessment starts with determining the quasi-static mechanical properties of cellular materials such as yield strength [49, 70]. Cyclic tests are then conducted at maximum applied stresses between 0.8 and 0.1 of the yield strength to assess the fatigue performance between 10^3 and 10^6 cycles. The fatigue strength of architected materials is usually determined by extrapolating the S-N curves to 10^6 cycles.

The failure process of architected materials under cyclic loading is vastly different from that of monolithic materials [48, 68, 49]. Figure 2.2 (A) illustrates the damage evolution process in three stages. Initially, there is a rapid strain accumulation within the first ∼100 cycles dominated by cyclic ratcheting. A relatively flat strain plateau is then observed resulting from a combination of ratcheting together with crack initiation and propagation. The number of cycles at which the crack initiation starts N_{i} can be dictated by the deviation of slope between minimum and maximum strains [69].

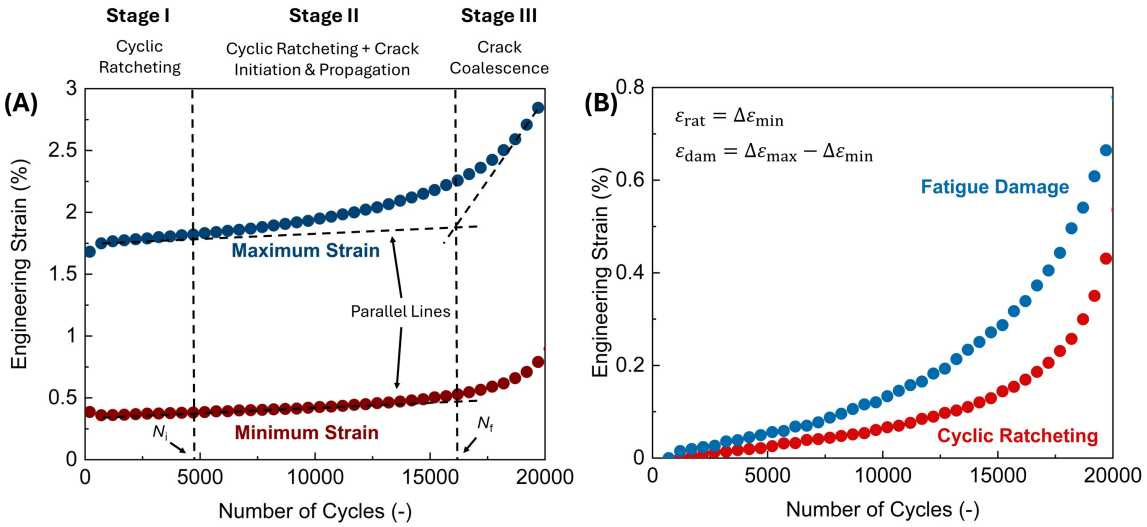


Fig. 2.2 (A) Maximum and minimum strain evolution of a BCC Ti-6Al-4V lattice under cyclic loading. (B) The cyclic ratcheting and fatigue damage strains of the lattice.

It has been proven that crack initiation starts earlier in the life cycle as the applied stress increases [69]. Finally, a sudden increase in strain is caused by the interaction of multiple cracks. The fatigue life N_f is determined by intersecting the line of minimum strain plateau with the line of rapid failure [48, 71, 69].

The cyclic ratcheting and fatigue damage (crack initiation and propagation) strains can be quantified based on the maximum and minimum strain curves [48, 69, 49]. The cyclic ratcheting strain ε_{rat} can be evaluated by the translation of minimum strain ε_{min} following [48]:

$$\varepsilon_{rat} = \varepsilon_{min,\,i} - \varepsilon_{min,\,1} = \Delta\varepsilon_{min} \tag{2.1}$$

where $\varepsilon_{min,\,i}$ and $\varepsilon_{min,\,1}$ are the minimum strain of the ith cycle and the first cycle, respectively. On the other hand, the fatigue damage strain ε_{dam} can be given by the

difference in strain range between the ith cycle and the first cycle following [48]:

$$\begin{aligned} \varepsilon_{\text{dam}} &= (\varepsilon_{\text{max, i}} - \varepsilon_{\text{min, i}}) - (\varepsilon_{\text{max, 1}} - \varepsilon_{\text{min, 1}}) \\ &= \Delta\varepsilon_{\text{max}} - \Delta\varepsilon_{\text{min}} \end{aligned} \tag{2.2}$$

where $\varepsilon_{\text{max, i}}$ and $\varepsilon_{\text{max, 1}}$ are the maximum strain of the ith cycle and the first cycle, respectively. An example of the analysis is provided in Figure 2.2(B). Clearly, both the ratcheting and damage strains increase at higher rates as the number of cycles proceeds. In this case, the fatigue damage strain dominates across the entire life cycle. This likely results from the large bending deformation in the BCC structure. Zhao et al. [72] suggested larger bending deformation of the struts could lead to a higher contribution of crack initiation and propagation to the overall failure process while increasing the buckling deformation of the struts could give rise to greater cyclic ratcheting strains. Yet, this statement was drawn from only three specimens and could be further validated with more types of lattice structures.

The cyclic ratcheting rate has also been evaluated in many previous works [48, 69, 49, 72]. This has been defined as the slope of the mean strain prior to N_{f}. The ratcheting rate shows a linear correlation with the applied stress when they are plotted in a log-log scale [48, 69, 49]. The correlation has been proven to be strongly dependent on the lattice topology [72], materials type [69, 43, 73], and relative density [48].

Similar to monolithic materials, the high cycle fatigue properties of architected materials are often characterized by fatigue strength [43, 74–77]. Li et al. [48]

demonstrated that the mathematical expression of the Gibson-Ashby model could also be used to describe the relationship between fatigue strength Σ_{f} and relative density ρ_r following:

$$\Sigma_{\mathrm{f}} = A\rho_r^m \tag{2.3}$$

where A and m are material constants. However, the underlying meanings of the parameters are to be explored. Some of the earlier works showed that the S-N curves normalized by the yield strength are independent of the relative density [78, 79]. Therefore, it was suggested that normalized fatigue strength, also known as endurance ratio, could be a useful parameter to inform the fatigue performance of a particular lattice topology. Yet, this was considered to be speculative in a recent review paper by Benedetti et al. [43]. They showed the normalized fatigue strength generally decreased as the relative density reduced. Thus, the comparison of endurance ratios across different types of lattices is only valid when the lattices are of similar relative density. Figure 2.3 provides a summary of the endurance ratios of different AM titanium lattices. The correlation between normalized fatigue strength and relative density is found to be similar to [43]. Multiple studies showed that TPMS-based structures demonstrated higher normalized fatigue strength than most of the strut-based structures owing to the continuous surface curvature and minimal stress concentrations at the nodes [80, 81, 49]. This has also been confirmed in this work (see Figure 2.3). Nevertheless, a later report showed some of the auxetic structures made of commercially pure titanium (CP-Ti) demonstrated higher endurance ratios than any other structures reported in

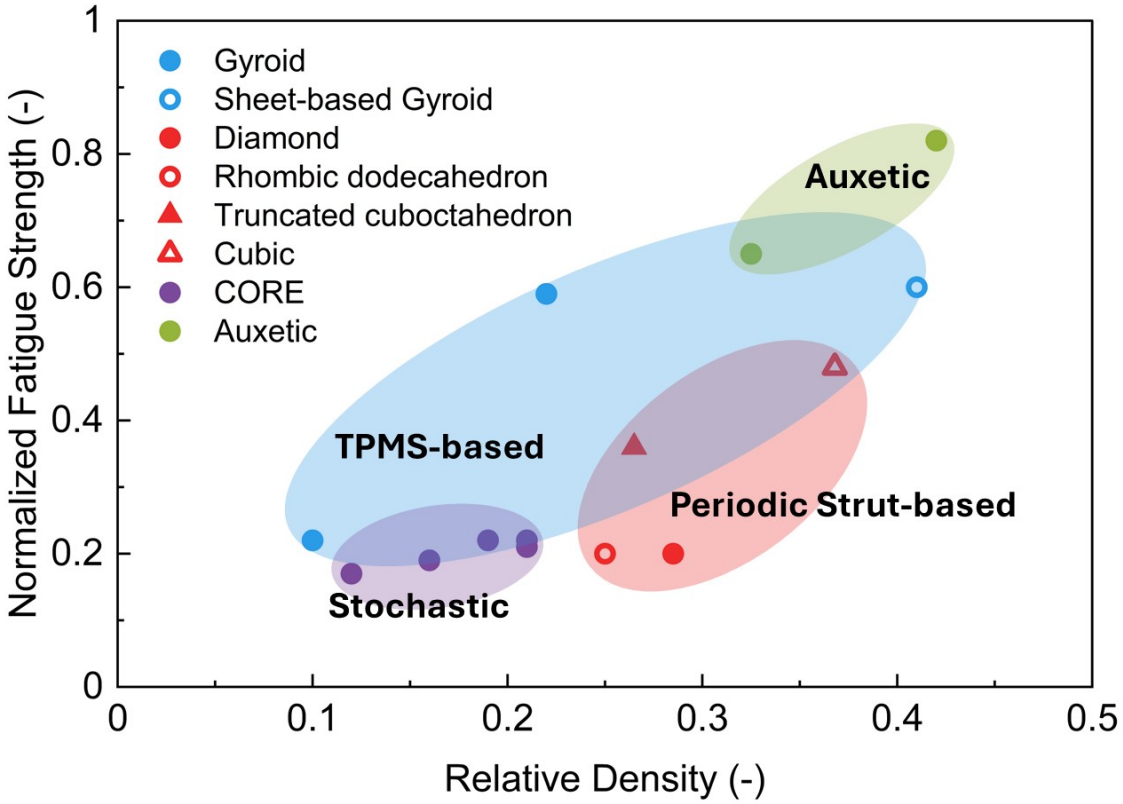


Fig. 2.3 Fatigue strength of AM titanium lattices normalized by the yield strength as a function of the relative density. Data was adapted from [81, 80, 85, 78, 79, 72, 83, 82].

the literature [82]. This results from the high compressive forces along the struts that hinder the fatigue crack initiation and propagation processes [75, 79]. Additionally, most of the fatigue research to date focuses on periodic strut-based and TPMS-based structures. Very few attempts have been made on stochastic lattices [83, 84]. The stochastic geometry not only offers improved isotropy to undertake complex loading conditions but also provides stronger damage tolerance [37, 5]. An assessment by Kechagias et al. [83] showed CORE lattices had comparable endurance ratios as the periodic strut-based counterparts. Research on stochastic lattices is still in its infancy and further effort is needed to confirm the potential of these structures.

Apart from the lattice topology, there is a growing curiosity in exploring the fatigue properties of lattices made of different materials [74, 86, 75]. Existing literature is largely dominated by Ti-6Al-4V lattices. However, it has been shown structures made of ductile materials such as CP-Ti, Ta, Co-Cr, and β Ti exhibit higher endurance ratios than Ti-6Al-4V counterparts [74, 75, 69]. The high ductility of these materials gives rise to a lower cyclic ratcheting rate and hinders fatigue crack propagation. Liu et al. [69] showed the β grains in Ti-24Nb-4Zr-8Sn alloy could form large plastic zones ahead of the crack tip leading to lower stress concentrations and crack propagation rates than Ti-6Al-4V lattices. This is very different from the scenario when monolithic materials are printed. The high cycle fatigue properties of monolithic materials are governed by the crack initiation process. Hence, the fine α' microstructure of AM Ti-6Al-4V can give rise to higher fatigue strength than CP-Ti and β Ti counterparts [87–89]. The difference in fatigue failure mechanisms between architected and monolithic materials suggests material utilization toward high ductility should be adopted for the fatigue-tolerant design of lattice structures. Moreover, examination of the fatigue crack initiation in monolithic materials may provide limited insight into the cyclic deformation process of architected materials.

The fatigue fracture behaviours of architected materials have been measured extensively [90, 68, 49, 72, 91]. Figure 2.4 shows an example of the damage evolution process of an AM Ti-6Al-4V lattice. Initial strut fracture can be observed at around 75% of fatigue life. Subsequently, multiple strut failure events occur up to 98% of the life cycle. After that, the structure starts to collapse and a shear band is formed at 45° to the

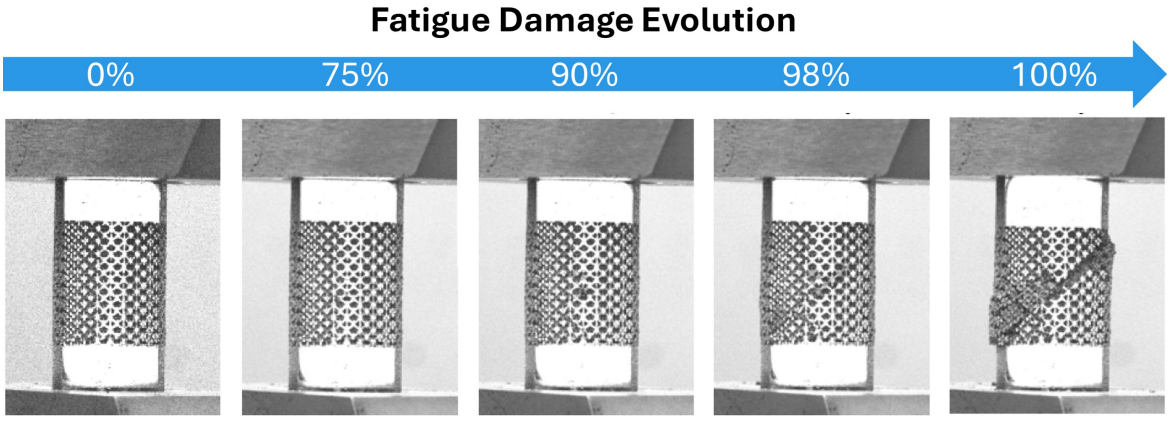


Fig. 2.4 Fatigue failure process of an AM Ti-6Al-4V lattice. Adapted from [90].

load direction. While shear fracture is the predominant deformation mode reported in the literature, Yang et al. [49] showed uniform deformation under cyclic loading could also occur in TPMS structures when the specimens are subject to high applied stresses (see Figure 2.5). The transition in the failure mode is yet to be understood.

The microscopic deformation of individual struts has also been revealed in a few reports, with a primary focus on lattices made of Ti-6Al-4V [48, 90, 82, 81]. Most of the literature shows that surface irregularities serve as the fatigue crack initiation sites in architected materials [48, 82, 81]. Crack propagation is characterized by fatigue striations and dimple fracture is observed at the end of the propagation path. Li et al. [48] proved when a Ti-6Al-4V lattice was under cyclic loading, dislocations were produced along the α' grain interface, which might retard the cyclic ratcheting of the structure. These findings are roughly consistent with the micromechanical behaviour of bulk Ti-6Al-4V alloys indicating some commonalities in fatigue behaviour are shared between monolithic and architected materials [19, 92].

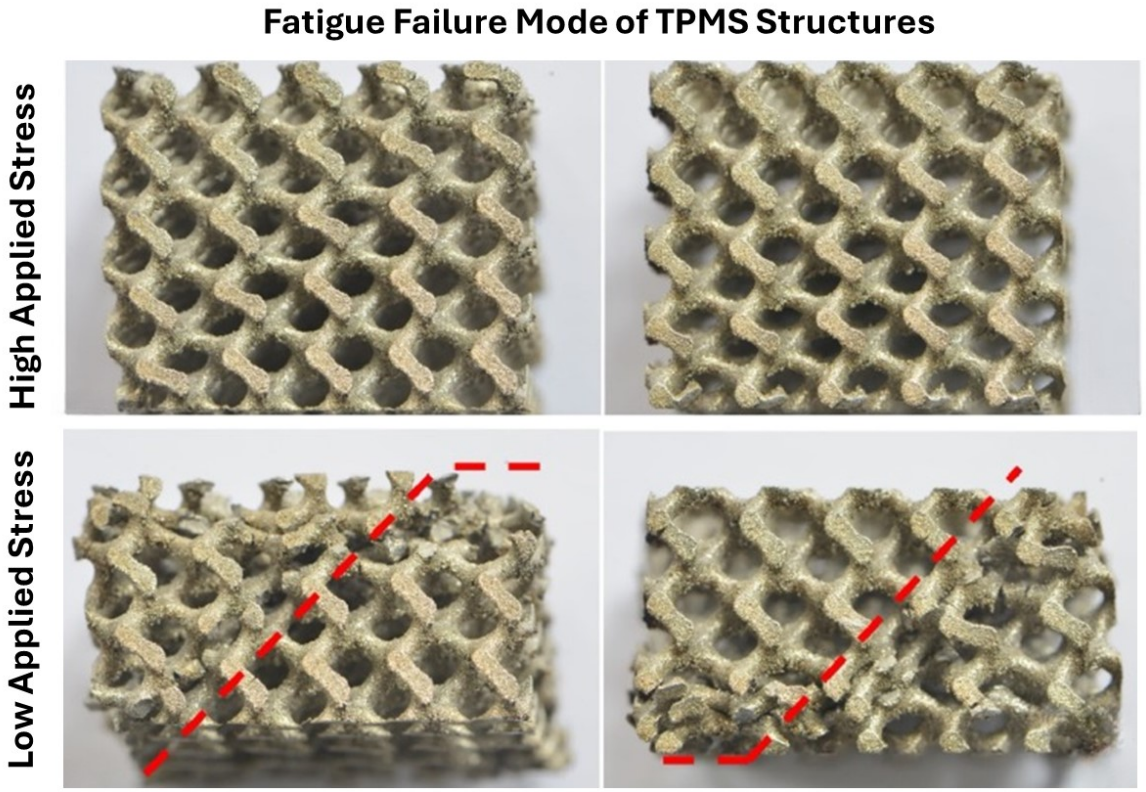


Fig. 2.5 Fatigue failure mode of TPMS structures tested at 0.9 (high) and 0.75 (low) of the yield strength. Adapted from [49].

2.3 Contribution of Structural Inhomogeneity to the Fatigue Fracture Process

The discussion so far has considered the influence of relative density, lattice topology, and material type on the high-cycle fatigue properties of architected materials. However, the variation in geometrical features as well as the processing conditions can induce structural inhomogeneities within the printed parts. These inhomogeneities include defects and microstructure triggered by the thermal cycling of the AM process. To date, there has been extensive research on the influence of these inhomogeneities on the fatigue properties of monolithic materials [19, 58, 57, 54, 93, 94]. Yet, not many

reports can be found on the correlation between these structure inhomogeneities and fatigue properties of architected materials [49, 81]. Owing to the different fatigue failure mechanisms between architected and monolithic materials, the influence of these inhomogeneities on the fatigue properties may differ. Hence, further effort is required to isolate their contribution to the fatigue fracture process and mitigate their influence through design and processing. Here, we summarize different structural inhomogeneities that arise from the AM process and discuss how they affect the fatigue performance of architected materials.

2.3.1 Surface Roughness

AM components are usually plagued by the as-built surface quality [60, 95, 96]. The rough surface primarily results from three factors: (1) the staircase effect intrinsic to the AM process, (2) partially melted powders adhered to the surface, and (3) melt pool instability such as incomplete melting and splashing [60, 19]. The working principles of AM techniques set fundamental limitations on the achievable surface quality of printed parts [97, 19]. Generally speaking, L-PBF adopts layer thicknesses of 20 μm - 100 μm, which are significantly lower than those of EBM (50 μm - 150 μm) and DMLS processes (40 μm - 1000 μm) [35, 98, 99]. Moreover, the L-PBF process also offers smaller spot sizes (50 μm - 180 μm) than the other two techniques [35, 99]. The combination of these two characteristics governs parts made by L-PBF smoother surfaces than EBM and DMLS counterparts.

The surface quality is not consistent across the printed parts [19, 3]. It is known that the downward-facing surface typically has a lower surface quality than the otherward-facing surface [100, 101]. This largely results from the dross formation in the overhang region [100, 101]. The loose powders below the downward-facing surface have lower thermal conductivity than the solid parts. Hence, when the energy beam interacts with these powders, excessive heat accumulates in the overhang region leading to the collapse of a quasi-steady melt pool, which results in the melting of excess materials [101]. Furthermore, when parts are printed at low angles (0° - 30°) relative to the build plate in the powder bed systems (L-PBF and EBM), support structures are often added to provide fixation of the parts [102, 35]. These structures need to be removed after the fabrication leaving connection marks on the sample surfaces, which degrades the surface quality of the specimens. On the other hand, support structures can also facilitate the heat transfer from specimens to the build plate, which gives rise to improved melt pool stability limiting the formation of dross defects [103–105].

The correlation between surface defects and fatigue properties of AM materials has been investigated extensively [49, 106–108]. These irregularities act as micro-notches for crack initiation leading to early fatigue failure. It has been proven the fatigue strength of monolithic materials made by AM is highly dependent on the size of the surface defect described by Murakami parameter $\sqrt{A_{\mathrm{P}}}$ where A_{P} is the projection area of the defect perpendicular to the load direction [109, 110]. Even though there is no numerical model correlating the surface defect and fatigue properties of architected materials

available in the literature to the authors' best knowledge, experimental evidence shows rough surfaces can also reduce the fatigue strength of architected materials [49, 81].

Evaluation of surface roughness is usually performed using the arithmetic mean height (R_a for a line and S_a for a surface) following [3]:

$$R_a(\text{for a line}) \text{ or } S_a(\text{for a surface}) = \frac{1}{N}\sum_{i=1}^{N}|h_n| \tag{2.4}$$

where N is the number of measured locations along a line or a surface and h_n is the height profile. However, several studies have suggested R_a and S_a are unsatisfactory for capturing the critical defects and other parameters such as maximum peak-to-valley height R_t and maximum valley depth below the mean profile R_v could better characterize the fatigue behaviour [108, 111, 61, 112].

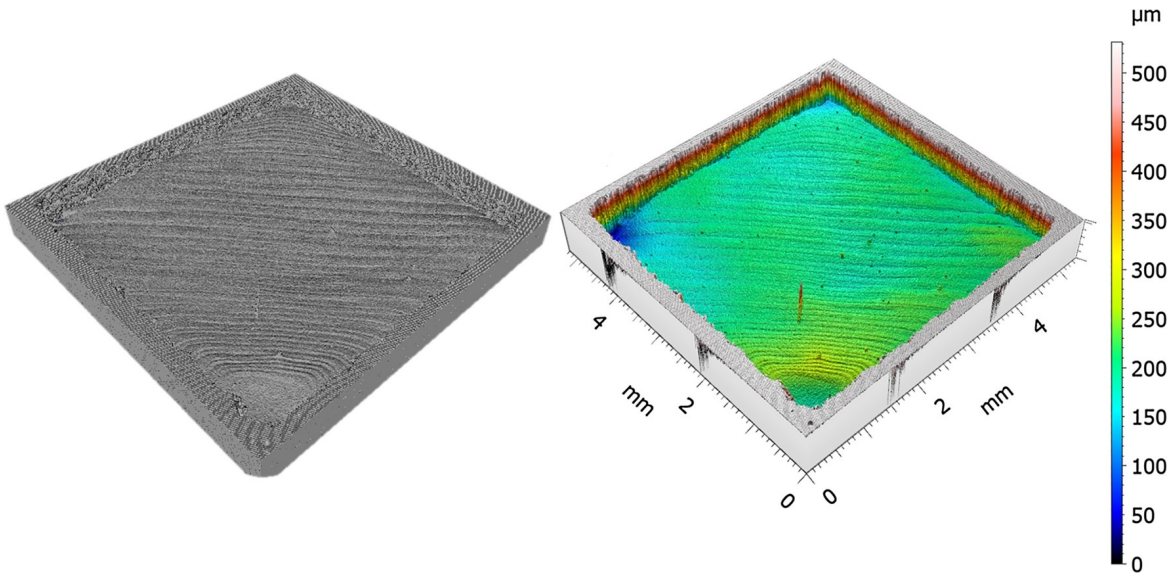


Fig. 2.6 Measurement of an internal surface by XCT. Adapted from [113].

Conventionally, surface quality is measured using the stylus profilometer but the stylus tip may be damaged by the protrusions when AM materials are measured [114]. Non-contact techniques including focus variation microscopy and confocal microscopy could serve as alternatives. Yet, the AM specimens may exhibit vastly different optical properties from the flat surface compromising the accuracy of the optical techniques. Recently, there has been an increasing interest in evaluating the surface roughness by X-ray computed tomography (XCT). The surface profile can be extracted from the volumetric data, which opens up this method for surface characterization [114, 115]. This is particularly suitable for architected materials since the measurement can be performed on curved surfaces as well as struts in different printing orientations. An example of measurement by XCT is shown in Figure 2.6. A recent report has also shown that XCT can capture deeper surface notches as compared to optical techniques [116]. Nevertheless, concerns have been raised about the improper calibration of edge detection algorithms and quantification of measurement error [117].

2.3.2 Geometrical Inaccuracy

The discrepancy between the printed specimens and designed files always exists governed by the finite size of the melt pool inherent in the AM techniques [7, 49, 77]. This is especially the case in architected materials when fine features such as struts and thin walls are printed. The melt pool size can be lowered to improve the printing accuracy by optimizing the processing conditions [118, 119]. However, this needs to be balanced with the prolonged printing duration incurred by the smaller melt pool. The

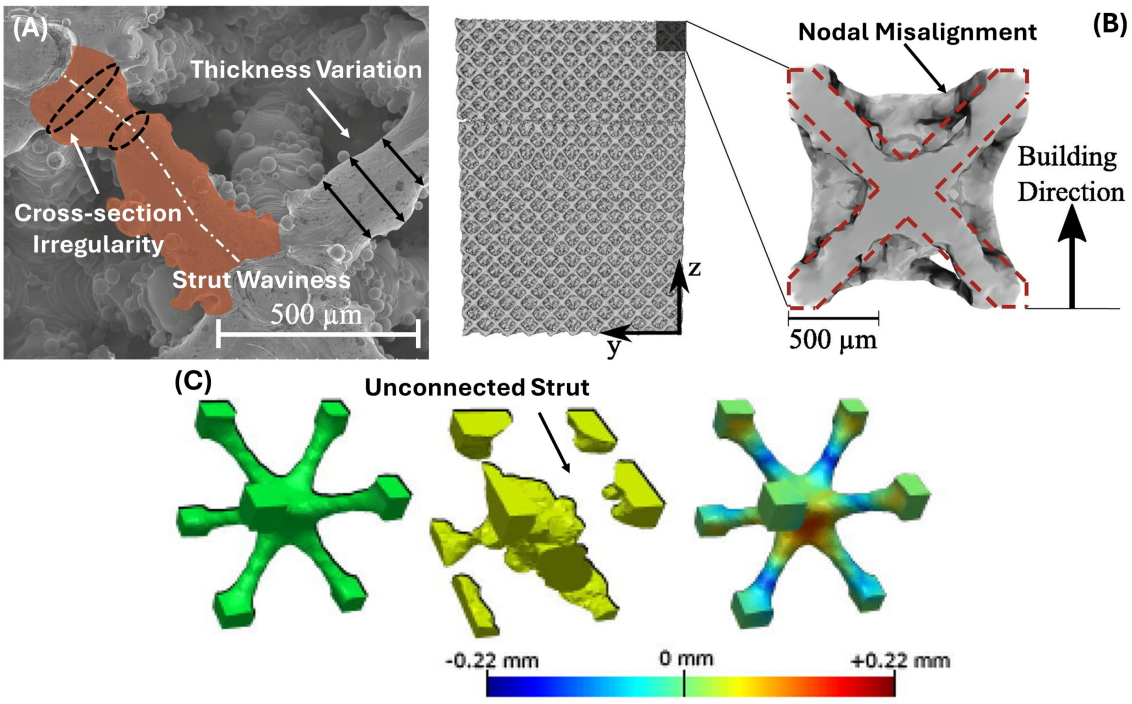


Fig. 2.7 Examples of (A) strut thickness variation, waviness, cross-section irregularity, (B) nodal misalignment, and (C) unconnected strut. Adapted from [7, 121].

morphology of the melt pool is also strongly dependent on the thermal properties of materials [119]. Under the same energy input, alloys with high thermal conductivity and low absorptivity such as AlSi10Mg would have a larger melt pool than stainless steel followed by Ti-6Al-4V [119]. Hence, processing parameters must be carefully tailored to attain the optimal melt pool size for different materials. Additionally, uncertainty may be further induced by the material shrinkage during the cooling stage of the manufacturing process [120].

As shown in Figure 2.7, the geometrical deviation reported in the literature can be primarily categorized into five different groups [122–125]:

- Strut thickness variation: Lattice structures often exhibit non-uniform distributions of strut thickness [122, 124, 126]. When the specimens are printed in powder bed systems, vertical struts are typically thinner than the designed thickness whereas horizontal struts are usually over-melted and thicker than the nominal value [126, 127]. This is mainly attributed to the dross formation together with the gravitational forces that drag the melt into the powders underneath the horizontal struts [128]. In addition, excessive accumulation of material has been observed near the nodes of strut-based structures [129, 130]. This likely results from the fusion of the melt when two adjacent struts are printed.

- Strut waviness: The central axis of the printed strut may also deviate from that of the designed profile [69]. Similar to the thickness variation, it has been shown horizontal struts exhibit larger deviations of the central axis than those printed in other orientations [131, 132].

- Cross-section irregularity: The shape of strut cross-sections can exhibit substantial differences from the nominal circular shape owing to the irregular distribution of materials [133, 134]. Several reports suggested horizontal struts are prone to be elliptical while vertical struts are circular [134, 133].

- Nodal misalignment: The node centres of the printed specimens may not coincide with those of the designed geometry as a result of the uneven accumulation of material [135, 133, 126]. Yet, the offset is usually quite small compared to the unit cell size when the lattices are printed in powder bed systems [133, 126].

- Unconnected strut: Struts may be unconnected in the as-printed state, especially when the feature size is approaching the processing limit of AM techniques (∼200 μm for L-PBF and ∼400 μm for EBM) [125, 7, 136]. Again, the unconnectivity is found more often in horizontal struts than in vertical struts owing to the lack of support when horizontal members are printed [125].

The correlation between these geometrical deviations and quasi-static mechanical properties of architected materials has been well studied [137, 135, 125]. However, little research can be found on their influence on fatigue properties [133, 138]. Unlike elastic modulus and yield strength, fatigue failure is generally caused by local damage development, which is highly sensitive to fine details [43]. Hence, it might be very difficult to analyze numerically the contribution of each type of geometrical inaccuracy to the fatigue fracture process. Lately, it has been proven possible to integrate XCT with finite element analysis (FEA) to accurately capture the stress state close to experimental conditions [139, 133, 138]. Amani et al. [139] found a better agreement in strut failure between experimental observation and simulation by adopting the XCT-based FEA model during the monotonic compression of AlSi10Mg lattices. This approach has been later adopted in the fatigue study of architected materials [133, 138]. The results suggested geometrical offset might introduce additional stress states such as strut bending leading to higher stress concentrations in the structure [133, 138].

2.3.3 Processing-induced Porosity

Porosity can be induced by the complex interaction between the energy beam and matter [3, 140, 141]. Previous research has revealed three primary pore formation mechanisms during the AM process: (1) At high energy density ($>10^5$ W cm^{-2}), the fusion process may shift from thermal conduction mode to keyhole mode resulting in the evaporation of alloying elements and deep penetration of the energy beam into the molten metal [142, 143]. Subsequently, this leads to the formation of vapour cavities and the collapse of these cavities can leave pores in the solidified material. These keyhole pores mainly consist of entrapped vapour and are largely spherical [142, 143]. (2) The atomization process of metallic powders can introduce gases into the powder particles [144, 145]. Furthermore, shielding gas in the chamber may also be entrapped in the melt pool during the manufacturing process resulting in the formation of pores [144, 145]. The gas pores are generally the smallest and exhibit spherical shapes. (3) Inadequate melting of the powder particles can lead to elongated irregular pores, also known as lack-of-fusion pores [144, 145]. Examples of the three types of pores are shown in Figure 2.8.

Based on the formation mechanisms, one can summarize it is possible to minimize the porosity level within AM parts by optimizing processing conditions [147, 148]. However, the local thermal conditions are also dependent on the geometrical features [149, 150]. For example, when inclined struts are printed, the overheating in the overhang region can lead to keyhole pore formation [101]. Thus, pores may tend to concentrate near the downward-facing surfaces, especially in low-angle struts [101].

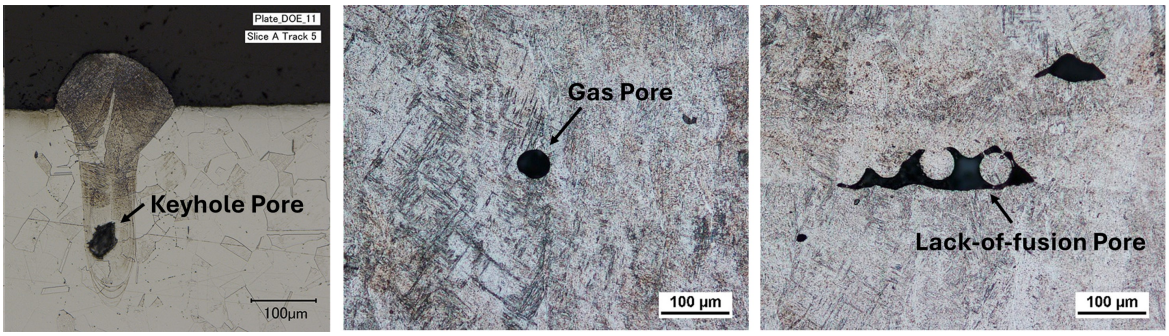


Fig. 2.8 Examples of a keyhole pore, a gas pore, and a lack-of-fusion pore. Adapted from [146, 144].

Moreover, the utilization of support structures can facilitate the heat transfer between parts and the build plate alleviating the entrapment of gas and keyhole pores in the solidified parts [102, 151]. Yet, this may not be applicable to all the components since it is very difficult to add support structures for the fabrication of lattice structures. This suggests the optimal processing conditions may differ between architected and monolithic materials, or even for different geometries. Often, contour scans are employed near the sample edges to achieve an improved surface finish whereas hatch scans are used to infill the interior to lower the porosity [152, 150]. Yet, the mismatch between contour and hatch tracks can give rise to the formation of near-surface pores [152, 150]. This phenomenon may not be very notable in lattice structures since every pore can be considered as subsurface in thin struts.

The effect of porosity on the fatigue fracture process of monolithic materials has been studied extensively in the literature [153–155]. It has been shown that only the internal pores near the initiation sites (≤ 1 pore diameter away from the initiation sites) can facilitate the surface-initiated fatigue fracture process [154, 58]. The contribution of the pores to the fatigue properties is primarily determined by their size, shape, and

distance from the crack initiation site [154]. In general, large elongated pores close to the initiation sites are detrimental to the fatigue resistance of AM materials [154]. On the other hand, most of the reports on architected materials showed pores could be found on the fatigue fracture surface but are far away from the initiation site suggesting porosity has a minimal influence on the failure process [49, 48, 69]. This was further supported by Boniotti et al. [156]. Their results confirmed cracks initiated from the surface even in the vicinity of internal porosity. Nevertheless, it has been shown fatigue crack initiation could also occur at internal pores in lattice structures but the final fracture is governed by those cracks initiated from the surface defects [72].

2.3.4 Residual Stress

The repeated addition of molten metals to solidified layers prompts the formation of residual stresses [157, 158]. These remaining stresses in the material are usually categorized into three groups based on their length scales [158, 159]. Type I residual stresses are in macroscopic scales and often result in part distortion or even delamination of layers. During the AM process, the newly deposited layers are usually hotter than the prior layers and hence the contraction of the solidifying material is constrained by the underlying substrate leading to the development of tensile residual stresses in the solidifying layer and compressive residual stresses in the underlying substrate [158, 159]. Type II residual stresses are on the scale of the microstructure and they are induced by local microstructural variations such as the anisotropic behaviour of each grain. Type III residual stresses are formed at the atomic level resulting from the

dislocations and other crystalline defects. In the AM literature, Type I residual stresses are almost the sole focus owing to their critical influence on mechanical properties and thus they form the focus of our following discussions [158, 159].

The formation mechanisms of type I residual stresses govern the top and bottom regions of AM specimens are usually subject to tensile stresses whereas the central parts tend to be in compression [160–162]. This has also been validated numerically (see Figure 2.9) [162]. The development of macroscopic residual stresses is strongly determined by the sample geometry [163–165]. Numerous studies reported as the sample height increased, there were larger residual stresses accumulated in the part [163–165]. Hence, special care must be taken during the fabrication of large components. The magnitude of residual stresses is also governed by material properties. Bartlett et al. [158] have stated that alloys with low thermal diffusivity and conductivity such as Ti-6Al-4V would be prone to the accumulation of high residual stresses. Gu et al. [166] suggested residual stresses could be minimized by adopting materials with low elastic modulus and coefficient of thermal expansion.

Two of the most commonly used approaches to alleviate residual stresses are build plate preheating and post-process heat treatments [167, 168, 163]. The EBM process has an inherent preheating step which often leads to lower residual stresses developed in EBM parts than L-PBF and DMLS counterparts [63, 169]. However, the parameters for these treatments need to be tailored to minimize any undesirable microstructural change [170]. Moreover, the addition of support structures can also lower the thermal gradient in the part reducing the risk of manufacturing failure [171, 172].

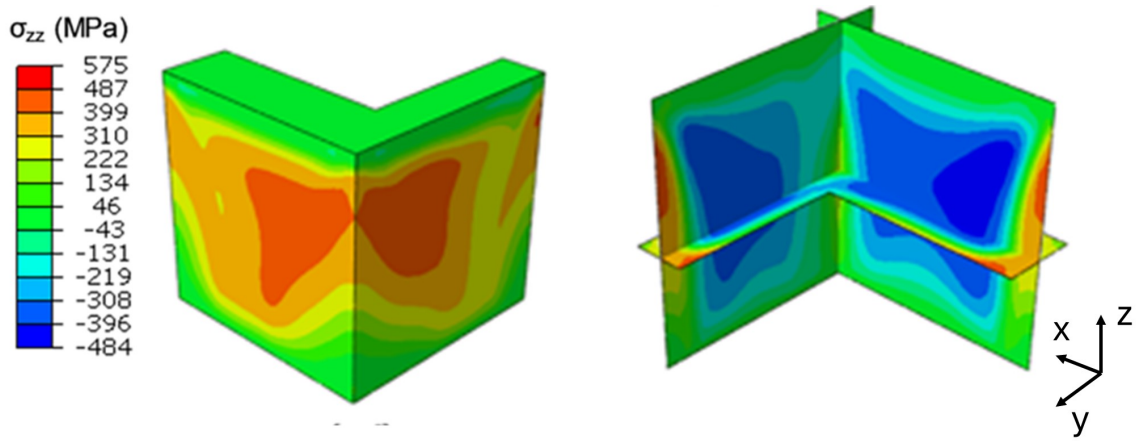


Fig. 2.9 Numerical simulations of residual stress accumulation along the build direction. Adapted from [162].

It is well known that tensile residual stresses can add to the applied stress facilitating the fatigue failure process whereas compressive residual stresses inhibit the fracture process [173–175]. Leuders et al. [176] proved tensile residual stresses can accelerate the fatigue crack propagation while the initiation process was greatly determined by the presence of porosity. This is further supported by the linear relationship between the fatigue crack growth rate of AM Ti-6Al-4V and maximum tensile residual stresses reported by Mukherjee et al. [177]. These results suggested residual stresses would have a profound influence on the fatigue properties of architected materials since crack propagation is one of the primary damage mechanisms as discussed in Sec. 2.2. The non-uniform distribution of residual stresses may give rise to anisotropic fatigue properties [178]. This is also expected to be notable in lattice structures due to the complex residual stress distributions arising from the geometry.

Measurement of residual stresses is usually performed by X-ray diffraction (XRD) and neutron diffraction (ND) following Bragg's law [176, 174, 175, 179]. However, these

non-destructive techniques are highly sensitive to the shape and surface condition of the specimens, and hence may not be applicable to architected materials. In a recent study, destructive micro-hole drilling integrated with digital image correlation (DIC) has been used to evaluate the residual stresses in lattice structures [133]. Despite proving residual stresses are strongly location-dependent in lattices, the technique could only quantify the residual stresses at the measurement positions.

2.3.5 Microstructure

AM parts typically exhibit fine microstructure and for several materials, columnar grains are formed [3, 35]. In most of the AM processes, the intensified energy beam triggers immediate grain nucleation and gives rise to competitive grain growth in the middle of the melt pool. Grains with easy growth directions aligned with the solidification front normal outgrow the misaligned grains during the solidification process leading to the development of columnar structures [180]. The rapid cooling rate subsequently renders the formation of fine grains governing the final microstructure.

The complex geometry of architected materials may give rise to a highly heterogeneous microstructure [181, 182]. Figure 2.10 depicts the grain structures within a 316L stainless steel lattice made by L-PBF. Elongated grains along the strut orientation can be observed as a result of the heat flux dissipation along the strut [182]. These grains are also found to be highly textured with preferred crystallographic orientations of $< 100 >$ – the easy growth direction for FCC crystals. Additionally, observations show

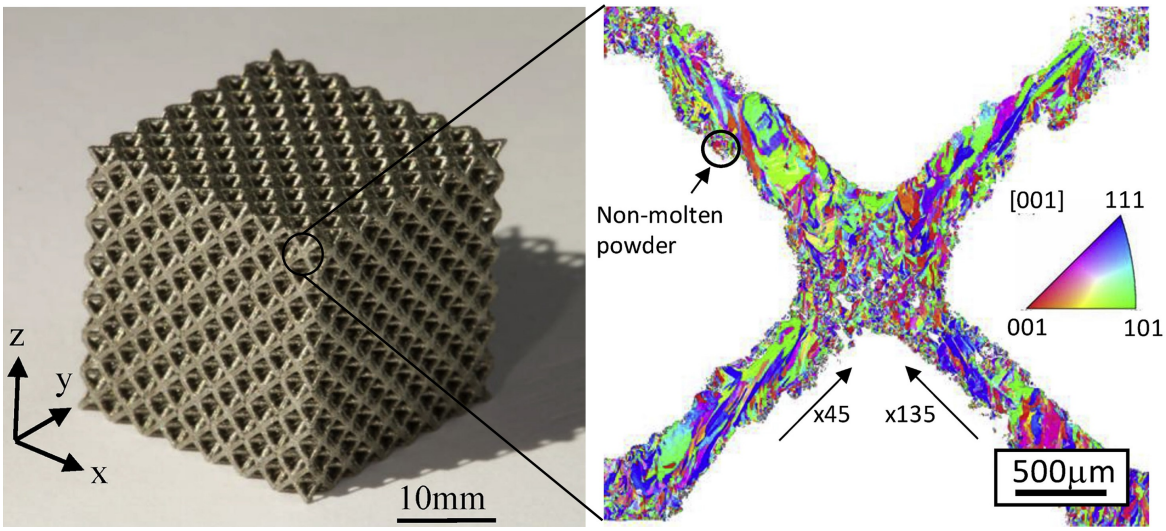


Fig. 2.10 Electron backscatter diffraction (EBSD) map of an L-PBF 316L stainless steel lattice. Adapted from [181].

that partially melted powders adhere to the downward-facing surface of the struts exhibiting a relatively isotropic microstructure.

Improved fatigue properties of architected materials can be attained by toughening the microstructure [90, 183, 74]. This is usually achieved by post-process heat treatments and HIP [90, 183]. The coarse microstructure can induce crack-blunting lowering the fatigue crack propagation rate [184].

2.4 Processing and Design Means of Improving Fatigue Behaviour

The presence of these structural inhomogeneities is inevitable in AM lattices. However, measures must be undertaken to curtail the imperfection levels limiting their influence

on the fatigue properties of architected materials. Here, we review both the processing and design approaches to prolong the fatigue life of lattice materials.

2.4.1 Customization of Processing Conditions

Processing parameters such as beam power, scan speed, and exposure time are the bedrock for the fabrication of fully dense AM parts [185, 18, 186, 152]. It has been proven possible to produce lattice structures with porosity levels $< 1\%$ when the processing parameters are optimized [185, 186]. Yet, it was also shown minimizing porosity through the optimization of processing parameters was only achievable in thick-walled structures resulting in an improved fatigue resistance [152]. The thin-walled specimens exhibited consistent porosity levels under various processing conditions, which seemly result from the poor surface quality [152].

The geometrical features and surface conditions are also strongly correlated with the processing parameters [186]. When the beam energy is low, insufficient melting of powders occurs resulting in poor surface quality and even unconnected struts in the as-printed condition. At a high beam energy, powders are overheated yielding melt pool instability and dross formation. These findings are largely consistent with those reported on monolithic materials [187, 116]. Großmann et al. [186] also proposed above a certain laser power threshold, a scaling law could describe the relationship between strut diameter d and laser parameters $d \propto \sqrt{P/v}$ (see Figure 2.11), where P is the laser power and v is scan speed.

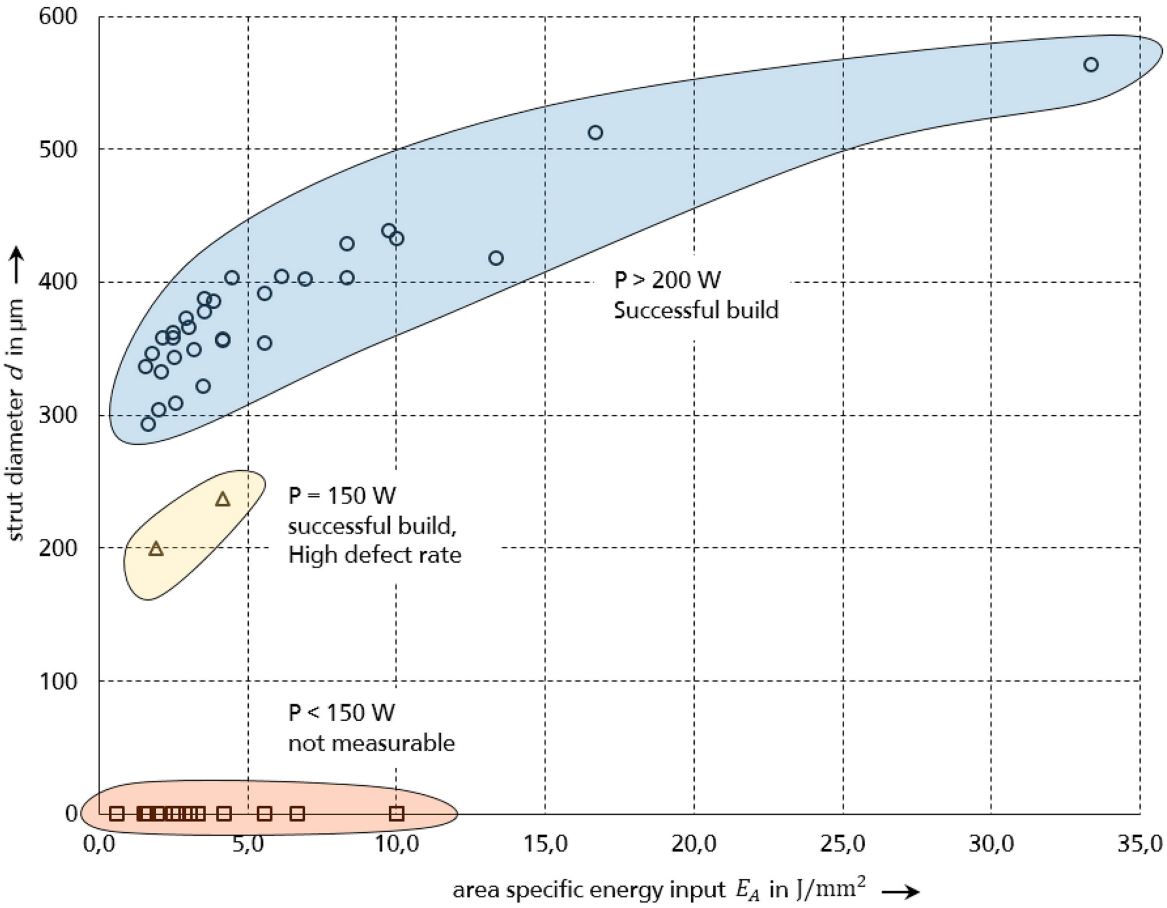


Fig. 2.11 Measured strut diameter of an AlSi10Mg lattice made by L-PBF as a function of the area-specific energy. Adapted from [186].

Furthermore, the contour scan strategy seems to be the optimal option for printing the thin features in lattice structures and has been adopted in many of the latest reports [183, 186, 185, 188, 189]. Ghouse et al. [185] compared the Ti-6Al-4V lattices printed with contour, points, and pulsing scan strategies and they proved that enhanced surface quality and minimized porosity level could be achieved in the contour specimens rendering an improved fatigue strength.

2.4.2 Post-processing

Post-process treatments are common practices for AM parts to mitigate the presence of undesirable manufacturing imperfections. Extensive numerical and experimental efforts have confirmed these approaches can attain superior fatigue properties [49, 183, 190, 90, 191].

After the printing, heat treatments are usually employed to relieve residual stresses within the AM components [183, 190, 153]. For some materials such as Ti-6Al-4V, this needs to be performed in a vacuum or inert gas atmosphere to minimize any oxygen contamination [183]. Very often, the elevated temperature during the process can also give rise to microstructural changes [190, 153]. Taking Ti-6Al-4V as an example, when the heat treatment temperature is below the β-transus temperature, the α' martensites are coarsened into α laths and these laths are collated in bundles within the prior-β grains [183]. After super-transus heat treatments, the coarse lamellar microstructure can be observed and there is almost no trace of prior-β grains, which leads to higher fatigue resistance than sub-transus heat treated and as-built counterparts [183].

HIP has proven to be an effective approach to close the porosity in AM parts [90, 192, 85]. At the same time, the microstructure can be coarsened as a result of the high temperature during the post-treatment [90, 192]. However, it remains controversial whether this approach is practical for improving the fatigue resistance of AM lattices. Despite minimal porosity ($< 1\%$) being achieved under optimal processing parameters, it has been shown HIP and stress relief treatments can improve the fatigue strength of

AM Ti-6Al-4V lattices by a similar extent, which largely results from the coarsening of microstructure [192].

Mechanical surface treatment is another avenue to enhance the fatigue resistance of AM parts [49, 193, 194]. However, several of the mechanical approaches such as machining and polishing are not applicable to architected materials as a result of the complex geometry. On the other hand, sandblasting has demonstrated its efficacy in removing partially melted powders by repeatedly propelling sand particulates onto the strut surface [49, 195]. A compressive residual stress layer is also formed in the subsurface region. The fatigue resistance of sandblasted lattices can thus be improved as a result of fewer micro-notches contributing to the initiation process and work-hardened surfaces retarding the cyclic ratcheting rate [49].

Furthermore, chemical etching can also improve the surface finish of lattice structures yielding an improved fatigue strength but the effectiveness of the technique is determined by the permeability of the lattice structure [192, 190]. This challenge may be overcome by a chemical-electrochemical approach called Hirtisation demonstrated in a recent study [191]. Uniform removal of surface defects was achieved by coupling electrochemical pulses with hydrodynamic flow resulting in an enhanced fatigue resistance of lattices after the treatment.

2.4.3 Design against Manufacturability

The defect level can also be lowered by careful lattice design improving the resilience to fatigue failure [186, 136, 133]. Based on our discussions in Sec. 2.3, struts printed

parallel to the build plate (horizontal struts) exhibit numerous issues including poor surface quality, inconsistent geometrical features, and high porosity level, which may deteriorate the mechanical integrity of lattice structures. Thus, attempts have been made to alter the build orientation of load-carrying struts [153]. The results showed when the load-carrying struts were printed vertically, the fatigue endurance ratio of a Cubic lattice could be more than double that of the horizontally printed specimens [153]. Moreover, several researchers have deliberately removed low-angle struts (0° - 30° relative to the build plate) during the design of stochastic lattices [185, 183]. Even though they haven't proven avoiding these struts could enhance the fatigue resistance of Ti-6Al-4V lattices, these studies set the basis for integrating optimal build orientation into lattice design.

Another design guideline would be to avoid the presence of long slender struts in the strut-based lattices [186, 133, 196, 197]. It has been reported these slender beams were prone to manufacturing failures such as unconnected struts disrupting the load distributions within the structures [186, 196, 197]. However, the strut length-to-thickness ratio often governs the mechanical properties of the lattices [47, 36]. A higher slenderness ratio typically gives rise to greater elastic modulus and yield strength. Thus, the attainable mechanical properties of the lattices are limited by the manufacturing imperfections arising from the high strut length-to-thickness ratio. Furthermore, improved geometrical accuracy can be achieved by increasing the cell size of the lattice while maintaining the same slenderness ratio [153, 126]. Dallago et al. [153] showed upscaling the cubic lattice by a factor of two could double the normalized fatigue

strength of the structure as a result of the lower geometrical deviation. Nevertheless, the cell size is constrained in certain applications such as biomedical implants to promote the integration of bone tissues into the implant structures [7].

One must also be aware of the manufacturing threshold of the AM process [7, 136, 198]. Tan et al.[136] concluded the minimum printable strut thickness is 200 μm for the L-PBF process and 400 μm for the EBM process. Below these thresholds, struts are likely to be disconnected in the as-printed state. The existence of the manufacturing limit is further confirmed by Zhang et al. [198]. They proved that strut connectivity was highly dependent on the strut orientation and layer thickness [198]. In general, the printable thickness is more limited as the struts are printed more horizontally and as the layer thickness increases.

2.4.4 Mitigation of Stress Concentrations

In strut-based structures, the nodal regions or the intersection of struts are often the foremost considerations since the overlapping strut volume may lower the effective loading area [199]. This has been attested by numerous studies that localized plasticity tends to develop near the nodal regions during fatigue failure [133, 192, 200]. In addition, variations in cross-section at the intersections may give rise to local stress concentrations. The synergetic effects of these aspects may lead to strut fracture under tensile loading or susceptible buckling conditions when the struts are loaded in compression [199]. Therefore, there is an increasing propensity to tailor the nodal geometry to ameliorate the mechanical durability of lattice structures.

One practice that has been demonstrated in a few reports is to adopt nodal fillets [199, 133, 201–203]. This enables smooth transitions near the nodal regions minimizing the stress concentrations. Dallago et al. [133] proved the fatigue strength of a filleted cubic lattice was twice higher than that of a non-filleted specimen. In a later study, they showed the fatigue resistance of the cubic lattice could be further improved by increasing the fillet radius [204]. It is noteworthy that adding a filleted node also significantly improves the monotonic properties [133, 201]. The elastic modulus and yield strength of the cubic lattice were raised by almost a factor of two in the work by Dallago et al. [133]. Hence, this approach may not be preferred for applications that require low stiffness or strength such as biomedical implants.

On top of that, subdivision surface algorithms have been employed to further smoothen the filleted node [205, 202]. This has been confirmed to be an effective approach to removing any additional discontinuity in surface curvature introduced by the fillets, which leads to uniform stress distributions as shown in Figure 2.12 [202]. Experimental results proved that an 8% increase in fatigue strength of a Cubic structure made of polyamide 12 could be attained by the subdivision algorithms as compared to the conventionally filleted counterparts resulting from the lower stress concentrations [202]. Again, this strategy would also increase the stiffness of the structure, which needs to be taken into consideration for certain applications.

The concept of TPMS can also be extended to strut-based structures to lower the stress concentration at the intersections [206, 201]. The continuous variation in cross-section along the strut length enables a close match between the loading area and

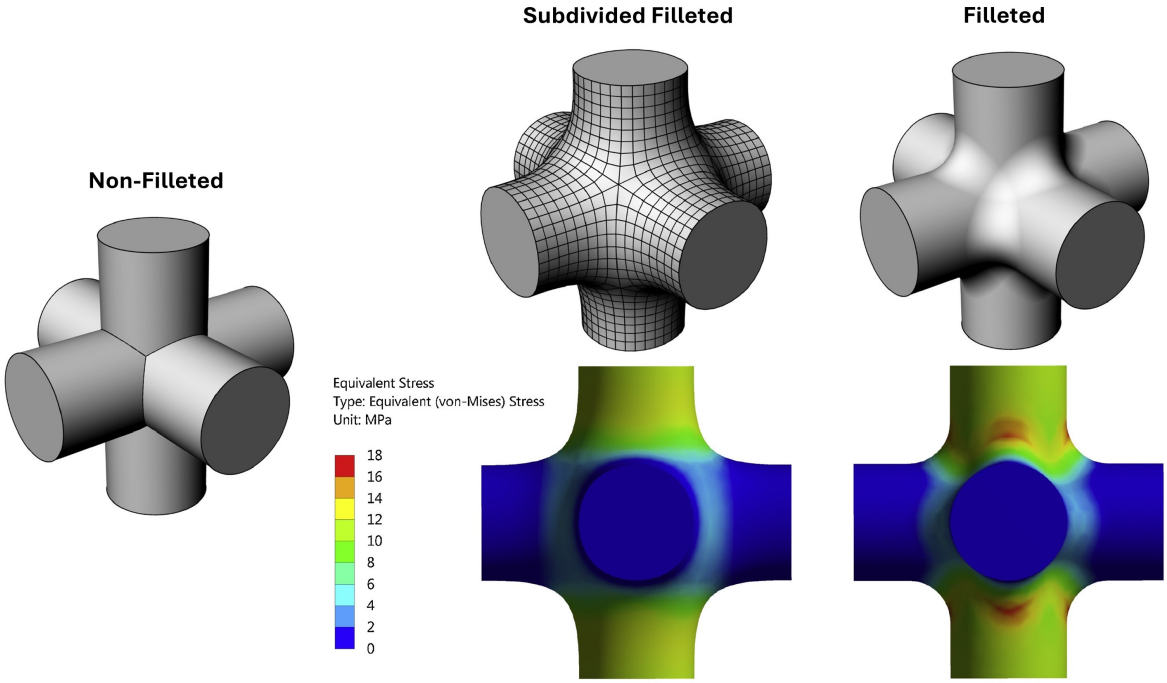


Fig. 2.12 Von mises stress distribution for subdivided filleted and conventionally filleted cells. Adapted from [202].

load distribution. Yang et al. [201] experimentally incorporated minimal surface into the design of a BCC lattice, i.e. I-WP, and compared it with filleted and non-filleted specimens. Their results suggested nodal fillet would only improve the fatigue strength of the BCC structure by 20% while the continuous surface could attain a 70% increase in fatigue strength. They also found the stress concentration could be minimized by optimizing the surface curvature. When the surface curvature is too low, stress concentrations could be observed at the intersections. As the curvature increases, the high-stress regions gradually shift to the middle of the strut as a result of the small thickness.

2.5 Recent Advances on the Fatigue-tolerant Design

In real engineering applications, lightweight and functionalization of components often require the implementation of unit cells in specific spatial configurations to integrate into large-scale structures. Hence, the mechanical durability of the components depends not only on the design of the unit cell but also on the arrangement of the unit cell. Furthermore, the integration of unit cells into engineering components involves a large number of design variables, which would be very challenging to testify with the traditional trial and error approach [207]. Modern artificial intelligence techniques, especially machine learning algorithms, may offer some practical solutions to derive relationships between design parameters and final properties. Thus, they form the focus of the following section.

2.5.1 Conformal Lattice Design and Topology Optimization

The design of regularly shaped components is usually guided by direct patterning – repeated translation of unit cells. However, this may lead to undesirable edge effects in components with irregular geometries whereby incomplete unit cells are generated to align with the component contour [208–210]. Conformal pattern design can address this issue by populating the unit cell to match the shape of the design space. This enables uniform load distribution within the structure maintaining the integrity of the unit cell. Examples of direct and conformal pattern designs are shown in Figure 2.13.

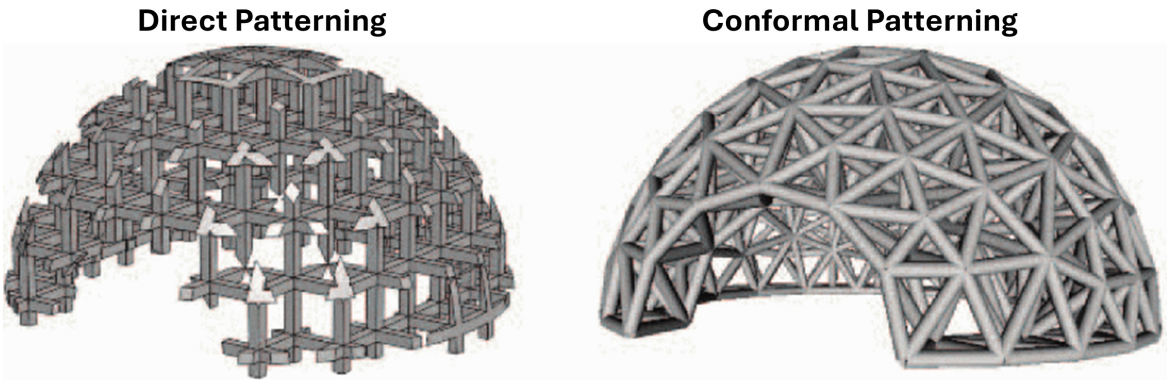


Fig. 2.13 An irregularly shaped component designed by direct patterning vs. conformal patterning. Adapted from [208].

The conformal design was initially realized with strut-based unit cells [211]. A two-step approach was developed starting with the generation of a 3D conformal hexahedral mesh followed by the distribution of unit cells into the confined hexahedral space. In later studies, efforts have been made to formulate the conformal design with controlled anisotropy [212, 213] and improved stiffness [213, 210]. A recent study also proved the applicability of this approach to TPMS-based unit cells [214]. The minimal stress concentrations offered by the conformal design are expected to govern an enhanced fatigue resistance but this will need to be validated with further experimental evidence.

Another pattern design strategy that would circumvent the edge effects is topology optimization, which involves optimizing the material distribution based on the simulation result [215, 216]. The materials are removed iteratively in low-stress regions until the optimization criteria are reached. It has been confirmed experimentally and numerically that lightweight and controllable mechanical properties can be attained

through this method [215, 216]. It is worth noting that this approach is not only applicable to pattern design but also to unit cell design [217, 218].

Manufacturing imperfections can also be taken into consideration during the simulation-driven design [219–221]. As we discussed in the previous section, overhang regions often exhibit high defect levels. Adding support structures is a common practice but this can result in material waster, prolonged manufacturing time, and high surface roughness [220, 222, 223]. An alternative approach would be the design of self-supporting structures by removing the struts below the minimum self-supporting angle. Some of the initial work employed the overhang angle constraint after the optimization process [220, 222]. Later research incorporated additional design parameters into the constraint such as minimal radial length scale [221], density gradients [223, 224], and feature sizes [225]. A recent study by Mass et al. [226] suggested a two-stage process: a discrete truss-based model was employed first to generate a self-supporting structure and a continuum topology optimization was performed to optimize the relative density. The final components demonstrated improved printability with limited additional computational cost as compared to conventional topology optimization as shown in Figure 2.14.

2.5.2 Hierarchical and Functional Gradient Design

The mechanical properties of architected materials can be further manipulated by introducing an additional layer of hierarchy (see Figure 2.15) [227–229, 4]. It has been shown these hierarchical structures demonstrate superior stiffness at low relative

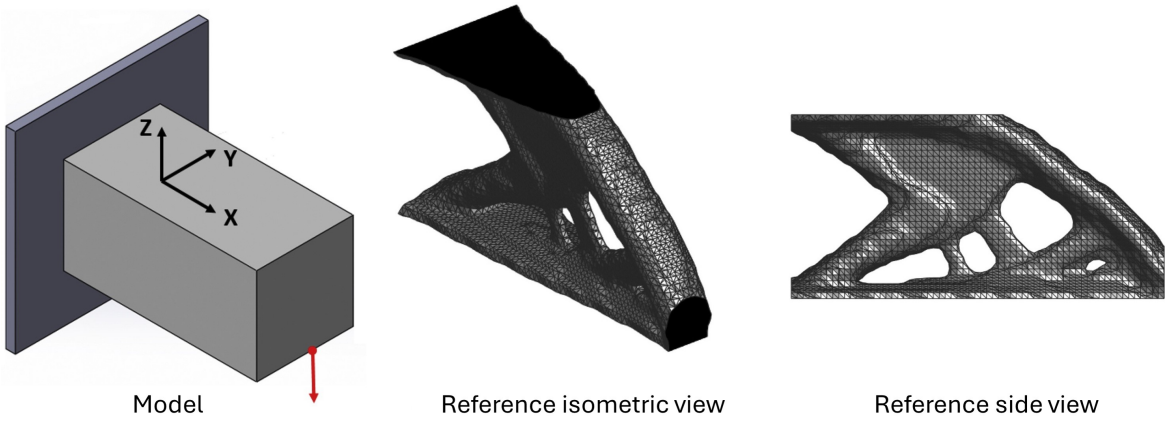


Fig. 2.14 Topology optimized 3D cantilever without the consideration of printing orientation. Adapted from [226].

density as well as amplified energy absorption capability [230–232]. Unprecedented Gibson-Ashby scaling relationships can also be found in some second-order lattices by which the exponent factors largely deviate from the first-order counterparts [4]. In particular, bending-dominated structures take more advantage of the structural hierarchy on stiffness than stretching-dominated specimens [4]. The hierarchical design may also induce high local stress concentrations reducing the macroscopic yield strength of the structure. Incorporating bending-dominated and stretching-dominated structures together into the hierarchical design can lead to hybrid properties [228].

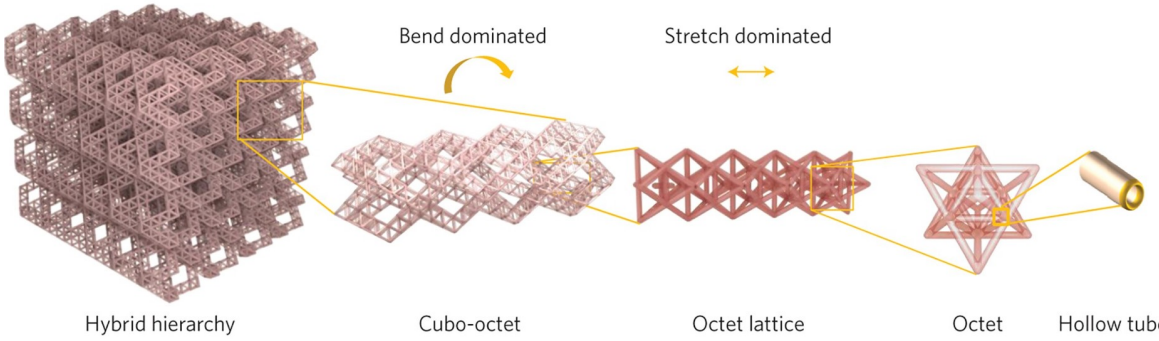


Fig. 2.15 A schematic illustration of the hierarchy levels of cubo-octet metamaterials. Adapted from [4].

Recent efforts have been focusing on understanding the correlation between hierarchical levels and the mechanical behaviour of these lattices [233–235]. The mechanical properties of these hierarchical structures are found to be largely governed by the lattice configurations and slenderness ratios at different hierarchy levels rather than the relative density [233, 235].

Functionally gradient design offers the ability to locally tailor the properties of mechanical components, which is particularly attractive for applications such as bone scaffolds [236]. The design principles usually rely upon varying the relative density [237, 238], unit cell dimension [237, 239], and unit cell type [240] (see Figure 2.16). However, the latter two methods are often plagued by manufacturing challenges and may result in debonding at the interfaces between layers.

Most of the initial studies proved the energy absorption capability of the structures could be vastly enhanced through functional gradient design [238, 241, 207]. Some of the recent work showed higher stiffness and strength of gradient structures could also be obtained [242, 49]. The fatigue properties of graded structures have been relatively scarcely examined [68, 77, 184, 243]. Zhao et al. [68] showed the fatigue strength of graded lattices outperformed the uniform counterparts since the crack propagation was retarded by the stress redistribution in low-strength constituents while the high-strength constituents limited the progressive accumulation of plastic strain. Later work also confirmed the gradient-orientation dependency of the fatigue properties of these graded structures [77, 184, 243]. Nevertheless, the early failure of

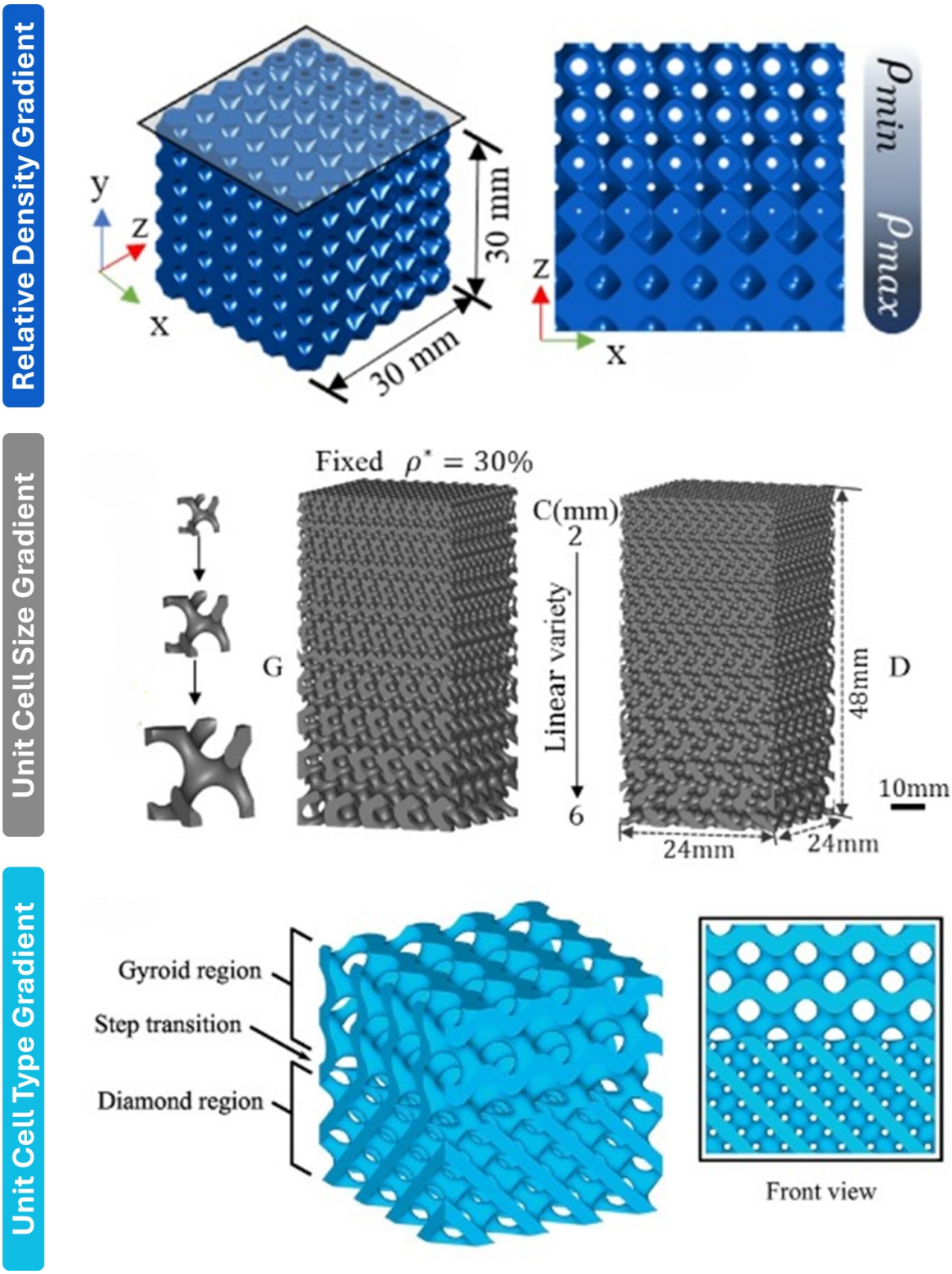


Fig. 2.16 A schematic illustration of functional gradient design in terms of relative density, unit cell dimension, and unit cell type. Adapted from [237, 239, 240].

the low-strength constituents may call into question the practicality of this approach in the healthcare industry.

2.5.3 Applications of Machine Learning Algorithms and Data-driven Approaches

Machine learning algorithms are gaining increasing popularity in the realm of lattice design owing to their robustness to navigate extensive amounts of data [207, 244, 245]. Specifically, this approach resonates with the topology optimization process since numerous iterations of design are required to output the final structure. Many previous studies have proven the efficiency of the optimization process can be greatly improved using these data-driven approaches [246, 244, 247]. It is also notable that the input for the machine learning models is largely dominated by the data generated by the FEA simulation. Thus, this modern technique may not be able to serve as an alternative to the topology optimization process but as a facilitator to devise interim results.

Currently, the majority of the research on machine learning-based topology optimization focuses on improving the stiffness [248, 246], strength [207, 249], and energy absorption [250, 251] of the lattice structures. Very few attempts have been made to develop the fatigue-tolerant design, which likely results from the shortage of training data and testing standards. Yet, we believe this data-driven approach can seize the potential of the rapid development in the understanding of the fatigue failure mechanisms of architected materials and how the structural inhomogeneities influence the fatigue fracture process in the near future.

2.6 Summary

Here, we have summarized the current state of the high cycle fatigue assessment of 3D-printed monolithic and architected materials. The compromised fatigue resistance of AM materials is one of the pivotal factors limiting their adoption in many critical sectors. This is particularly the case for architected materials owing to their high surface-to-volume ratios and stress localization within the geometry. Implementation of fatigue testing standards can facilitate the development of architected materials with consistent and reliable properties.

The fatigue properties of architected materials are strongly influenced by the unit cell type. In general, TPMS-based structures offer higher fatigue endurance than strut-based specimens as a result of the nominal discontinuity in stress distributions. A few auxetic structures show the highest normalized fatigue strength benefiting from the high compressive force along the strut. The adoption of ductile materials can retard the cyclic ratcheting and fatigue crack propagation leading to improved fatigue tolerance of lattice structures.

Furthermore, the structural inhomogeneities induced by the AM process hinder the lattice materials from attaining desirable properties. Some notable inhomogeneities include surface defects, geometrical deviations, pores, residual stress fields, and non-uniform microstructure. Numerous reports demonstrate the influence of these inhomogenieties can be reduced through mindful processing routines such as optimizing processing parameters and post-process treatments as well as careful selections of design variables.

The spatial configuration of the unit cell also governs the final properties of the AM components. Conformal pattern design and topology optimization have proven to be more compatible with irregularly shaped components than the traditional repeated translation of unit cells. Hierarchical and functional gradient design provides an additional level of flexibility to tailor the mechanical durability of the AM components. The prompt evolution of data-driven approaches can rapidly predict the properties of AM components facilitating the discovery of novel designs.

2.7 Conclusion remarks

As discussed above, extensive efforts have been made to unravel the fatigue behaviour of 3d-printed monolithic materials. Yet, very few reports have examined the fatigue properties of architected materials. It has been shown ambiguously the two types of materials exhibit different failure mechanisms under cyclic loading. What remains uncertain is whether the understanding of monolithic material behaviour sheds some light on the fatigue behaviour of architected materials. Additionally, even though the effect of structural inhomogeneities on the fatigue fracture process has been widely reported in the literature, the interplay between these inhomogeneities remains largely unclear. Furthermore, is there any additional guideline for the design of lattice structures such that the influence of these inhomogeneities on fatigue resistance can be minimized?

The proposed research has addressed these questions rigorously through a combination of systematic experimentation, numerical analysis, and computational modelling. The results have not only demystified the enigma above but have also served as guidelines for the design of fatigue-tolerant components.

Chapter 3

On the Size-dependent Fatigue Behaviour of Laser Powder Bed Fusion Ti-6Al-4V

3.1 Introduction

In general, the optimization of geometrical features requires sub-structures to be printed in different thicknesses. Thus, the variation in characteristic cross-sectional area together with a combination of processing parameters can introduce structural inhomogeneity within the component [252, 98]. This can be detrimental to the mechanical integrity of the component, especially the fatigue behavior [52–54]. This can be regarded as the Archilles' heel of the AM process, limiting the adoption of the

technology in many critical sectors. To unleash the full potential that AM promises, the influence of sample size on the fatigue properties must be better understood.

The size-dependent fatigue behaviour of conventionally manufactured metallic material has been reported previously in the literature [253, 254]. It is well-known that as the sample size increases, there is an increasing probability of encountering a larger defect thus provoking macroscopic failure [253, 255]. But does this general principle hold for materials made by AM? Several reports have demonstrated the fatigue performance of net-shape AM Ti-6Al-4V is relatively inferior as compared to the conventionally manufactured counterpart – due to the presence of surface defects and porosity [19, 256, 57, 255]. This may result in a potentially different size effect phenomenon. An improvement in fatigue life has been found as the sample size increases owing to the enhanced surface quality [257–259]. However, the size-dependent fatigue behaviour of AM materials has not been researched yet in sufficient depth. The interplay between surface defects, porosity, and microstructure during the fatigue fracture process is still not clear. Furthermore, very little research has been found on the fatigue scatter – one of the key requirements to consider for the implementation of many applications.

With this in mind, we designed and fabricated net-shape AM specimens of different sizes to assess them in service conditions. The sample sizes chosen in this work correspond to the thicknesses of many engineering components, such as biomedical implants and heat exchangers. We performed uniaxial tensile tests to determine their quasi-static mechanical behavior. We addressed the fatigue properties – fatigue life

and fatigue scatter – as a function of the sample size. We focused particularly on their performance between 10^4 and 10^6 cycles to provide fundamental insight into the cyclic deformation behaviour of intricate component, especially metallic lattice. We revealed the microstructural features – grain size and texture – using high-resolution electron microscopy. The surface roughness and processing-induced porosity were quantified using X-ray computed tomography, which provides structural information of the specimens in three dimensions [252, 260, 261]. We analyzed the fracture surfaces to understand the fatigue fracture process. Rationalization of our findings sheds light on how best to mitigate any structural inhomogeneity arising from the AM process.

3.2 Methods

To study the effect of sample size on the fatigue properties, specimens with two gauge diameters were considered: ∅ 1.3 mm and ∅ 2.0 mm – see Table 3.1. The two sample geometries are detailed in Figure 3.1(A). A summary of sample dimensions is provided in Table 3.1. The difference in gauge length-to-diameter ratio between the two specimens is expected to only influence the calculated fracture strain but has minimal effect on the elastic modulus, yield strength, and ultimate tensile strength [262]. Owing to the larger gauge length-to-diameter ratio, the ∅ 2 mm specimen is expected to have a smaller fracture strain as compared to the ∅ 1.3 mm specimen after necking.

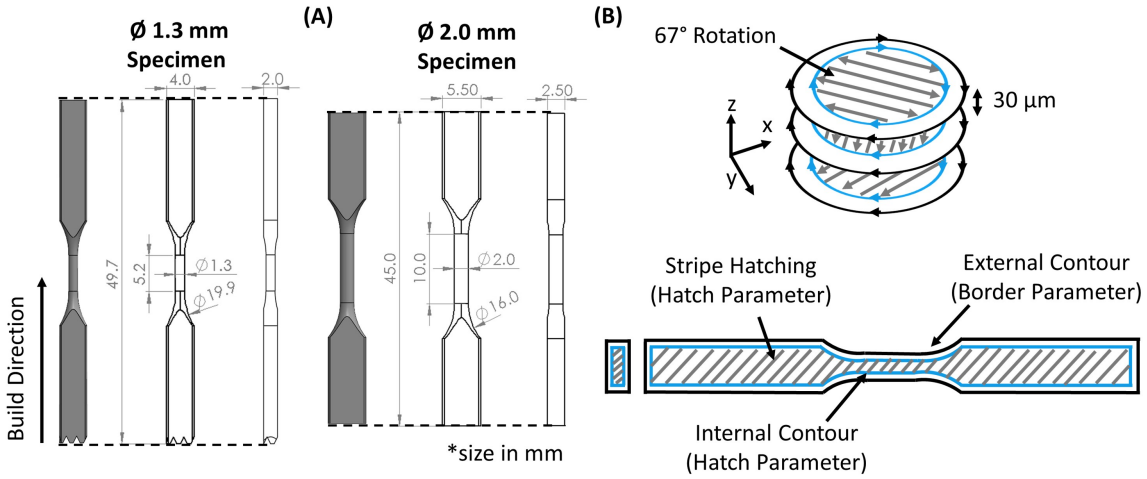


Fig. 3.1 (A) Geometries of the 2 tensile specimens used in this study. (B) Schematic illustrations of laser path along different consecutive layers and laser path along each cross-sectional plane.

Samples	Gauge Diameter	Gauge Length	Gauge length-to-diameter ratio
A	1.3 mm	5.2 mm	4
B	2 mm	10 mm	5

Table 3.1 A summary of dimensions of samples used in this study.

3.2.1 Processing by Laser Powder Bed Fusion

Tensile samples were produced using a Renishaw AM400 machine with a modulated 200 W ytterbium fibre laser. The powder fed into the machine was electrode induction-melted gas atomised Ti-6Al-4V provided by Renishaw plc. The processing parameters used are detailed in Table 3.2. A stripe hatching laser scan path pattern was employed with the path frame of reference being rotated by 67° after each layer was added (Figure 3.1(B)). To achieve an optimal surface finish, two contour passes were performed near the free surfaces after each layer – the internal one using hatch parameters and the external one using border parameters (Figure 3.1(C)). All samples were fabricated on a single build plate. The samples were stress relieved at 800 °C for 4 hours in a vacuum

furnace and sandblasted using safti grit at 2 bar. The post-processing was employed to examine the samples in the service conditions.

Ti-6Al-4V	Hatch Parameters	Border Parameters
Layer Thickness	30 μm	30 μm
Laser Power	200 W	100 W
Laser Scan Speed	0.786 m/s	0.750 m/s
Point Distance	55 μm	45 μm
Hatch Distance	65 μm	65 μm
Exposure Time	50 μs	40 μs
Spot Size (Radius)	35 μm	35 μm

Table 3.2 Processing parameters used for the manufacturing of tensile samples.

3.2.2 Assessment of Static & Dynamic Mechanical Behaviour

An Instron ElectroPuls E10k system with a 10 kN load cell was employed to measure the mechanical properties of the samples at room temperature. Uniaxial tensile tests were performed under displacement rate control at a strain rate of 2×10^{-3} s^{-1}. A non-contact iMetrum video extensometry system was used to measure the macroscopic strain of the sample on a 5.2 mm or a 10 mm gauge length.

Tensile fatigue tests were conducted under load control at a frequency of 30 Hz and an R ratio of 0.1. Maximum stresses of 600, 500 and 400 MPa were applied. At each applied stress, three tests were repeated. All samples were tested until fracture.

3.2.3 Characterization by Electron Microscopy

The microstructures were examined by a Zeiss Merlin field emission gun scanning electron microscope (FEG-SEM) equipped with a Bruker electron backscatter diffraction

(EBSD) detector. Scans were performed on surfaces parallel to the build direction. The beam was operated at a 20 kV accelerating voltage and a 20 nA current. For the analysis of α lath thickness distribution, the diffraction patterns were collected at 400 $\times$ 300 resolution with a step size of 0.22 μm. For the α lath texture analysis and the reconstruction of prior-β grains, the diffraction patterns were stored at 400 $\times$ 300 resolution with a step size of 0.55 μm.

Fractography was performed to examine the fracture behaviour of samples after fatigue tests using a JEOL 6500F FEG-SEM. The locations at which fatigue cracks initiate were identified to investigate the failure mechanisms.

3.2.4 X-ray Computed Tomography (XCT)

X-ray computed tomography of the tensile samples was carried out with an ImageiX CT system (North Star Imaging Inc., Minnesota, USA). During the measurement, each sample was placed 25.5 mm in front of the tungsten transmission target X-ray source filtered by a Cu foil of 0.95 mm thickness. Scans were performed at 140 kV tube voltage, 71 μA tube current, 5 μm focal spot size and 1 Hz frame rate. The isotropic voxel size was 4.7 μm - any feature smaller than 14.1 μm was deemed unresolvable [263]. Projection images were reconstructed using a filtered back Projection algorithm in the efX-ct software (version 1.9.5.12, North Star Imaging Inc., Minnesota, USA). Avizo 9.7 software was used to analyse the data. Solid parts were segmented using Otsu's method [264].

A summary of the samples tested in this Chapter is shown in Table 3.3.

Specimen	Sample	Tensile Test	Fatigue Test	Fractography
∅ 1.3 mm	Sample 1	Yes	No	No
∅ 1.3 mm	Sample 2	Yes	No	No
∅ 1.3 mm	Sample 3	Yes	No	No
∅ 1.3 mm	Sample 4	No	Yes (σ_{max} = 600 MPa)	Yes
∅ 1.3 mm	Sample 5	No	Yes (σ_{max} = 600 MPa)	Yes
∅ 1.3 mm	Sample 6	No	Yes (σ_{max} = 600 MPa)	Yes
∅ 1.3 mm	Sample 7	No	Yes (σ_{max} = 500 MPa)	Yes
∅ 1.3 mm	Sample 8	No	Yes (σ_{max} = 500 MPa)	Yes
∅ 1.3 mm	Sample 9	No	Yes (σ_{max} = 500 MPa)	Yes
∅ 1.3 mm	Sample 10	No	Yes (σ_{max} = 400 MPa)	Yes
∅ 1.3 mm	Sample 11	No	Yes (σ_{max} = 400 MPa)	Yes
∅ 1.3 mm	Sample 12	No	Yes (σ_{max} = 400 MPa)	Yes
∅ 2.0 mm	Sample 1	Yes	No	No
∅ 2.0 mm	Sample 2	Yes	No	No
∅ 2.0 mm	Sample 3	Yes	No	No
∅ 2.0 mm	Sample 4	No	Yes (σ_{max} = 600 MPa)	Yes
∅ 2.0 mm	Sample 5	No	Yes (σ_{max} = 600 MPa)	Yes
∅ 2.0 mm	Sample 6	No	Yes (σ_{max} = 600 MPa)	Yes
∅ 2.0 mm	Sample 7	No	Yes (σ_{max} = 500 MPa)	Yes
∅ 2.0 mm	Sample 8	No	Yes (σ_{max} = 500 MPa)	Yes
∅ 2.0 mm	Sample 9	No	Yes (σ_{max} = 500 MPa)	Yes
∅ 2.0 mm	Sample 10	No	Yes (σ_{max} = 400 MPa)	Yes
∅ 2.0 mm	Sample 11	No	Yes (σ_{max} = 400 MPa)	Yes
∅ 2.0 mm	Sample 12	No	Yes (σ_{max} = 400 MPa)	Yes

Table 3.3 A summary of the samples tested in this work.

3.3 Results

3.3.1 Quasi-static Behaviour

The quasi-static mechanical response of samples with different sizes is illustrated in Figure 3.2(A). The tests were conducted following ASTM E8 standards [262]. The values of elastic modulus, yield strength, ultimate tensile strength, and fracture strain are summarised in Figure 3.2(B). The ∅ 2 mm specimens demonstrate on average 14 GPa higher elastic modulus, 70 MPa higher yield strength, and 2% larger fracture

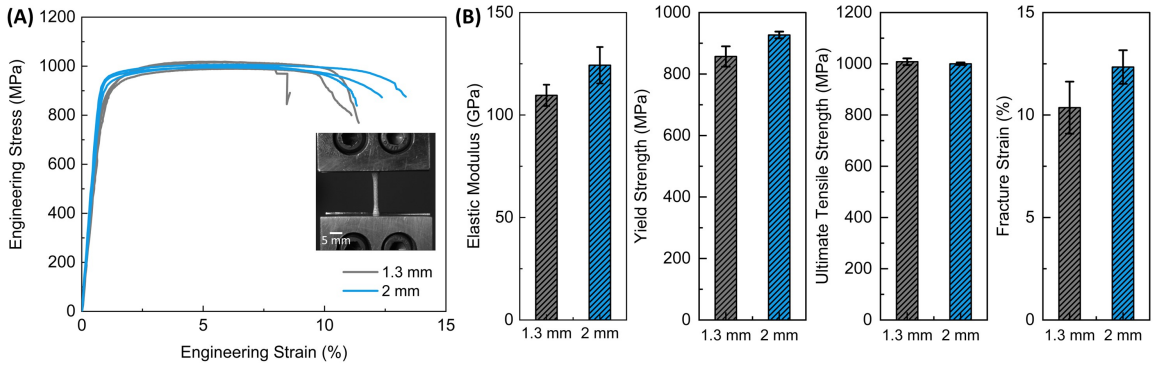


Fig. 3.2 (A) Engineering stress-strain curves of AM Ti-6Al-4V at a strain rate of 2×10^{-3} s^{-1}. (B) Elastic modulus, yield strength, ultimate tensile strength, and fracture strain of the 2 specimens under study. Error bars represent the standard deviation from 3 repetitions.

strain but similar ultimate tensile strength as compared to the ⌀ 1.3 mm specimens. A smaller fracture strain associated with the larger gauge length-to-diameter ratio samples is not observed. Instead, other factors are contributing to the larger fracture strain of the sample with the larger gauge length-to-diameter ratio. The fracture strain of the larger specimen would be even higher if the two specimens were of the same sample geometry. This size dependency is rationalized in Sec. 3.4.1.

3.3.2 Dynamic Behaviour in Fatigue

The fatigue performance of the 2 specimens is presented in Figure 3.3(A). At all applied stresses, the larger specimens exhibit higher average cycles to failure than the smaller specimens. The differences in average cycles to failure increase as the maximum applied stress (σ_{max}) decreases. When $\sigma_{max} = 600$ MPa, the ⌀ 2 mm specimen only demonstrates 11% higher average cycles to failure than the ⌀ 1.3 mm specimen, and the differences become 27% and 130% at σ_{max} values of 500 MPa and 400 MPa, respectively.

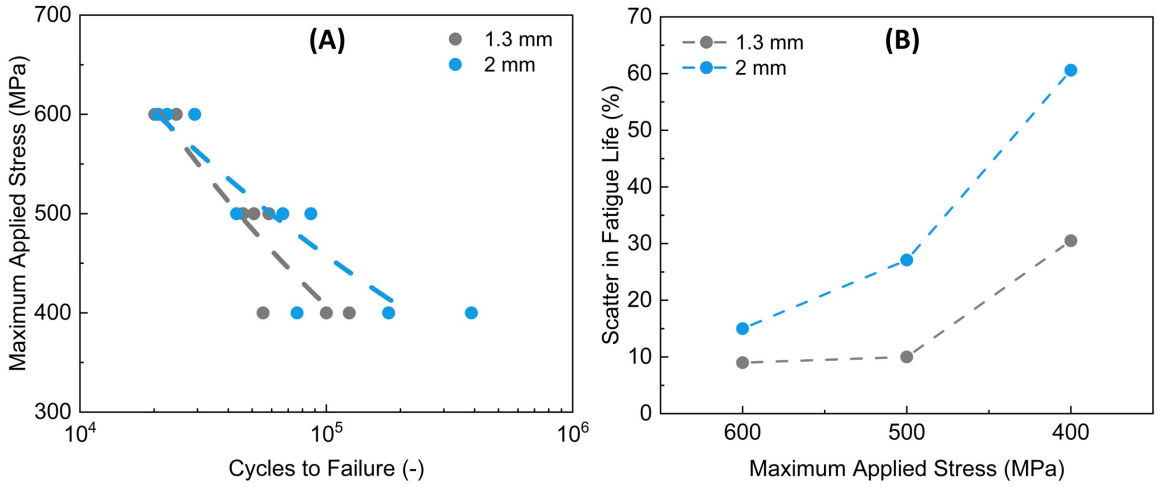


Fig. 3.3 (A) Maximum applied stress vs. cycles to failure for the specimens manufactured in this work. Three measurements are performed per condition. (B) Correlation between scatter in fatigue life and maximum applied stress for different tested specimens.

To quantify the scatter in fatigue life at each applied stress, the coefficient of variation is used, defined as [265]:

$$\text{Coefficient of Variation} = \frac{\text{Standard Deviation}}{\text{Mean}} \tag{3.1}$$

Results are shown in Figure 3.3(B). At all applied stresses, the ⌀ 2 mm specimen demonstrates higher fatigue scatter as compared to the ⌀ 1.3 mm specimen. Similar to the average cycles to failure, the difference in scatter in fatigue life also increases as the maximum applied stress decreases. At $\sigma_{\max} = 600$ MPa, the larger specimen exhibits 6% higher scatter in fatigue life than the smaller specimen, and the difference becomes 17% and 30% at $\sigma_{\max}$ equal to 500 MPa and 400 MPa, respectively. The variation in fatigue properties between the 2 specimens is analyzed in Sec. 3.4.3.

3.3.3 Microstructural characterization

The microstructural differences between the 2 specimens inherited from the AM process might also contribute to variations in fatigue properties. In our specimens, the microstructure consists of more than 95% of thin α laths organized in bundles within the prior-β grains. These grains are usually elongated parallel to the build direction. The size and texture of α laths and prior-β grains have been found to be strongly correlated with the fatigue properties of AM parts [266]. Hence, we describe the change in microstructure as a function of the sample size in this section by means of EBSD statistical analysis. In addition, we examine the microstructural features in the middle and edge sections of each specimen separately owing to the different processing parameters employed in these regions (Figure 3.4(A)). The edge section is defined as 200 μm away from the sample surface based on the width of the two contour passes.

α lath microstructure

Figure 3.4(B-E) presents the EBSD images of the 2 specimens under study. The α lath microstructure is clearly revealed. The thickness distribution of the α lath was measured by fitting an ellipse to each grain. The thickness of the lath was evaluated by the length of the short axis of the ellipse. More than 1500 α laths were analysed to obtain a statistical distribution for each sample. A summary of the results is shown in Figure 3.4(F). The lath thickness in the ⌀ 2 mm specimen is larger than that in the ⌀ 1.3 mm specimen. This coarser microstructure can be related to the higher thermal

mass of the larger samples. When larger samples are fabricated, they retain more heat and their average temperatures are higher than the smaller ones. This results in slower cooling rates and faster kinetics of martensitic decomposition [267, 260, 268].

Figure 3.5(A) shows the EBSD map of the α lath microstructure at a lower magnification. The contour pole figure quantifies the texture strength for the three plane families $\{0001\}$ $\{\bar{1}100\}$ and $\{\bar{1}2\bar{1}0\}$ with respect to the x-y plane of the sample. Among them, $\{0001\}$ exhibits the strongest texture, and it is parallel to the build direction. To compare the texture strength of different specimens, their α texture indices were evaluated as shown in Figure 3.5(B) [269]. There is no significant difference in the texture of the α lath microstructure between the 2 specimens under study and the variation between the middle and edge sections of each specimen is also negligible.

Cross sectional prior-β grain microstructure

The prior-β grains are reconstructed from the descendant α lath structure using the MTEX 5.8.2 tool box following the transformation indicated in Figure 3.5(C) [270]. In this method, each α lath is analysed together with the surrounding α laths to isolate the suitable prior-β grain based on the following Burgers orientation relationship [252]:

$$(110)_\beta//(0001)_\alpha, [111]_\beta//[11\bar{2}0]_\alpha \tag{3.2}$$

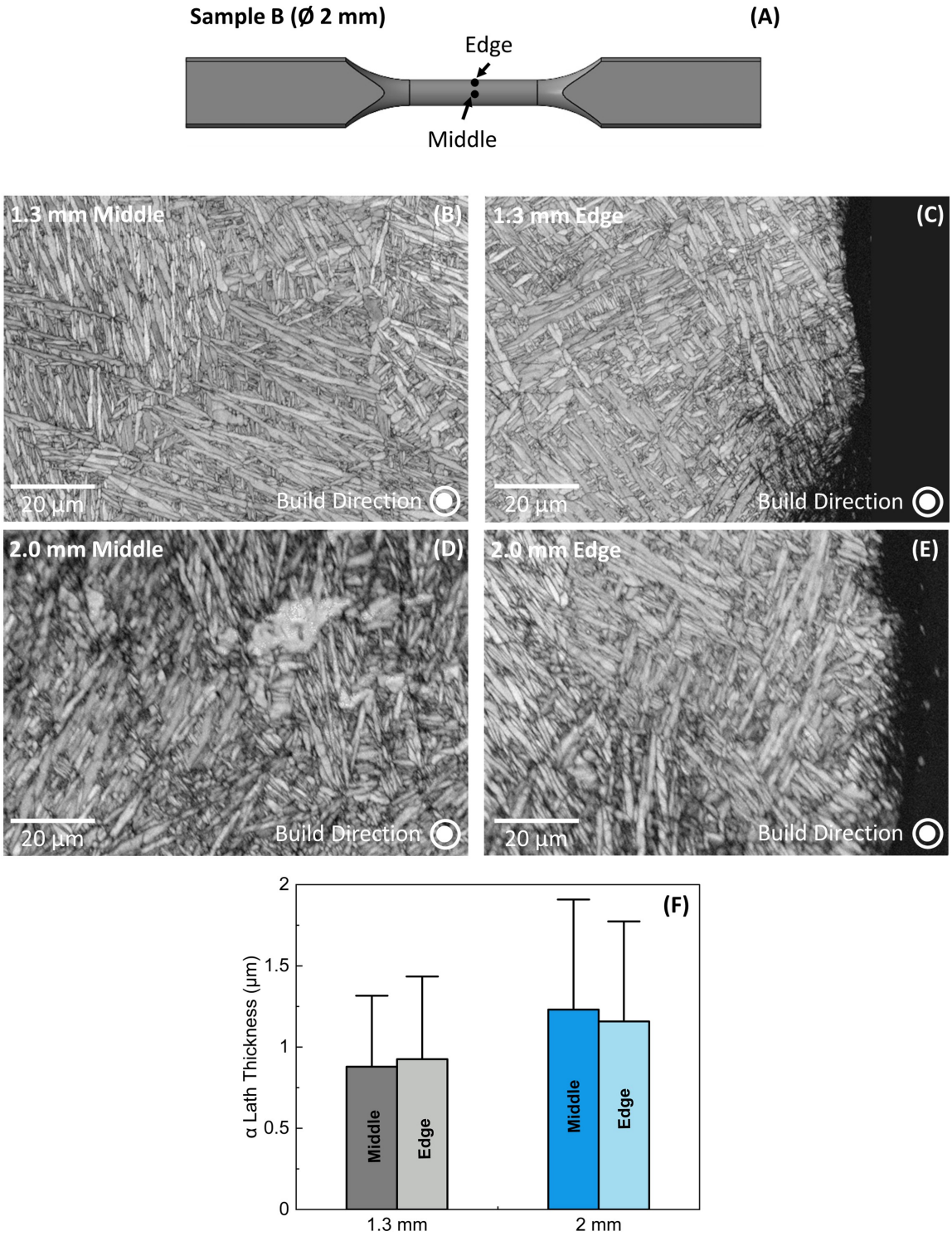


Fig. 3.4 (A) Schematic illustration of the positions at which the microstructural characterizations are performed in this work. (B-E) Cross sectional microstructure of the 2 specimens under study characterized by EBSD. (F) Average α lath thickness $\pm$ 1 standard deviation of the 2 specimens.

When the surrounding laths are of the same prior-β orientation, these laths are associated with the same prior-β grain. The procedure is iterated across the whole set of laths.

Figure 3.5(D) presents the cross sectional EBSD map of the reconstructed prior-β grain. A grid plan pattern is observed in the middle section resulting from the 67° rotation of the stripe hatching scan between successive layers. On the other hand, irregular grains are formed in the edge section due to the contour scan. The texture strength for the three plane families {100} {110} and {111} with respect to the x-y plane of the sample is shown in the contour pole figure. In the ⌀ 1.3 mm specimen, the (100) texture component is the strongest among the three whereas both the (100) and (111) exhibit similar texture strength in the ⌀ 2 mm specimen. A transfer of texture between prior-β and α phases resulting from the crystallographic nature of the transformation can also be observed. The Burgers orientation relationship between the 2 phases – $(110)_\beta//(0001)_\alpha$ – is revealed in the pole figures corresponding to these directions. The texture ring along the $(110)_\beta$ is also observed along the $(0001)_\alpha$. This confirms the success of our reconstruction.

The prior-β texture indices of the 2 specimens are shown in Figure 3.5(E) [269]. The ⌀ 2 mm specimen demonstrates a 36% weaker texture as compared to the ⌀ 1.3 mm specimen. The higher average temperatures within the larger specimen may give rise to a smaller thermal gradient, leading to fewer grains growing along the same direction [271, 51]. However, such a variation in texture is not preserved during the martensitic transformation. The displacive phase transformation weakens the variant

selection in Ti-6Al-4V alloys resulting in a weakly textured α lath microstructure [272–274]. In addition, the difference in texture between the middle and edge sections is not significant.

The sizes of the prior-β grains are measured for the 2 specimens. Results are shown in Figure 3.5(F). Similar to our measurements on the α lath thickness, the $\varnothing$ 2 mm specimen exhibits larger prior-β grains than the $\varnothing$ 1.3 mm specimen, which results from the slower cooling rate during the manufacturing process. The coarser prior-β grains provide smaller numbers of α lath nucleation sites, which hinders nucleation and promotes propagation [275]. No significant difference in prior-β grain size can be found between the middle and edge sections of each specimen.

Longitudinal prior-β grain microstructure

The microstructure along the longitudinal plane is presented in Figure 3.6(A) and (B). All the specimens show columnar grains along the build direction. The contour pole figure confirms (100) is the strongest texture component in the smaller specimen while (100) and (111) are equally strong in the larger specimen. The texture indices and grain widths extracted from these maps are shown in Figure 3.6(C) and (D). The larger specimen demonstrates a weaker texture and larger columnar grain widths as compared to the smaller specimen, which is in agreement with the cross sectional microstructure.

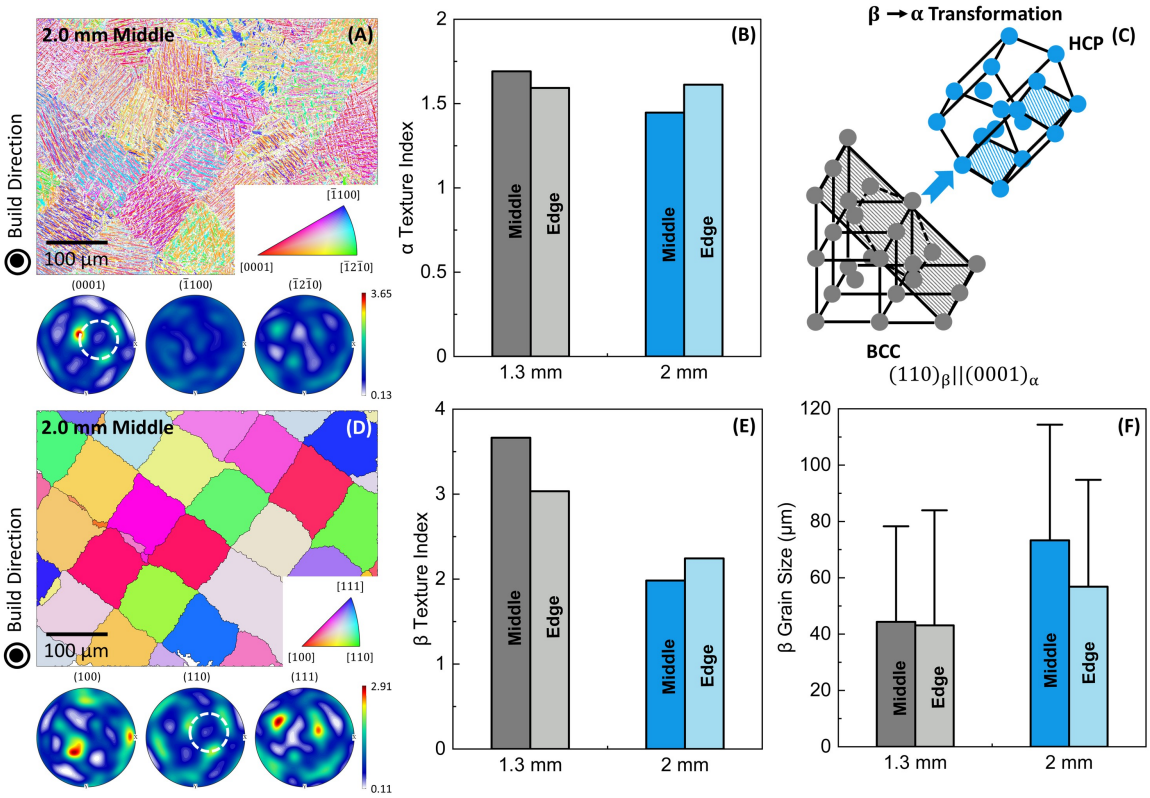


Fig. 3.5 (A) Cross sectional EBSD map and orientation distribution function pole figure of the α lath microstructure of the ⌀ 2.0 mm sample. (B) Texture index of the α lath microstructure of the 2 specimens under study. (C) Schematic illustration of $\beta \rightarrow \alpha$ transformation during the AM process of Ti-6Al-4V. (D) Cross sectional EBSD map and orientation distribution function pole figure of the reconstructed prior-β microstructure of the ⌀ 2.0 mm sample. (E) Texture index and (F) grain size of the reconstructed prior-β microstructure of the 2 specimens.

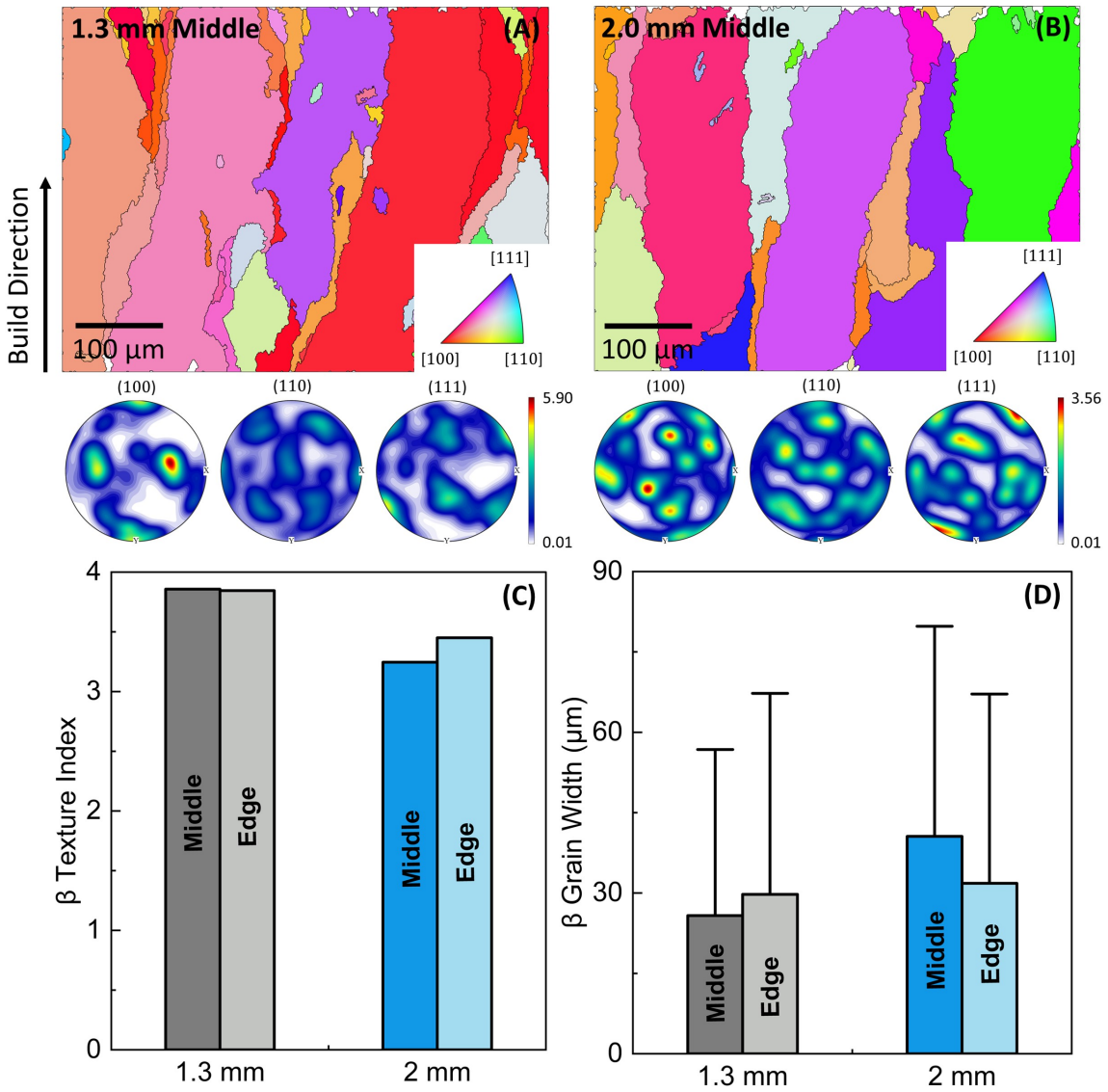


Fig. 3.6 Longitudinal EBSD map and orientation distribution function pole figure of the reconstructed prior-β microstructure of the (A) $\varnothing$ 1.3 mm sample and (B) $\varnothing$ 2.0 mm sample. (C) Texture index and (D) grain size of the reconstructed prior-β microstructure of the 2 samples.

3.3.4 Surface roughness

The surface quality of the 2 specimens was measured by comparing the XCT data with the CAD design. The XCT data is spatially registered with the CAD design by first aligning their centre of mass and principle axes as well as maximizing their mutual volume through translation and rotation. The distances between their surfaces are computed based on the closest points from the tomography data to the CAD design. As shown in Figure 3.7(A), the red region represents the hills above the CAD design surface and the blue region represents the troughs below the surface. The surface roughness (R_a) is evaluated by integration over the entire profile x of length l, which can be given by [252]

$$R_a = \frac{1}{l}\int_0^l |h(x)|dx \tag{3.3}$$

where $h(x)$ is the relative height of the profile. Results are shown in Figure 3.7(B). The surface roughness of the ⌀ 2 mm specimen is only around 50% of that of the ⌀ 1.3 mm specimen. This may be explained by the higher melt pool stability in the ⌀ 2 mm specimen [276, 277, 3]. The higher temperature within the larger specimen enables powder particles to be melted more completely, minimizing balling effect.

3.3.5 Processing-induced porosity

The porosity of different samples is evaluated using the XCT data (Figure 3.8(A)). Spatial distributions of the pores in the x-y plane of the 2 specimens are shown in Figure 3.8(B). In both cases, porosity occurs largely near the sample surfaces. This

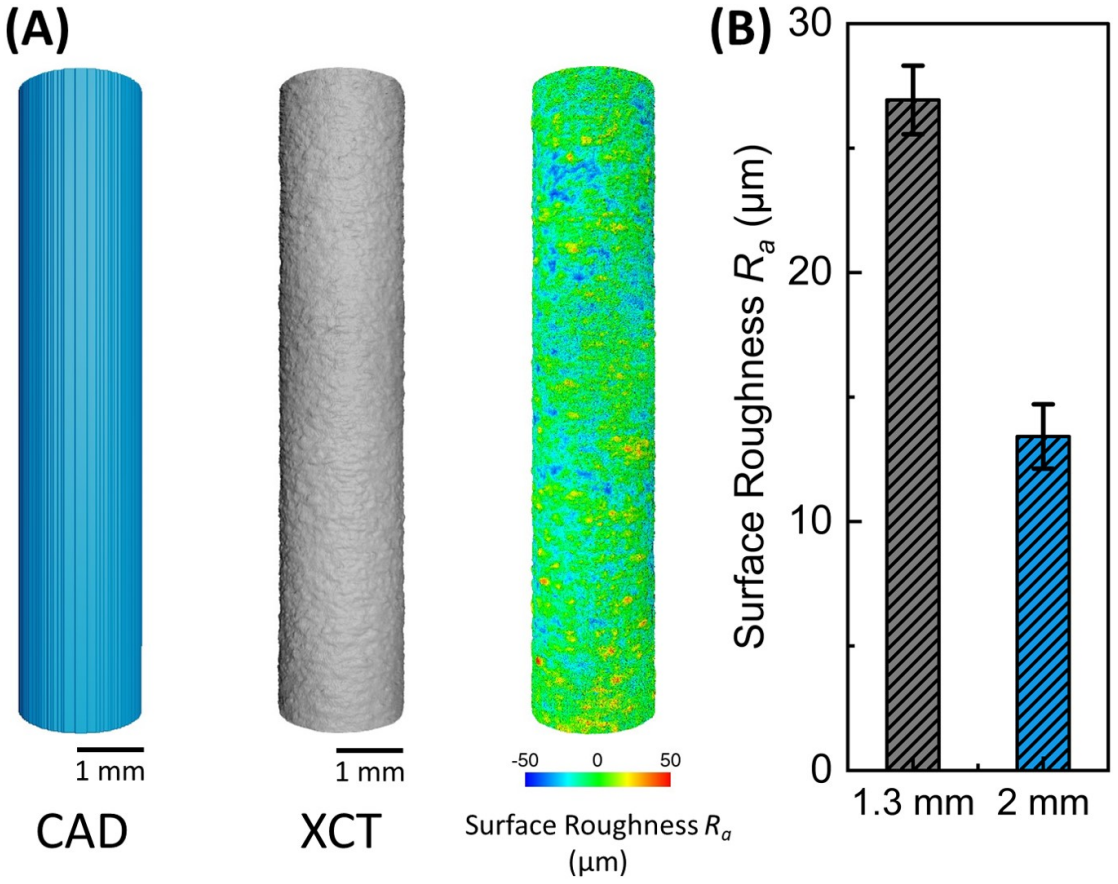


Fig. 3.7 (A) An example of the comparison between CAD design and computed tomography data. Red regions represent hills and blue regions represent pits. (B) Surface roughness (R_a) of the 2 specimens under study. Error bars represent the standard deviation from 3 repetitions.

statement is further supported by the quantification in Figure 3.8(C). Nearly all the pores are found to be within 0.4 mm of the sample surfaces. Such a spatial dependency results from the mismatch between the stripe hatching and contour scan patterns and the gaps between contour passes [278–280].

The size and number density of the pores are also critical to the fatigue performance of AM component [110, 154]. The size of the pores is characterized by the Murakami parameter $\sqrt{A_\mathrm{p}}$ where A_p is the projection area, and their number density is given by the number of pores per unit volume [110, 254]. Results are shown in Figure 3.8(D). The ⌀ 2 mm specimen exhibits a larger maximum pore size and higher number of pores per unit volume than the ⌀ 1.3 mm specimen. This can be explained by the classical size effect phenomenon [253, 265]. As the sample volume becomes larger, there is an increase in probability of encountering a large defect.

In addition, pore morphology is another important factor to consider. Irregular pores can be detrimental to the mechanical performance of the metallic part since a large stress concentration can be induced at the tips of sharp pore edges [281]. Hence, the irregularity of the pore is evaluated by the sphericity (Ψ) – a measure of how much the shape of the object deviates from a perfect sphere ($\Psi = 1$), which is given by [57]:

$$\Psi = \frac{\pi^{\frac{1}{3}}(6V_\mathrm{P})^{\frac{2}{3}}}{S_\mathrm{P}} \tag{3.4}$$

where V_P is the pore volume and S_P is the surface area of the pore. The correlation between the sphericity and the equivalent diameter of the pore is present in Figure 3.8(E). In both specimens, as the pores become larger, they tend to be more irregular.

Based on the value of the sphericity, we classify the pores into two categories: gas pores and lack-of-fusion pores. Keyhole pores are not expected due to the processing conditions employed in this study [282]. Above a sphericity of 0.7, the pores are categorized as gas pores and below 0.7, they are considered as lack-of-fusion pores [283]. The orientation of the lack-of-fusion pores can strongly influence the mechanical performance of the component [170]. When these irregular pores orient perpendicular to the loading direction, they could potentially deteriorate the mechanical performance the most. This is further supported by the results in Figure 3.8(F). Those perpendicularly-oriented pores also exhibit a larger maximum projection area $A_{\mathrm{p,\ max}}$ relative to the loading direction, which suggests they can possibly be the most critical pores within the specimens.

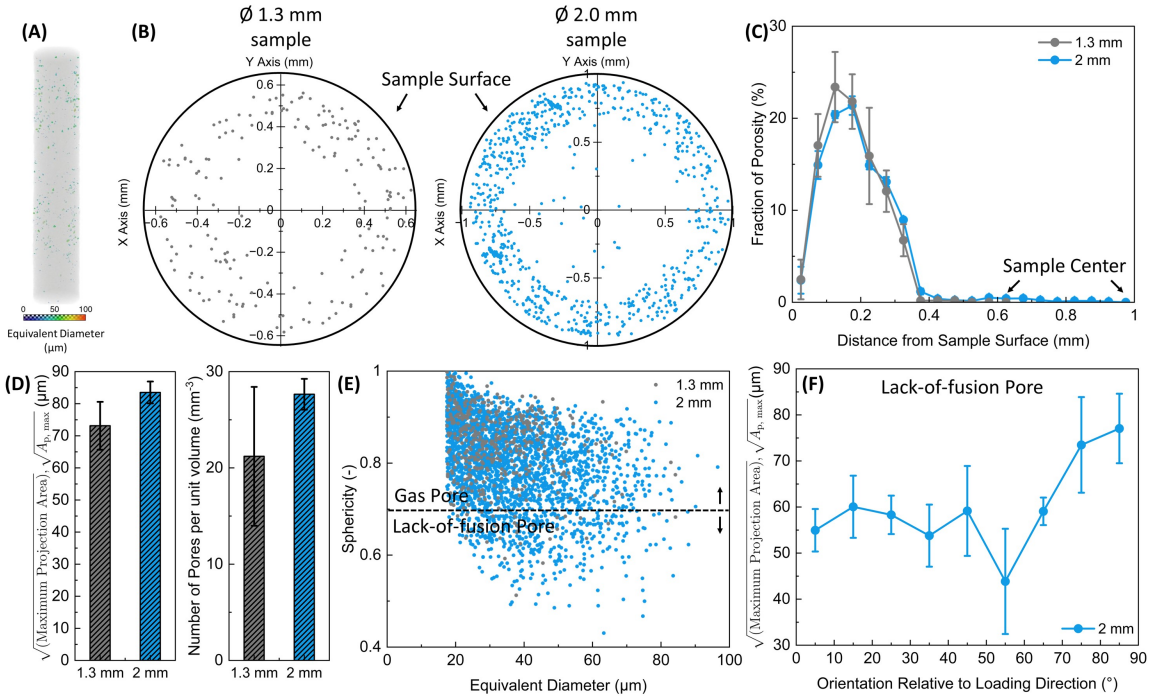


Fig. 3.8 (A) 3D rendered XCT images of a ⌀ 2.0 mm sample and pores inside the sample. (B) Projection view of the porosity distribution along the build direction in the 2 specimens under study. (C) Fraction of porosity against the distance from sample surface. (D) $\sqrt{\text{Maximum Projection Area}}$, $\sqrt{A_{\text{p, max}}}$, and number of pores per unit volume of the 2 specimens. Error bars represent the standard deviation from 3 repetitions. (E) Sphericity vs. equivalent diameter of pores detected in this study. (F) $\sqrt{A_{\text{p, max}}}$ of lack-of-fusion pores as a function of the orientation relative to the loading direction.

3.4 Discussion

Through systematic mechanical testing and characterisation, we have revealed and quantified the significant impact of sample size on the fatigue properties, surface roughness, processing-induced porosity, and microstructural development of AM Ti-6Al-4V. Nevertheless, the results presented as yet require further rationalization and deeper understanding can be gained via more detailed analysis.

3.4.1 Rationalization of the variation in tensile properties

- **Elastic modulus, yield strength, and ultimate tensile strength:** In AM parts, the presence of geometrical deviations and porosity decreases the minimal cross-sectional area leading to reductions in static strength [284, 285]. The smaller average cross-sectional area can also lower the measured elastic modulus. Here, we quantify the average and minimal cross-sectional area of the XCT data. The results are then normalized by the designed values as shown in Figure 3.9(B). The larger specimen demonstrates around 5% higher proportions of both average and minimal cross-sectional areas than the smaller specimen, which indicates its results obtained from the engineering stress-strain curves are closer to the actual values.

  If we take the average and minimal cross-sectional areas into account to correct the values of the elastic modulus and static strength separately, the differences in these properties between the two specimens become much smaller as shown

in Figure 3.9(C). Nevertheless, the ⌀ 1.3 mm specimen still exhibits a 9 GPa lower elastic modulus than the ⌀ 2 mm specimen, which can be attributed to the higher surface roughness of the smaller specimen. The surface irregularity can introduce plasticity into the sample even within the elastic region leading to an additional strain at a given stress [286].

On the other hand, the smaller specimen displays a comparable yield strength and an 80 MPa higher tensile strength than the larger specimen. Owing to the smaller α lath thickness in the ⌀ 1.3 mm specimen, one would expect a higher yield strength (σ_{y}) following the Hall-Petch relationship [275]:

$$\sigma_{\mathrm{y}} = \sigma_0 + \frac{k_{\mathrm{y}}}{\sqrt{d}} \tag{3.5}$$

where σ_0 is a materials constant, k_{y} is a strengthening coefficient, and d is the α lath thickness. However, this might be diminished by the lower surface quality of the specimen [252]. Furthermore, the smaller lath thickness provides more grain boundaries for dislocations to pile up leading to higher work hardening and thus higher tensile strength [287].

- **Fracture strain:** The variation in fracture strain mainly results from two factors: surface roughness and microstructural difference. A significant reduction in surface quality of the smaller specimen gives more crack initiators resulting in premature failure [288]. Additionally, the finer microstructure can lead to lower crack tortuosity which facilitates the crack growth rate [289].

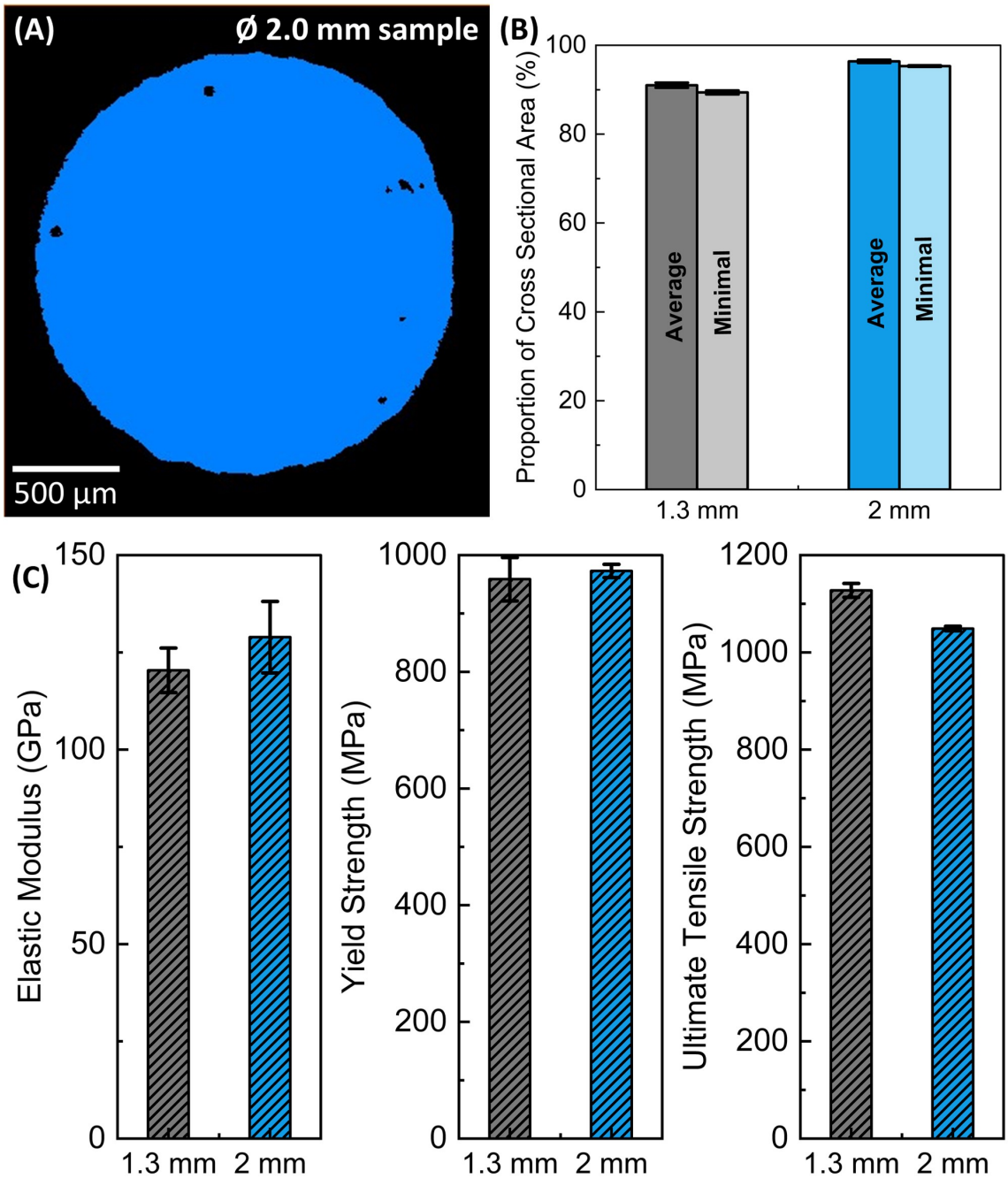


Fig. 3.9 (A) A segmented cross-sectional XCT slice of a ∅ 2.0 mm sample. (B) Proportions of average and minimal loading areas of the 2 specimens. (C) Corrected values of elastic modulus, yield strength, and ultimate tensile strength of the 2 specimens under study considering the effective loading area. Error bars represent the standard deviation from 3 specimens.

3.4.2 Fatigue fracture behaviour

Figure 3.10(A) shows the morphology of the fracture surface of a fatigue tested sample. Clearly, three steps are involved in the fatigue fracture process. In region I, the cracks are initiated from surface defects. The surrounding regions are relatively flat, which indicates a slow growth rate. In region II, more grooves can be observed – which is representative of faster but steady crack growth. A zoomed-in view of this region displays the striation pattern formed by plastic blunting and sharpening of the crack tip under cyclic loading. Once the crack length reaches a certain threshold, the crack grows rapidly in an unstable manner. More details of the crack growth process can be found in Appendix 1. In region III, a dimpled fracture surface resulting from microvoid coalescence during the final failure can be observed.

The fatigue crack initiation sites for both types of specimens can be identified. In all the tested samples, the fatigue cracks initiate from the surface defects, which indicates surface quality is the most critical factor for the fatigue properties of the net-shape AM Ti-6Al-4V [60, 290]. Such a surface initiated fracture process can be explained by linear elastic fracture mechanics. The stress intensity factor range (ΔK) for an arbitrarily shaped defect is given by [57]

$$\Delta K = Y \Delta\sigma \sqrt{\pi \sqrt{A_{\mathrm{p}}}} \tag{3.6}$$

where Y is a geometrical factor, $\Delta\sigma$ is the range of the applied stress, and $\sqrt{A_{\mathrm{p}}}$ is the square root of the projection area of a defect perpendicular to the load direction. The

geometrical factor for an internal defect is 0.50 and that for a surface defect is 0.65 [291, 292]. This means for defects of the same size, a surface defect can give rise to a higher stress intensity factor than an internal defect at the same applied stress. Hence, a surface defect is more likely to be the initiation site as compared to an internal defect.

In addition, some samples exhibit multiple fatigue crack initiation sites as shown in Figure 3.10(B). However, no significant variation in cycles to failure has been found between these samples and those in which a single crack initiates. The probability of occurrence is also not vastly different between the two types of specimens. Several studies have reported that a pore cluster near the fatigue crack initiation site can increase the stress concentration and facilitate the initiation process [154, 293]. Here, we account for a pore cluster near the initiation site when the distance between the pore and the initiation site is below 1 pore diameter. The effect of the pore on the local stress near the initiation site becomes negligible when they are further apart [154]. The probability of occurrence is no less than $\frac{1}{3}$ for both types of specimens, which indicates the influence of internal porosity on the fatigue fracture process can not be neglected. No significant difference in contingency has been found between the two types of specimens in our study.

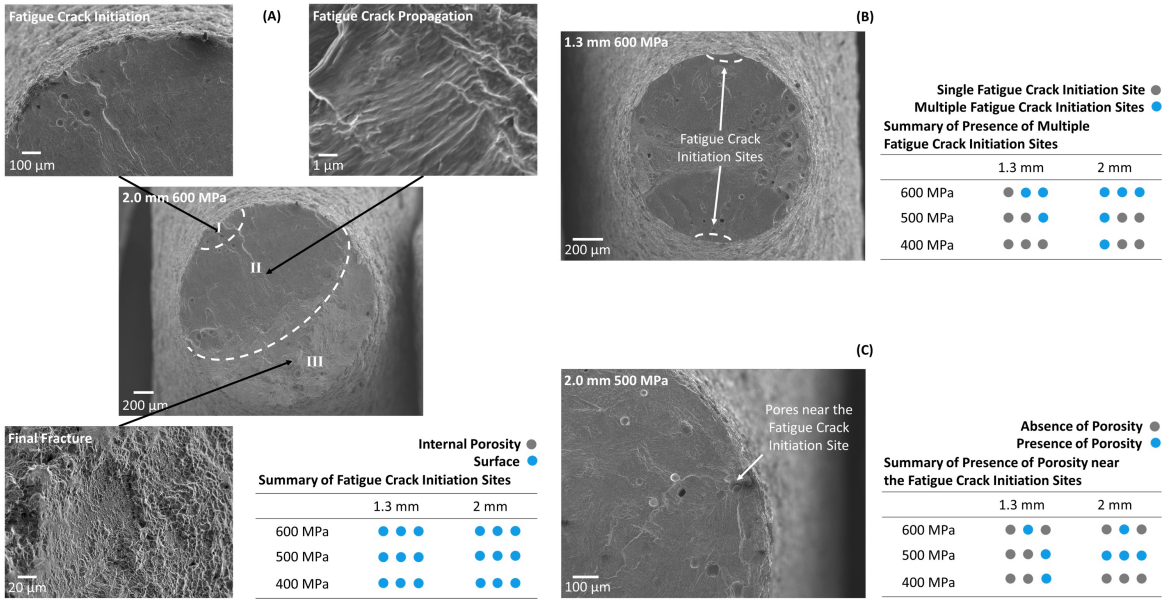


Fig. 3.10 Summary of fatigue fracture behaviours including (A) fatigue crack initiation sites, (B) presence of multiple fatigue crack initiation sites, and (C) presence of porosity near the fatigue crack initiation sites for all the tested samples.

To understand the fracture behavior quantitatively, we evaluate the striation spacing for all the tested samples. A zoomed-in view at a magnification of 10000× is captured at the centre of region II for each tested sample. This is around 380 μm from the initiation site for the ⌀ 1.3 mm specimen and 600 μm from the initiation site for the ⌀ 2.0 mm specimen. The image intensity perpendicular to the striations is extracted using ImageJ and the striation spacing is determined by the distance between each peak as shown in Figure 3.11(B). The spacing between 5 striations is analysed for each sample to ensure the repeatability of the result. Results are presented in Figure 3.11(C). For both types of specimens, the fatigue striation spacing decreases as $\sigma_{\max}$ decreases. This can be explained by a slower crack growth rate ($\frac{da}{dN}$) induced by a lower stress intensity factor range (ΔK) following the Paris' law [289]:

$$\frac{da}{dN} = C(\Delta K)^n \tag{3.7}$$

where C and n are materials constant. A lower incremental crack length gives rise to shorter striation spacing. Furthermore, the ⌀ 2 mm specimen exhibits larger striation spacing than the ⌀ 1.3 mm specimen at all applied stresses. This can be attributed to the different crack lengths of the observation locations in the two types of specimens. The observations were made at larger crack lengths for the larger specimens, which results in higher ΔK and thus larger incremental crack length.

To provide quantitative evidence of the fatigue crack growth process, we measure the variation in striation spacing during the fracture process. Zoomed-in views at four

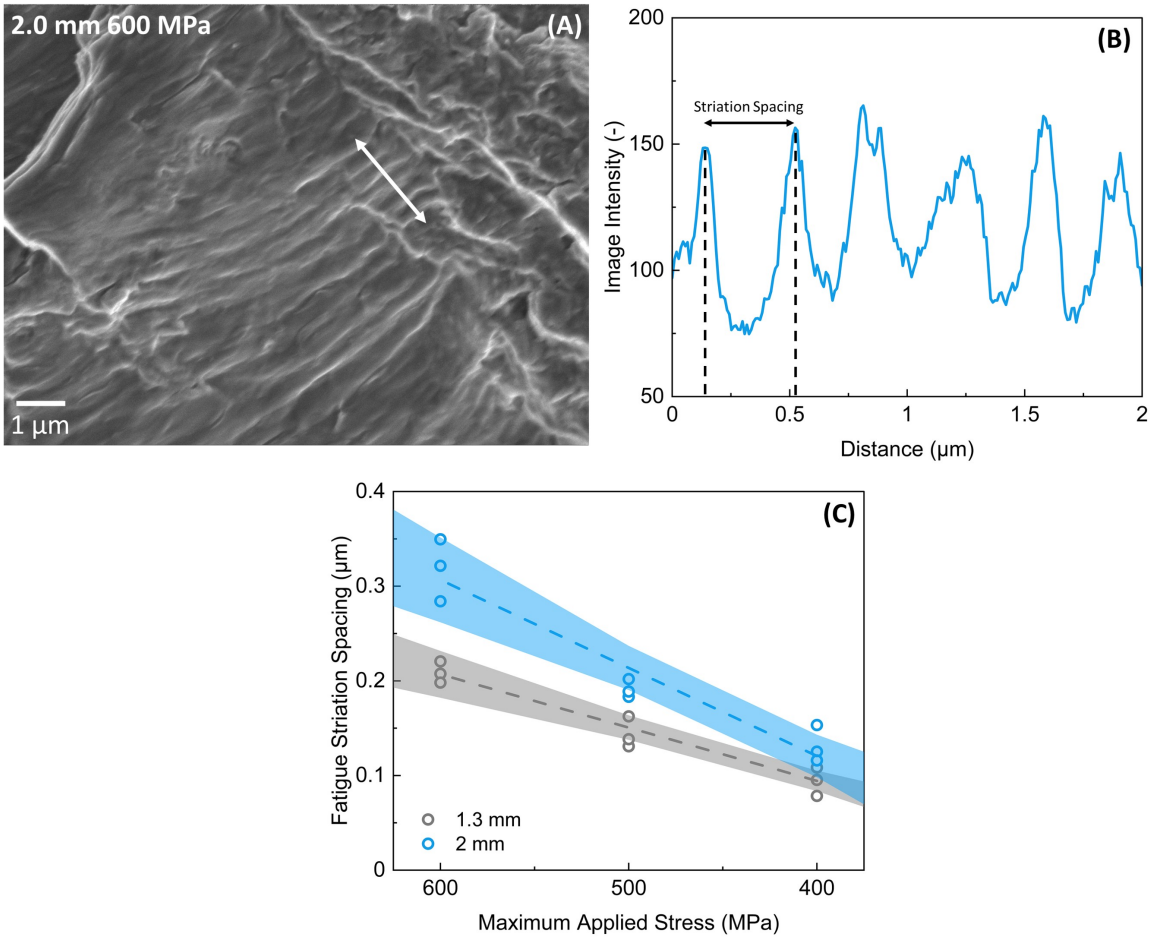


Fig. 3.11 (A) Fatigue striations observed on the fracture surface of a ∅ 2.0 mm sample tested at σ_{max} of 600 MPa. The arrow shows where the striation spacing analysis is performed. (B) Image intensity vs. distance along the arrow shown in (A). Striation spacing is characterized by the distance between the 2 peaks. (C) Correlation between fatigue striation spacing and maximum applied stress for the 2 specimens under study. Shaded area represents 95% confidence interval from 5 repetitions.

different locations are captured along the fatigue propagation path as shown in Figure 3.12(A). The spacing between 5 striations is analysed at each location. Results are shown in Figure 3.12(B). In both cases, almost no striations can be observed within a normalized distance of 0.3. Above 0.3, the striation spacing increases as the distance from the initiation site increases. This results from the higher ΔK at larger crack lengths leading to larger incremental crack lengths. Moreover, the striation spacing of the two types of specimens almost overlaps at the same distance from the initiation site, which confirms the crack growth behaviour can be described by Paris' law in Equation 7. The deviation in the number of cycles to propagate the crack between the two types of specimens mainly results from the difference in the propagation length.

Based on the evaluation of striation spacing, we estimate the proportion of the fatigue life during which the crack propagates for all the tested samples. The length of the fatigue propagation path is measured using ImageJ as shown in Figure 3.13(A). For samples with multiple crack initiation sites, all propagation paths are considered. The number of cycles to propagate the crack across the specimen is then estimated by dividing the total propagation path length by the striation spacing at the centre of region II. This is then normalized by the cycles to failure to determine the proportion of the lifetime spent in the propagation stage. Results are shown in Figure 3.13(B). The proportion of fatigue propagation cycle is lower than 40% for all the samples, which indicates crack propagation is not the dominant stage of the failure process and fatigue failure is eventually initiation process controlled. This confirms that our tests were performed in the high cycle fatigue regime [50, 294, 295]. Additionally, the

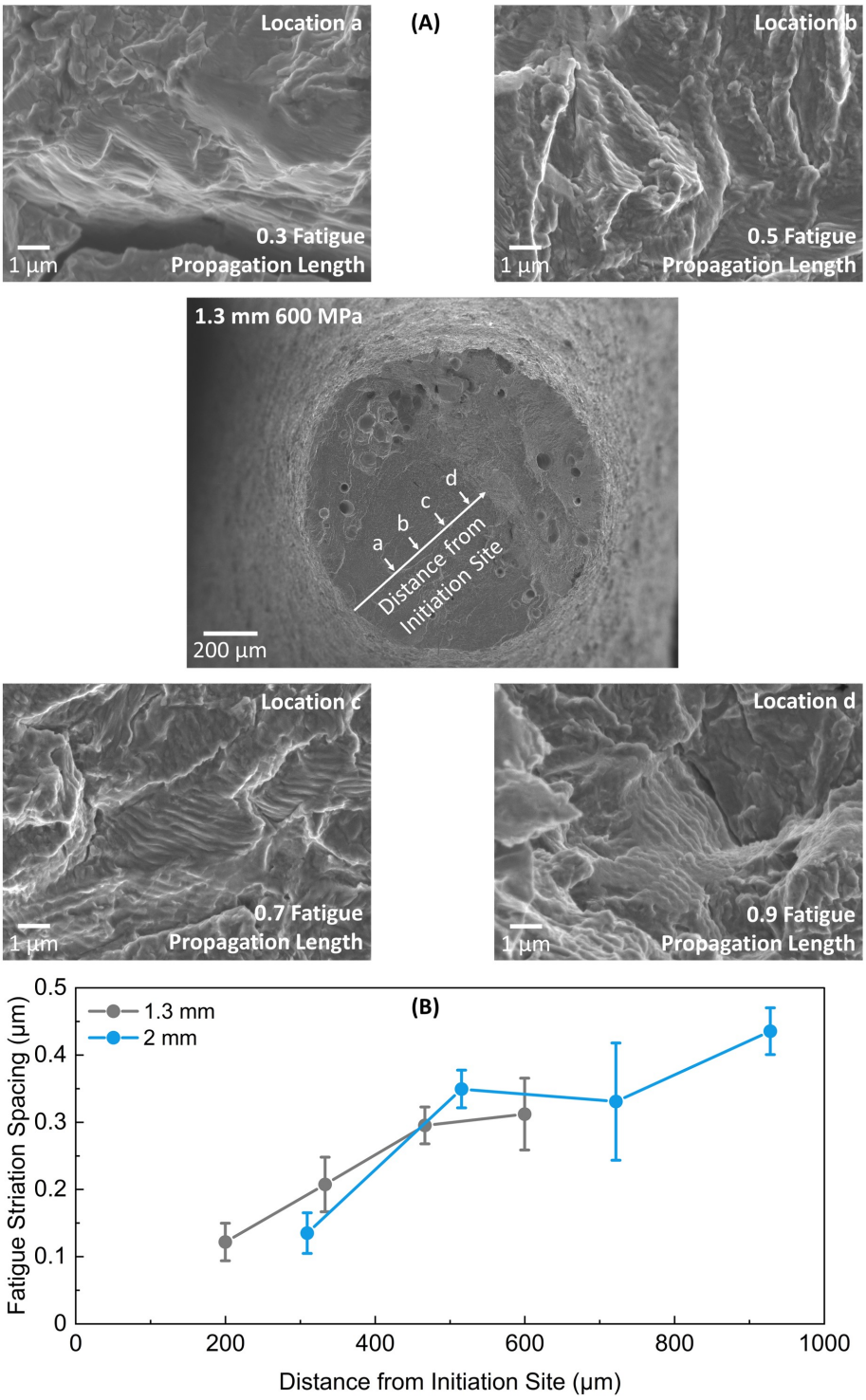


Fig. 3.12 (A) An example of the measurement of the distance from the initiation site. (B) Correlation between fatigue striation spacing and distance from the initiation site for the 2 specimens tested at 600 MPa. Error bars represent the standard deviation from 5 repetitions.

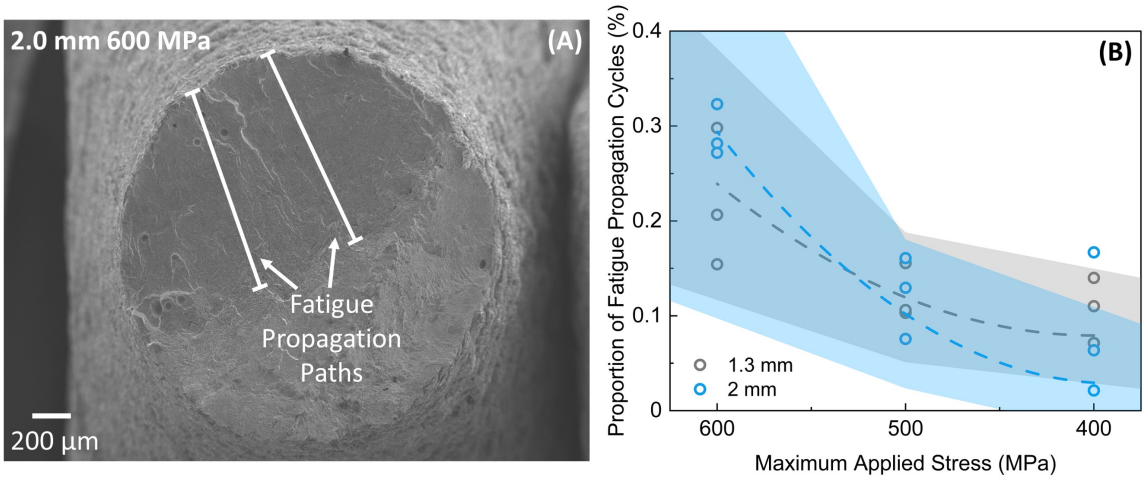


Fig. 3.13 (A) An example of the measurement of the length of fatigue propagation path. (B) Estimated proportion of fatigue propagation cycles as a function of the maximum applied stress. 95% confidence interval from 5 repetitions is shown in shaded area.

proportion of fatigue life due to crack propagation decreases as $\sigma_{\max}$ decreases for both types of specimens. This implies the failure process becomes more initiation driven as the stress is decreased.

It is crucial to note that the approach described above doesn't provide an accurate evaluation of the fatigue propagation cycle but it gives a good estimation of the proportion of fatigue propagation during the entire fracture process. The results are valid to shed light on the fatigue fracture process and the trend in behaviour with $\sigma_{\max}$ would remain the same.

3.4.3 Rationalization of the variation in fatigue properties

On the basis of the results presented in Sec. 3.4.2, the difference in fatigue properties between the two types of specimens can be rationalized. The surface initiated fracture process at all applied stresses confirms the higher fatigue resistance of the ∅ 2 mm

specimen is primarily due to the 50% lower surface roughness as compared to the ⌀ 1.3 mm specimen. As $\sigma_{\max}$ decreases, the number of cycles required to initiate a crack from a surface defect becomes more dominant in determining the fatigue life, leading to a larger difference in the average number of cycles to failure.

Having surface defects as the initiation sites cannot completely eliminate the contribution of internal porosity to the fatigue fracture process. We have measured the $\sqrt{\text{Projection Area}}$, $\sqrt{A_{\text{p}}}$, of the pore cluster near the fatigue initiation site for each of the tested sample. Results are shown in Figure 3.14. ◯ is used to denote samples without a pore cluster near the initiation site. For both types of specimens, pore clusters can be found near the initiation site in samples with the lowest cycles to failure at each applied stress. This highlights that internal porosity can degrade the fatigue performance of AM Ti-6Al-4V even when the fatigue crack is initiated from a surface defect. It is noteworthy that only the interaction between surface defects and internal pores on the fracture surface has been assessed in this study. The coalescence with any pores below or above the surface cannot be detected, which may also facilitate the fatigue fracture process [296].

Furthermore, the internal porosity has been found to contribute more to the fatigue fracture process of the larger specimen than that of the smaller specimen for the following two reasons. (1) The 50% lower surface roughness of the larger specimen results in a smaller stress intensity factor range, which means a smaller contribution to the failure process from the surface defects. (2) A higher number density of pores with larger sizes have been found close to the sample surface in the larger specimen

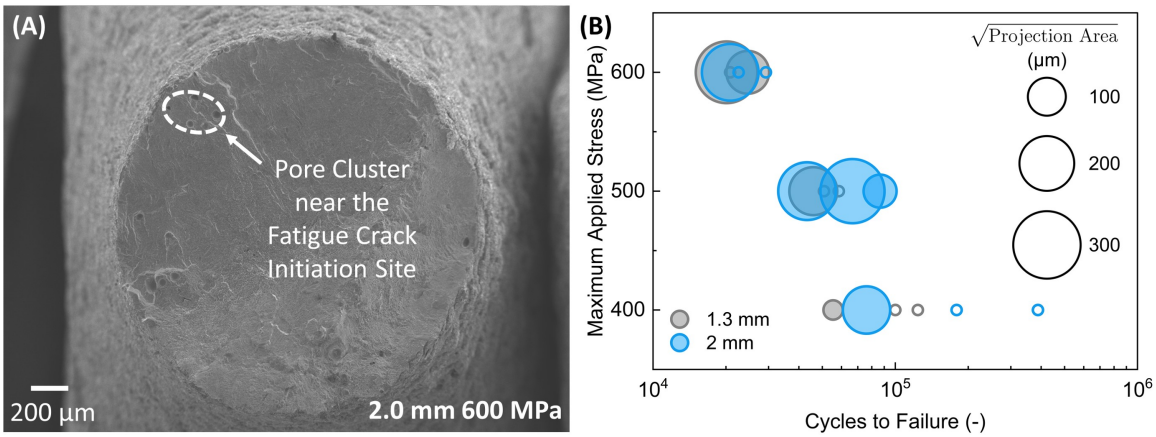


Fig. 3.14 (A) An example of the measurement of the projection area, A_p, of pore cluster near the fatigue crack initiation site. (B) $\sqrt{A_p}$ of the pore cluster for different tested specimens. ◯ represents the specimens without pore cluster near the initiation site.

(Sec. 3.3.5), which potentially gives rise to a higher stress concentration. This has been confirmed by the fracture surface analysis.

The more significant contribution from the internal porosity to the fracture process in the larger specimen may explain the higher scatter in fatigue life, which can be associated with the larger variation in pore characteristics, primarily pore size, in these specimens [154]. As the stress is decreased, the precise location and orientation of the pore cluster can have a significant effect on the stress concentration at the initiation site and therefore the number of cycles to initiate a crack. Hence, initiation becomes sensitive to the proximity of the pore clusters, giving rise to increased scatter.

Finally, the microstructural differences between the two types of specimens cannot be totally discounted. Several studies have reported that a finer microstructure can give rise to a higher fatigue strength in the high cycle fatigue regime since a higher number of grain boundaries can impede the dislocation motion [92, 297, 19]. However, this is not in agreement with our results. Here, the presence of surface defects and internal

porosity dominates the failure process. Nevertheless, the coarser microstructure of the larger specimen exhibits a stronger defect tolerance. A higher threshold for stress intensity factor range is needed to trigger the crack growth [256, 19]. Additionally, thicker α laths tend to induce more corrugated crack paths, which provides a higher resistance to fatigue crack growth in the larger specimen [298, 299].

3.5 Summary and Conclusions

To study the effect of sample size, we have performed systematic mechanical testing, high-resolution electron microscopy, and X-ray computed tomography on L-PBF Ti-6Al-4V material to evaluate the variation in fatigue behaviour and how this is influenced by microstructure, surface quality, and processing-induced porosity. Two sample sizes have been considered: ∅ 1.3 mm and ∅ 2.0 mm. The following specific conclusions can be drawn from this chapter:

- The larger specimen exhibits superior fatigue life in the high cycle fatigue regime: at $\sigma_{\max} = 600$ MPa, it is 11% greater; at $\sigma_{\max} = 500$ MPa, it is 27% greater; at $\sigma_{\max} = 400$ MPa, it is 130% greater. The scatter in fatigue life is approximately double that of the smaller specimen.

- Surface defects serve as the fatigue crack initiation sites for all the cases in this work. A reduction of surface roughness by 50% in the larger specimen contributes positively to the higher fatigue life. As $\sigma_{\max}$ decreases, the fracture process

becomes more surface initiation-driven leading to larger differences in fatigue life between the two types of specimen.

- Clusters of pores have often been found near the crack initiation sites thus facilitating the fatigue initiation process. The larger contribution of porosity to the fatigue fracture process is likely to be contributing to the higher fatigue scatter exhibited by the larger specimens. At lower $\sigma_{\max}$, the stress concentration from any pore cluster becomes a more dominant factor in determining the number of cycles for crack initiation.

- It seems that the different microstructure has only a minimal influence on the variation in fatigue behaviour observed. Nonetheless, the thicker α laths of the larger specimen can give rise to a higher tolerance to defects and more tortuous crack paths, which impedes fatigue crack growth.

Chapter 4

Orientation Matters: Assessing the Cyclic Deformation Behaviour of Laser Powder Bed Fusion Ti-6Al-4V

4.1 Introduction

Collective wisdom in the realm of topological optimization entails elements to be printed in different build orientations. However, the alternating heat localization along with the staircase effect yields structural inhomogeneity within the component [98, 243]. The significance of the inhomogeneity on the mechanical durability of the component, particularly the fatigue behaviour, is often underestimated, which gives rise to severe ramifications in practice and hinders the certification of the AM process [57, 43, 58].

Hence, in order to capitalize on the tremendous opportunities that AM offers, the orientation dependency of the fatigue behaviour must be elucidated.

So, how does printing orientation influence the fatigue behaviour of AM materials? Existing research has focused on machined specimens with the effect of surface roughness often neglected or not emphasised [176, 300–303]. However, machining is not applicable to complex structures in service conditions, which calls into question the relevance of most of the research to date. On the other hand, studies on as-built specimens have usually been restricted to three orientations: 0°, 45°, and 90° with respect to the build plate [61, 304–306]. The broad rule-of-thumb so far is that the 90° specimen demonstrates the highest fatigue strength as a result of the optimal surface finish. But this might as well oversimplifies the situation. Intricate components often require a multitude of printing orientations. One attempt has been made to assess the fatigue behaviour of the specimens printed in five different orientations [200]. Yet, the focus on one test condition and inconsistent sample preparation of this study limit our ability to derive further insight into the factors that influence the fatigue behaviour. Generally speaking, the synergistic effects of microstructure, surface defects, and porosity during the fatigue fracture process need further studies. Furthermore, it is still uncertain how the orientation influences the deformation behaviour. In intricate components, the local stress state and history are likely determined by the deformation response. Thus, when determining the fatigue response of a component, it is crucial to understand the effect of orientation on the elastic and plastic, as well as the fatigue properties.

The present study was initiated with the above in mind. Ti-6Al-4V specimens were designed and printed in seven build orientations. The overarching goal of this work is twofold: first to rationalize the variation in the deformation and fatigue behaviour of AM materials as a function of the build orientation; then determine the implication of the orientation effect on the behaviour of an intricate component. Hereinafter, we determined the elastic and plastic properties as well as the fatigue life of AM specimens between 10^4 and 10^6 cycles to inform the behaviour of metallic lattices. A combination of high-resolution microscopy and X-ray computed tomography was employed to examine structural inhomogeneities. We then probed the fracture surface to shed light on the cyclic deformation process. Finally, analytical and finite element solutions were developed for the behaviour of an octet-truss lattice material to confirm the importance of build orientation in practice.

4.2 Experimental Methods

4.2.1 Design of Experimentation

In order to study the effect of printing orientations on the elastic, plastic, and fatigue properties, samples were printed in seven different orientations relative to the build plate: 0°, 15°, 30°, 45°, 60°, 75°, and 90°, as shown in Figure 4.1(A). All samples were designed with a gauge length of 5.2 mm and a gauge diameter of 1.3 mm.

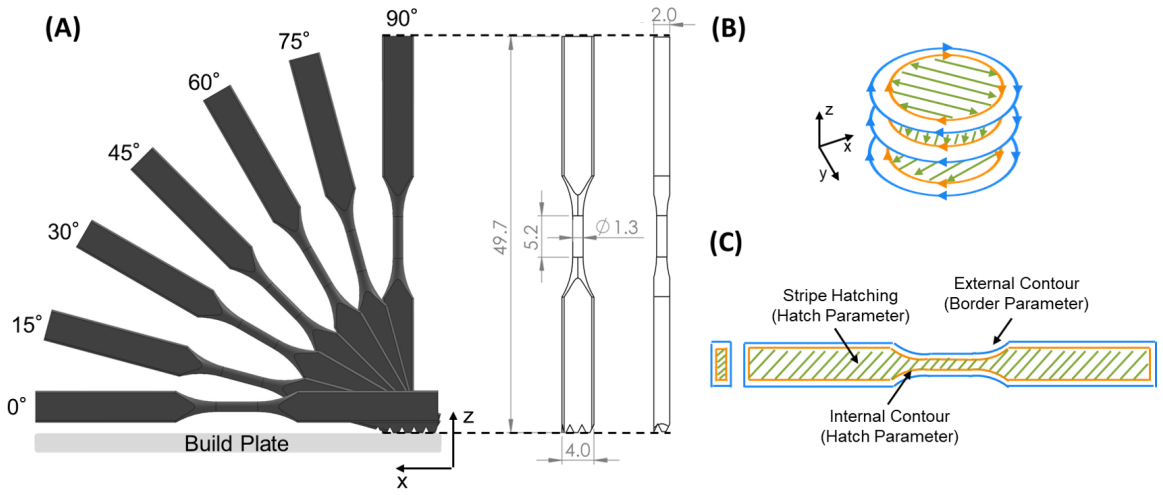


Fig. 4.1 (A) Geometries of the 7 tensile specimens used in this study. Schematic illustrations of (B) laser path along different consecutive layers and (C) laser path along each cross-sectional plane.

4.2.2 Processing by Laser Powder Bed Fusion

A Renishaw AM400 machine with a modulated 200 W ytterbium fibre laser was employed to produce the tensile samples. Electrode induction-melted gas atomised Ti-6Al-4V powders were fed into the machine. Table 4.1 details the processing parameters used in this study. A stripe hatching laser scan path pattern with a 67° rotation between each layer was adopted (Figure 4.1(B)). Two contour passes were performed near the free surfaces after each layer to achieve an optimal surface quality. We used hatch parameters for the internal pass and border parameters for the external pass (Figure 4.1(C)). For specimens below 30°, support structures were added. We employed heat treatment to all the samples at 800℃ for 4 hours in a vacuum furnace and sandblasted them using safti grit at 2 bar. We applied post-processing to assess the samples in the service conditions.

Ti-6Al-4V	Hatch Parameters	Border Parameters
Layer Thickness	30 μm	30 μm
Laser Power	200 W	100 W
Laser Scan Speed	0.786 m/s	0.750 m/s
Point Distance	55 μm	45 μm
Hatch Distance	65 μm	65 μm
Exposure Time	50 μs	40 μs
Spot Size (Radius)	35 μm	35 μm

Table 4.1 Processing parameters used for the manufacturing of tensile samples.

4.2.3 Assessment of Static & Dynamic Mechanical Behaviour

The mechanical behaviour at room temperature was examined using an Instron ElectroPuls E10k system with a 10kN load cell. Uniaxial tensile tests were conducted under displacement rate control at a strain rate of 2×10^{-3} s^{-1}. The macroscopic strain of the sample was measured on a 5.2 mm gauge length using a non-contact iMetrum video extensometry system.

Tensile fatigue tests were performed under load control at a frequency of 30 Hz and an R ratio of 0.1. Specimens were tested at maximum applied stresses of 600 MPa, 500 MPa, and 400 MPa. At each applied stress, we repeated three tests. All specimens were tested until rupture.

4.2.4 Characterization by Electron Microscopy

Microstructures were characterized using a Zeiss Merlin field emission gun scanning electron microscope (FEG-SEM) equipped with a Bruker electron backscatter diffraction (EBSD) detector. Surfaces parallel to the build direction were examined. Scans were performed at a 20 kV accelerating voltage and a 20 nA current. To evaluate the α lath

thickness distribution, the diffraction patterns were acquired at 400 × 300 resolution with a step size of 0.22 μm. To analyze the α lath Schmid factor and reconstruct prior-β grains, the diffraction patterns were collected at 400 × 300 resolution with a step size of 0.55 μm.

Fracture surfaces of the samples after fatigue tests were examined using a JEOL 6500F FEG-SEM. Fatigue crack initiation sites were identified to determine the failure mechanisms.

4.2.5 X-ray Computed Tomography (XCT)

An ImageiX CT system (North Star Imaging Inc., Minnesota, USA) was employed to conduct the X-ray computed tomography of the tensile samples. The gauge sections of the samples were detected for the quantification of surface quality and porosity level. During the scan, each sample was positioned 25.5 mm in front of the tungsten transmission target X-ray source filtered by a Cu foil of 0.95 mm thickness. The scan conditions were: 140 kV tube voltage, 71 μA tube current, 5 μm focal spot size, and 1 Hz frame rate. We set the isotropic voxel size to be 4.7 μm and thus any feature smaller than 14.1 μm cannot be resolved [263]. Reconstruction of the projection images was performed following a filtered back Projection algorithm in the efX-ct software (version 1.9.5.12, North Star Imaging Inc., Minnesota, USA). The data was analyzed using Avizo 9.7 software. Segmentation of the solid parts was performed using Otsu's method [264].

A summary of the samples tested in this Chapter is shown in Table 4.2.

Specimen	Sample	Tensile Test	Fatigue Test	Fractography
0°	Sample 1	Yes	No	No
0°	Sample 2	Yes	No	No
0°	Sample 3	Yes	No	No
0°	Sample 4	No	Yes ($\sigma_{\max} = 600$ MPa)	Yes
0°	Sample 5	No	Yes ($\sigma_{\max} = 600$ MPa)	Yes
0°	Sample 6	No	Yes ($\sigma_{\max} = 600$ MPa)	Yes
0°	Sample 7	No	Yes ($\sigma_{\max} = 500$ MPa)	Yes
0°	Sample 8	No	Yes ($\sigma_{\max} = 500$ MPa)	Yes
0°	Sample 9	No	Yes ($\sigma_{\max} = 500$ MPa)	Yes
0°	Sample 10	No	Yes ($\sigma_{\max} = 400$ MPa)	Yes
0°	Sample 11	No	Yes ($\sigma_{\max} = 400$ MPa)	Yes
0°	Sample 12	No	Yes ($\sigma_{\max} = 400$ MPa)	Yes
15°	Sample 1	Yes	No	No
15°	Sample 2	Yes	No	No
15°	Sample 3	Yes	No	No
15°	Sample 4	No	Yes ($\sigma_{\max} = 600$ MPa)	Yes
15°	Sample 5	No	Yes ($\sigma_{\max} = 600$ MPa)	Yes
15°	Sample 6	No	Yes ($\sigma_{\max} = 600$ MPa)	Yes
15°	Sample 7	No	Yes ($\sigma_{\max} = 500$ MPa)	Yes
15°	Sample 8	No	Yes ($\sigma_{\max} = 500$ MPa)	Yes
15°	Sample 9	No	Yes ($\sigma_{\max} = 500$ MPa)	Yes
15°	Sample 10	No	Yes ($\sigma_{\max} = 400$ MPa)	Yes
15°	Sample 11	No	Yes ($\sigma_{\max} = 400$ MPa)	Yes
15°	Sample 12	No	Yes ($\sigma_{\max} = 400$ MPa)	Yes
30°	Sample 1	Yes	No	No
30°	Sample 2	Yes	No	No
30°	Sample 3	Yes	No	No
30°	Sample 4	No	Yes ($\sigma_{\max} = 600$ MPa)	Yes
30°	Sample 5	No	Yes ($\sigma_{\max} = 600$ MPa)	Yes
30°	Sample 6	No	Yes ($\sigma_{\max} = 600$ MPa)	Yes
30°	Sample 7	No	Yes ($\sigma_{\max} = 500$ MPa)	Yes
30°	Sample 8	No	Yes ($\sigma_{\max} = 500$ MPa)	Yes
30°	Sample 9	No	Yes ($\sigma_{\max} = 500$ MPa)	Yes
30°	Sample 10	No	Yes ($\sigma_{\max} = 400$ MPa)	Yes
30°	Sample 11	No	Yes ($\sigma_{\max} = 400$ MPa)	Yes
30°	Sample 12	No	Yes ($\sigma_{\max} = 400$ MPa)	Yes
45°	Sample 1	Yes	No	No
45°	Sample 2	Yes	No	No
45°	Sample 3	Yes	No	No
45°	Sample 4	No	Yes ($\sigma_{\max} = 600$ MPa)	Yes
45°	Sample 5	No	Yes ($\sigma_{\max} = 600$ MPa)	Yes
45°	Sample 6	No	Yes ($\sigma_{\max} = 600$ MPa)	Yes

45°	Sample 7	No	Yes (σ_{max} = 500 MPa)	Yes
45°	Sample 8	No	Yes (σ_{max} = 500 MPa)	Yes
45°	Sample 9	No	Yes (σ_{max} = 500 MPa)	Yes
45°	Sample 10	No	Yes (σ_{max} = 400 MPa)	Yes
45°	Sample 11	No	Yes (σ_{max} = 400 MPa)	Yes
45°	Sample 12	No	Yes (σ_{max} = 400 MPa)	Yes
60°	Sample 1	Yes	No	No
60°	Sample 2	Yes	No	No
60°	Sample 3	Yes	No	No
60°	Sample 4	No	Yes (σ_{max} = 600 MPa)	Yes
60°	Sample 5	No	Yes (σ_{max} = 600 MPa)	Yes
60°	Sample 6	No	Yes (σ_{max} = 600 MPa)	Yes
60°	Sample 7	No	Yes (σ_{max} = 500 MPa)	Yes
60°	Sample 8	No	Yes (σ_{max} = 500 MPa)	Yes
60°	Sample 9	No	Yes (σ_{max} = 500 MPa)	Yes
60°	Sample 10	No	Yes (σ_{max} = 400 MPa)	Yes
60°	Sample 11	No	Yes (σ_{max} = 400 MPa)	Yes
60°	Sample 12	No	Yes (σ_{max} = 400 MPa)	Yes
75°	Sample 1	Yes	No	No
75°	Sample 2	Yes	No	No
75°	Sample 3	Yes	No	No
75°	Sample 4	No	Yes (σ_{max} = 600 MPa)	Yes
75°	Sample 5	No	Yes (σ_{max} = 600 MPa)	Yes
75°	Sample 6	No	Yes (σ_{max} = 600 MPa)	Yes
75°	Sample 7	No	Yes (σ_{max} = 500 MPa)	Yes
75°	Sample 8	No	Yes (σ_{max} = 500 MPa)	Yes
75°	Sample 9	No	Yes (σ_{max} = 500 MPa)	Yes
75°	Sample 10	No	Yes (σ_{max} = 400 MPa)	Yes
75°	Sample 11	No	Yes (σ_{max} = 400 MPa)	Yes
75°	Sample 12	No	Yes (σ_{max} = 400 MPa)	Yes
90°	Sample 1	Yes	No	No
90°	Sample 2	Yes	No	No
90°	Sample 3	Yes	No	No
90°	Sample 4	No	Yes (σ_{max} = 600 MPa)	Yes
90°	Sample 5	No	Yes (σ_{max} = 600 MPa)	Yes
90°	Sample 6	No	Yes (σ_{max} = 600 MPa)	Yes
90°	Sample 7	No	Yes (σ_{max} = 500 MPa)	Yes
90°	Sample 8	No	Yes (σ_{max} = 500 MPa)	Yes
90°	Sample 9	No	Yes (σ_{max} = 500 MPa)	Yes
90°	Sample 10	No	Yes (σ_{max} = 400 MPa)	Yes
90°	Sample 11	No	Yes (σ_{max} = 400 MPa)	Yes
90°	Sample 12	No	Yes (σ_{max} = 400 MPa)	Yes

Table 4.2 A summary of the samples tested in this work.

4.3 Experimental Results

4.3.1 Quasi-static Behaviour

The quasi-static mechanical performance of the 7 specimens is presented in Figure 4.2(A). The summarized values of yield strength, ultimate tensile strength, and fracture strain are shown in Figure 4.2(B). Both yield strength and ultimate tensile strength exhibit an increase when the build orientation increases from 0° to 15°, a drop from 15° to 75°, and a final increase from 75° to 90°. The 15° specimen demonstrates 84 MPa higher yield strength and 53 MPa higher ultimate tensile strength on average than the 75° specimen. On the other hand, there is an inversion of the tendency with the fracture strain. The 15° specimen shows around 9% lower average fracture strain than the 75° specimen. This orientation dependency is further discussed in Sec. 4.4.1.

4.3.2 Dynamic Behaviour in Fatigue

The fatigue response of samples with different build orientations is illustrated in Figure 4.3(A). At all applied stresses, cycles to failure generally increase as the build orientation increases and a final drop in cycles to failure is observed for the 90° specimen. The only exception is at $\sigma_{\max} = 500$ MPa, where the drop starts from the 75° specimen.

The scatter in fatigue life at each applied stress is evaluated by the coefficient of variation. Results are shown in Figure 4.3(B). The 75° specimen shows the highest

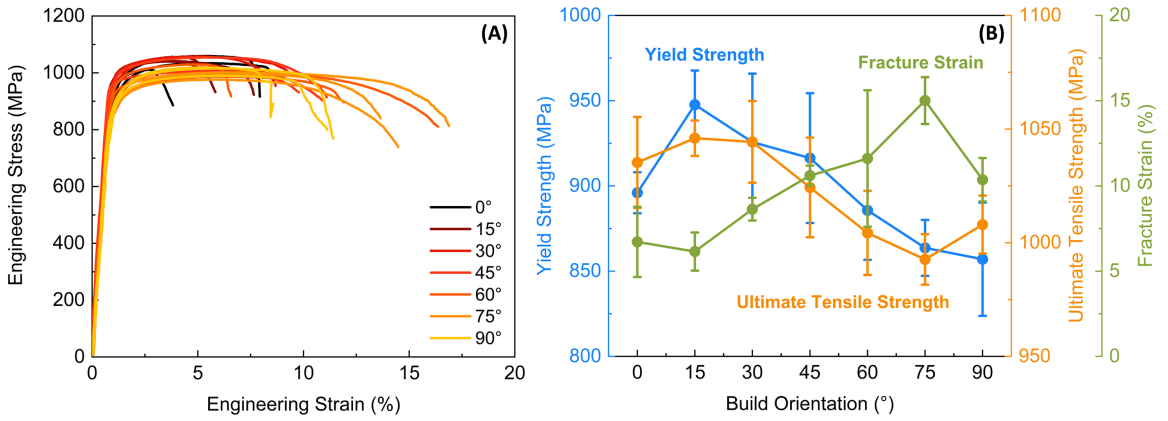


Fig. 4.2 (A) Engineering stress-strain curves of AM Ti-6Al-4V at a strain rate of 2×10^{-3} s^{-1}. (B) Yield strength, ultimate tensile strength, and fracture strain vs. build orientation of the 7 specimens under study. Error bars represent the standard deviation from 3 repetitions.

fatigue scatter at $\sigma_{max} = 500$ MPa (74%) followed by the 45° specimen at $\sigma_{max} = 500$ MPa (63%). No significant correlation between the fatigue scatter and applied stress can be observed. The orientation dependency of the fatigue properties is rationalized in Sec. 4.4.3.

4.3.3 Microstructural Characterization

Figure 4.4(A-G) shows the EBSD images of the α lath microstructure. The thickness distribution of the lath is measured using stereological statistical analysis. An ellipse is fitted to each grain and the thickness of the lath is determined by the length of the short axis of the ellipse. For each sample, more than 1500 α laths were analyzed to obtain a statistical distribution. Results are present in Figure 4.4(H). All the specimens demonstrate average lath thickness between 1 μm and 1.3 μm. No significant

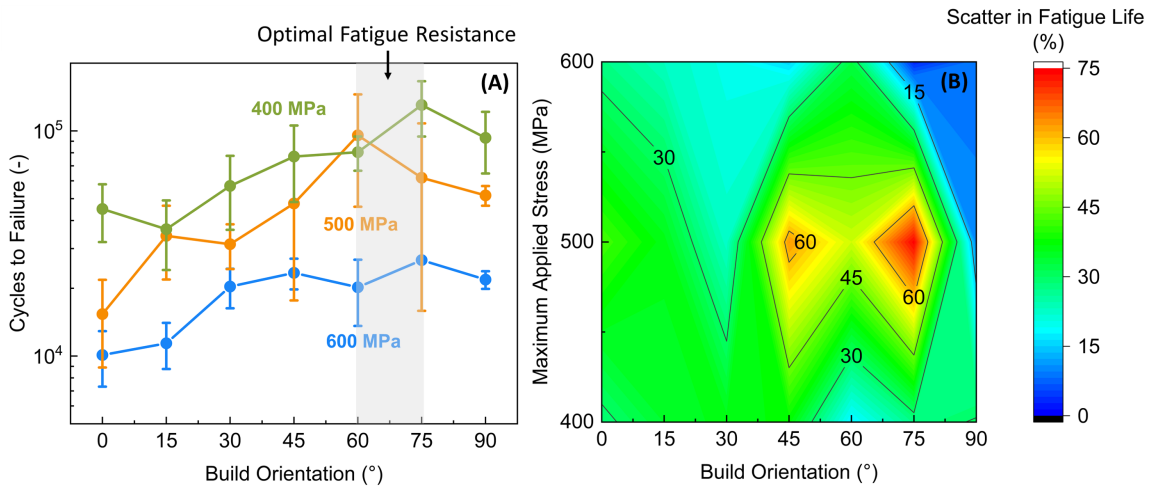


Fig. 4.3 (A) Cycles to failure vs. build orientation for the specimens manufactured in this work. Error bars represent the standard deviation from 3 repetitions. (B) Calculated map of scatter in fatigue life as a function of build orientation and maximum applied stress for the 7 specimens.

difference in the lath thickness can be observed among the specimens of different build orientations.

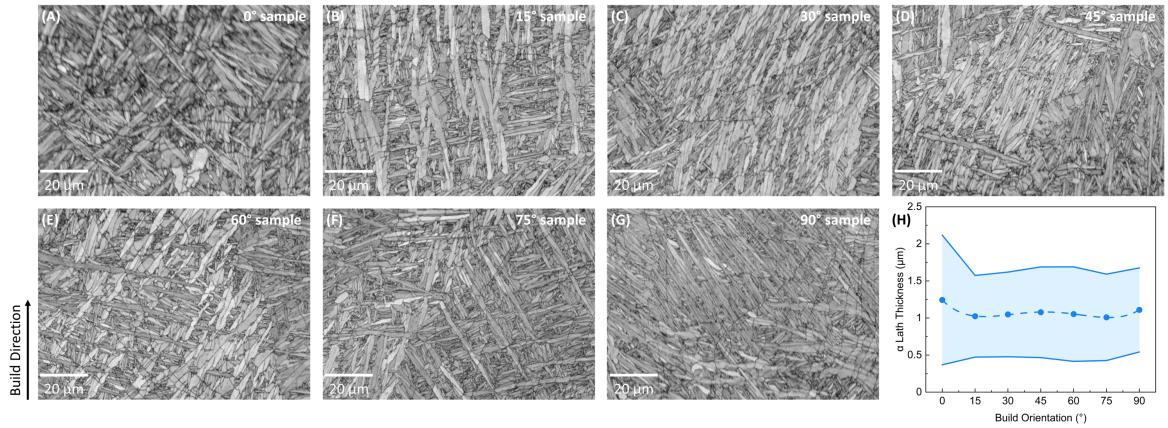


Fig. 4.4 (A-G) Longitudinal microstructure of the 7 specimens under study. (H) Average α lath thickness $\pm$ 1 standard deviation vs. build orientation of the 7 specimens.

Figure 4.5 displays the EBSD maps of the 7 specimens at lower magnifications. All microstructures are composed of more than 95% thin α laths organized in bundles inherited from the prior-β grains. The contour pole figure confirms {0001} has the

strongest texture among the three plane families {0001} $\{\bar{1}100\}$ and $\{\bar{1}2\bar{1}0\}$ in α microstructure with respect to the x-z plane of Figure 4.2(B) (Figure 4.6(A)). The quantification of the texture strength in Figure 4.6(B) shows all the specimens exhibit α texture indices below 2.5, which suggests the α microstructure of L-PBF Ti-6Al-4V is weakly textured [307, 98]. Additionally, the variation in texture strength of different specimens is minimal.

We reconstruct the prior-β grains from the descendant α lath structure using the MTEX 5.8.2 tool box following the transformation indicated in Figure 4.4 [270, 308, 309]. Each α lath is analyzed together with the neighbouring α laths to find the suitable prior-β grain based on the following Burgers orientation relationship:

$$(110)_\beta//(0001)_\alpha, [111]_\beta//[11\bar{2}0]_\alpha \tag{4.1}$$

If the neighbouring laths are of the same prior-β orientation, these laths are associated with the same prior-β grain. The process iterates across the whole set of laths.

As shown in Figure 4.5, columnar grains along the build orientation can be observed. The remelting and resolidification of each layer give rise to epitaxial grain growth opposing the maximum temperature gradient [98, 19]. The contour pole figure of Figure 4.6(A) exhibits the texture strength for the three plane families {100} {110} and {111} in the prior-β microstructure with respect to the x-z plane of Figure 4.1(B). In all the specimens, the {100} texture component is the strongest [58]. The crystallographic nature of the $\beta \rightarrow \alpha$ transformation is also clearly revealed by the transfer of texture.

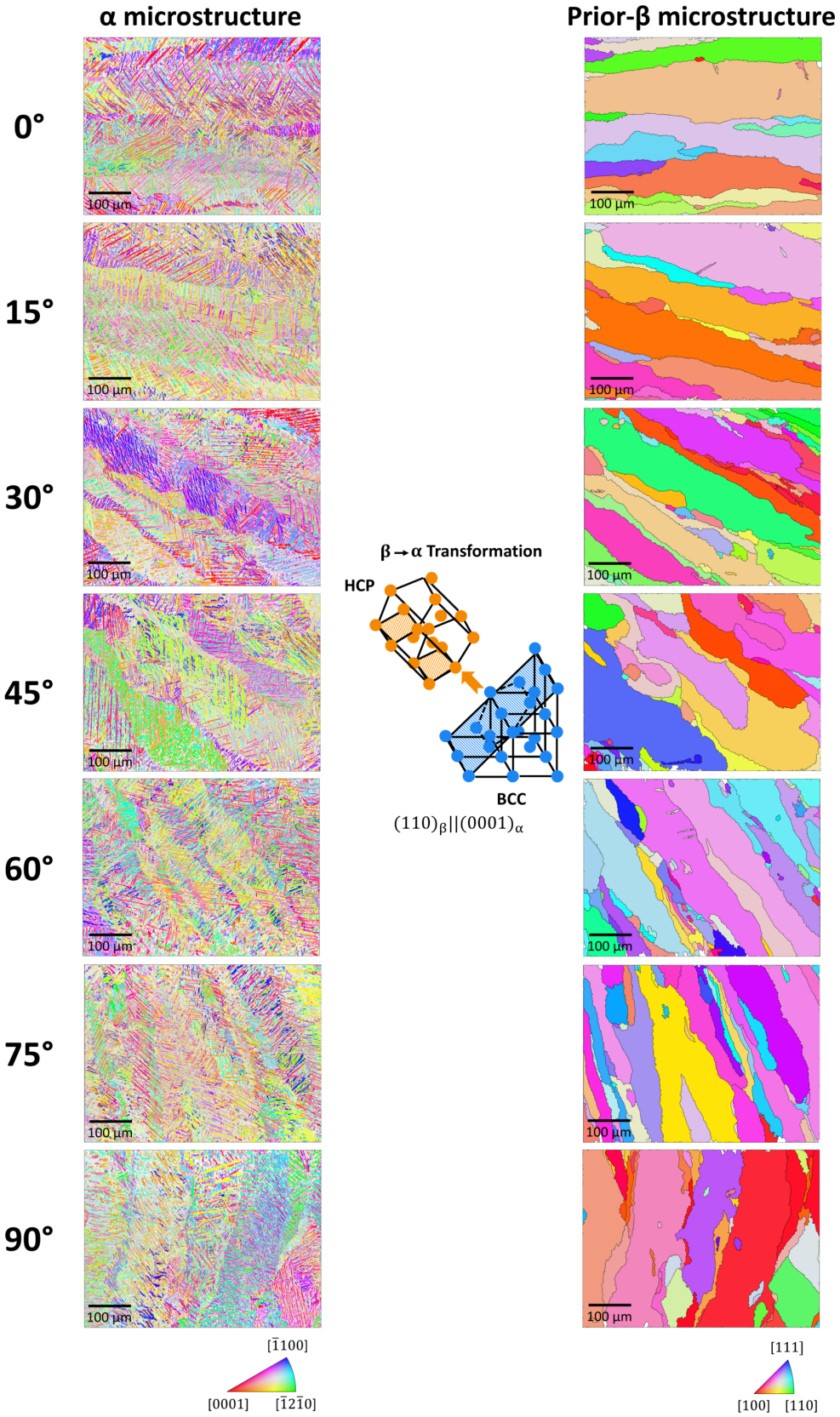


Fig. 4.5 Longitudinal EBSD maps of the α lath and the associated reconstructed prior-β microstructure of the 7 specimens under study.

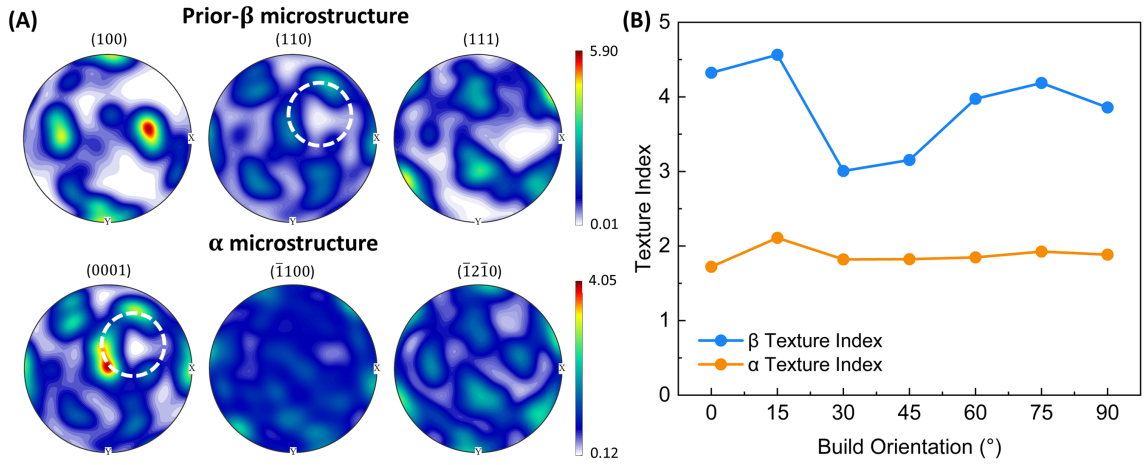


Fig. 4.6 (A) Contour pole figures of the α and prior-β microstructure of the 90° specimen. The texture rings confirm the $\beta \rightarrow \alpha$ transformation during the solidification process. (B) Texture index vs. build orientation for all the specimens.

The pole figure shows the Burgers orientation relationship between the two phases – $(110)_\beta//(0001)_\alpha$. The same texture ring can be observed along both $(110)_\beta$ and $(0001)_\alpha$, which confirms the success of our reconstruction.

Unlike the α microstructure, the prior-β grains demonstrate significant variations in texture strength across different specimens. The β texture index of the 15° specimen is more than 50% higher than that of the 30° specimen. Nevertheless, the martensitic transformation during the solidification process deteriorates the variant selection in Ti-6Al-4V alloys, resulting in a weakly textured α lath microstructure [272–274].

4.3.4 Surface Roughness

The surface profiles of different specimens were evaluated using the XCT data. Cross-sectional images on both the sagittal and coronal planes were extracted from the tomography data. After binarization, the specimen edges were detected and analyzed

using Image-J as shown in Figure 4.7(A). The surface roughness (R_a) for each line profile was then computed. Results are shown in Figure 4.7(B). Apart from the 90° specimen, the downward-facing surfaces of all other specimens exhibit higher surface roughness than the otherward-facing surfaces as a result of dross formation [100, 101]. When the laser enters the overhang regions, the loose powders underneath the downward-facing surface hinder heat dissipation owing to the low thermal conductivity, resulting in the collapse of the quasi-steady state melt pool. The excessive heat then leads to a keyhole-like melt mode, which causes a drilling effect.

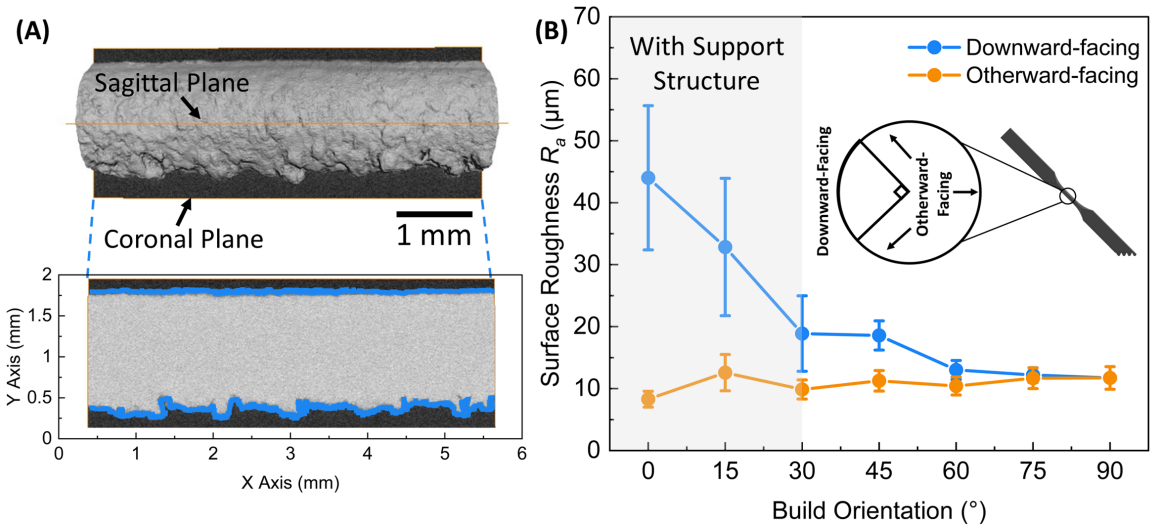


Fig. 4.7 (A) An example of the surface roughness (R_a) measurement on the 0° specimen. (B) Downward-facing and otherward-facing surface roughness (R_a) as a function of the build orientation. Error bars represent the standard deviation from 3 repetitions.

Moreover, the difference in surface roughness between the downward-facing and otherward-facing surfaces is significantly reduced when the build orientation increases from 0° to 75°. This can be attributed to the less pronounced dross formation as the overhang regions become smaller [101]. Additionally, no significant difference in surface

roughness can be found between the 30° and 45° specimens. The presence of support structures transfers the heat from the samples to the build plate, which improves the melt pool stability and reduces the dross formation [103–105]. However, after the support structure is removed, connection marks are introduced into the sample surfaces deteriorating the surface quality [151, 310]. The combination of these two factors gives rise to the comparable surface roughness between the two specimens.

4.3.5 Processing-induced Porosity

The presence of porosity was also identified and quantified using the XCT data (Figure 4.8(A)). Figure 4.8(B) shows the spatial distributions of the pores in the x-y plane of the 0°, 30°, and 90° specimens. In the 0° sample, the pores are mostly near the downward-facing surface. In the 30° sample, they start to populate near the otherward-facing surface. In the 90° sample, the pores are uniformly distributed close to the entire sample surface.

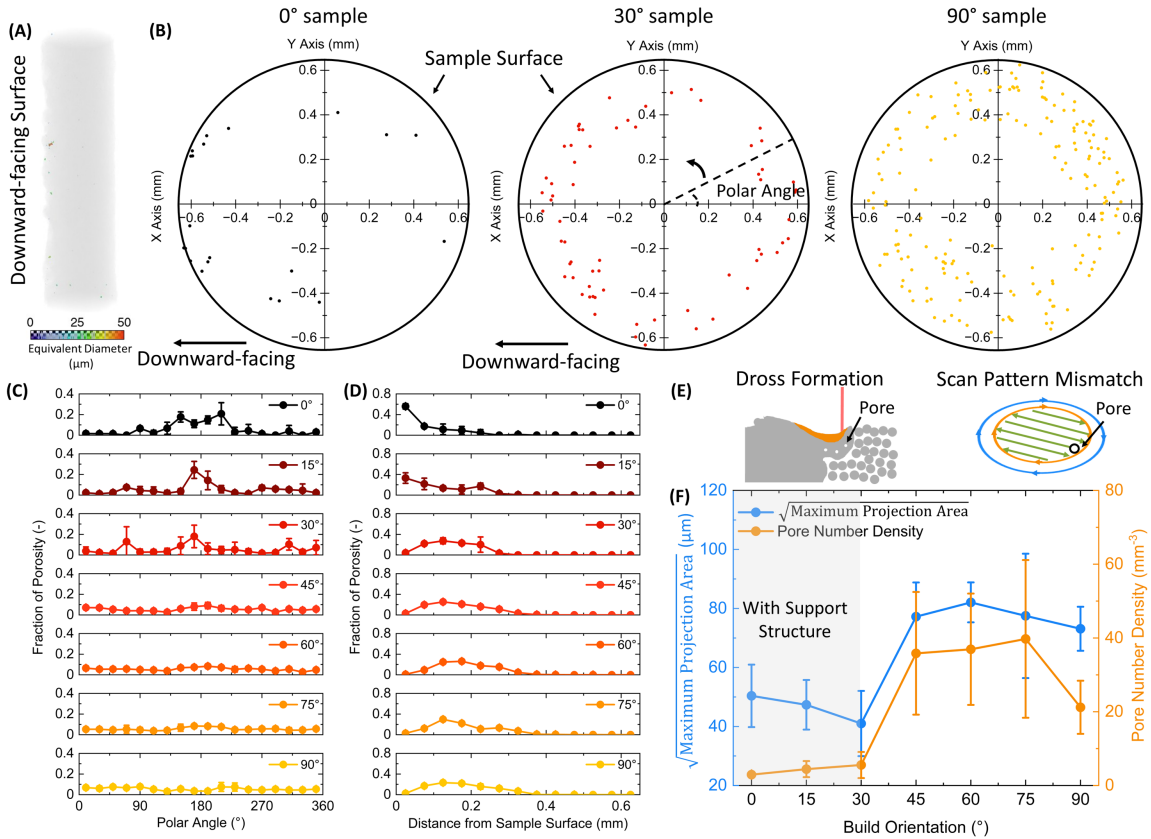


Fig. 4.8 (A) 3D rendered XCT images of a 0° sample and pores inside the sample. (B) Projection view of the porosity distribution along the build direction in the 0°, 30°, and 90° samples. (C) Fraction of porosity against the polar angle. (D) Fraction of porosity against the distance from the sample surface. (E) Schematic illustration of the pore formation mechanisms. (F) $\sqrt{\text{Maximum Projection Area}}$, $A_{\text{p, max}}$, and number of pores per unit volume as a function of the build orientation.

We further confirm this statement by the quantification in Figure 4.8(C). In the 0° sample, more than 60% of the pores are found to be close to the downward-facing surface. This value decreases to 38% in the 30° sample. In the 90° sample, only 20% of the pores are adjacent to the downward-facing surface, which is similar to the pore populations adjacent to other-oriented surfaces within the specimen. The variation in the spatial distribution of the pores can be explained by the pore formation mechanisms [100, 101]. When the build orientation is 0°, the heat accumulation at the overhang regions introduces an instability in the melt pool, resulting in gas entrapment and incomplete melting of the powder particles. As the build orientation increases, the overhang regions become smaller. Fewer pores are generated as a result of the excess heat.

In addition, the distances of the pores from the sample surface are depicited in Figure 4.8(D). In the 0° sample, more than 70% of the pores are within 0.1 mm of the sample surface. When the build orientation increases, the pores start to distribute more towards the centre of the sample. In the 90° sample, more than 80% of the pores are found to be between 0.1 mm and 0.4 mm away from the sample surface. This suggests the pore formation mechanisms are different in different specimens (Figure 4.8(E)). As we discussed above, the pores are mainly induced by dross formation in the 0° sample. When the samples are built more vertically, the majority of the pores are formed due to the mismatch between the strip hatching and contour scan patterns and the gaps between contour passes [278–280].

The size and number density of the pores are also important factors to consider for the fatigue performance of AM components [110, 154]. The size of the pores is given by the Murakami parameter $\sqrt{A_\mathrm{p}}$, where A_p is the projection area in the plane normal to the loading direction, and their number density is characterized by the number of pores per unit volume [110, 254]. Results are shown in Figure 4.8(F). When the build orientation is 30° or below, the maximum $\sqrt{A_\mathrm{p}}$ of the pores within all the specimens is lower than 50 μm on average, and the average number density of the pores is smaller than 6 mm^{-3}. As the build orientation increases to 45° or above, the pores have maximum $\sqrt{A_\mathrm{p}}$ larger than 70 μm on average, and a number density higher than 20 mm^{-3}. The substantial difference in the porosity level results from the use of support structures when the build orientation is 30° or below [103]. These support structures can facilitate the heat transfer between samples and build plate, lowering the thermal gradient within the samples, which enables more pores to escape into the atmosphere [103–105].

4.4 Discussion & Evaluation of Experimental Results

The above results provide quantitative evidence of the strong orientation dependency of the surface quality, processing-induced porosity, and microstructural development of AM Ti-6Al-4V and how this influences the elastic, plastic, and fatigue properties.

However, these results warrant further rationalization and deeper understanding can be gained via more detailed analysis.

4.4.1 Rationalization of the variation in tensile properties

AM often introduces geometrical deviations and porosity in the printed parts, which may reduce the effective loading area resulting in lower yield strength and ultimate tensile strength [284, 285]. To evaluate the effective loading area, we measure the minimum cross sectional area of a specimen from the XCT data [17, 284]. Figure 4.9(B) presents the results normalized by the designed area. The effective loading area generally decreases as the samples are built more vertically. The 0° specimen demonstrates 6.8% higher effective loading area compared to the 90° specimen.

We then proceed by correcting the tensile properties with the effective loading area. Results are shown in Figure 4.9(C). The corrected values of yield strength and ultimate tensile strength exhibit similar trends to the uncorrected values. The 15° specimen has a 64 MPa higher average yield strength than the 75° specimen while the 30° specimen has a 49 MPa higher average ultimate tensile strength than the 75° specimen. The variation in both properties can be attributed to the slip behaviour of α grains.

In hcp crystals, there are five different families of slip systems, namely the basal $\langle a \rangle$, prismatic $\langle a \rangle$, pyramidal $\langle a \rangle$, first order pyramidal $\langle a+c \rangle$, and second order pyramidal $\langle a+c \rangle$ slip systems with 30 possible slip systems in total, as shown in Figure 4.10(A). Among them, basal $\langle a \rangle$, prismatic $\langle a \rangle$, and first order pyramidal $\langle a+c \rangle$ are the main operating deformation systems at room temperature [311–313]. When grains start to

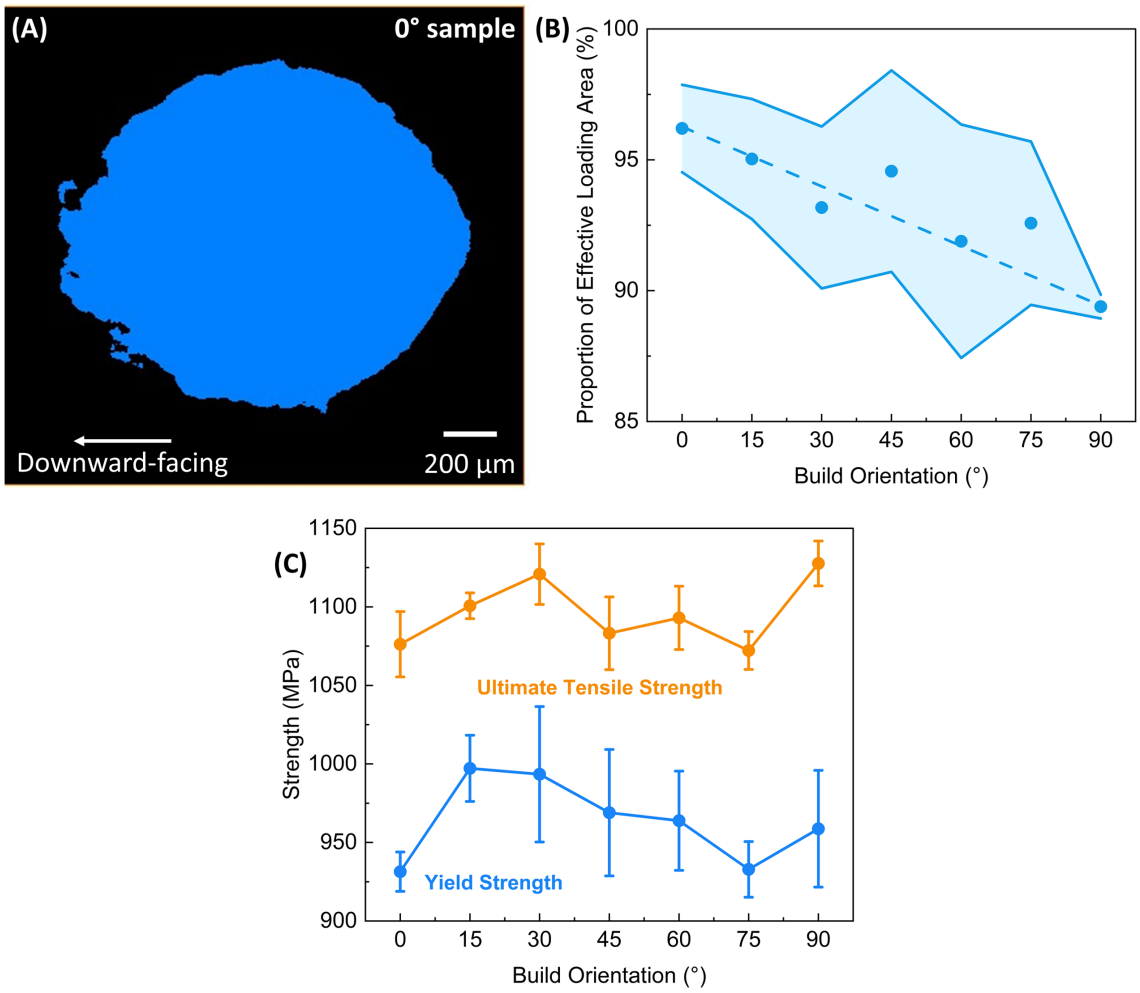


Fig. 4.9 (A) A segmented cross-sectional XCT slice of a 0° sample. (B) Proportion of effective loading area ± 1 standard deviation vs. build orientation of the 7 specimens under study. (C) Corrected values of yield strength and ultimate tensile strength as a function of the build orientation. Error bars represent the standard deviation from 3 repetitions.

deform, the shear stress acting in the slip direction on the slip plane needs to reach a critical value to activate the slip activity and the critical shear stress τ_C can be evaluated following Schmid's law:

$$\tau_C = \sigma_a m \tag{4.2}$$

where σ_a is the applied normal stress to activate the slip activity and m is the Schmid factor.

Based on this theory, grains with high Schmid factors (0.4-0.5) require a relatively low applied stress to trigger dislocation motion [314, 315]. Hence, we evaluate the proportion of grains with high Schmid factors in each specimen and the results are shown in Figure 4.10(B). Among the three families of slip systems, the trend in how the proportion of grains with high Schmid factors for the prismatic $\langle a \rangle$ slip system varies with build orientation is consistent with how the yield strength and ultimate tensile strength changes with orientation (see Figure 4.9(B)). This suggests the prismatic $\langle a \rangle$ slip system governs the plastic deformation of the specimens. This is consistent with previous literature [314, 316, 317]. During the plastic deformation of L-PBF Ti-6Al-4V, strain localization starts from the α grains with high prismatic Schmid factors, owing to the lower value of τ_c for the prismatic $\langle a \rangle$ slip system, compared to the other slip systems.

Also, when there are more grains with high prismatic Schmid factors, more slip activity is triggered during the plastic deformation. The increased amount of dislocation

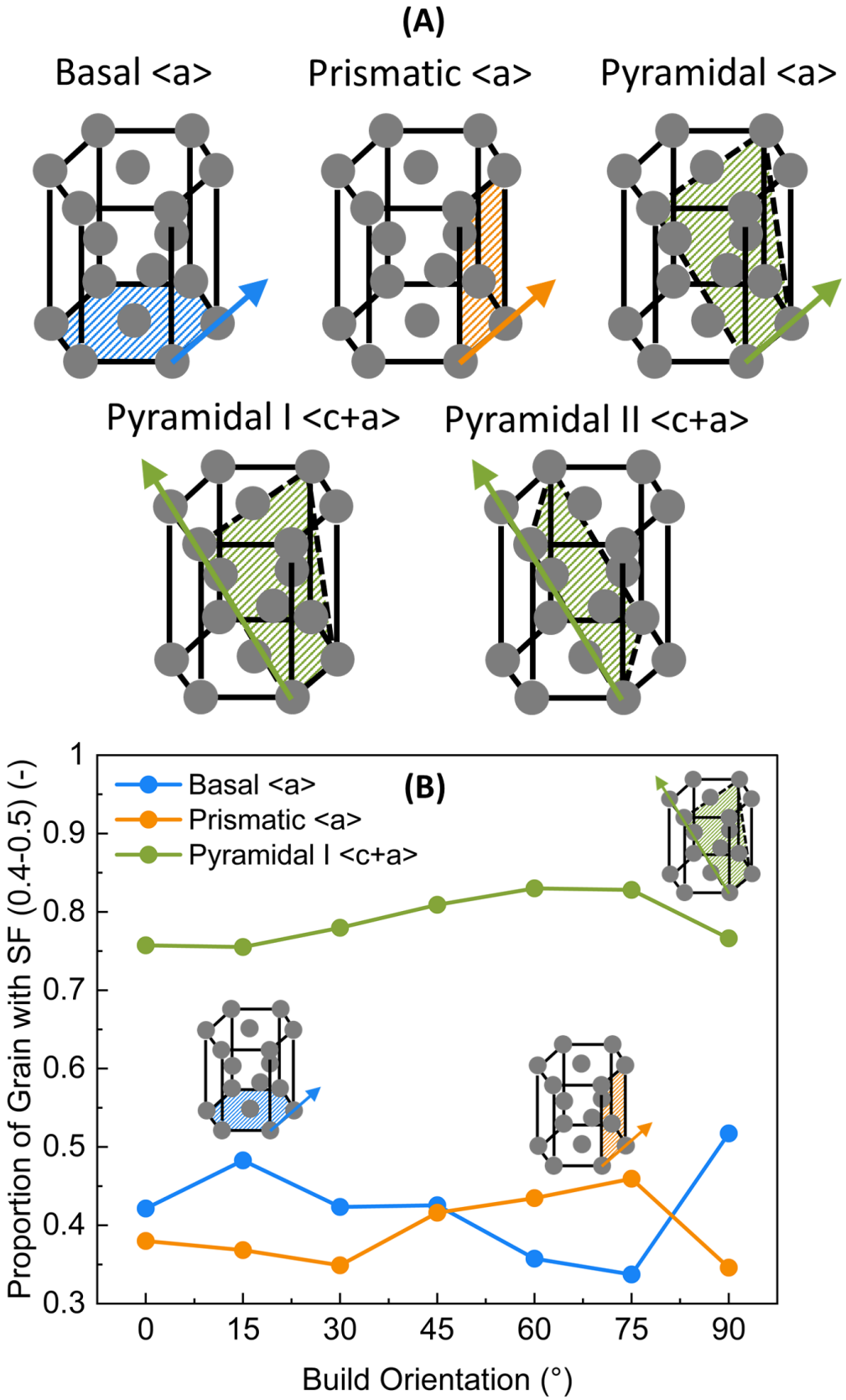


Fig. 4.10 (A) Schematic illustration of the slip systems in Ti-6Al-4V. (B) Schmid factors of basal ⟨a⟩, prismatic ⟨a⟩, and pyramidal I ⟨c+a⟩ slip systems as a function of the build orientation.

motion results in a higher fracture strain of the specimen [318]. This is also consistent with the experimental trend indicated in Figure 4.2(B).

4.4.2 Fatigue fracture behaviour

The fracture surface morphology of a sample after fatigue testing is shown in Figure 4.11. Three steps in the fatigue fracture process are clearly revealed. In region I, surface defects serve as the fatigue crack initiation sites. Relatively flat surrounding regions can be observed, which suggests the crack growth rate is slow. In region II, the increased number of grooves indicates faster but steady crack growth. At high magnification, the striation pattern can be observed, which results from the plastic blunting and re-sharpening of the crack tip under cyclic loading. Once the crack reaches a critical size, fast fracture occurs. In region III, a dimpled rupture becomes dominant as a result of microvoid nucleation, growth, and coalescence during final failure.

We proceed to identify the fatigue crack initiation sites for the 7 specimens under study. All the samples demonstrate surface-initiated fracture processes, which confirms surface roughness governs the fatigue performance of net-shape AM Ti-6Al-4V [60, 17]. Based on linear elastic fracture mechanics, an arbitarily shaped surface defect exhibit a higher geometrical factor Y (0.65) as compared to an internal defect (0.50) [291, 292]. This indicates for defects of the same size, a higher stress intensity factor ΔK can be induced by a surface defect than an internal defect following

$$\Delta K = Y \Delta \sigma \sqrt{\pi \sqrt{A_{\mathrm{p}}}} \tag{4.3}$$

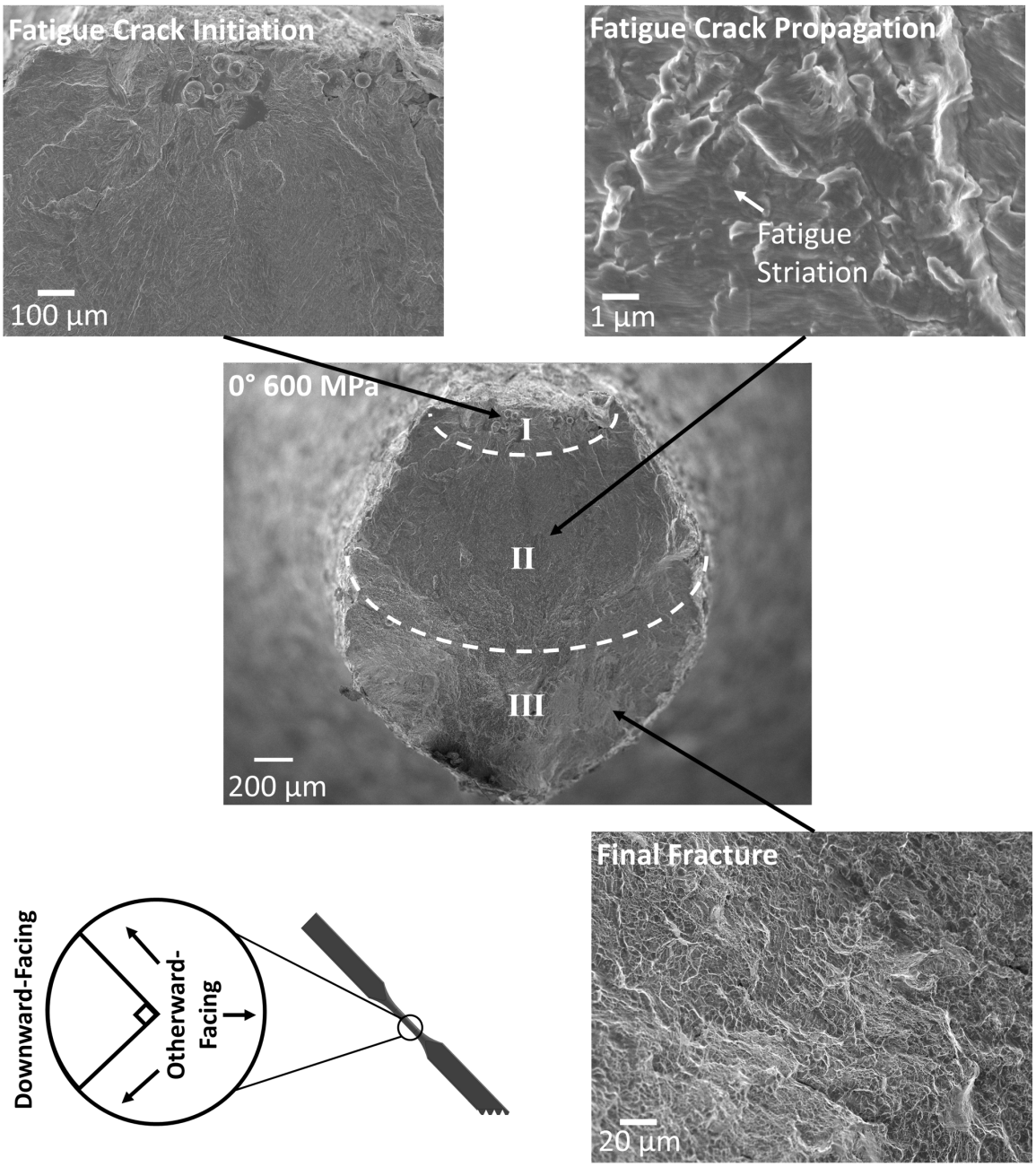


Fig. 4.11 Summary of fatigue crack initiation sites for the 7 specimens under study.

where $\Delta\sigma$ is the applied stress range and $\sqrt{A_{\mathrm{p}}}$ is the square root of the projection area of a defect perpendicular to the load direction.

Furthermore, when the build orientation is below 30°, all the cracks are initiated from the downward-facing surfaces since the surface roughness of the downward-facing surface is at least 90% higher than that of the otherward-facing surface. The larger defects on the downward-facing surface with higher stress intensity factors are more prone to crack initiation during the fracture process. As the build orientation increases to 45° or above, defects on the otherward-facing surface start to serve as fatigue crack initiation sites since the differences in surface quality between the otherward-facing and downward-facing surfaces become smaller. However, in most of the samples, the initiation process still starts from the downward-facing surfaces. When the build orientation is 75°, cracks are initiated from otherward-facing surfaces in 8 out of 9 samples owing to the relatively homogeneous surface roughness across the sample surface.

The presence of porosity can increase the stress concentration and degrade the fatigue performance even when the cracks are initiated from surface defects [17, 154, 293]. The stress distribution around a pore perpendicular to the load direction is given following Kirsch's Solution [319]:

$$\begin{aligned} \sigma_{rr} &= \frac{3\sigma}{2}((\frac{r}{d})^2 - (\frac{r}{d})^4) \\ \sigma_{\Theta\Theta} &= \sigma(1 + 2(\frac{r}{d})^2) \\ \tau_{r\Theta} &= 0 \end{aligned} \tag{4.4}$$

where σ is the applied stress, r is the radius of the pore, and d is the distance from the pore center. This indicates the maximum principal stress is 3 times the applied stress σ at the pore edge. However, it reduces to $\frac{11}{9}\sigma$ at a distance of 1 pore diameter from the pore edge, which is close to the far field stress σ. Hence, we define a pore cluster as near the initiation site when it's no more than 1 diameter away from the site. Results are shown in Figure 4.12 (A). Clearly, when the build orientation is 45° or below, no pore can be observed close to the fatigue initiation site for the following two reasons. (1) The poor quality of the surface, especially the downward-facing surface, results in a high stress intensity factor governing the failure process. (2) Very few pores can be found in the specimens with build orientations of 30° or below. At a build orientation of 60° or above, pores start to facilitate the initiation process owing to the lower surface roughness and higher porosity levels.

4.4.3 Rationalization of the variation in fatigue properties

On the basis of the results presented above, the orientation dependency of the fatigue properties can be rationalized. Having surface defects as the initiation sites confirms that at all applied stresses, the build orientation increases from 0° to 60°, the increase in fatigue life results from the reduction in surface roughness of the downward-facing surface. At 75°, the low surface roughness of the otherward-facing surface gives rise to the optimal fatigue resistance of the specimen. When the samples are built vertically, their surface quality and porosity level are comparable to those of the 75° specimen but a reduction in fatigue life can be observed. This can be explained by the dominance of

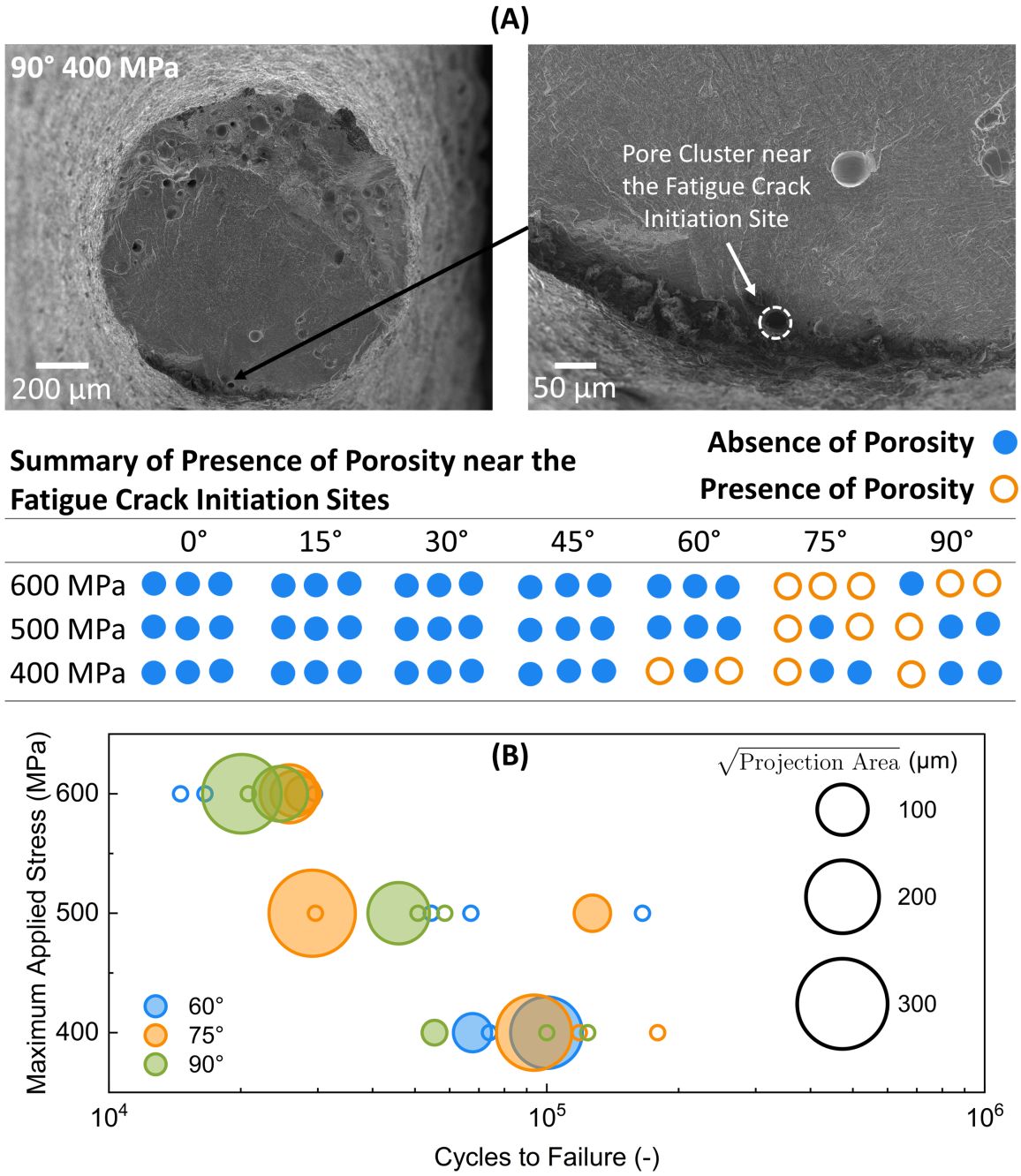


Fig. 4.12 (A) Summary of presence of porosity near the fatigue crack initiation sites for all the tested samples. (B) $\sqrt{A_p}$ of the pore cluster for the 60°, 75°, and 90° samples.

basal slip activity in Ti-6Al-4V alloys under cyclic loading [320, 317, 321]. Based on Stroh's theory [322], the fatigue crack formation along the basal planes results from the restricted slip on this plane in the hcp crystal. The slip activity of the surrounding soft grains would induce a transfer of stress to grains with hard α orientations, thus introducing additional tensile stress, which leads to failure along the basal plane. Moreover, since the applied stress is well below the yield strength, the elastic anisotropy of the hcp crystal can also contribute to inhomogeneity of the stress state. The stiffness of the α phase is the greatest when the load direction is parallel to the c-axis. Compatibility of deformation with surrounding grains of different crystallographic orientations dictates that for a given applied load, these grains will support the highest tensile stresses in the material [323]. Hence, even though the prismatic $\langle a \rangle$ slip system has a lower τ_c value, the stresses on the basal planes govern the crack formation process under cyclic loading. Here, we quantify the fraction of grains with c-axes near-parallel (0°-10°) to the loading direction as shown in Figure 4.13. The lower fatigue life of the 90° specimen results from the higher proportion of stiff grains than the 75° specimen.

The contribution of porosity to the fatigue fracture process can give rise to a variation in fatigue life [94]. Here, the $\sqrt{\text{Projection Area}}$, $\sqrt{A_\text{p}}$, of the pore cluster near the initiation site is evaluated for every tested sample with a build orientation of 60° or above. Results are presented in Figure 4.12(B). We use ◯ to denote samples when no pore cluster can be observed near the initiation site. Apart from those with the absence of pore clusters, the samples with the lowest fatigue life at each applied stress are all associated with pore clusters close to the initiation sites, which confirms porosity

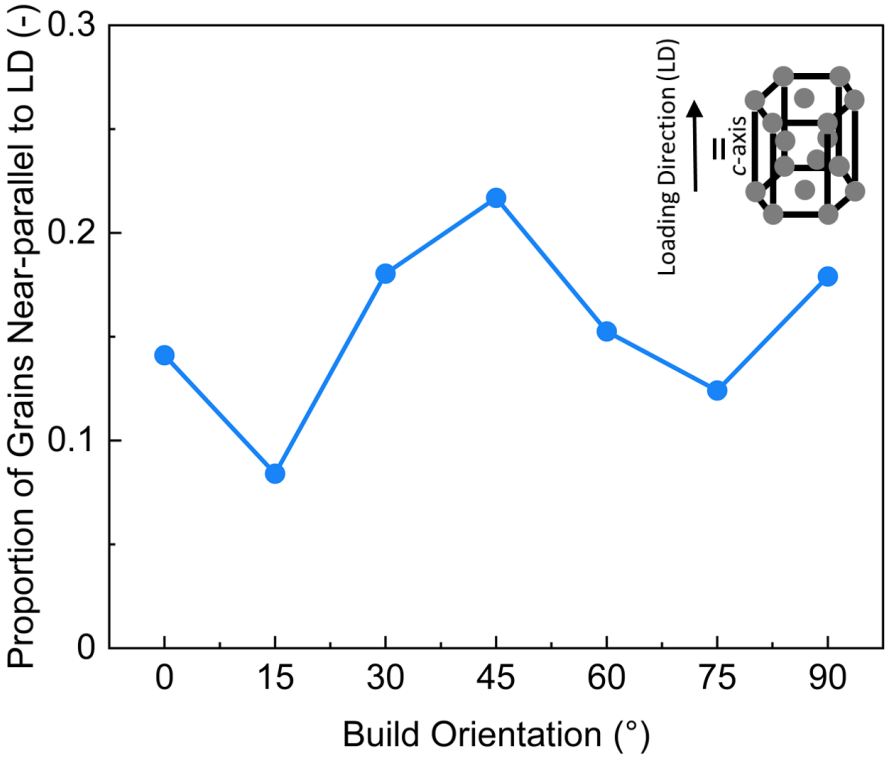


Fig. 4.13 Fraction of grains with *c*-axes near-parallel (0°-10°) to the loading direction as a function of the build orientation.

can facilitate the surface-initiated fracture process. Hence, the maximal fatigue scatter of the 75° specimen at 500 MPa can be attributed to the large variation in the size and number of pores near the initiation sites.

On the other hand, the 45° specimen exhibits a high fatigue scatter at 500 MPa without any contribution of pore clusters to the fracture process. The difference in fatigue life results from the variation in the initiation sites. The sample with the highest cycles to failure exhibits a crack initiation site on the otherward-facing surface whereas the cracks are initiated from the downward-facing surface in the other two samples. This indicates the fatigue failure is not governed by the most critical defect but is rather a statistical process. The probability of occurrence of a number (n) of random defect clusters in an arbitrary area A can be given following the Poisson distribution [324]:

$$P(n) = \frac{e^{-\lambda A}(-\lambda A)^n}{n!} \tag{4.5}$$

where λ is the average defect density. When the build orientation is 45°, the average surface roughness R_a of the downward-facing surface is only 7.3 μm higher than that of the otherward-facing surface, which gives rise to a higher probability of crack initiation from the otherward-facing surface than the specimens with build orientations of 30° or below.

It is noteworthy that three tests per condition provide limited insights into the variation in fatigue properties. Yet, it offers solid evidence of the fatigue life of L-PBF Ti-6Al-4V as a function of the build orientation and gives an indication of the

orientation dependency of the scatter in fatigue life, especially given the large differences in fatigue scatter between different specimens.

4.5 Orientation Effect on the Deformation Response of an Octet-truss Lattice Material

It is of practical interest to elucidate the influence of build orientation on the performance of intricate components such as metallic lattices. To achieve this goal, we determine the effect of build orientation on the elastic, plastic, and fatigue properties of a simple regular lattice structure, using the results of Sec. 4.3 as input. A stretch-dominated octet-truss lattice is adopted since the structure is governed by tensile deformation. The geometrical details of the lattice are shown in Figure 4.14. The strut length is 13.0 mm and the strut thickness is 1.3 mm. The diameter of the strut is consistent with the gauge section of the tensile sample. Here, we consider two scenarios: standard and optimized. In the standard form, the lattice is fabricated vertically and the struts are printed in the 0° and 45° directions. When the build orientation is optimized, we build the structure 30° relative to the build plate and the strut orientations are 30° and 75°.

Our primary objective here is to determine the effect of build orientation on fatigue performance. An important step in this process is determining how build orientation influences the elastic and plastic reponse of the lattice structure and the stresses experienced by each strut within the lattice for a given loading history. We advance

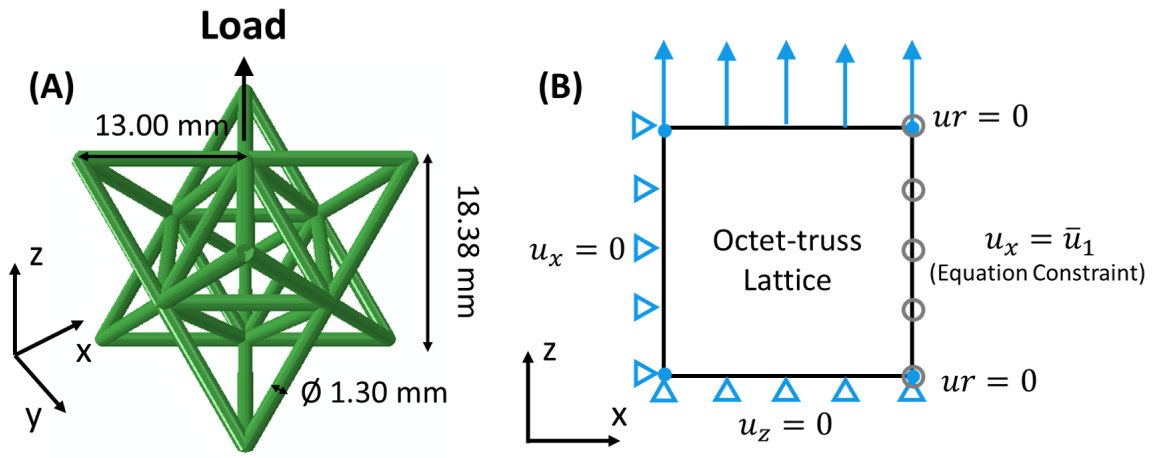


Fig. 4.14 (A) Geometrical details of the octet-truss lattice for the FEA simulation. (B) Boundary conditions used in the FEA simulation.

the analytical solutions developed by Deshpande et al. [47] of the elastic and plastic response to account for the orientation effect of the strut. The results of the analysis are verified using finite element analysis (FEA) simulation. In these analyses, we derive generic relationships that can be applied to any material and manufacturing set-up. We then apply these results to determine the elastic compliance and plastic collapse for a Ti-6Al-4V octet-truss lattice made by L-PBF based on the material properties presented in Table 4.2 and Figure 4.2(B). The resulting stress state in the individual struts determined from these calculations is then combined with the effect of orientation on fatigue strength to determine the fatigue performance of the lattice material.

Figure 4.15 shows a sketch of the primitive cell with the associated co-oridinate system. In each primitive cell, there are 6 struts: AB, BC, AD, BC, BD, and CD. Each strut is shared between two primitive cells, which indicates there are three struts per primitive cell. Since there are 8 primitive cells and 12 internal elements within the

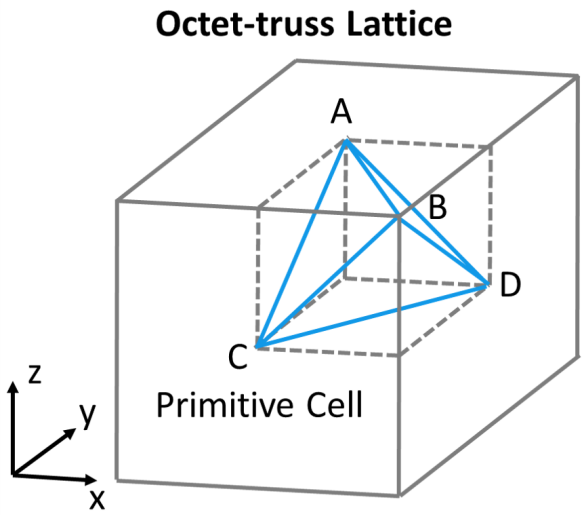


Fig. 4.15 Schematic illustration of the primitive cell within the octet-truss lattice.

octet-truss lattice, there are 24 struts in total. The relative density $\bar{\rho}$ of the lattice is

$$\bar{\rho} = \frac{24\pi a^2 l}{2\sqrt{2}l^3} = 6\sqrt{2}\pi(\frac{a}{l})^2 \tag{4.6}$$

where a and l are the radius and length of a strut, respectively.

4.5.1 Description of Finite Element Modelling

Finite element analysis (FEA) simulations of face-centred cubic (fcc) lattices were performed using ABAQUS Standard (v2017). Each strut in the structure was represented by a Timoshenko beam element (B31 in the ABAQUS notation) with a circular cross-section of diameter 1.3 mm. In-house MATLAB codes were developed to discretize each strut into multiple B31 elements depending on the length of the

strut, such that every element is shorter than 1 mm. Mesh convergence studies were performed to confirm the accuracy of the discretization.

The Ti-6Al-4V alloy was modelled as a linear elastic, perfectly plastic material. The material properties are detailed in Table 4.2. The properties of the struts were assigned based on their build orientations.

Ti-6Al-4V	0°	30°	45°	75°
Elastic Modulus	125 GPa	120 GPa	119 GPa	110 GPa
Poisson Ratio	0.3	0.3	0.3	0.3
Yield Strength	896 MPa	926 MPa	916 MPa	864 MPa

Table 4.3 Materials properties used in finite element analysis.

We set symmetrical boundary conditions to describe the behaviour of a unit cell as shown in Figure 4.14(B). All the nodes on the bottom surface were set to be stationary in z-direction while the nodes on the top surface were imposed by a displacement that is equivalent to the applied load. Translations along the x- and y-directions were prohibited for the nodes on the $x = 0$ and $y = 0$ planes, respectively. The nodes on their opposing surfaces were constrained to share the same displacement in the direction of the associated surface normal. Rotations of the nodes at the vertices were set to zero.

As shown in Figure 4.14(A), a tensile load is imposed on the top of the lattice in the z-direction and the maximum tensile stress within the structure is recorded.

4.5.2 Analysis of Elastic Response

It proves convenient to describe the material response with respect to the principal materials axes (x, y, z) defined in Figure 4.14. We take any strut that lies within an

x-y plane as having an elastic modulus $E_{0\check{r}}$. All other struts make an angle of 45° with respect to the reference plane and have a modulus $\alpha E_{0\check{r}}$, thus for this structure, the elastic response can be expressed in terms of $E_{0\check{r}}$, α, and $\bar{\rho}$. This applies for any chosen orientation of the octet-truss with respect to the growth direction, although the reference value of $E_{0\check{r}}$ depends on the orientation employed. The variation of the modulus with strut orientation destroys the cubic symmetry of the structure and the response is orthotropic, such that

$$\begin{pmatrix} E_x \\ E_y \\ E_z \\ \Gamma_{yz} \\ \Gamma_{xz} \\ \Gamma_{xy} \end{pmatrix} = \begin{pmatrix} S_{11} & -S_{12} & -S_{13} & 0 & 0 & 0 \\ & S_{11} & -S_{23} & 0 & 0 & 0 \\ & & S_{33} & 0 & 0 & 0 \\ & \text{SYM} & & S_{44} & 0 & 0 \\ & & & & S_{55} & 0 \\ & & & & & S_{66} \end{pmatrix} \begin{pmatrix} \Sigma_x \\ \Sigma_y \\ \Sigma_z \\ \Sigma_{yz} \\ \Sigma_{xz} \\ \Sigma_{xy} \end{pmatrix} \tag{4.7}$$

where E_x, E_y, and E_z are the normal macroscopic strains with respect to the principal axes, Γ_{yz}, Γ_{xz}, and Γ_{xy} are the engineering shear strains and Σ_x, Σ_y etc. are the corresponding stresses. The components of the compliance matrix S_{ij} are determined by choosing the deformation field (i.e. displacements of the nodes in Figure 4.14(A)) that minimises the total potential energy of the structure for a given applied macroscopic stress.

We consider the side of the primitive cell to be of unit length. The volume of the unit cell is then unity and each strut is of length $\sqrt{2}$. We consider the situation where the primitive cell experiences macroscopic strain $[E] = [E_x, E_y, E_z, \Gamma_{yz}, \Gamma_{xz}, \Gamma_{xy}]^{\mathrm{T}}$. Struts AB and CD lie in the plane of the powder bed and have an elastic modulus $E_{0\check{r}}$, with all the other struts oriented at 45° to this plane and having an elastic modulus $\alpha E_{0\check{r}}$.

Let n^{s} be a unit vector pointing along a strut "s". The elongation of a strut e_{s} is related to the macroscopic strains through the kinematic relationship $e_{\mathrm{s}} = [N_{\mathrm{s}}][E]$, where $[N_{\mathrm{s}}] = \sqrt{2}[n_x^{\mathrm{s}} n_x^{\mathrm{s}}\ n_y^{\mathrm{s}} n_y^{\mathrm{s}}\ n_z^{\mathrm{s}} n_z^{\mathrm{s}}\ n_y^{\mathrm{s}} n_z^{\mathrm{s}}\ n_x^{\mathrm{s}} n_z^{\mathrm{s}}\ n_x^{\mathrm{s}} n_y^{\mathrm{s}}]$. The stored elastic strain energy in a strut is

$$\begin{aligned} U_{\mathrm{s}} &= \frac{1}{2} E_{\mathrm{s}} e_{\mathrm{s}}^{s} \frac{\pi}{\sqrt{2}} (\frac{a}{l})^2 \\ &= \frac{1}{2} E_{\mathrm{s}} [E]^{\mathrm{T}} [N_{\mathrm{s}}]^{\mathrm{T}} [N_{\mathrm{s}}][E] \frac{\pi}{\sqrt{2}} (\frac{a}{l})^2 \end{aligned} \tag{4.8}$$

where E_{s} is the modulus of the strut. The total stored energy is then the sum of the contributions of each strut, i.e. $U = \sum_{\mathrm{struts}} U_{\mathrm{s}}$. For a given applied stress $[\Sigma]$, the total potential energy

$$\Omega = U - [E]^{\mathrm{T}}[\Sigma] \tag{4.9}$$

Choosing the macroscopic strains that minimise the total potential energy gives

$$[\Sigma] = [D][E] \tag{4.10}$$

where $D = \sum_{\mathrm{s}} E_{\mathrm{s}} [N_{\mathrm{s}}]^{\mathrm{T}} [N_{\mathrm{s}}] \frac{\pi}{\sqrt{2}} (\frac{a}{l})^2$ is the stiffness matrix for the octet-truss. Inverting $[D]$ gives the compliance matrix $[S]$ of Equation 4.7.

Since the $\frac{a}{l}$ ratio is small, we assume the struts to be pin-jointed at the nodes. We find

$$\begin{gathered}\frac{1}{S_{11}}=\frac{1}{S_{33}}=\frac{\bar{\rho}\alpha E_{0\check{\mathrm{r}}}}{3(2+\alpha)}\\ \frac{1}{S_{12}}=\frac{\bar{\rho}\alpha E_{0\check{\mathrm{r}}}}{3(2-\alpha)}\\ \frac{1}{S_{13}}=\frac{1}{S_{23}}=\frac{\bar{\rho}E_{0\check{\mathrm{r}}}}{3}\\ \frac{1}{S_{44}}=\frac{1}{S_{55}}=\frac{\bar{\rho}\alpha E_{0\check{\mathrm{r}}}}{12}\\ \frac{1}{S_{66}}=\frac{\bar{\rho}E_{0\check{\mathrm{r}}}}{12}\end{gathered} \tag{4.11}$$

When the lattice is loaded uniaxially in the z-direction, the macroscopic strain experienced in the direction of loading is

$$E_z=\frac{3(2+\alpha)\Sigma_z}{\bar{\rho}\alpha E_{0\check{\mathrm{r}}}} \tag{4.12}$$

The uniaxial response for the two build orientations considered here (which have different values of $E_{0\check{\mathrm{r}}}$ and α) are compared with the FEA calculations in Figure 4.16. The results are in good agreement, which demonstrates the appropriateness of the assumptions employed in the analysis. The analysis also provides details of the stress state in each strut. We return to this in Sec. 4.5.3 when we analyse the fatigue behaviour of the structure.

4.5.3 Analysis of Plastic Collapse

Failure of the octet-truss lattice occurs by either plastic yielding or, when loaded in compression, by elastic buckling of the struts [243, 43]. The plastic yielding load of a

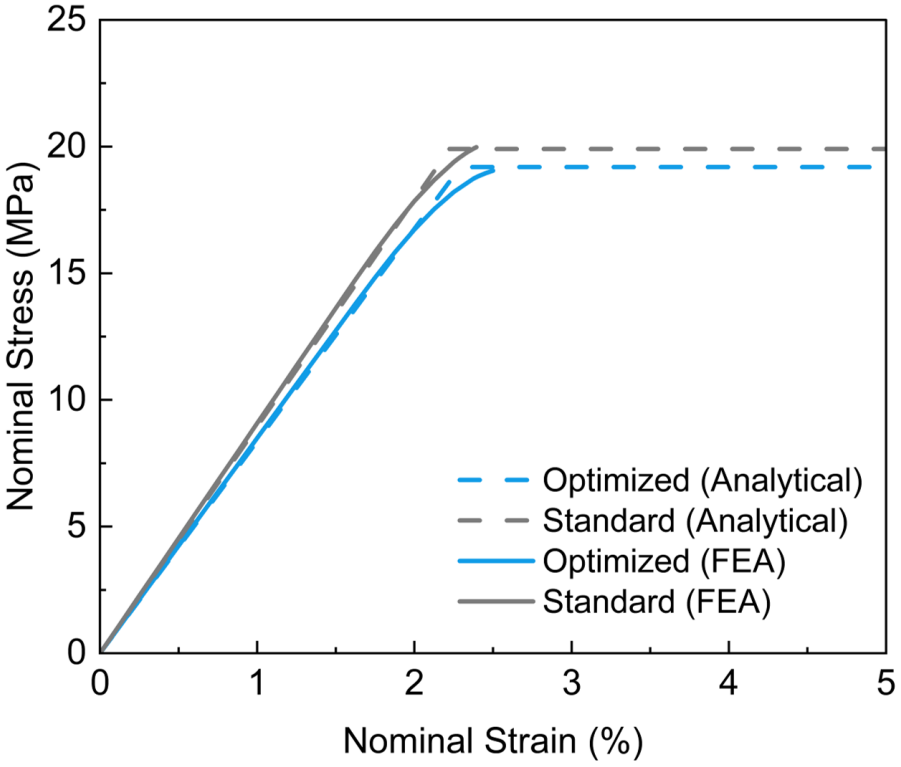


Fig. 4.16 Comparison between the analytical solution and FEA calculation for the standard and optimized conditions.

strut P_Y is given by

$$P_Y = \pi a^2 \sigma_Y \tag{4.13}$$

where σ_Y is the yield strength of the solid material, while the Euler buckling load P_E is given by

$$P_E = \frac{n^2 \pi^3 E_s a^4}{4l^2} \tag{4.14}$$

where E_s is the axial modulus of the strut and the factor n depends on the buckling mode. Given that the struts can be assumed to be pin-jointed, the rotational stiffness of the nodes is zero, and the factor $n = 1$. In this case, the plastic yielding load P_Y is smaller than the Euler buckling load P_E for Ti-6Al-4V struts with the ratio $\frac{a}{l}$ considered here, which suggests the lattice collapses by plastic yielding of the struts in both tension and compression. Here, we determine the collapse load of the octet-truss employing the upper bound limit load theorem when it is subjected to arbitrary combinations of normal stresses Σ_x, Σ_y, and Σ_z. For slender struts, we can again assume that the members are pin-joint where they meet at nodes. The yield condition of an engineering material (either a homogeneous material, a composite material, or a lattice structure) can be expressed in the form

$$F = \Phi - \sigma_Y^{0\check{r}} = 0 \tag{4.15}$$

where Φ defines the shape of the yield surface and is a homogeneous function of degree 1 in stress (see for example Cocks [325]) and σ_Y is a suitably chosen yield strength. By employing the upper bound approach described by Cocks [325], it can readily be

shown that for a pin-joint structure with n struts

$$\Phi \geq \frac{(\Sigma_x dE_x^c + \Sigma_y dE_y^c + \Sigma_z dE_z^c)V}{\sum_{i=1}^{n} \beta_i |de_i^c| A_i l_i} \tag{4.16}$$

where the subscript "c" refers to any assumed compatible collapse mechanism, in which the elongation of each member de_i^c is compatible with an assumed macroscopic incremental strains dE_x^c, dE_y^c, and dE_z^c; β_i is the ratio of the yield strength of members "i" to the reference value $\sigma_Y^{0\check{r}}$; A_i and l_i are the cross-sectional area and length of member "i" and V is the total volume of the structure.

We consider the same primitive unit cell of Figure 4.15 as analyzed in Sec. 4.5.1 and the form of the displacement field as the elastic deformation analysis. Following the expression for the yield surface in Equation 4.16 when the octet-truss is subjected to macroscopic normal stresses, Σ_x, Σ_y, Σ_z, we proceed by taking the orientation effect into consideration. The yield strengths of the struts can be given by

$$\begin{gathered} \sigma_Y^{\mathrm{AB}} = \sigma_Y^{\mathrm{CD}} = \sigma_Y^{0\check{r}} \\ \sigma_Y^{\mathrm{AC}} = \sigma_Y^{\mathrm{AD}} = \sigma_Y^{\mathrm{BD}} = \sigma_Y^{\mathrm{BC}} = \sigma_Y^{45\check{r}} = \beta \sigma_Y^{0\check{r}} \end{gathered} \tag{4.17}$$

where $\sigma_Y^{0\check{r}}$ and $\sigma_Y^{45\check{r}}$ are the yield strengths of the struts oriented at 0° and 45° to the build plate, respectively, and β is the ratio between $\sigma_Y^{45\check{r}}$ and $\sigma_Y^{0\check{r}}$. We can write

$$\Phi_{\mathrm{L}} = \frac{12}{\bar{\rho}} \frac{\Sigma_z dE_z + \Sigma_y dE_y + \Sigma_x dE_x}{2|dE_x + dE_y| + 2\beta|dE_x + dE_z| + 2\beta|dE_y + dE_z|} \tag{4.18}$$

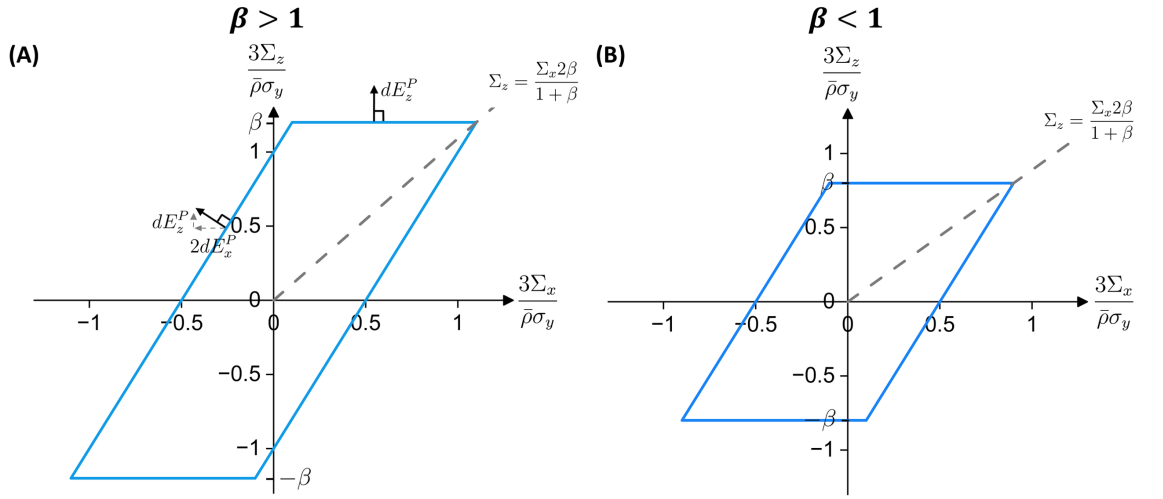


Fig. 4.17 Yield surface Φ of the octet-truss lattice defined by the analytical solution when (A) $\beta > 1$ and (B) $\beta < 1$.

When the lattice is only subjected to a stress Σ_z, $\bar{u_x} = \bar{u_y} = \frac{u_x}{u_z} = \frac{u_y}{u_z}$ by symmetry. Then,

$$\Phi_{\mathrm{L}} = \frac{3}{\bar{\rho}} \frac{\Sigma_z}{|\bar{u_x}| + \beta|1 + \bar{u_x}|} \tag{4.19}$$

for any assumed mechanisms of collapse (dE_x, dE_y, dE_z). We consider the situation where $\Sigma_x = \Sigma_y$. The symmetry dictates that $dE_x = dE_y$. We can then write Equation 4.18 in the form

$$\Phi_{\mathrm{L}} = \frac{3}{\bar{\rho}} \left(\frac{\Sigma_z + 2\Sigma_x d\bar{E}_x}{|d\bar{E}_x| + \beta|1 + d\bar{E}_x|} \right) \tag{4.20}$$

where $d\bar{E}_x = \frac{dE_x}{dE_z}$.

For a given combination of Σ_z and Σ_x, we choose the value of $d\bar{E}_x$ that provides the maximise value of Φ_{L}. Doing this for all possible combinations of Σ_z and Σ_x gives the yield surface of Figure 4.17.

The form of the yield surface is sensitive to the value of β and, for this loading condition, consists of two pairs of straight lines. The position of the horizontal lines, which correspond to the mechanisms in which $dE_x^P = dE_y^P = 0$, depends on the value of β, while those of the sloped lines, which corresponds to a mechanism in which $dE_x^P = dE_y^P = -dE_z^P$, and are independent of β. Of interest here is the response under uniaxial loading ($\Sigma_x = \Sigma_y = 0$). The uniaxial yield strength and mechanism of plastic deformation is given by the location where the Σ_z axis crosses the yield surface. For $\beta > 1$, the value of the axial stress at yield is

$$\Sigma_z^Y = \frac{\bar{\rho}\sigma_Y^{0\check{r}}}{3} \tag{4.21}$$

and the plastic deformation mechanism is $dE_x^P = dE_y^P = -dE_z^P$ while for $\beta < 1$, Figure 4.17(B) gives a yield strength

$$\Sigma_z^Y = \frac{\beta\bar{\rho}\sigma_Y^{0\check{r}}}{3} \tag{4.22}$$

When $\beta = 1$, there is a vertex on the yield surface where it intersects the Σ_z axis and the mechanism can lie anywhere within the fan of vectors bounded by the above two mechanisms. This result suggests a small variation in strut properties can have a large influence on how the structure plastically deforms at yield. Since $\beta > 1$ when the lattice is fabricated vertically, the uniaxial yield strength of the structure is given by Equation 4.21 and is independent of β. When the lattice is built 30° relative to the build plate, $\beta < 1$, the yield strength is described by Equation 4.22 which depends on the value of β. The limit load predictions for structures built the x-y plane at 0° and

30° to the build plate are added to the elastic prediction in Figure 4.16. The difference in magnitude of the macroscopic yield strength arises from the different values of $\sigma_Y^{0\check{r}}$ for the struts in the reference x-y plane as well as the different values of β for the two build orientations. The results are compared in Figure 4.16 with full elastic-plastic FEA solutions which agree with the analytical results. The slight discrepancy results from the small amount of bending of the beams in the FEA calculations.

4.5.4 Analysis of Failure under Cyclic Loading

We now consider the response under cyclic loading. We consider the situation where the uniaxial load Σ_z is cycled at $R = 0.1$ and a peak load corresponding to 0.4, 0.3, and $0.2\Sigma_z^Y$. For these loading conditions, the response remains elastic throughout the loading cycle. We can thus use the elastic analysis described in Sec. 4.5.2 to determine the stress history in each strut. The maximum stress and stress range occurs in the strut at 45° to the x-y plane following

$$\sigma_{\text{local}} = \frac{\alpha E_{0\check{r}} \Sigma_z (S_{33} - S_{13})}{2} = \frac{3\Sigma_z}{\bar{\rho}} \tag{4.23}$$

Failure of the entire structure occurs when these struts fail [48, 49, 326]. The number of cycles to failure can be determined by employing the local stress history together with the data of Figure 4.3, since this was determined at the same R ratio. The results are shown in Figure 4.18. By optimizing the orientation, we improve the fatigue strength of the lattice at 10^6 cycles by 51%, which highlights the significance of the build

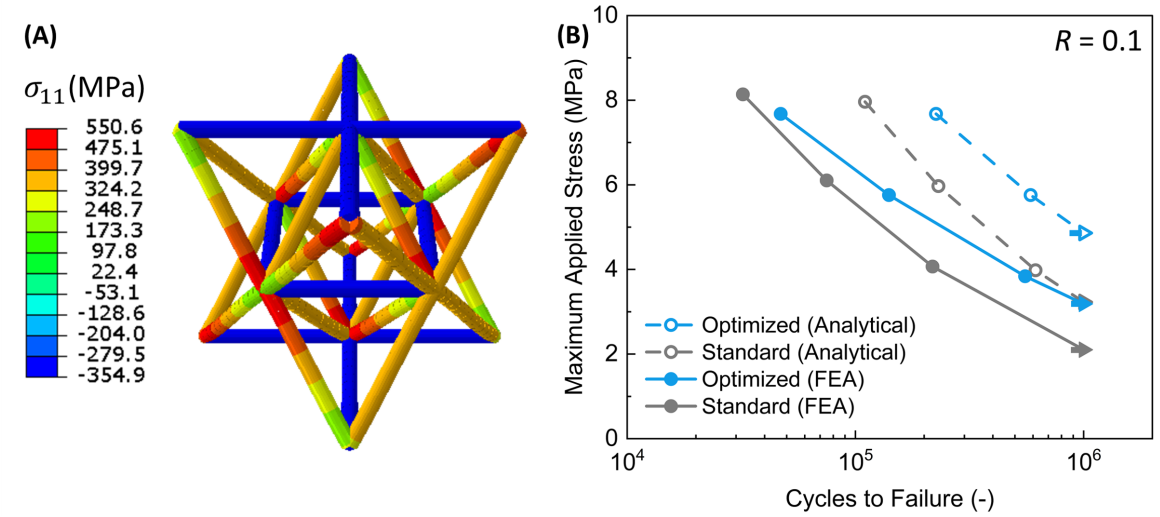


Fig. 4.18 (A) FEA calculation of the octet-truss lattice at $0.4\Sigma_z^Y$. (B) Maximum applied stress vs. cycles to failure for the lattice accounting for the orientation effect.

orientation in the design of mechanically durable intricate components. We compare the analytical solutions with comparable calculations employing stresses from FEA simulations at the appropriate cyclic load levels. Even though the trend in behaviour is consistent with the analytical results, the small amount of bending experienced by the struts raises the local stress significantly and results in a decrease in the fatigue life at a given stress level.

This is very different from the results for elastic and plastic properties. In the analytical calculation, we assume the nodes are pin-jointed and the stress states in the struts are purely uniaxial. In practice, the struts are also subject to bending stresses when the structure is under tensile loading. The calculations for elastic compliance and yield strength are global calculations. When the struts are slender, the stored strain energy (elastic response) and energy dissipation (plastic response) due to bending is much smaller than that due to axial deformation. Hence, the bending of the strut

has minimal influence on the elastic modulus and yield strength of the lattice. On the other hand, fatigue failure of a structure results from local damage development. The local bending stress on the surface of the strut can facilitate crack initiation and propagation, which needs to be considered for the fatigue calculations. Thus, to assess the fatigue behaviour of the lattice accurately, it is critical to perform an FEA calculation, whereas the analytical calculation provides accurate evaluations of the elastic and plastic responses.

It is also important to note that for the octet-truss with the combination of loading conditions and material properties considered here, there is a strong degree of both kinematic and static determinancy. Hence, the stresses in the struts as determined from the analytical calculations are independent of the materials properties (i.e. $E_{0\check{r}}, \sigma_Y^{0\check{r}}, \alpha$, and β), as illustrated in Equation 4.23 for the 45° struts. For more complex lattice structures and more general variations in properties, the symmetries that lead to these results no longer hold and how the material properties vary with build orientations plays an important role in determining the stresses experienced by the struts and how this influences the fatigue strength of the structure. The procedure described here can readily be applied to determine the performance of these more general structures.

4.6 Summary and Conclusions

In this study, orientation effects that influence the fatigue behaviour of Ti-6Al-4V components produced by laser powder bed fusion has been explained by means of

systematic mechanical testing, high-resolution electron microscopy, X-ray computed tomography, analytical, and FEA calculation. Seven different build orientations have been considered. The following specific conclusions can be drawn from this work:

- Dynamic fatigue tests reveal the specimen built at 75° to the build plate demonstrate the optimal fatigue resistance. An increase in fatigue life with the build orientation from 0° and 75° has been confirmed owing to the improved surface quality. The lower fatigue life of the 90° specimen may result from the large proportion of grains near-parallel to the loading direction.

- Below 30°, the fatigue cracks are initiated from the downward-facing surface for all the cases. The $\geq 90\%$ higher R_a of the downward-facing surface contributes to this effect. Above 45°, defects on the otherward-facing surface start to serve as the fatigue crack initiation sites as a result of the smaller difference in R_a between downward-facing and otherward-facing surfaces.

- Pore clusters can facilitate the surface-initiated fatigue fracture process, whose role can be explained using Kirsch's Solution for the elastic stress state in the vicinity of a pore. The large difference in pore sizes near the initiation sites gives rise to the maximal fatigue scatter of the 75° specimen at 500 MPa. The statistical nature of the failure process is also revealed by the variation in the initiation site of the 45° specimen, which leads to inconsistent fatigue lives.

- Analytical and FEA calculations of the fatigue strength of a simple lattice structure confirms the dependence of fatigue behaviour on build orientation in

intricate components. By optimizing the build orientation, we predict the fatigue strength of the metallic lattice to be improved by 51% at 10^6 cycles. The results illustrate the key role build orientation plays in the cyclic deformation behaviour of engineering components.

Chapter 5

Cyclic Deformation Behaviour of Metallic Metamaterial

5.1 Introduction

The fatigue fracture process of metamaterials commences with the accumulation of plastic strain followed by crack initiation and propagation [48, 68, 43]. After that, the coalescence of multiple cracks leads to sudden failure of the structure. The hallmark of lattice failure under cyclic loading is the formation of shear bands [90, 184, 76]. However, an assessment of a triply periodic minimal surface (TMPS) structure shows uniform deformation during cyclic loading may also occur at high applied stresses [49]. This prompts our curiosity does the change in failure mode occur in all types of lattice topologies. Furthermore, the customization of properties requires metamaterials to be printed with different relative densities [243, 147]. Varying the strut thickness-to-length

ratios could diverge the local stress state [181]. What remains in question is how – under cyclic loading – the global deformation characteristics are dictated by the different combinations of axial tension, bending, and buckling of struts.

In light of these aforementioned issues, we design and fabricate two types of metamaterials: a bending-dominated body-centred cubic (BCC) structure and a stretching-dominated face-centred cubic (FCC) structure [47, 129]. We couple in-situ observations together with fatigue testing to provide direct evidence of the deformation behaviour under cyclic loading. As will be seen, micromechanical analysis of the local stress state in the structure offers fundamental insight into the fatigue fracture process.

5.2 Methods

5.2.1 Design and Fabrication of Metamaterials

Two lattice topologies were considered in this study: BCC and FCC (see Figure 5.1(A)). The nodal connectivity of BCC and FCC structures is equal to 8 and 12, respectively. For each type of topology, three specimens with different unit cell sizes were generated. The unit cell sizes of BCC structures range from 1.25 mm to 2.5 mm while the FCC unit cell sizes are between 2 mm and 3.5 mm. Both structures have strut radii a of 0.15 mm.

The globally constrained dimensions of the specimens are roughly 10 mm $\times$ 10 mm $\times$ 17.5 mm. Integral numbers of unit cells were infilled into the volume. The designed

relative densities ρ_r of the two structures are given by [47, 129]

$$\rho_r^{\mathrm{BCC}} = 3\sqrt{3}\pi(\frac{a}{l})^2 \tag{5.1}$$

$$\rho_r^{\mathrm{FCC}} = 6\sqrt{2}\pi(\frac{a}{l})^2 \tag{5.2}$$

where l is the strut length. The designed relative densities of all the specimens under study are shown in Figure 5.1(B).

All the specimens were produced with Ti-6Al-4V alloy – the "workhorse" titanium alloy in the aerospace and biomedical industry. The fabrication was performed by Alloyed Ltd. in a Renishaw AM250 machine using L-PBF. We employed a contour scanning strategy with 50 W laser power, 30 μm point distance, 2000 mm/s scan speed, 30 μm layer thickness, and 50 μs exposure time. The conditions were chosen for the production of highly dense specimens. Heat treatments were applied in the vacuum for 4 h at 800 °C to relieve the residual stress.

5.2.2 Assessment of Static & Dynamic Mechanical Behaviour

The mechanical responses of the metamaterials were assessed using an Instron ElectroPuls E10k system. Quasi-static compression tests were performed at a strain rate of 10^3 s^{-1} to determine the applied stress for fatigue tests. A 10 kN load cell was used to measure the loading response and a non-contact iMetrum video extensometry system was employed to capture the displacement. We speckled the grips to accurately measure

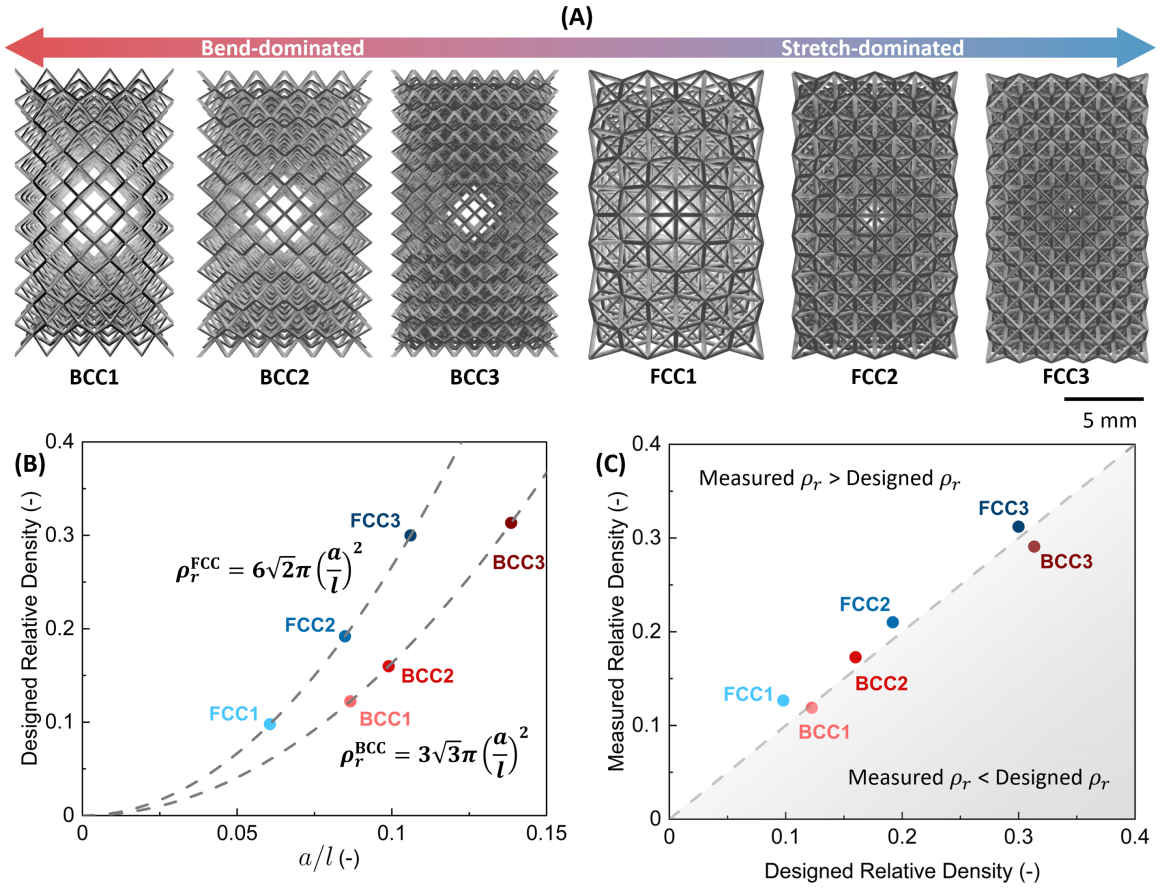


Fig. 5.1 (A) Geometries of the BCC and FCC structures in this study. (B) Designed relative density as a function of the designed thickness-to-length ratio of the two types of structures under study. (C) Measured relative density vs. designed relative density for all the specimens.

the displacement of the surfaces near the structures. The tests were terminated after 30% engineering strain.

Compression fatigue responses were measured at a frequency of 30 Hz and a R ratio of 0.1. We applied the maximum stresses of 0.8, 0.6, 0.4, 0.3, 0.2, and $0.1\sigma_Y$. The tests were stopped after 5% compressive strain. The deformation process was recorded using a digital camera.

5.2.3 X-ray Computed Tomography (XCT)

X-ray computed tomography (XCT) scans were acquired with an ImageiX CT system (North Star Imaging Inc., Minnesota, USA). During the acquisition, the tungsten transmission target X-ray source was filtered by a Cu foil of 0.95 mm thickness. The following scan conditions were applied: 140 kV tube voltage, 71 μA tube current, 5 μm focal spot size, and 1 Hz frame rate. This gave an isotropic voxel size of 16 μm and a resolving power of 48 μm [263]. Reconstruction of the projection images was conducted based on a filtered back projection algorithm in the efX-ct software (version 1.9.5.12, North Star Imaging Inc., Minnesota, USA). The data was analyzed using the Avizo 9.7 software. Segmentation of solid parts was performed using Otsu's method [264]. The relative densities of all the printed specimens were measured using the XCT data (Figure 5.1(C)). The measured values show good correlations with the designed values. Small discrepancies may result from processing-induced defects [7, 49, 44].

A summary of the samples tested in this Chapter is shown in Table 5.1.

5.3 Results and Discussion

5.3.1 Quasi-static Mechanical Behaviour

The quasi-static mechanical behaviours of BCC and FCC structures are evaluated in the form of stress-strain curves as shown in Figure 5.2(A) and (B). Both types of structures exhibit similar linear responses during elastic deformation but their behaviours are vastly different in the plastic regime. After yielding, the BCC structures show flat stress plateaux followed by densification whereas sudden collapses of the FCC structures can be observed before the recovery of strength.

The two distinct failure processes result from the different local stress states of the structures [327, 43]. In BCC structures, struts largely deform by bending, which yields a compliant deformation behaviour under monotonic loading [328]. On the other hand, the deformation of FCC structures is primarily governed by strut stretching [47]. The axial tension of the strut is deficient in dissipating deformation energy resulting in sudden failure of the structures.

The deformation modes of both types of structures are further validated by the Gibson-Ashby model [329]. Their elastic modulus E can be described following

$$E = C_1 {\rho_r}^{n_E} \tag{5.3}$$

and their yield strength Σ^Y can be estimated from

$$\Sigma^Y = C_2 {\rho_r}^{n_{\Sigma^Y}} \tag{5.4}$$

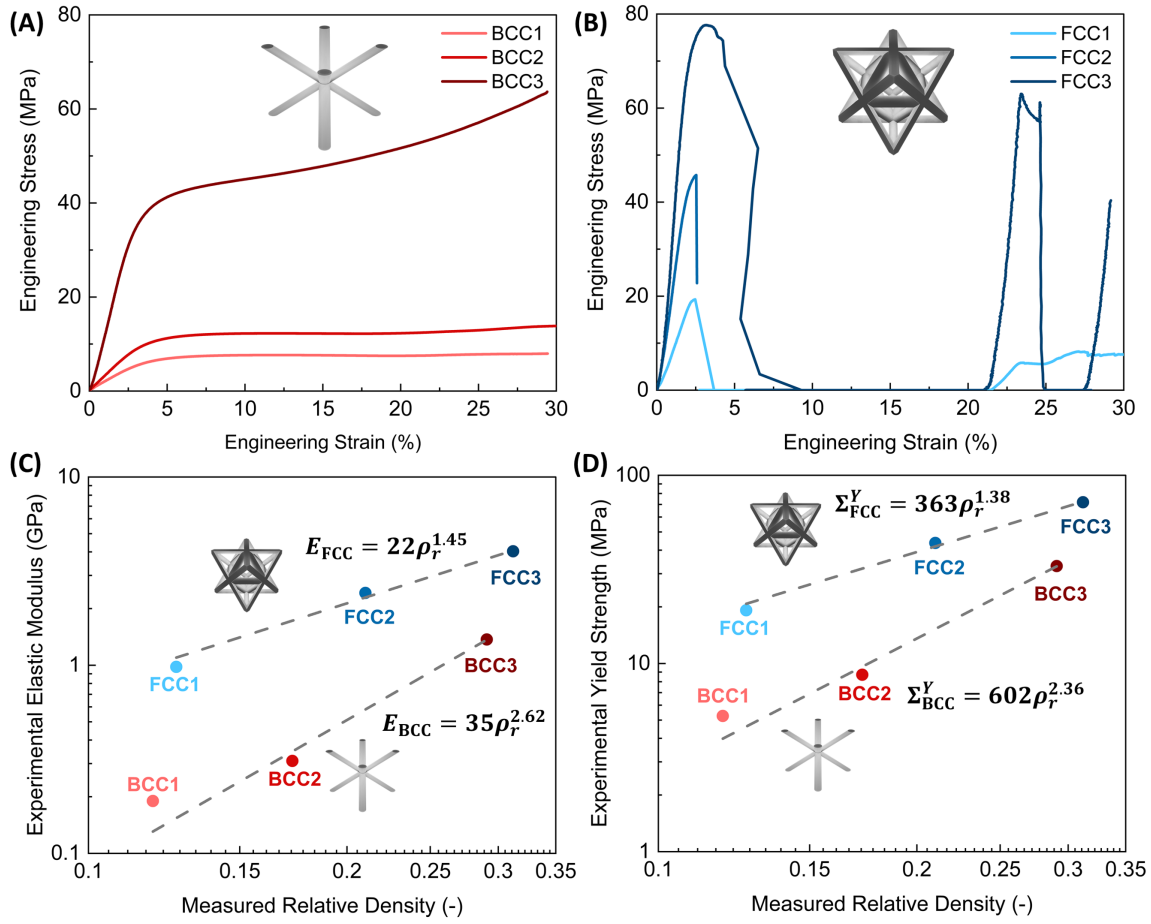


Fig. 5.2 Engineering stress-strain curves of (A) BCC and (B) FCC structures measured at a strain rate of 10^{-3} s^{-1}. For different tested structures, plots of (C) elastic modulus vs. relative density and (D) yield strength vs. relative density.

where C_1, C_2, n_E, and n_{Σ^Y} are lattice constants. For an ideal bending-dominated structure, $n \approx 2$. For an ideal stretching-dominated structure, $n \approx 1$. Results are shown in Figure 5.2(C) and (D). The exponent factors n_E and n_{Σ^Y} of BCC structures are 2.62 and 2.36, respectively, which confirms bending is the primary deformation mode. Conversely, for FCC structures, $n_E = 1.45$ and $n_{\Sigma^Y} = 1.38$, indicating the structures largely fail by axial tension.

5.3.2 Dynamic Behaviour in Fatigue

The fatigue responses of the lattices are measured at maximum applied stresses below the yield strength of the structures Σ^Y. We have estimated the fatigue strength Σ^{f} by extrapolating the fitted curves to 10^6 cycles (Figure 5.3(A)). The fatigue strength Σ^{f} is then correlated with the relative density on a logarithm scale following

$$\Sigma^{\mathrm{f}} = A{\rho_r}^m \tag{5.5}$$

where A and m are lattice constants. Results are shown in Figure 5.3(B). Interestingly, the exponent factor m for BCC structures is 2.35, which is roughly the same as the yield strength exponent factor n_{Σ^Y} (2.36). However, the fatigue strength exponent factor m for FCC structures (1.87) is significantly higher than their yield strength exponent factor n_{Σ^Y} (1.38).

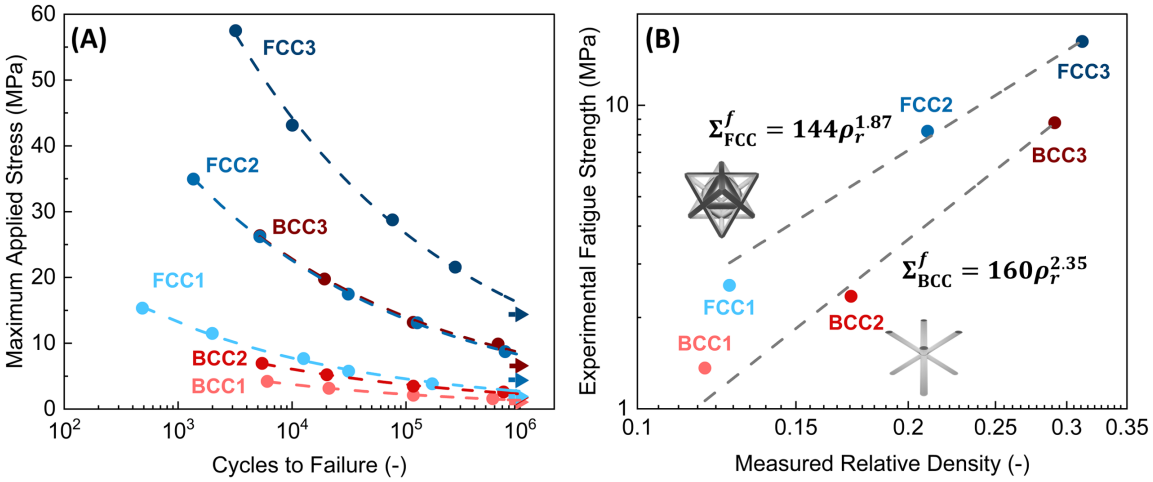


Fig. 5.3 (A) Maximum applied stress vs. cycles to failure for the metamaterials fabricated in this work. (B) Correlation between fatigue strength at 10^6 cycle as a function of relative density on a logarithm scale.

5.3.3 Deformation Behaviour under Monotonic Loading

The monotonic failure modes of the BCC and FCC structures are illustrated in Figure 5.4. The two types of structure show completely different deformation processes. In BCC structures, each strut is primarily subject to bending leading to the development of plastic hinges near the nodes. As the structures are compressed, struts rotate around the nodes, and the accumulation of plastic strain near the nodes interacts with each other resulting in the formation of continuous plastic deformation zones [330, 102]. The uniform deformation of the BCC structures gives rise to the stress plateau after yielding in the stress-strain curves (see Figure 5.2(A)). In FCC structures, the horizontal struts deform primarily by axial tension whereas the diagonal struts are subject to compression and bending [47]. During the compression, the diagonal struts undergo inelastic buckling together with the accumulation of plastic strain leading to the deflection of the struts [69, 331]. The localized instability generates an inclined shear plane, which results in load redistribution in the neighbouring layers. The propagation of the localized shear plane gives rise to the shear deformation. The buckling instability of the struts provokes the stress drop in the stress-strain curves as shown in Figure 5.2(B).

5.3.4 Damage Evolution Process during Cyclic Loading

Figure 5.5 shows the failure process of the BCC1 lattice under cyclic loading at maximum stress of $0.6\Sigma^Y$. The deformation of the structure begins with the rapid accumulation of maximum strain. After 2% of the cycles to failure, the increase in

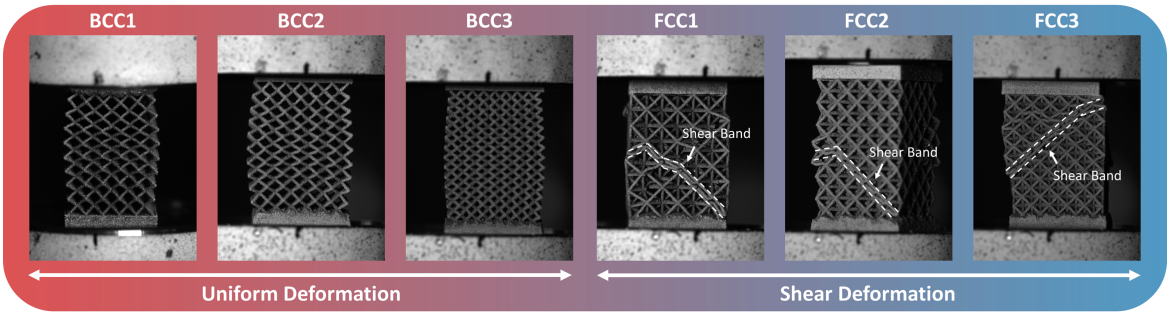


Fig. 5.4 Deformation behaviour of the two types of specimens under monotonic loading at engineering strains of 15%. Note that the compression test for BCC2 lattice was stopped at an engineering strain of 2.5% since the collapse of the structure triggers the failure limit of the mechanical testing system.

maximum strain becomes slower and no failure can be observed. When the number of cycles increases to 90% of fatigue life, multiple strut failure events occur leading to the formation of a shear band and subsequent collapse of the structure. It is noteworthy that the location of the shear band is governed by the initially failed struts. The shear band is around 45° relative to the load direction, which is consistent with the direction of maximum shear stress [332].

5.3.5 Fatigue Fracture Behaviour

The cyclic deformation modes of all the tested specimens are shown in Figure 5.6. Both types of structures primarily fail by shear deformation, which indicates the fatigue failure of metamaterials is more prone to local damage development than monotonic failure [48]. In most cases, the bending of the struts under cyclic loading leads to the fracture near the nodes in the BCC structures while the axial tension of the horizontal struts governs the strut failure in the FCC structures. Yet, exceptions do exist.

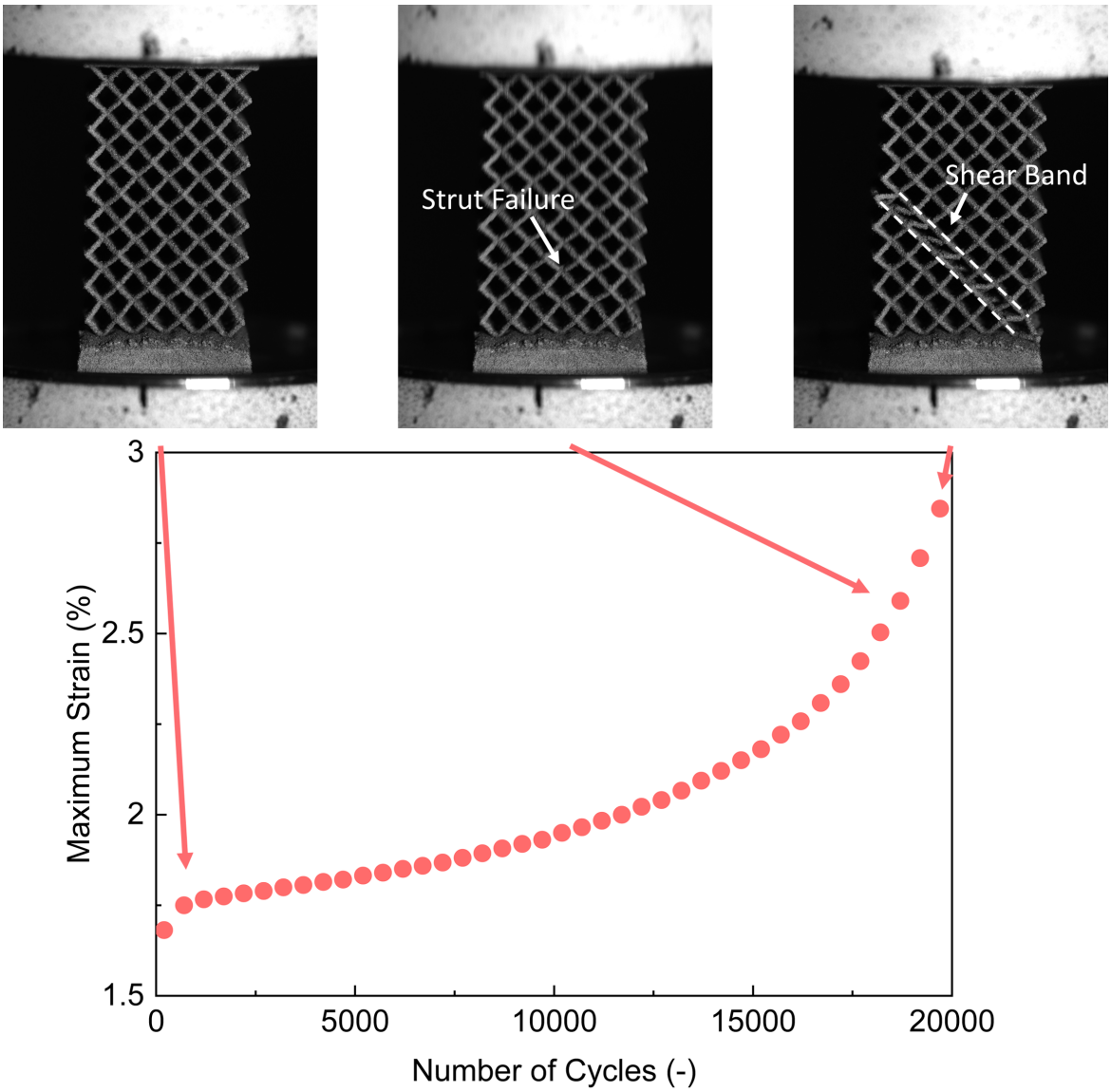


Fig. 5.5 Maximum strain vs. number of cycles for the BCC1 lattice tested at $0.6\Sigma^Y$ and associated in-situ observations on the deformation behaviour of the lattice using a digital camera.

At high applied stresses, the BCC2 and BCC3 structures deform uniformly under cyclic loading, which is consistent with their quasi-static deformation behaviour. A similar phenomenon has also been revealed by Yang et al. [49] on the TPMS structure. When the BCC structures are subject to uniaxial stress Σ_z in the z-direction, the bending moment around the node M can be given by [328, 129]

$$M = \frac{\Sigma_z l^3}{6\sqrt{6}} \tag{5.6}$$

and the corresponding maximum bending stress along the strut $\sigma_{\text{b, max}}$ can be evaluated by

$$\sigma_{\text{b, max}} = \frac{Ma}{I} = \frac{\Sigma_z}{3\sqrt{6}\pi}(\frac{l}{a})^3 \tag{5.7}$$

where I is the second moment of inertia of the circular beam. Additionally, the axial stress along the strut σ_{axial} can be given by [328, 129]

$$\sigma_{\text{axial}} = \frac{\Sigma_z}{3\sqrt{3}\pi}(\frac{l}{a})^2 \tag{5.8}$$

The maximum bending stress scales with the strut thickness-to-length ratio in a cubic function whereas a quadratic relationship correlates the axial stress with the strut thickness-to-length ratio. Hence, as the strut thickness-to-length ratio decreases, the BCC structures become less dominated by the local bending stress under compression. The higher contribution of the axial compression is more likely to give rise to a homogeneous accumulation of plastic strain at high applied stresses leading to the

development of uniform deformation [330, 102]. On the other hand, when the strut thickness-to-length ratio is high, bending stresses contribute more to the deformation of the BCC structures. The local tensile stress is prone to triggering fatigue crack initiation and propagation, which may lead to earlier strut failure. The load redistribution into neighboring unit cells governs the formation of a shear band.

Specimen	Sample	Compression Test	Compression Fatigue Test
BCC1	Sample 1	Yes	No
BCC1	Sample 2	No	Yes ($\Sigma_{\max} = 0.8\Sigma^Y$)
BCC1	Sample 3	No	Yes ($\Sigma_{\max} = 0.6\Sigma^Y$)
BCC1	Sample 4	No	Yes ($\Sigma_{\max} = 0.4\Sigma^Y$)
BCC1	Sample 5	No	Yes ($\Sigma_{\max} = 0.3\Sigma^Y$)
BCC2	Sample 1	Yes	No
BCC2	Sample 2	No	Yes ($\Sigma_{\max} = 0.8\Sigma^Y$)
BCC2	Sample 3	No	Yes ($\Sigma_{\max} = 0.6\Sigma^Y$)
BCC2	Sample 4	No	Yes ($\Sigma_{\max} = 0.4\Sigma^Y$)
BCC2	Sample 5	No	Yes ($\Sigma_{\max} = 0.3\Sigma^Y$)
BCC3	Sample 1	Yes	No
BCC3	Sample 2	No	Yes ($\Sigma_{\max} = 0.8\Sigma^Y$)
BCC3	Sample 3	No	Yes ($\Sigma_{\max} = 0.6\Sigma^Y$)
BCC3	Sample 4	No	Yes ($\Sigma_{\max} = 0.4\Sigma^Y$)
BCC3	Sample 5	No	Yes ($\Sigma_{\max} = 0.3\Sigma^Y$)
FCC1	Sample 1	Yes	No
FCC1	Sample 2	No	Yes ($\Sigma_{\max} = 0.8\Sigma^Y$)
FCC1	Sample 3	No	Yes ($\Sigma_{\max} = 0.6\Sigma^Y$)
FCC1	Sample 4	No	Yes ($\Sigma_{\max} = 0.4\Sigma^Y$)
FCC1	Sample 5	No	Yes ($\Sigma_{\max} = 0.3\Sigma^Y$)
FCC1	Sample 6	No	Yes ($\Sigma_{\max} = 0.2\Sigma^Y$)
FCC1	Sample 7	No	Yes ($\Sigma_{\max} = 0.1\Sigma^Y$)
FCC2	Sample 1	Yes	No
FCC2	Sample 2	No	Yes ($\Sigma_{\max} = 0.8\Sigma^Y$)
FCC2	Sample 3	No	Yes ($\Sigma_{\max} = 0.6\Sigma^Y$)
FCC2	Sample 4	No	Yes ($\Sigma_{\max} = 0.4\Sigma^Y$)
FCC2	Sample 5	No	Yes ($\Sigma_{\max} = 0.3\Sigma^Y$)
FCC2	Sample 6	No	Yes ($\Sigma_{\max} = 0.2\Sigma^Y$)
FCC3	Sample 1	Yes	No
FCC3	Sample 2	No	Yes ($\Sigma_{\max} = 0.8\Sigma^Y$)
FCC3	Sample 3	No	Yes ($\Sigma_{\max} = 0.6\Sigma^Y$)
FCC3	Sample 4	No	Yes ($\Sigma_{\max} = 0.4\Sigma^Y$)
FCC3	Sample 5	No	Yes ($\Sigma_{\max} = 0.3\Sigma^Y$)
FCC3	Sample 6	No	Yes ($\Sigma_{\max} = 0.2\Sigma^Y$)

Table 5.1 A summary of the samples tested in this work.

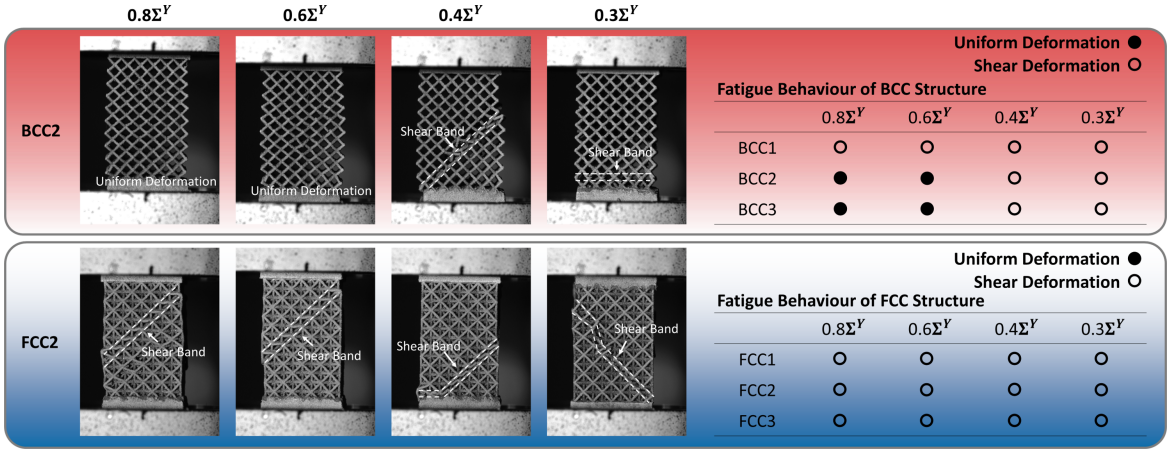


Fig. 5.6 Summary of the deformation behaviour of the BCC and FCC structures under cyclic loading.

5.4 Summary and Conclusions

In summary, we have integrated systematic mechanical testing and in-situ observations to unravel the fatigue behaviour of BCC and FCC metamaterials made by laser powder bed fusion. Our results show the BCC structures fail by either uniform or shear deformation whereas the FCC structures only undergo shear fracture. When the strut thickness-to-length ratio is low, the BCC structures become more dominated by axial compression during deformation, which is more likely to form continuous plastic deformation zones at high applied stresses. At a high strut thickness-to-length ratio, the higher contribution of bending stresses to the deformation gives rise to the development of local damage resulting in shear fracture. Conversely, the tensile deformation of the horizontal struts in the FCC structures triggers local strut failure leading to the formation of shear bands under cyclic loading at all applied stresses.

Chapter 6

Stochastic or Deterministic: Duality of Fatigue Behaviour of Metallic Lattice

6.1 Introduction

The failure of lattice materials under cyclic loading undergoes a series of complex events including cyclic ratcheting, fatigue crack initiation and propagation, and coalescence of cracks [43, 49, 48, 77]. The fatigue cracks usually form at the surface of the stress concentration and the processing-induced defects may raise the local stresses leading to early failure of the struts [49, 133, 153]. In periodic cellular structures, the stress distributions are more or less consistent across different unit cells, and thus damage localization is highly determined by the presence of processing-induced

defect [49, 68, 333]. The randomness of defect formation gives rise to stochastic failure processes in these structures during cyclic loading [82, 333, 67]. A recent report on the cubic lattice has shown that the unconnected struts can disrupt the strut failure activities and reduce the normalized fatigue strength of the structure by a factor of roughly 2 [153]. This suggests the fatigue resistance of the periodic structures is highly sensitive to the presence of defects undermining the consistency of their mechanical durability. But does this hold for lattices with stochastic geometries? Inspired by biological structures, there is an increasing capitalization of incorporating disorder in the design of lattice materials [5, 85, 334, 335]. This has proven to be a promising avenue to diffuse deformation activity and retard the onset of failure under monotonic loading [336, 337]. For example, the fatigue fracture of a random trabecular structure requires strut failures at multiple locations decelerating the crack propagation process [338]. Hence, we posit that integrating randomness in lattice design would improve the mechanical tolerance to manufacturing defects during cyclic loading – the paramount puzzle for the development of fatigue-resistant components.

Guided by polycrystalline microstructures, we encoded randomness in the design of architected materials by adopting Voronoi geometry. We integrated experimental measurements, including in-situ observation and interrupted tests with X-ray computed tomography (XCT), and numerical simulations to elucidate the two distinct deformation behaviours of metallic lattices under cyclic loading. The deformation mode is directly correlated with the strut connectivity of the lattice. By assuming each of the unconnected struts as a "macroscopic crack", analysis of the stress state in the vicinity

of the crack proves there is a transition crack length, below which the fatigue life of the lattice is independent of the crack length. These findings offer fundamental insights into the cyclic deformation process of metallic lattice and map out the trajectory for the design of mechanically durable components.

6.2 Methods

6.2.1 Design and Manufacturing of the Lattices

Voronoi structures (V) were employed as the lattice topologies in this study (see Figure 6.1(A)). A standard Voronoi tessellation is applied to produce these structures using the Rhinoceros 6 (Robert McNeel & Associates, USA) 3D modelling software. For their generation, a number of seeds were randomly distributed in a defined 3D space. The set of all points whose distances to the seed are no greater than their distances to the other seed were considered to belong to a Voronoi cell (C) as shown in Figure 6.1(B). The points with equal distances to both seeds form a strut between two Voronoi cells. The positions where struts meet are called junctions. This leaves two design parameters to control the final structure: strut thickness and number of cells per unit volume.

Rectangular specimens of 15.5/17.5 mm height, 10 mm width, and 10 mm thickness were filled with lattices. V1, V3, and V5 are 15.5 mm in height while V2 and V4 are 17.5 mm in height. A range of strut thicknesses and number of cells per mm^3 were chosen to achieve a relative density below 0.4 as shown in Figure 6.1(C).

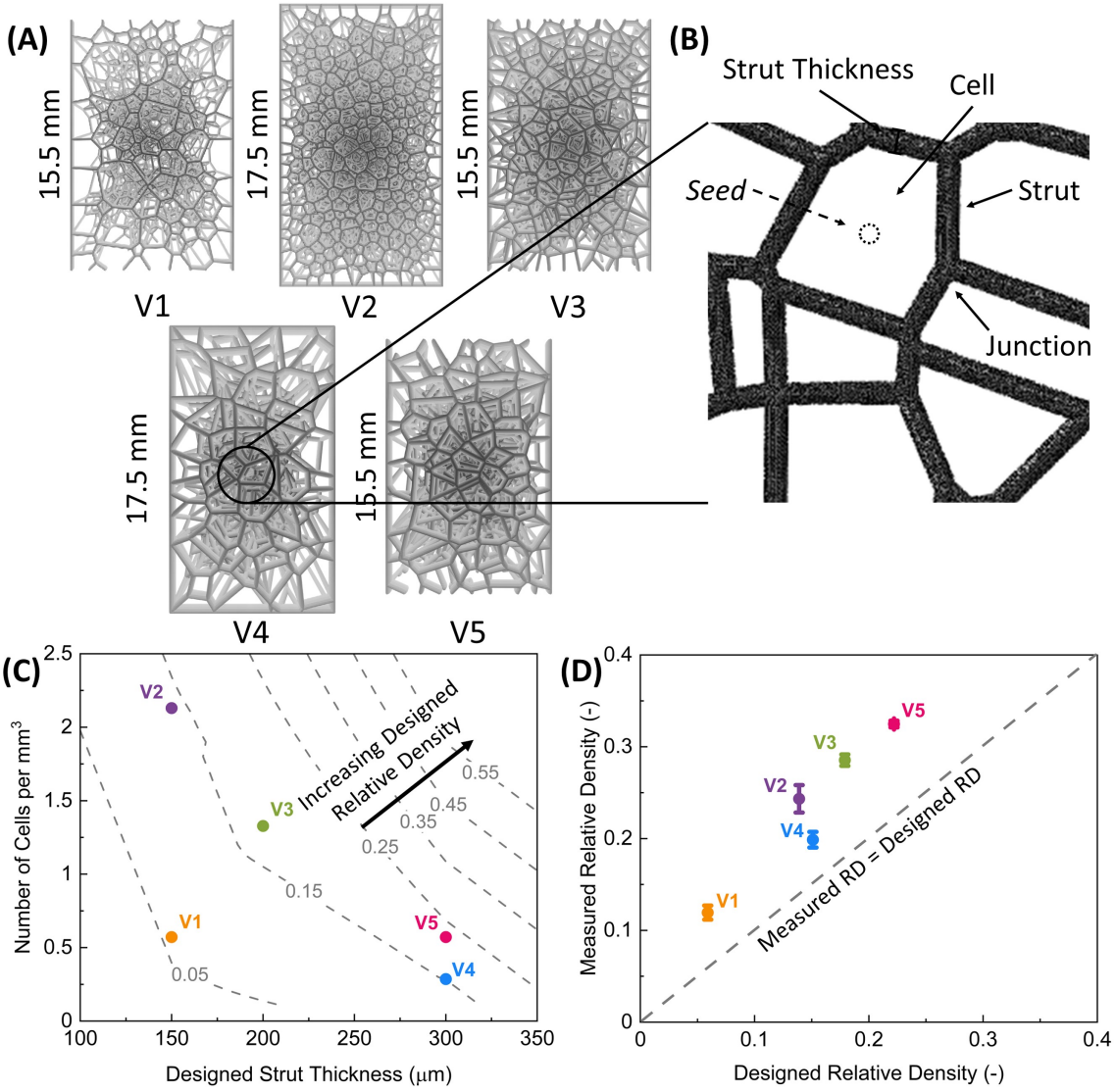


Fig. 6.1 (A) Geometries of the 5 Voronoi lattices in this study. (B) Schematic illustration of Voronoi cells and terms used in this work. (C) Contour plot of designed relative density as a function of designed strut thickness and number of Voronoi cells per mm^3 identifying the locations of structures V1-V5 studied. (D) Measured relative density vs. designed relative density for the 5 structures under study.

The metallic lattices were produced using the titanium alloy Ti-6Al-4V – the most commonly used titanium alloy in aerospace and biomedical industries. A Renishaw AM250 machine was used to produce the tested specimens. A contour scanning strategy was applied with 50 W laser power, 30 μm point distance, 2000 mm/s scan speed, 30 μm layer thickness, and 50 μs exposure time. The parameters were optimized for highly dense conditions. After fabrication, the specimens were removed from the build plate and heat-treated in the vacuum for 4 h at 800 °C to remove residual stress.

6.2.2 Assessment of Static & Dynamic Mechanical Behaviour

We performed monotonic compression tests at a strain rate of 10^3 s^{-1} to determine the applied stress for fatigue tests. The loading response was extracted from a 10 kN load cell while the displacement was measured using a non-contact iMetrum video extensometry system. The grips were speckled in order to accurately measure the displacement of the surfaces near the specimens and the deformation of the lattices. The tests were stopped after 30% engineering strain.

Compression fatigue tests were performed at a frequency of 30 Hz and an R ratio of 0.1. Maximum stresses of 0.8, 0.6, 0.4, 0.3, and $0.2\Sigma_Y$ were applied. At each stress, three tests were repeated before runout. Specimens were tested up to 5% compressive strain. The deformation behaviours of the lattices were captured using a digital camera.

6.2.3 X-ray Computed Tomography (XCT)

We acquired X-ray computed tomography (XCT) scans with an ImageiX CT system (North Star Imaging Inc., Minnesota, USA). During the scan, a Cu foil of 0.95 mm thickness was equipped to filter the tungsten transmission target X-ray source. We employed the following scan conditions: 140 kV tube voltage, 71 μA tube current, 5 μm focal spot size, and 1 Hz frame rate. This provided an isotropic voxel size of 16 μm and a resolving power of 48 μm [263]. Three specimens were measured for each of the five geometries to ensure repeatability – a total of 15 specimens were scanned. We then reconstructed the projection images using a filtered back projection algorithm in the efX-ct software (version 1.9.5.12, North Star Imaging Inc., Minnesota, USA). The data analysis was performed with the Avizo 9.7 software. The relative densities of the specimens were measured using the XCT data as shown in Figure 6.1(D). The measured relative densities for all structures are higher than the designed values possibly due to powders trapped in small cells.

6.2.4 Finite Element Modelling

We performed finite element analysis (FEA) simulations of the lattices using ABAQUS Standard (v2017). We described each strut in the lattice by a Timoshenko beam element (B31 in the ABAQUS notation). Each strut was discretized into several B31 elements by in-house MATLAB codes based on the strut length such that each element is shorter than 0.1 mm. We then performed mesh convergence studies to prove the accuracy of the discretization.

A linear elastic, linear kinematic hardening model was used to describe the Ti-6Al-4V alloy. Table 6.1 shows the material properties used in this work. These were assigned to all the struts in the structure.

Elastic Modulus	Poisson's Ratio	Yield Strength	Kinematic Hardening Modulus
110 GPa	0.3	900 MPa	1.1 GPa

Table 6.1 Material properties of AM Ti-6Al-4V employed in the FEA model.

The boundary conditions were set to describe the behaviour of the structure clamped by two solid plates. Two centroids, one on the bottom and another on the top surfaces of the specimens, were assigned as master nodes. All nodes on the bottom surfaces were constrained with the bottom master node to be encastre while the nodes on the top surfaces were constrained with the top master node to be imposed to a load.

A summary of the samples tested in this Chapter is shown in Table 6.2.

Specimen	Sample	Compression Test	Compression Fatigue Test
V1	Sample 1	Yes	No
V1	Sample 2	No	Yes ($\Sigma_{\max} = 0.8\Sigma^Y$)
V1	Sample 3	No	Yes ($\Sigma_{\max} = 0.8\Sigma^Y$)
V1	Sample 4	No	Yes ($\Sigma_{\max} = 0.8\Sigma^Y$)
V1	Sample 5	No	Yes ($\Sigma_{\max} = 0.6\Sigma^Y$)
V1	Sample 6	No	Yes ($\Sigma_{\max} = 0.6\Sigma^Y$)
V1	Sample 7	No	Yes ($\Sigma_{\max} = 0.6\Sigma^Y$)
V1	Sample 8	No	Yes ($\Sigma_{\max} = 0.4\Sigma^Y$)
V1	Sample 9	No	Yes ($\Sigma_{\max} = 0.4\Sigma^Y$)
V1	Sample 10	No	Yes ($\Sigma_{\max} = 0.4\Sigma^Y$)
V1	Sample 11	No	Yes ($\Sigma_{\max} = 0.3\Sigma^Y$)
V1	Sample 12	No	Yes ($\Sigma_{\max} = 0.3\Sigma^Y$)
V1	Sample 13	No	Yes ($\Sigma_{\max} = 0.3\Sigma^Y$)
V1	Sample 14	No	Yes ($\Sigma_{\max} = 0.2\Sigma^Y$)
V2	Sample 1	Yes	No
V2	Sample 2	No	Yes ($\Sigma_{\max} = 0.8\Sigma^Y$)
V2	Sample 3	No	Yes ($\Sigma_{\max} = 0.8\Sigma^Y$)
V2	Sample 4	No	Yes ($\Sigma_{\max} = 0.8\Sigma^Y$)
V2	Sample 5	No	Yes ($\Sigma_{\max} = 0.6\Sigma^Y$)

V2	Sample 6	No	Yes ($\Sigma_{\max} = 0.6\Sigma^Y$)
V2	Sample 7	No	Yes ($\Sigma_{\max} = 0.6\Sigma^Y$)
V2	Sample 8	No	Yes ($\Sigma_{\max} = 0.4\Sigma^Y$)
V2	Sample 9	No	Yes ($\Sigma_{\max} = 0.4\Sigma^Y$)
V2	Sample 10	No	Yes ($\Sigma_{\max} = 0.4\Sigma^Y$)
V2	Sample 11	No	Yes ($\Sigma_{\max} = 0.3\Sigma^Y$)
V3	Sample 1	Yes	No
V3	Sample 2	No	Yes ($\Sigma_{\max} = 0.8\Sigma^Y$)
V3	Sample 3	No	Yes ($\Sigma_{\max} = 0.8\Sigma^Y$)
V3	Sample 4	No	Yes ($\Sigma_{\max} = 0.8\Sigma^Y$)
V3	Sample 5	No	Yes ($\Sigma_{\max} = 0.6\Sigma^Y$)
V3	Sample 6	No	Yes ($\Sigma_{\max} = 0.6\Sigma^Y$)
V3	Sample 7	No	Yes ($\Sigma_{\max} = 0.6\Sigma^Y$)
V3	Sample 8	No	Yes ($\Sigma_{\max} = 0.4\Sigma^Y$)
V3	Sample 9	No	Yes ($\Sigma_{\max} = 0.4\Sigma^Y$)
V3	Sample 10	No	Yes ($\Sigma_{\max} = 0.4\Sigma^Y$)
V3	Sample 11	No	Yes ($\Sigma_{\max} = 0.3\Sigma^Y$)
V4	Sample 1	Yes	No
V4	Sample 2	No	Yes ($\Sigma_{\max} = 0.8\Sigma^Y$)
V4	Sample 3	No	Yes ($\Sigma_{\max} = 0.8\Sigma^Y$)
V4	Sample 3	No	Yes ($\Sigma_{\max} = 0.8\Sigma^Y$)
V4	Sample 4	No	Yes ($\Sigma_{\max} = 0.6\Sigma^Y$)
V4	Sample 5	No	Yes ($\Sigma_{\max} = 0.6\Sigma^Y$)
V4	Sample 6	No	Yes ($\Sigma_{\max} = 0.6\Sigma^Y$)
V4	Sample 7	No	Yes ($\Sigma_{\max} = 0.4\Sigma^Y$)
V4	Sample 8	No	Yes ($\Sigma_{\max} = 0.4\Sigma^Y$)
V4	Sample 9	No	Yes ($\Sigma_{\max} = 0.4\Sigma^Y$)
V4	Sample 10	No	Yes ($\Sigma_{\max} = 0.3\Sigma^Y$)
V5	Sample 1	Yes	No
V5	Sample 2	No	Yes ($\Sigma_{\max} = 0.8\Sigma^Y$)
V5	Sample 3	No	Yes ($\Sigma_{\max} = 0.8\Sigma^Y$)
V5	Sample 4	No	Yes ($\Sigma_{\max} = 0.8\Sigma^Y$)
V5	Sample 5	No	Yes ($\Sigma_{\max} = 0.6\Sigma^Y$)
V5	Sample 6	No	Yes ($\Sigma_{\max} = 0.6\Sigma^Y$)
V5	Sample 7	No	Yes ($\Sigma_{\max} = 0.6\Sigma^Y$)
V5	Sample 8	No	Yes ($\Sigma_{\max} = 0.4\Sigma^Y$)
V5	Sample 9	No	Yes ($\Sigma_{\max} = 0.4\Sigma^Y$)
V5	Sample 10	No	Yes ($\Sigma_{\max} = 0.4\Sigma^Y$)
V5	Sample 11	No	Yes ($\Sigma_{\max} = 0.3\Sigma^Y$)

Table 6.2 A summary of the samples tested in this work.

6.3 Results

6.3.1 Quasi-static Mechanical Behaviour of the Voronoi Lattice

The quasi-static mechanical responses of the Voronoi structures are measured in the form of stress-strain curves as shown in Figure 6.2(A). All the specimens exhibit an initial elastic deformation followed by a yielding of the structure and a subsequent collapse and finally a recovery of strength due to the densification of the porous structure. V5 lattice even presents a further stress drop after the strength recovery.

The initial loading segment of the engineering strain-stress curve was utilized to determine the elastic modulus E and yield strength Σ_Y of specimens with various lattice types. The elastic modulus is defined as the slope of the linear elastic region, while the yield strength is determined from the offset yield point at 0.2% plastic strain.

The elastic modulus and yield strength of the lattices are quantified as a function of the relative density ρ/ρ_s (see Figure 6.2(B) and (C)). Gibson-Ashby model is fitted to describe the relationship following:

$$E = C_1(\rho/\rho_s)^{n_E} \tag{6.1}$$

for the elastic modulus of the lattice and

$$\Sigma_Y = C_2(\rho/\rho_s)^{n_{\Sigma_Y}} \tag{6.2}$$

for the yield strength of the lattice [329]. C_1, C_2, n_E, and n_{Σ_Y} are lattice constants. The exponent factors n_E and n_{Σ_Y} are dependent on the deformation mode: for stretch-dominated cells n_E and $n_{\Sigma_Y} \approx 1$ and for bend-dominated cells n_E and $n_{\Sigma_Y} \approx 2$. The n_E and n_{Σ_Y} exponents of Voronoi structures are 1.8 and 2.1, respectively, which suggests bending is the denominating deformation mode for Voronoi structures.

6.3.2 Dynamic Behaviour in Fatigue

To characterize mechanical durability, we performed compression fatigue tests at maximum applied stresses below the yield strength of the structure Σ_Y. This allows us to focus particularly between 10^3 and 10^6 cycles to examine the behaviour of the lattice in the high cycle regime [68, 49]. The fatigue strength Σ_f is determined by extrapolating the fitted curves to 10^6 cycles (see Figure 6.3(A)). We then correlate Σ_f with ρ/ρ_s on a logarithm scale in Figure 6.3(B) following:

$$\Sigma_\mathrm{f} = A(\rho/\rho_\mathrm{s})^m \tag{6.3}$$

where A and m are lattice constants. The exponent factor m for fatigue strength (2.1) was found to be the same as that for yield strength (2.1), which suggests the dominant deformation mode under cyclic loading is consistent with that under monotonic loading [48].

We proceed by evaluating the scatter in fatigue life using the coefficient of variation of fatigue life from the three repeats at each Σ_Y. The fatigue scatter for the specimens

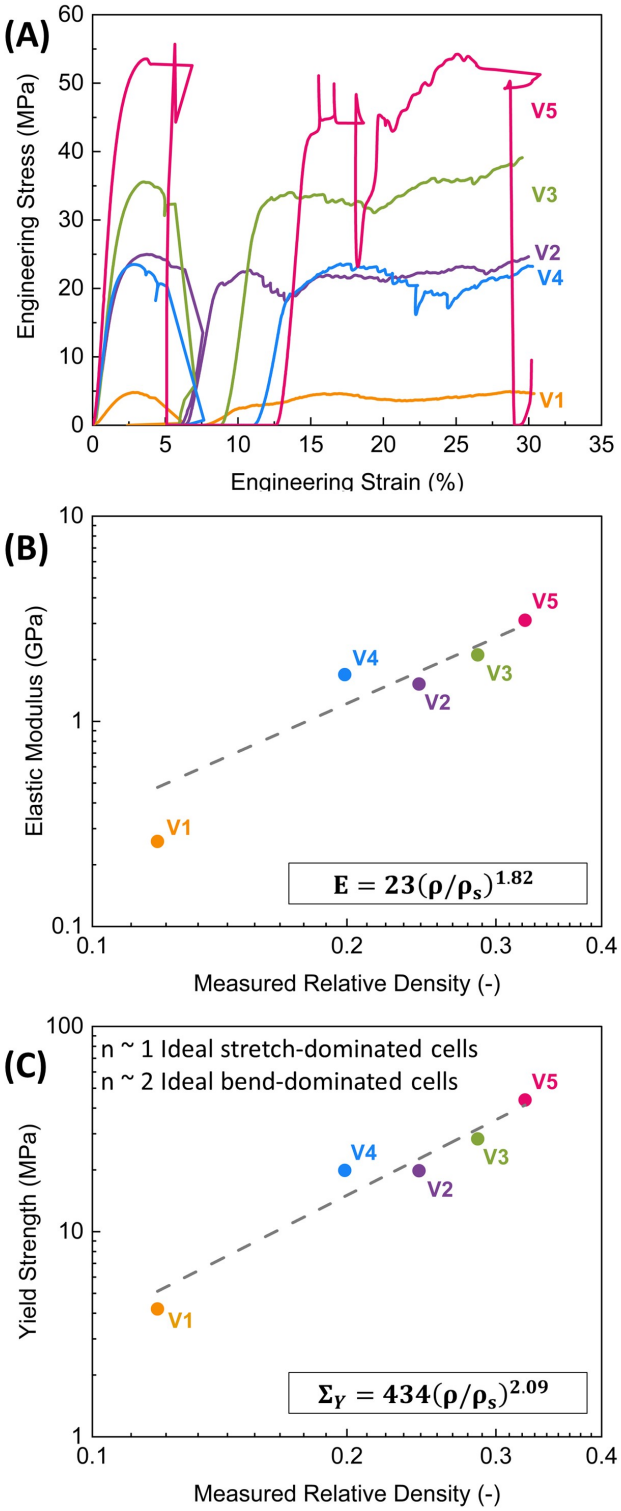


Fig. 6.2 (A) Engineering stress-strain curves measured at a strain rate of 10^{-3} s^{-1}. For different tested lattices, plots of (B) elastic modulus vs. relative density and (C) yield strength vs. relative density.

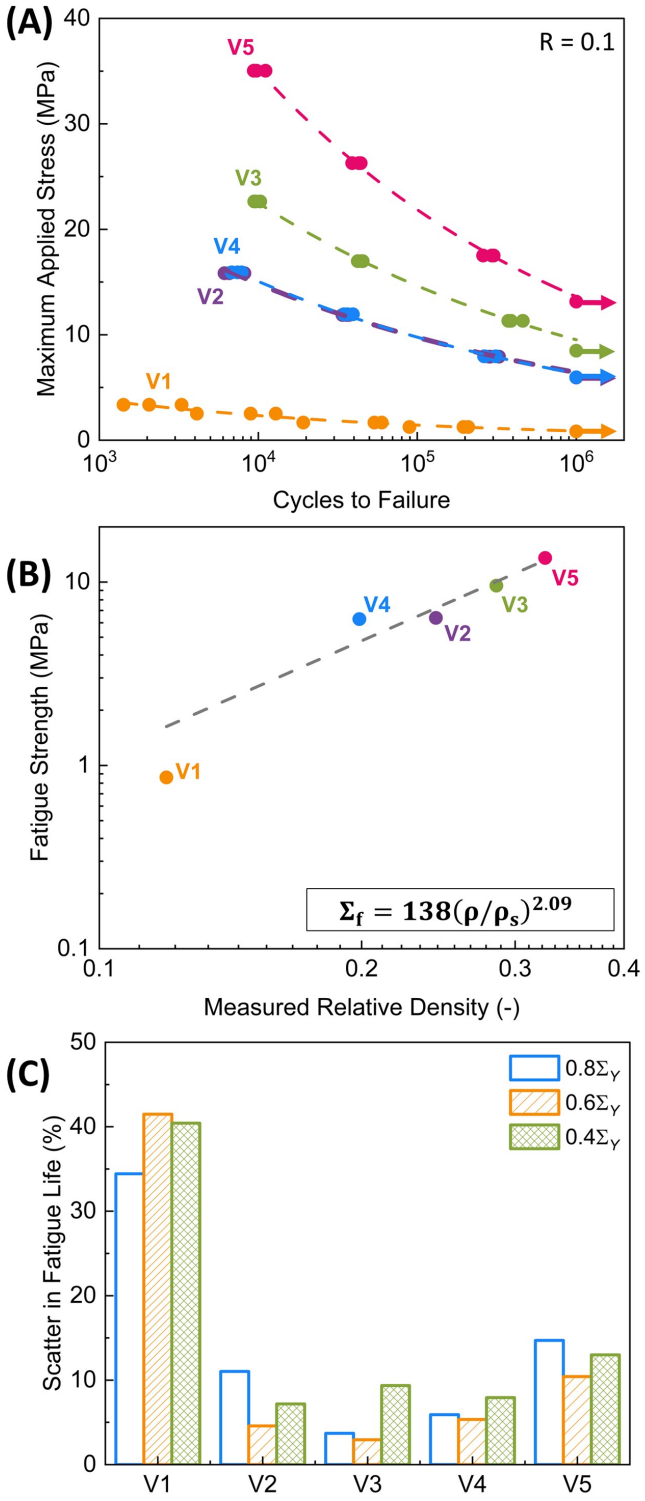


Fig. 6.3 (A) Maximum applied stress vs. cycles to failure for the lattices manufactured in this work. Three measurements are performed per condition before runout. (B) Correlation between fatigue strength at 10^6 cycle as a function of relative density on a logarithm scale. (C) Scatter in fatigue life for the lattices at different applied stresses. The scatter is given by the coefficient of variation of the fatigue life.

is shown in Figure 6.3(C). Clearly, V1 exhibits fatigue scatters of $> 30\%$ at all applied stresses whereas the scatters of the other specimens are only 15% at most. The vast difference in the consistency of fatigue properties can give rise to significant uncertainty in the durability of structural components.

6.3.3 Characterization of the Lattice Processability

Here, we report the measurement of processing-induced defects in the lattices using X-ray computed tomography (XCT). The results can then be used to inform the fatigue behaviour of the Voronoi structures.

Surface Roughness

The surface profiles of the lattices are evaluated as a function of the lattice geometry. To avoid the influence of the strut orientation, only vertical and horizontal struts are considered [200, 339]. We then extract cross-sectional images of 3 struts from each orientation and detect the strut edges using Image-J as shown in Figure 6.4. R_a is used as the surface roughness parameter in this work. In every specimen, the downward-facing surface of the horizontal strut shows higher surface roughness than its upward-facing surface and the vertical strut surface because of the dross formation [100, 101]. The low thermal conductivity of the titanium powders below the downward-facing surface curtails the heat dissipation in the overhang regions, which gives rise to the overheating of the melt pool. The increased recoiled pressure then results in the formation of deeper depression zones solidifying into large deformities.

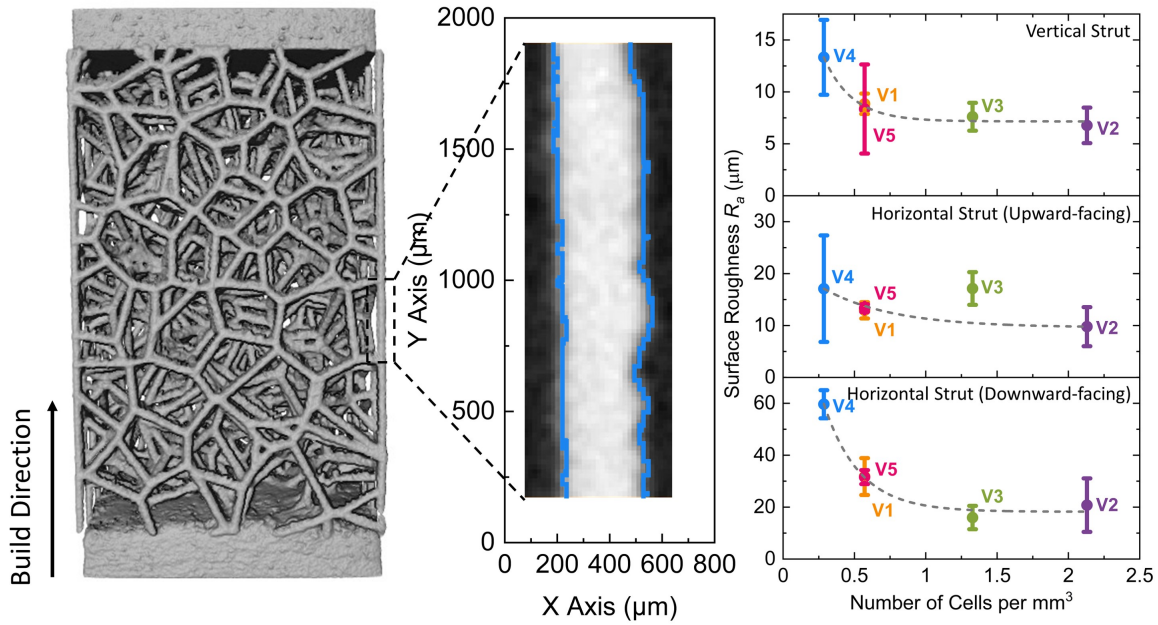


Fig. 6.4 Surface quality characterization of different Voronoi structures. (A) shows an example of the edge profile extracted from a vertical strut of the V4 lattice using Image-J. (B) illustrates the surface roughness (R_a) of vertical, horizontal (upward-facing), and horizontal (downward-facing) struts as a function of the number of cells per mm^3.

Additionally, there is an inverse correlation between R_a and the cell number density. This may result from the closer proximity of struts as the number of cells per unit volume increases. The reduced spacing between printed features can lead to slower cooling rates, which leads to higher melt pool stability and less balling effect [259, 276, 277, 340].

Strut Thickness Variation

We measure the strut thicknesses of the specimens using the method described in Hildebrand et al. [341]. A maximal sphere is fitted to every point in the lattice and the diameter of the sphere is quantified. Results are shown in Figure 6.5(A). To evaluate

the thickness variation along the strut, we extract the thickness profiles of five struts from the V4 lattice (see Figure 6.5(B)). All the struts exhibit higher thicknesses at the junctions than the designed value whereas the central parts of the struts have lower thicknesses. Such a thickness variation along the strut can be attributed to the geometrical shrinkage during the rapid cooling process [342, 120, 343]. When the laser enters the junction, the adjacency of the printed features induces a larger melt pool, which gives rise to a higher thickness [344, 186]. The average thicknesses $\pm$ 1 standard deviation for different structures are shown in Figure 6.5(C). All the structures demonstrate average thicknesses no more than 32 μm different from the designed values. We then quantify the thickness variation using the coefficient of variation. Results are present in Figure 6.5(D). As the strut thickness increases, the coefficient of variation is reduced which leads to an improved strut consistency. During the manufacturing process, the thicker struts preserve more heat resulting in slower cooling rates [267]. The higher temperature within the thicker strut may give rise to more stable melt pools, which leads to reduced local heterogeneity.

Processing-induced Porosity

The porosity levels of the specimens are assessed using XCT data. An example of a pore embedded in the strut is shown in Figure 6.6(A). The presence of these pores can degrade the fatigue performance of AM components [97, 339, 154]. The number density and size of the pores are displayed in Figure 6.6(B) and (C), respectively. Here, the number density of the pores is evaluated by the number of pores per unit volume

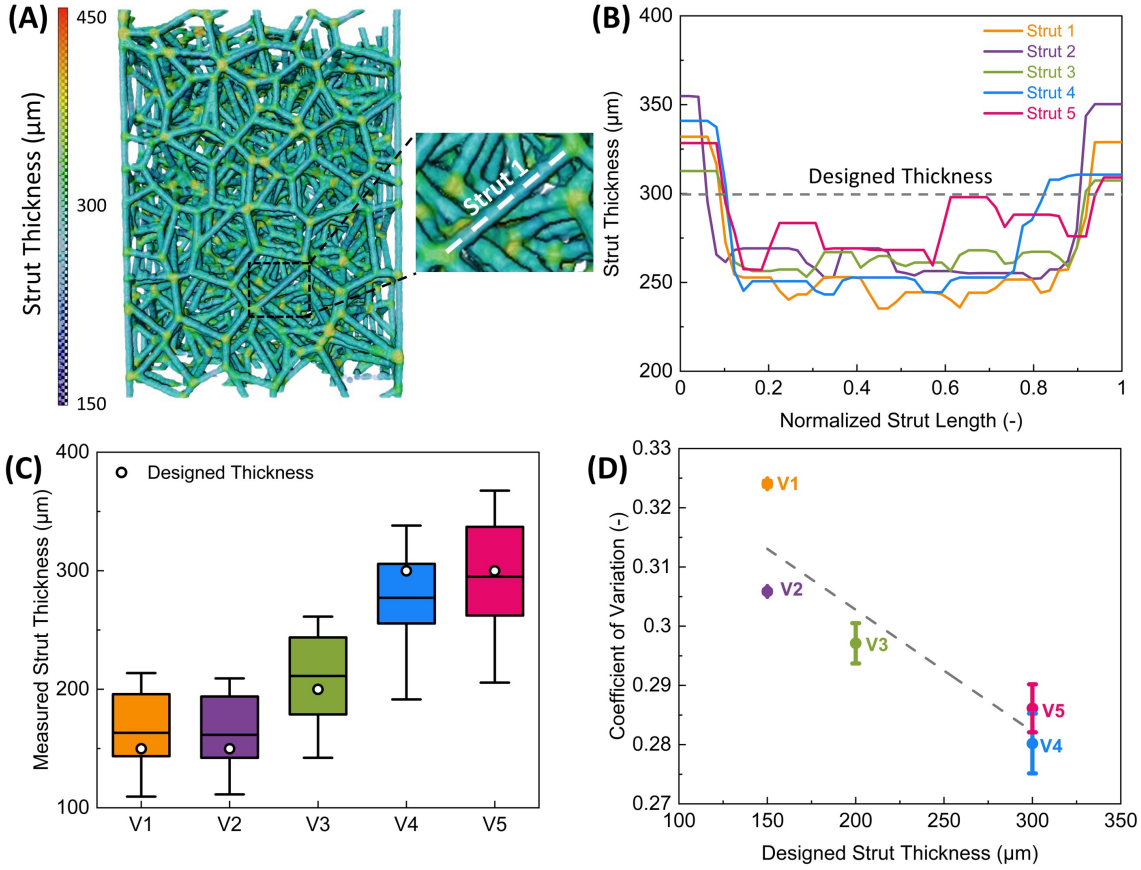


Fig. 6.5 (A) An example of the thickness map computed for the V4 lattice. (B) Example of strut thicknesses measured along 5 different struts in the V4 lattice. (C) Box plots showing the designed value, mean ± 1 standard deviation, and interquartile range. (D) Coefficient of variation of the strut thickness as a function of the designed value for the 5 structures under study.

of the consolidated lattice while their pore size is given by the equivalent diameter d following [97]

$$d = \sqrt[3]{\frac{6V}{\pi}} \tag{6.4}$$

where V is the pore volume. In all the tested samples, the number density of the pores is lower than 0.1 mm^{-3}, which suggests porosity may hardly interact with the microcracks during the fatigue fracture process. As the designed strut thickness increases, both the pore number density and maximum pore size in the lattices increase resulting in a higher probability of pores contributing to the failure process. This can be explained by the size effect phenomenon that has been reported on both the conventionally manufactured and AM materials [97, 253, 265]. When the sample thickness increases, the probability of encountering a large pore becomes higher.

Geometrical Deviation

The geometrical deviation of the printed specimen is assessed by comparing the XCT data with the CAD design. For each specimen, a $3 \times 3 \times 3$ mm^3 sub-volume is analysed. Spatial registration of the XCT data with the CAD design is performed by aligning the centre of mass and principle axes. Their overlapping volume is maximized by employing a series of translations and rotations. The distances between the closest points on their surfaces are then evaluated to determine any dimensional discrepancy from the design. Results are shown in Figure 6.7(A). The excess of material is shown in red and the lack of material is shown in blue. The root mean square error (RMSE) of the geometrical deviation is quantified for the entire sub-volume. Figure 6.7(B)

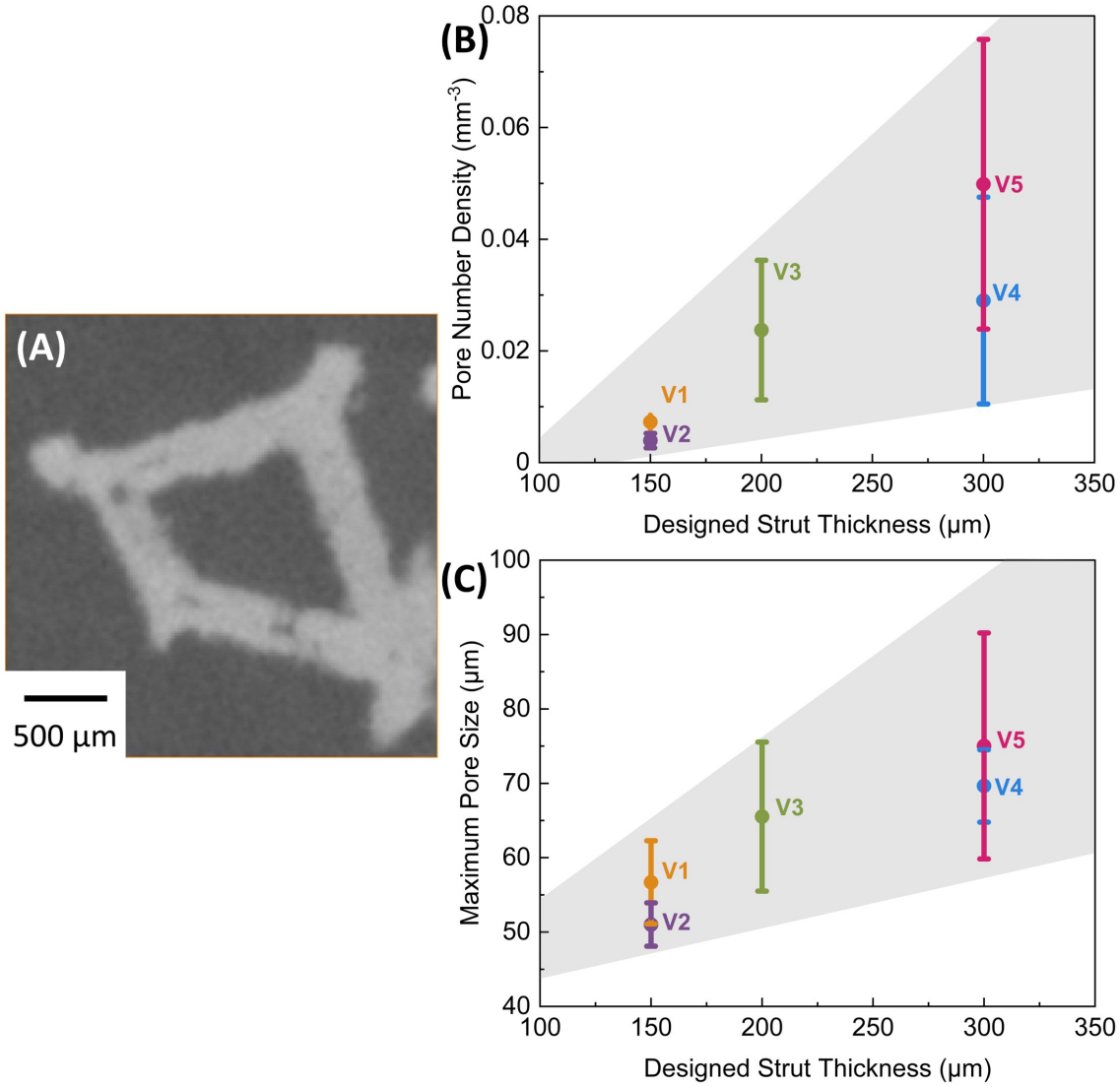


Fig. 6.6 (A) An example of a processing-induced porosity within the strut of V4 lattice. (B) Measured pore number density as a function of the designed strut thickness. (C) Measured maximum pore size as a function of the designed strut thickness.

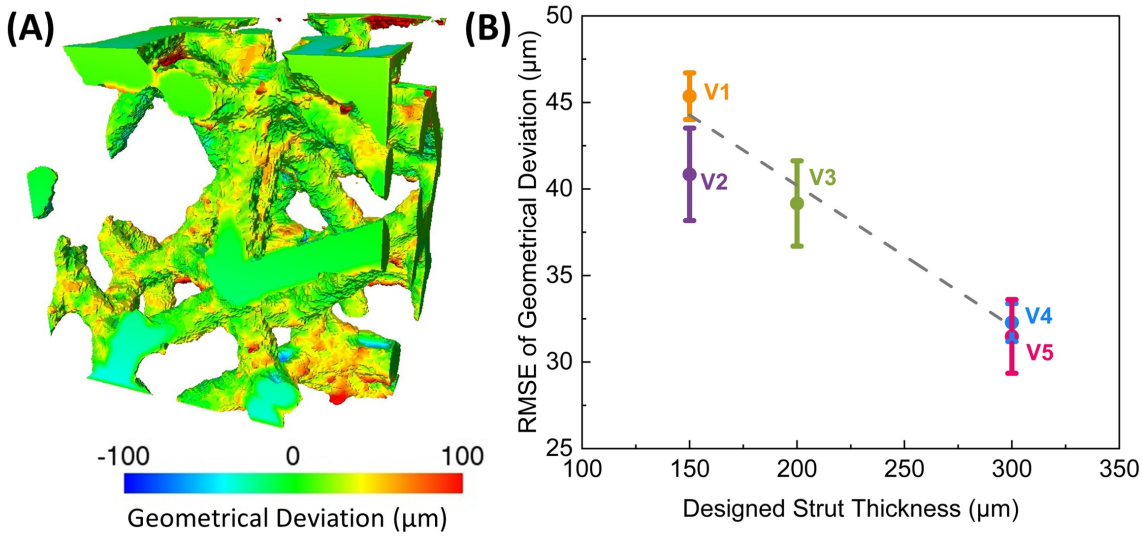


Fig. 6.7 (A) An example of the comparison between CAD design and computed tomography data. Red regions represent excess of material and blue regions represent lack of material. (B) Root mean square error (RMSE) of the geometrical deviation as a function of the designed strut thickness.

shows its correlation with the designed strut thickness. The differences in geometrical deviation across the five specimens are marginal. An increase in strut thickness results in a slightly lower RMSE value, which gives rise to higher dimensional accuracy. This possibly results from the higher temperature in the specimen when thicker features are printed [267]. The lower cooling rate can improve the melt pool stability reducing the irregular distribution of the material.

Strut Unconnectivity

We also observe unconnected struts in the lattices even in the as-printed state as shown in Figure 6.8(A). The fraction of unconnected struts in the specimens is evaluated using X-ray computed tomography (XCT) and results are shown in Figure 6.8(B). Clearly, when the designed strut thickness is 150 μm, more than 2.5% of the struts

are found to be broken in the as-printed state. As the strut thickness increases to 200 μm or above, the fractions of unconnected struts are below 1%. Moreover, we also unveil the orientation dependency of the unconnected strut relative to the build plate in Figure 6.8(C). For V1 lattice, more than 16% of the struts are unconnected when the build orientation is 20° or below and the probability of unconnectivity is lower than 9% in other printing orientations. For V2 lattice, the probability of unconnectivity is 9% when the build orientation is 20° or below and lower than 3% when the struts are printed in other orientations. The orientation dependency of the unconnectivity is significantly weakened when the strut thickness increases to 200 μm or above.

These results are very similar to the findings by Zhang et al. [198]. They confirmed there was a processing limit for the electron beam melting (EBM) technique, below which there was a high probability of strut unconnectivity [198]. They also proved the low-angle struts were more likely to be unconnected than the high-angle struts [198]. Here, we confirm the processing limit also exists for the L-PBF technique. When the struts are printed with the same layer thickness, the minimal printable thickness for L-PBF ($\sim$ 200 μm in this work) seems to be lower than that for EBM ($\sim$ 400 μm in work by Zhang et al. [198]), which likely results from the larger spot size of the EBM technique [35]. The unconnected struts appear to be present in most of the printed structures but the influence of these unconnected struts on the fatigue fracture processes of the Voronoi structures remains largely unclear, and this will be rationalized in Sec. 6.4.1.

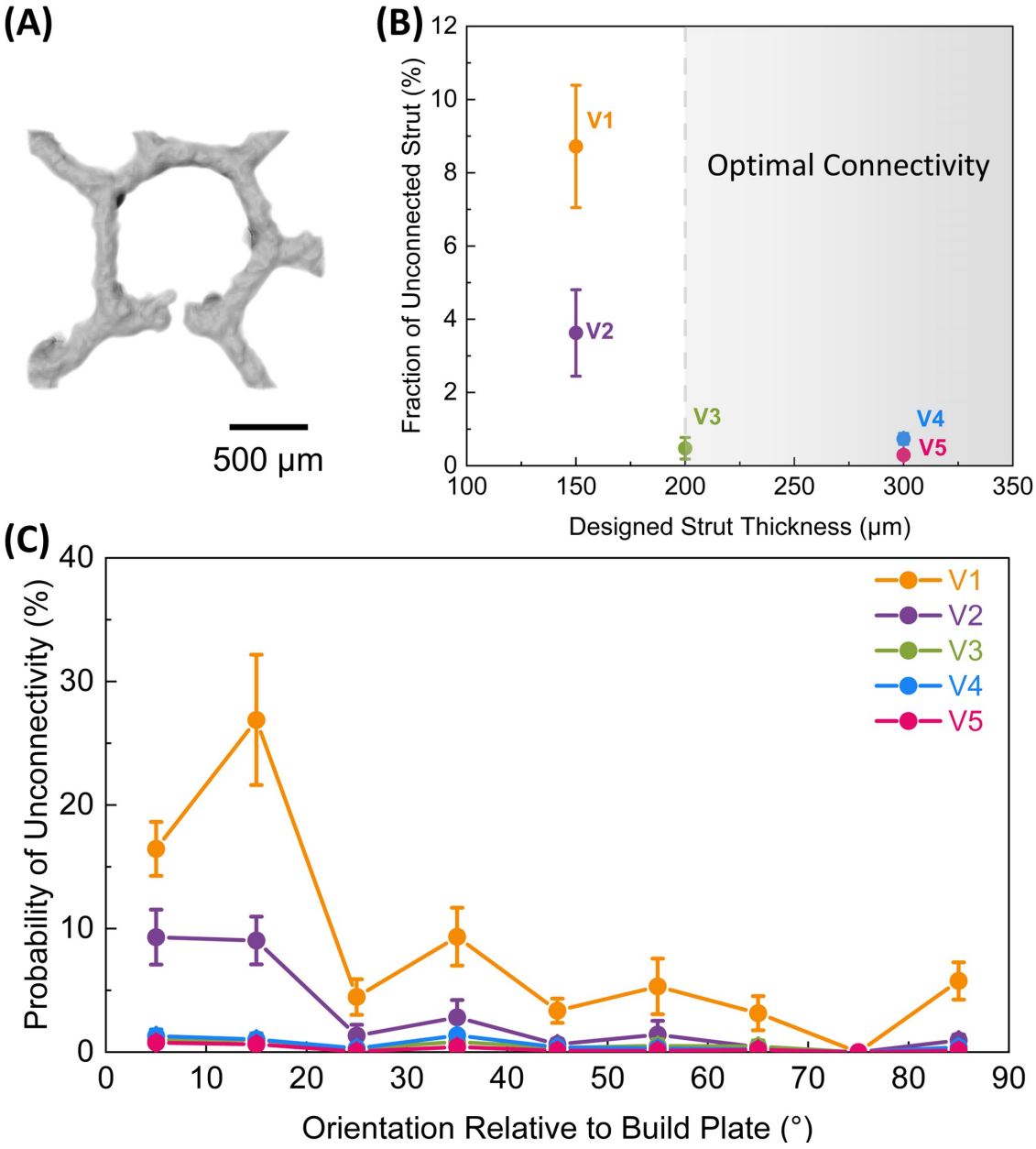


Fig. 6.8 (A) An example of a unconnected strut after manufacturing. (B) Fraction of unconnected strut against the designed strut thickness for all Voronoi structures. (C) Probability of unconnectivity vs. orientation of strut relative to build plate.

6.4 Discussion

6.4.1 Duality of Fatigue Fracture Process

The failure process during cyclic loading is depicted in Figure 6.9. Here, we take the V4 lattice tested at $0.6\Sigma_Y$ as an example. Initially, the maximum strain gradually accumulates as the number of cycles increases and no strut failure can be observed. At around 90% of cycles to failure, initial strut failure occurs triggering the collapse of the structure, which leads to a rapid increase in maximum strain. The initially failed struts are subject to susceptible fracture conditions and govern the mechanical integrity of Voronoi lattices.

We proceed by capturing the strut failure events in all the tested samples. Figure 6.10 shows the failure locations of V3, V4, and V5 lattices at different applied stresses. Strut failures can be observed consistently at the same locations for these structures, which suggests deterministic deformation behaviour is not only limited to the V4 lattice. The deterministic strut failures give rise to the low fatigue scatter of these structures in Figure 6.3(C).

FEA calculations are performed to elucidate the origin of the deterministic failure. We hypothesize that the unconnected struts have a great influence on the load distribution within the lattice structure, which likely governs the strut failure location [125]. Hence, struts are randomly removed from the designed files based on the quantification of the probability of strut unconnectivity in Figure 6.8(C). We examine three configurations for each structure. Results are shown in Figure 6.11. For each

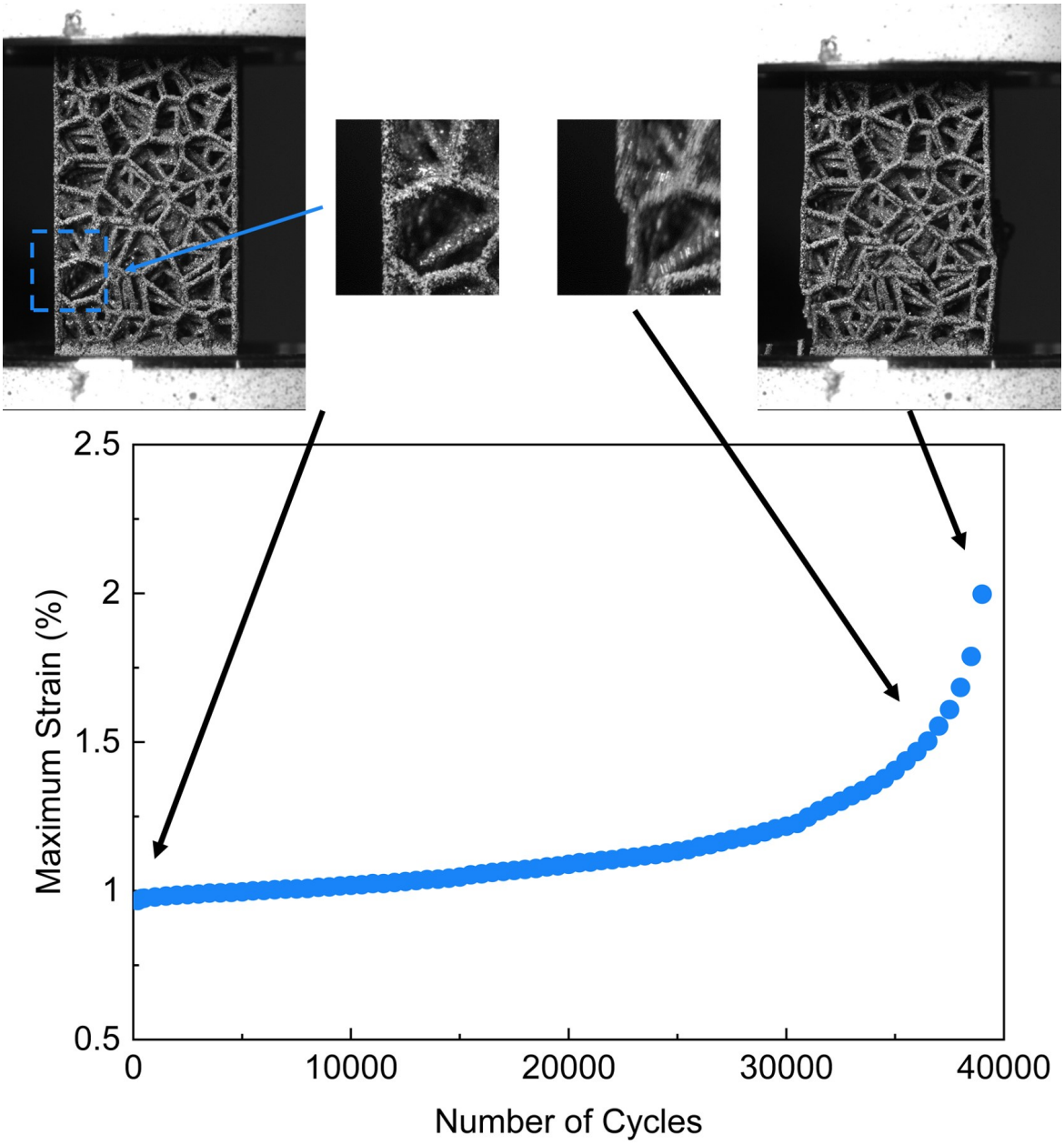


Fig. 6.9 Plot of the variation of maximum strain vs. number of accumulated fatigue cycles (R = 0.1, frequency = 30 Hz, maximum stress = 0.6 Σ_Y), and associated in-situ surface observations on the deformation behaviour of V4 lattice using digital camera. Note that no strut failure was observed at the surface before 35000 cycles (>90% of life) and the final collapse is associated with the initial strut failure.

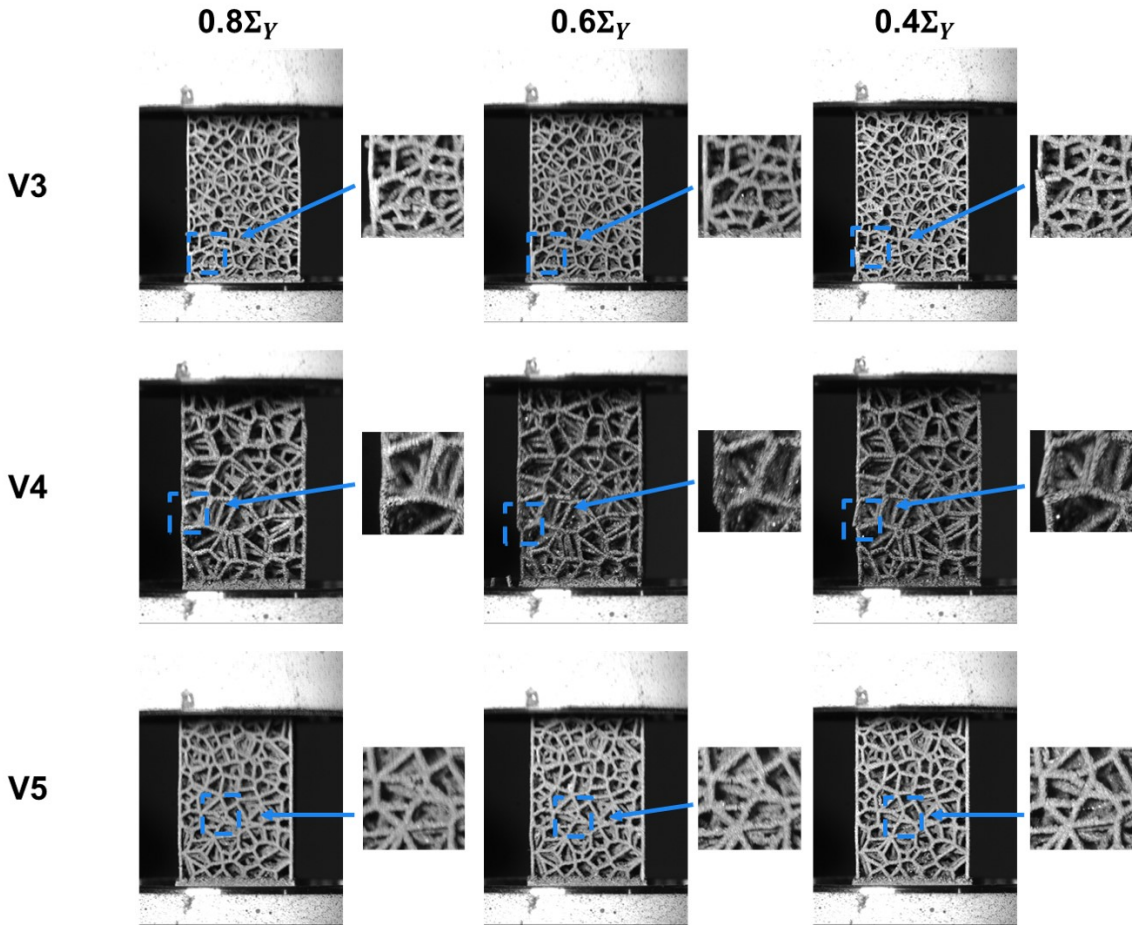


Fig. 6.10 Macroscopic observations on the initial strut failures of V3, V4, and V5 lattices at different maximum stresses confirming that they occur at around the same position within each structure.

specimen, the stress distributions are consistent across different configurations, which further confirms the deterministic strut failure results from the high lattice connectivity of these structures. This indicates deterministic deformation behavior during cyclic loading can be expected in any Voronoi structure with a designed strut thickness of 200 μm or above, or potentially any stochastic lattice with an optimal strut connectivity.

The deterministic failure of these Voronoi structures is also very different from the stochastic fracture process of the periodic structures [49, 68, 333, 153]. The initial strut failure seems to be primarily guided by the designed geometry of the lattice structure rather than the presence of processing-induced defects. A controllable fatigue fracture process may be attained in these Voronoi structures by tailoring the geometrical design.

Moreover, the failure locations of V1 and V2 lattices are identified as shown in Figure 6.12. In contradiction with deterministic deformation behaviour, strut failures occur randomly within these structures. However, this stochastic failure process does not necessarily result in a high fatigue scatter (see Figure 6.3(C)). V1 lattice shows fatigue scatters of $> 30\%$ at all applied stresses while the V2 lattice exhibits comparable scatters in fatigue life as the other structures ($< 15\%$). This suggests the random design of Voronoi lattices offers some degree of tolerance to the defects within the structure.

We then perform FEA calculations on three configurations of each of the V1 and V2 lattices after the same strut removal procedure as described above. Results are shown in Figure 6.13. The stress concentrations are randomly distributed across the three configurations of each structure. This suggests when the designed strut thickness is 150

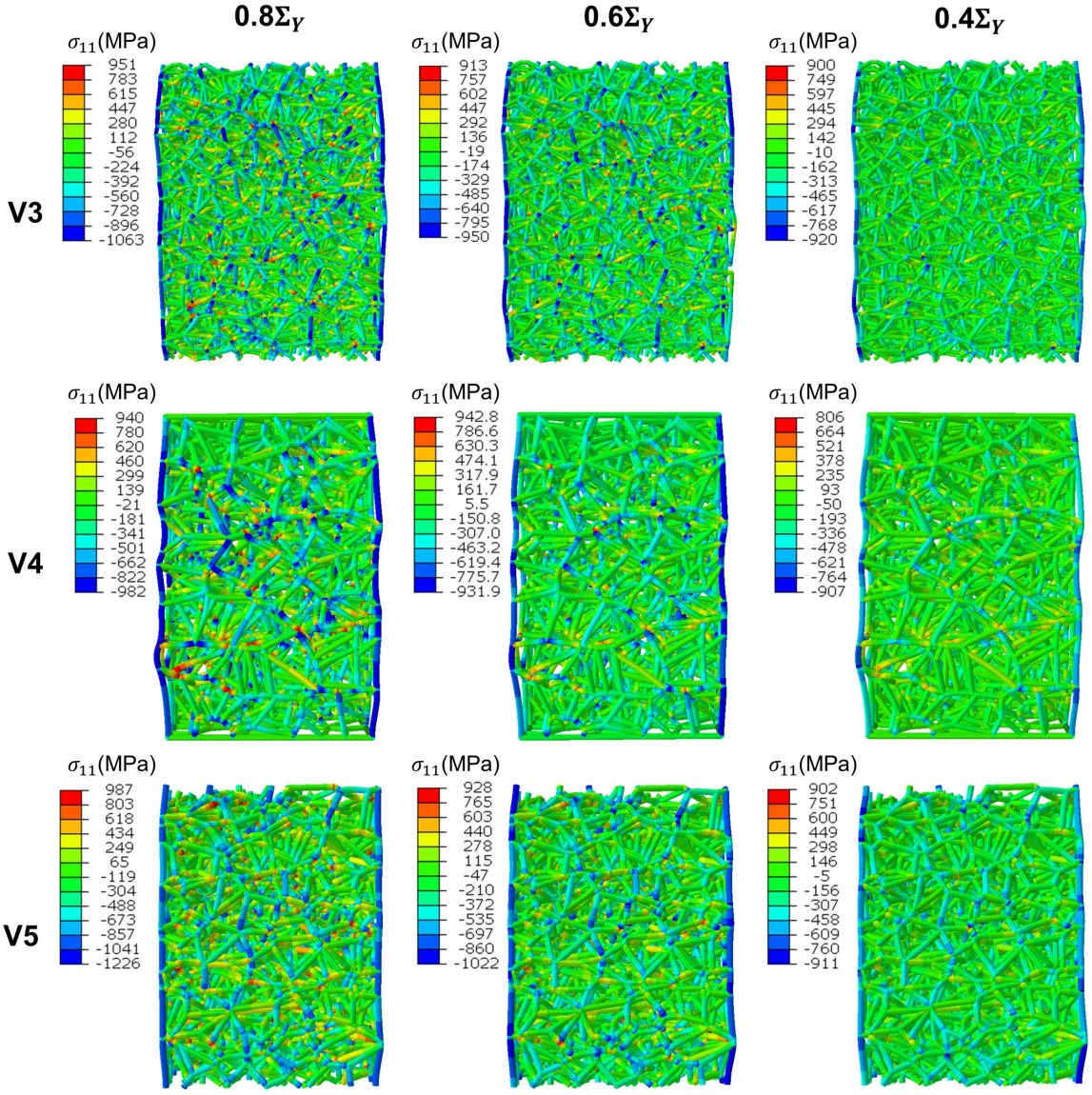


Fig. 6.11 FEA calculation of the V3, V4, and V5 lattices at different maximum stresses.

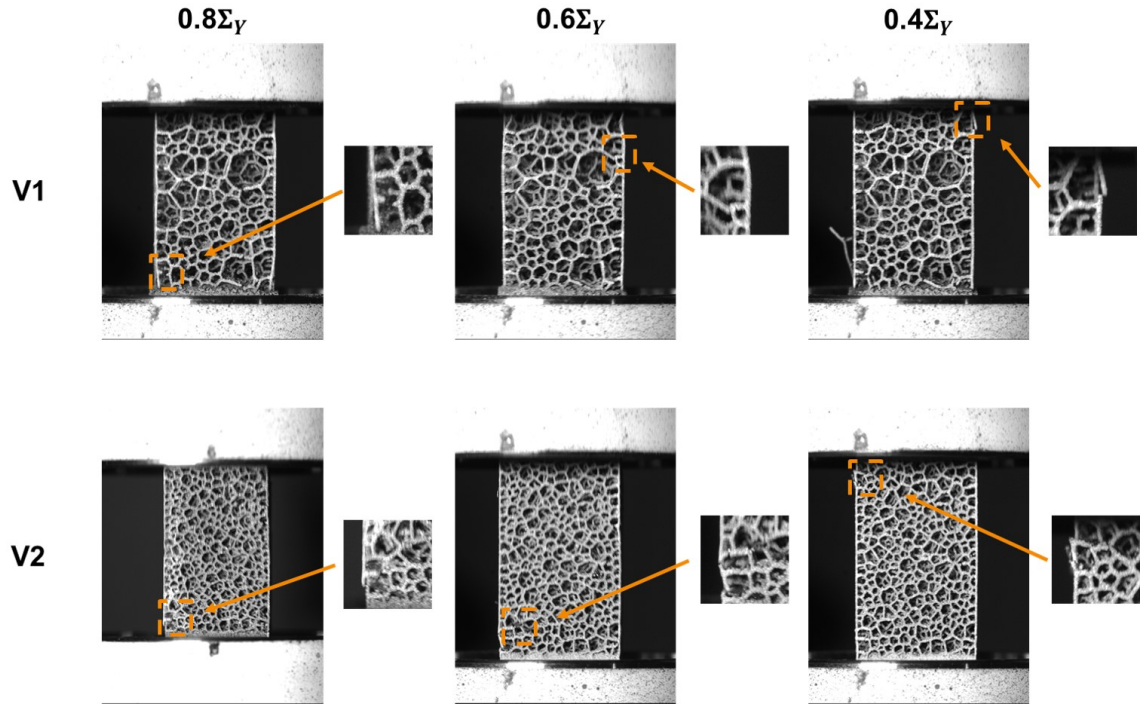


Fig. 6.12 Macroscopic observations on the initial strut failure of V1 and V2 lattices at different maximum stresses confirming that they occur randomly within each structure.

μm, the poor strut connectivity disrupts the stress distribution within the structure resulting in a stochastic strut failure process.

These results align with the previous report on the cubic lattice, where it has been shown the strut failure under cyclic loading is disrupted by the unconnected struts and the normalized fatigue strength of the cubic structure has been reduced by a factor of about 2 [153]. The commonality between our results and the work on the periodic cubic lattice suggests that the stochastic strut failure events resulting from the high level of unconnected struts may be conceived in all types of meta-biomaterials.

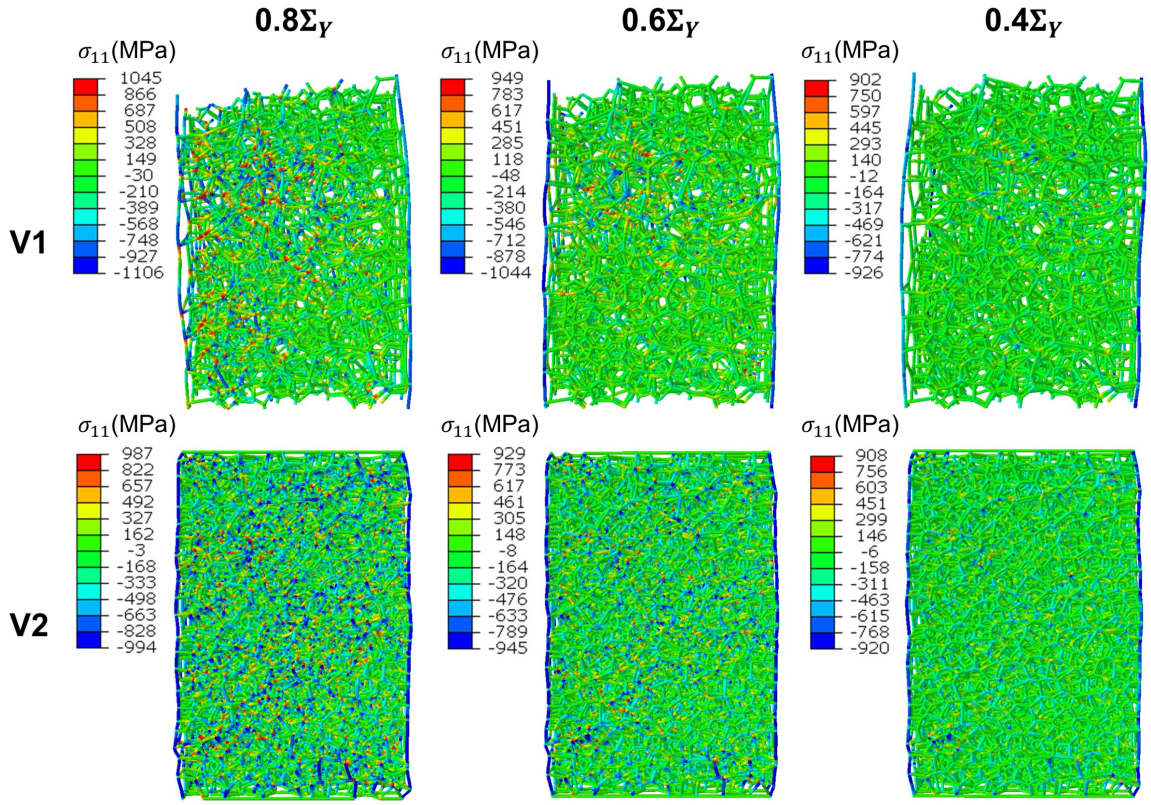


Fig. 6.13 FEA calculation of the V1 and V2 lattices at different maximum stresses.

6.4.2 Rationalization of the Role of Defects during Cyclic Loading

What remains in question is how the other processing-induced defects characterized in Sec. 6.3.3 contribute to the fatigue fracture process. Surface defects can act as microcracks raising the stress concentration in the strut when the strut is subject to tension or bending [49, 81]. Previous research shows poor surface quality can shorten the fatigue lives of metallic lattices but has negligible influence on the strut failure location [49, 195]. This is further supported by the macroscopic observations of the strut failure in this work. Even though the R_a value of the downward-facing surface of the horizontal strut is more than three times higher than that of the vertical strut in the V4 lattice, the initial strut failure observed was found to be a vertical strut. This is consistent across the five specimens. The strut failure location is more or less governed by the stress distribution within the structure.

Furthermore, the porosity evolution during the fatigue fracture process has also been monitored. The tests are performed on the V4 lattice at a maximum stress $\sigma_{\max}$ = 0.6 Σ_Y until initial strut failures occur. We interrupt the tests at every 20% of the cycles to failure based on the result in Figure 6.9 and XCT scans are acquired during the interruption as well as before and after the tests – a total of 6 XCT scans are performed. Figure 6.14(A) shows the strain evolution during the interrupted tests. When the maximum strain reaches around 1.5%, the struts start to fail, which agrees with the result in Figure 6.9. The average pore size also shows minimal variation

across the fatigue fracture process (see Figure 6.14(B)). To understand how pores contribute to the failure of individual struts, we reconstruct the porosity distribution within the struts that initially fail prior to the test. Results are depicted in Figure 6.14(C). All the initially failed struts are free of pores, which suggests porosity has minimal contribution to the strut failure under cyclic loading. This is then confirmed by the fractography of initially failed struts after the test. No pores can be observed on the fracture surfaces of any failed strut confirming porosity has negligible influence on the fatigue performance of lattice material.

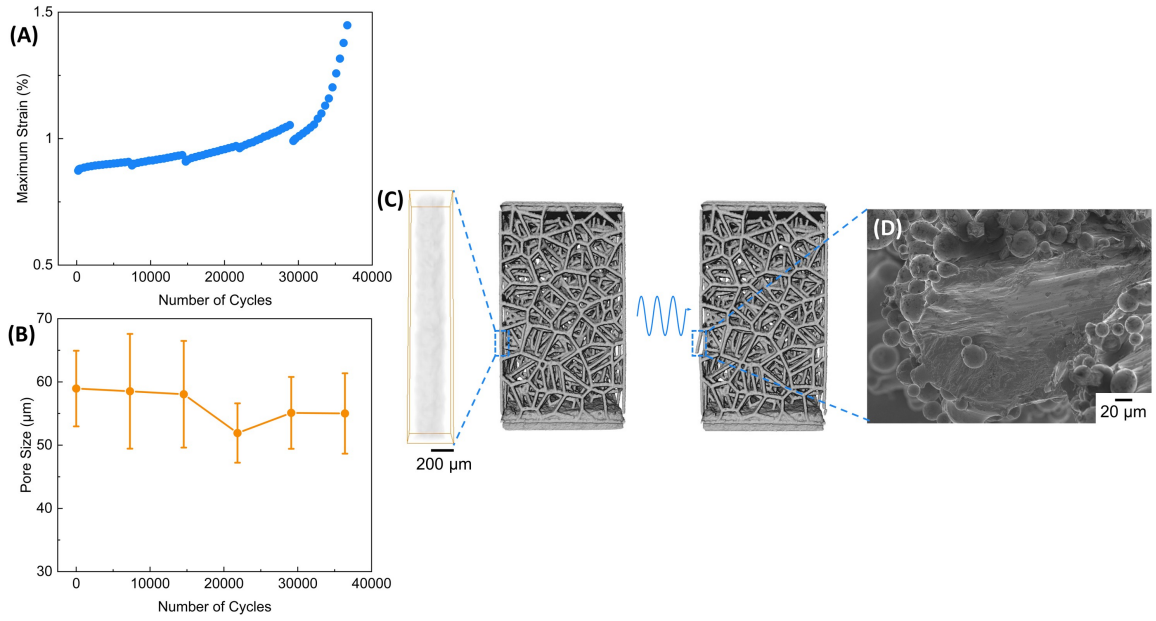


Fig. 6.14 Results of interrupted fatigue tests together with XCT for V4 lattice. (A) shows the variation of maximum strain vs. number of accumulated fatigue cycles until initial strut failure. (B) illustrates the associated variation in pore size vs. number of accumulated fatigue cycles. (C) shows the volume of V4 lattice before testing and after initial strut failure reconstructed from computed tomography. The initially failed strut was used for pore size and distribution analysis. (D) shows the fracture surface of the initially failed strut.

The variation in strut thickness can give rise to uneven stress distribution along the strut [345, 346, 69]. For example, in the V4 lattice, the thickness at the central part of the strut is around 250 μm whereas the thickness at the junctions can reach up to 350 μm (see Figure 6.5(B)). When they are subjected to the same load, the stress would differ by 96%. However, this thickness variation can be found in almost all the struts, which limits its effect locally along the strut and thus has marginal significance on the determination of critical strut failure.

Additionally, morphological differences between the printed specimens and the CAD design lead to unpredictable stress localization and even different failure mechanisms [139, 347, 348]. The level of dimensional accuracy across the five specimens is similar and the heterogeneity arising from the manufacturing is random within each sample. However, the randomness of the deviation still gives rise to deterministic strut failure processes (see Figure 6.10), which suggests that strut failure is largely regulated by the intrinsic design of the lattice.

The presence of these processing-induced defects has a complex effect on the damage localization in the lattice structure and has been studied broadly in antecedent research [49, 195, 345, 346, 69, 139, 347, 348]. Nonetheless, in this work, none of these aspects show evidence of determining pivotal strut failure and thus has limited influence on the bimodal deformation behaviour.

6.4.3 Damage Evolution during the Cyclic Deformation Process

To unravel the deformation process in three dimensions, interrupted fatigue tests together with XCT are employed to identify the strut failures. Results are shown in Figure 6.15. No strut failure can be observed until around 95% of the cycles to failure, which confirms the results from the digital camera. On the other hand, strut failure can be found both on the exterior and the interior of the lattice indicating the initial strut failure observed from the digital camera may be the result of sequential strut failures.

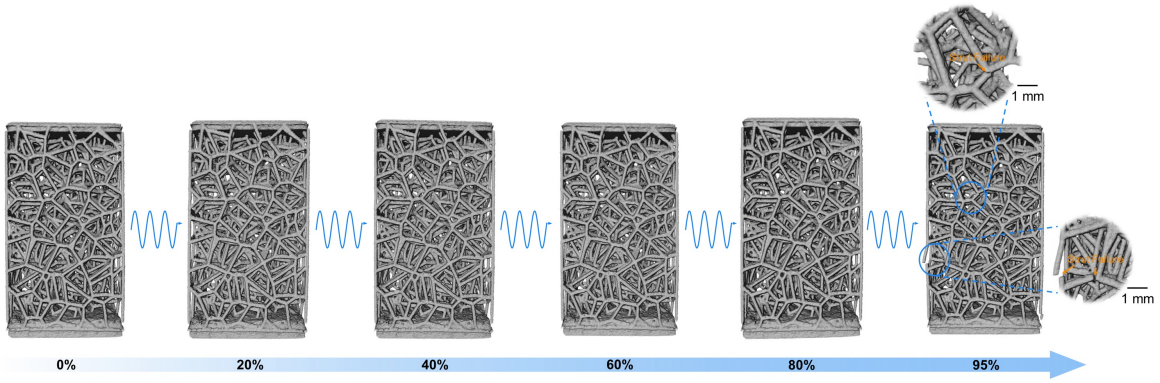


Fig. 6.15 3D rendered XCT images of the V4 lattice during the interrupted fatigue tests ($R = 0.1$, frequency $= 30$ Hz, $\sigma_{\max} = 0.6\Sigma_Y$).

Failure of the Voronoi structure under cyclic loading occurs by strut bending and stretching or, when loaded in compression, by elastic buckling of the strut [49, 326]. To provide further insight into the failure of each individual strut, finite element analysis (FEA) of the V4 lattice is performed. Struts are randomly removed based on the probability of unconnectivity as a function of the build orientation in Figure 6.8(C).

Figure 6.16 shows the distribution of axial stress σ_{11} and bending moment along the strut M_1 at $\sigma_{\max} = 0.6\Sigma_Y$. The loading conditions of the three failed struts are clearly revealed. Strut 1 deforms primarily under compression while Strut 2 and 3 are largely under bending. Although it is well known that bending of the strut causes strut failure [201, 306], compression doesn't necessarily result in strut fracture [49], which calls into question the failure process of Strut 1.

We proceed by assessing the fracture conditions near Strut 1 with the XCT data since only the strut failure nearby would significantly influence the loading condition of Strut 1 [349, 350]. A fractured strut is observed behind Strut 1 and the FEA calculation confirms the fracture results from the bending of the strut. The strut is subjected to the highest tensile stress among all the struts nearby, which governs the most susceptible fracture condition. We then remove this strut and re-examine the loading condition of Strut 1 after the prior strut failure. The strut is still primarily subject to compression and the effective length of the strut l has been increased from 2.40 mm to 3.73 mm, which leads to a more susceptible buckling condition. The Euler buckling load P_E, which is given by

$$P_E = \frac{n^2 \pi^3 E_s r^4}{4l^2} \tag{6.5}$$

where E_s is the axial modulus of the strut, r is the radius of the strut, and the factor n depends on the buckling mode, is lowered from 75 N to 31 N if the strut is assumed to be pin-jointed ($n = 1$). These correspond to engineering stresses of 1060 MPa and

440 MPa, respectively. The former value is above the yield strength of AM Ti-6Al-4V ($\sigma_y \approx 900$ MPa) whereas the latter value is no more than 50% of the yield strength. Hence, the buckling failure of Strut 1 would only occur after the strut behind Strut 1 fails. To conclude, the strut behind Strut 1 fails primarily due to bending, which increases the effective length of Strut 1 by 55%. This reduces the Euler's critical load well below the yield strength of the material resulting in the buckling failure of Strut 1.

It is also worth noting that the analysis above has ignored the influence of surface defect, strut thickness variation, and geometrical deviation. The presence of these defects may increase the local compressive stress, which leads to earlier buckling failure of the strut [351].

6.4.4 Analysis of Fatigue Failure Process

The failure of a lattice material that contains unconnected struts can be analyzed following the approach adopted by Maiti et al. [352] and Gibson and Ashby [329] and confirmed by the FEA by Fleck and Qiu [353]. They assume each of the unconnected struts as a "macroscopic crack" and the size of a crack is equivalent to the cell size of the lattice. When the unconnected struts form together, the size of the cluster of unconnected struts is determined by the number of unconnected struts that form together. These authors also demonstrate that if the structure contains a crack-like defect arising from a number of adjacent unconnected struts, the maximum tensile

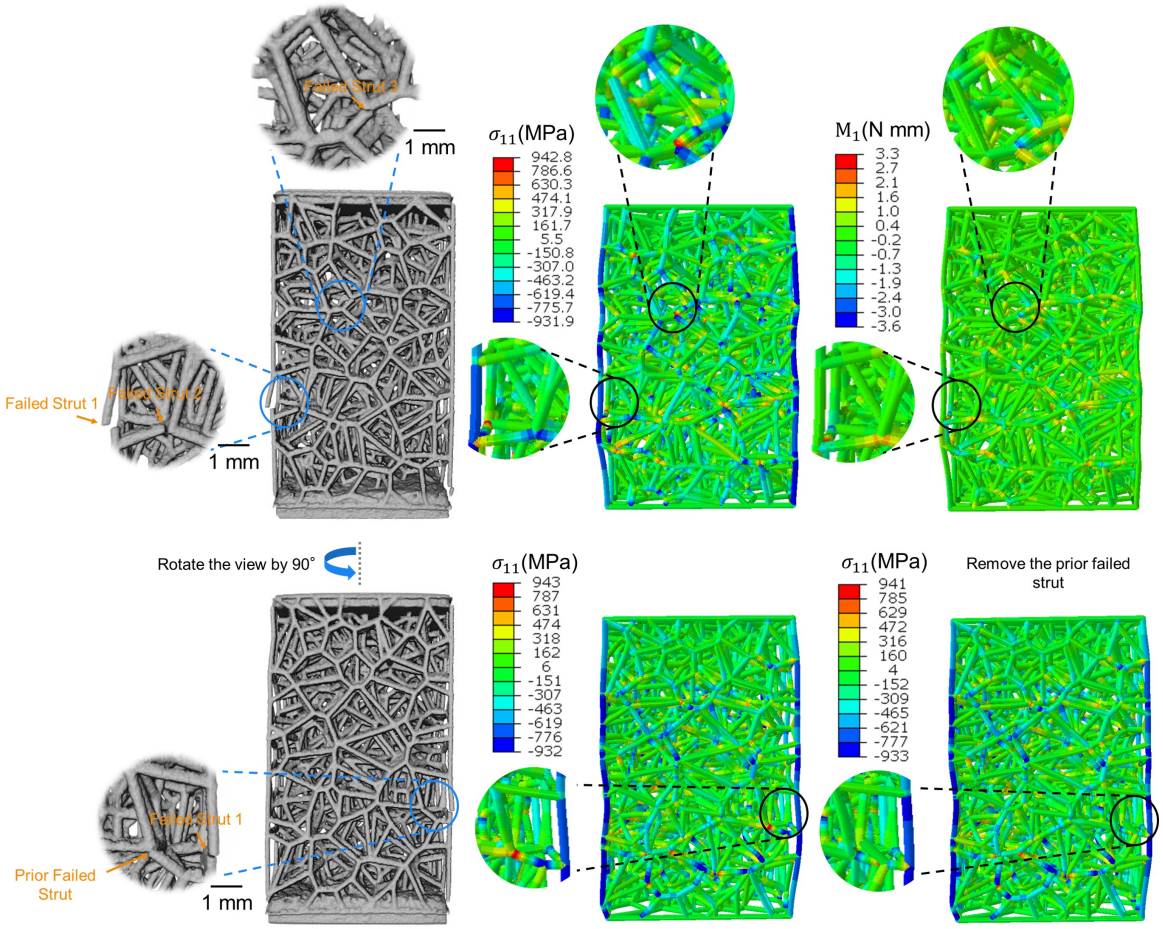


Fig. 6.16 FEA calculation of the V4 lattice at $\sigma_{\max} = 0.6\Sigma_Y$. The loading condition of each failed strut is revealed to shed light on the failure process.

stress in a strut adjacent to the crack tip $\sigma_{\max}$ is [352, 329, 353]

$$\sigma_{\max} = \frac{K_I}{D\sqrt{l}}\left(\frac{\rho_s}{\rho}\right)^2 \tag{6.6}$$

for a bending-dominated structure under mode I loading, where K_I is the mode I stress intensity factor, D is a constant that depends on the detailed structure of the lattice and l is the characteristic strut length. Under cyclic loading, the maximum stress range, $\Delta\sigma_{\max}$, is related to the stress intensity factor range, ΔK_I, through the

same relationship. Now assume that the body contains a penny-shaped crack of radius a which arises from m adjacent unconnected struts, such that $m \approx (\frac{a}{l})^2$, then

$$\Delta\sigma_{\max} = \frac{2\Delta\sigma}{D\sqrt{\pi}} m^{\frac{1}{4}} (\frac{\rho_s}{\rho})^2 \tag{6.7}$$

where $\Delta\sigma$ is the applied macroscopic stress range. For a lattice with no unconnected struts, the maximum stress range in any strut in the structure is given by

$$\Delta\sigma_{\max} = \frac{\Delta\sigma}{F} (\frac{\rho_s}{\rho})^2 \tag{6.8}$$

where F is a constant that depends on the detailed topology of the lattice structure. Note that the location of the strut that experiences this maximum stress range is the same for all the samples with the same structure. Failure will occur first in the strut that experiences the highest stress range and this will determine the location of the failure and the subsequent evolution of the failure process. This will be in a deterministic location if the value of $\Delta\sigma_{\max}$ is given by Equation 6.7 is greater than that given by Equation 6.6, but it will be in a random location if the converse is true since the location of the unconnected struts occurs randomly in the structure.

The crux of the matter is that for a given type of lattice, the transition from deterministic to stochastic only depends on the number of adjacent unconnected struts m, and is independent of other parameters, such as the size of the cells or the relative density of the lattice. The value of $m = m_T$ at this transition, above which the number of unconnected struts m is sufficient to lead to a higher $\Delta\sigma_{\max}$ value given by Equation

6.6 than that given by Equation 6.7 and disrupt the strut failure location, is very sensitive to the ratio of the two geometric parameters D and F. Whether the failure is stochastic or deterministic is then determined by the probability that a cluster consisting of more than m_T unconnected struts occurs in the body to form a defect that is perpendicular to the direction of the applied load. We do not evaluate this point further here, but the form of the above relationships helps to explain a number of experimental observations.

For the structures with strut thicknesses greater than or equal to 200 μm (i.e. V3, V4, and V5), the fraction of unconnected struts is low, and the probability of there being a cluster of defects in excess of m_T is extremely small. Thus, Equation 6.7 determines the fatigue failure for all samples, the scatter is small and the location is deterministic. For specimen V1 with a strut thickness of 150 μm, however, there is a high number of unconnected struts and there is a strong probability of finding a cluster significantly in excess of m_T. This results in a significantly high scatter and the location of the failure process within the lattice, as well as a lower-than-expected fatigue strength than suggested by the projection of the deterministic results to the lower density of the V1 specimens (as shown in Figure 6.3(B)). Specimen V2, which also has a strut thickness of 150 μm, contains a much smaller fraction of unconnected struts. The experimental results suggest there is a high probability of clusters of defects existing, but a much lower probability of clusters existing that are comparable with those that are present in specimen V1. Since the stress range, and therefore the fatigue strength, are not very sensitive to the precise value of m, we see only a small scatter in

fatigue strength about a value that is comparable with the strengths for the specimens with larger strut thicknesses (see Figure 6.3(B)), but the location of the failure process can be randomly located within the structure.

To further confirm the influence of unconnected struts on the fatigue properties of Voronoi lattices, we normalized the maximum applied stress with the yield strength to evaluate the normalized fatigue strength of the lattice – one of the key parameters to assess the fatigue performance of meta-biomaterials [74, 195]. Results are shown in Figure 6.17(A). The normalized S-N curve for the V1 lattice is much lower than those for the other lattices and the curves for the other specimens largely overlap each other. This is similar to the findings in the previous studies [48, 152]. The normalized S-N curves for the lattices with the same topology are very similar when they are of similar relative densities [43]. This has been further validated by the normalized fatigue strength of the lattices in Figure 6.17(B). V2, V3, V4, and V5 lattices exhibit a similar normalized fatigue strength above 0.30, which is significantly higher than that of the V1 lattice (0.20). The substantially lower normalized fatigue strength of the V1 lattice results from the high probability of clusters of unconnected struts above the critical size m_T.

The above results prove that meta-biomaterials with random geometries exhibit a certain tolerance to manufacturing defects under cyclic loading. When the clusters of unconnected struts are smaller than the critical size, these unconnected struts have minimal influence on the fatigue lives of the lattice structures. The initial strut failure locations can be predicted by computational modelling, and thus the fatigue

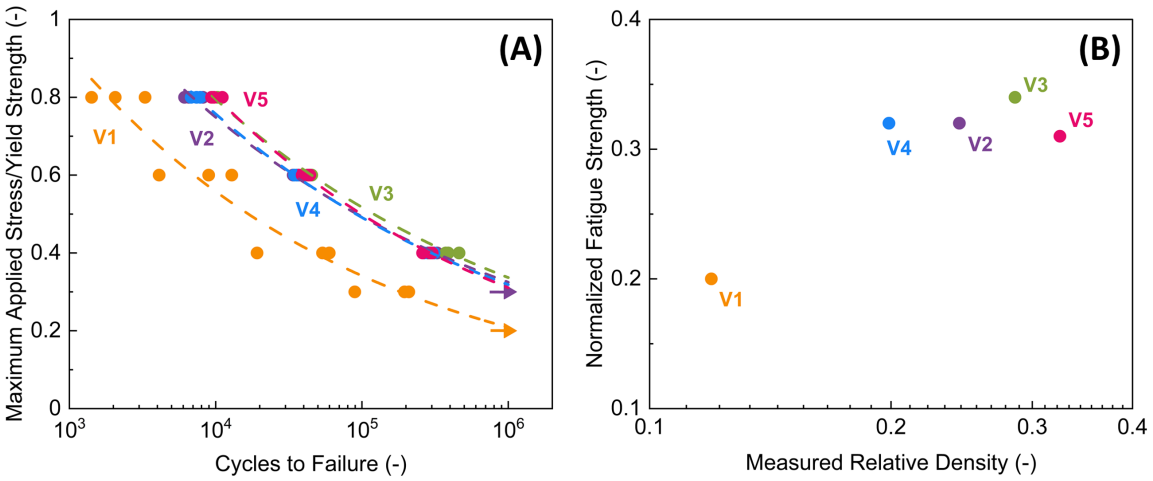


Fig. 6.17 (A) Maximum applied stress normalized with the yield strength against cycles to failure for the lattices manufactured in this work. (B) Correlation between normalized fatigue strength at 10^6 cycle and measured relative density for the Voronoi structures.

fracture processes of the structures can be controlled by mindful geometrical design to attain consistent mechanical durability. On the other hand, the periodic structures are expected to have a much lower tolerance to defects. The stress distribution is largely consistent across different unit cells and thus the presence of unconnected struts is more likely to give a higher $\Delta\sigma_{\max}$ value from Equation 6 than that from Equation 6.7, which disrupts the strut failure events and gives inconsistent fatigue properties.

6.5 Summary and Conclusions

In this work, we unveil the bimodal fatigue behaviour of metallic lattices. Voronoi structures with a range of strut thicknesses and numbers of cells per unit volume are fabricated. We prove that for structures with a strut thickness of 200 μm or above, the strut failure location is largely consistent. As the strut is thinned to 150 μm,

the strut failure process becomes stochastic leading to inconsistent fatigue lives. The processing limit of the laser powder bed fusion technique contributes to the different deformation behaviours. It has also been shown the fatigue scatter may be reduced as the cell number density increases. Different from monolithic materials, porosity has a minimal influence on the fatigue fracture process in metallic lattices. These results enrich our knowledge of lattice materials and form the foundation for the development of fatigue-tolerant design.

Chapter 7

Conclusions and Future Work

7.1 Conclusion remarks

This research aimed to study the fatigue behaviour of 3D-printed architected materials and their constituent elements. Ti-6Al-4V alloy was chosen as the parent material for its broad application in the aerospace and biomedical sectors. The correlation in the understanding of fatigue behaviour between monolithic and architected materials was established by integrating experimental efforts with computational modeling. Critical insights are summarized here to guide the design of mechanically durable intricate components.

The size effect phenomenon of the fatigue behaviour of the constituent elements was identified and quantified. Smaller elements demonstrated lower fatigue resistance than their larger counterparts as a result of better surface finish. The differences in their fatigue lives became more significant at higher applied stresses as the fracture

process was more dominated by the initiation stage. In addition, the larger elements exhibited double fatigue scatter as compared to the smaller ones owing to the higher contribution of porosity to the fatigue fracture process.

The orientation dependency of the fatigue behaviour of the constituent elements was confirmed through an assessment of seven different build orientations relative to the build plate. The 75° element exhibited the optimal fatigue resistance resulting from the superior surface quality and the small proportion of grains near-parallel to the loading direction. When the build orientation was 30° or below, the fatigue crack initiation sites were on the downward-facing surface due to the high surface roughness in the overhang regions. Above 45°, the cracks started to initiate from the otherward-facing surface. It was also shown that the influence of pore clusters on the surface-initiated fatigue fracture process could be described by Kirsch's Solution under elastic deformation. The high fatigue scatter of the 75° specimen was governed by the large differences in pore size.

The influence of build orientation on the elastic, plastic, and fatigue properties of a stretching-dominated octet-truss lattice was elucidated later. Two types of scenarios were evaluated: (1) the lattice was vertically built and (2) the lattice was printed 30° relative to the build plate. Analytical calculation was developed to consider the orientation effect of the strut. This was then validated by the finite element analysis (FEA) simulation. The results suggested the fatigue strength of the octet-truss lattice could be enhanced by around 50% at 10^6 cycles by carefully choosing the build orientation.

To confirm the significance of the understanding of constituent elements on the fatigue behaviour of architected materials, we evaluated experimentally the fatigue fracture process of bending-dominated body-centred cubic (BCC) and stretching-dominated face-centred cubic (FCC) structures. We proved that either uniform deformation or shear fracture could occur in the BCC structures while the FCC structures only failed by the formation of shear bands. At low strut thickness-to-length ratios, the axial compression of the strut contributed more to the cycle deformation process of the BCC structures resulting in the formation of continuous plastic deformation zones at high applied stresses. As the strut thickness-to-length ratios increased, strut bending became more dominant in the deformation governing stress localization in the structure, which led to shear failure. These results suggest that the fatigue failure of architected materials is highly determined by the local stress state within the structures.

This work was then extended to assess the influence of design variables on the fatigue behaviour of architected materials. We designed and printed five Voronoi structures with a range of strut thicknesses and numbers of cells per unit volume. A minimal strut thickness of 200 μm was identified for the laser powder bed fusion technique, above which the strut failure of the lattices occurred more or less at the same location during cyclic loading. As the strut was thinned to 150 μm, random strut failure was observed leading to high fatigue scatter. The fatigue scatter seemed also to be reduced as the cell number density was increased.

In summary, this study has correlated the knowledge of the fatigue behaviour of 3D-printed architected materials with constituent elements. Mindful selection of design variables was shown to be critical for the design of fatigue-tolerant components.

7.2 Future Work

The current research prompts our curiosity about several further questions including (1) improving the analysis of the inconsistent fatigue properties; (2) developing frameworks for assessing the fatigue fracture processes of architected materials; and (3) confirming the practicality of fatigue-tolerant design.

7.2.1 Statistical Analysis of Fatigue Scatter

As suggested above, the scatter in fatigue life is one of the key factors in determining the reliability of mechanical components. However, very few reports on AM materials have considered the consistency in fatigue properties and the research is especially lacking in the field of architected materials [107, 94].

The analysis of the inconsistent fatigue properties in this study is limited by the number of repeated tests at each testing condition. A maximum of three repeats at each condition can only inform the general trend of the fatigue scatter. More than 10 repeats at each condition are needed to derive a solid quantitative analysis. One of the most popular statistical approaches to analyze fatigue data is the two-parameter

Weibull distribution following:

$$f(N) = \gamma N^{(\gamma-1)} \exp(-N^{\gamma}) \tag{7.1}$$

where γ is the shape parameter and N is the number of cycles to failure. It is assumed in the analysis that the fatigue strength of the component is governed by the most detrimental defect. The probability of fatigue failure exceeding a certain number of cycles to failure can be evaluated. The approach is also applicable to assess the scalability of the parts.

It is noteworthy that most of the statistical analysis requires extensive amounts of experimental data. The results of this study can serve as the basis for future researchers to decide which data warrants further analysis. For example, the size effect phenomenon in Chapter 3 may be of interest since the higher fatigue scatter by the larger specimens can hinder the upscaling capability of AM techniques. Additional efforts can also be made on the stochastic failure of Voronoi structures in Chapter 6 to quantify the defect tolerance after incorporating randomness in the lattice design.

7.2.2 Development of Fracture Mechanism Map

The work presented in Chapter 5 reported different cyclic deformation behaviours of architected materials through the assessment of BCC and FCC structures. While the lattice topologies were chosen for their simplicity in design, the key insights are expected to be generalized through further numerical analysis. It has been proven

that the failure mechanisms of the lattice structures are strongly correlated with the unit cell type and design variables. FCC and BCC structures exhibit distinct failure modes while the failure behaviour in BCC structures may vary based on the strut thickness-to-length ratio. The fatigue failure process in architected materials is highly dependent on the local stress state. Thus, micromechanical analysis of the strut bending, buckling, and axial tension can be used to inform the failure of the structure.

7.2.3 Validation of Fatigue-tolerant Design

Several design principles have been derived from this study. Yet, these guidelines need to be experimentally validated to confirm their practicality. Based on Chapter 4, one can conclude that struts printed 0° - 30° relative to the build plate need to be removed in lattice design owing to their poor surface quality. This is further supported by our results in Chapter 6. These low-angle struts are also more prone to be unconnected in the as-printed states. Furthermore, a minimal strut thickness of 200 μm is identified to govern the consistency in fatigue properties. Implementation of these principles into future design of architected materials would verify the robustness and creditability of this research.

List of figures

1.1 Examples of metallic components made by AM including Alloyed rocket nozzle adapted from ref. [10], General Electric GE9X high-bypass turbofan adapted from ref. [11], Captiva TriboLOX-l titanium lumbar cage adapted from ref. [12], Optisys radio frequency antenna adapted from ref. [13], Alloyed automotive light-emitting diode (LED) headlight adapted from ref. [14], and Eplus3D heat exchanger adapted from ref. [15]. 2
1.2 A schematic illustration of the powder bed system. 3
1.3 Three classes of commonly used architected materials. Adapted from ref. [43]. 7

2.1 Maximum applied stress vs. cycles to failure for AM Ti-6Al-4V against conventionally manufactured counterparts. Data provided includes Ti-6Al-4V prepared by L-PBF [61], L-PBF and then heat treatment (HT) [62], EBM [63], EBM and then hot isostatic pressing (HIP) [64], DMLS [65], DMLS and then HIP [64], forging [66], and wrought [65]. 15
2.2 (A) Maximum and minimum strain evolution of a BCC Ti-6Al-4V lattice under cyclic loading. (B) The cyclic ratcheting and fatigue damage strains of the lattice. 17
2.3 Fatigue strength of AM titanium lattices normalized by the yield strength as a function of the relative density. Data was adapted from [81, 80, 85, 78, 79, 72, 83, 82]. 20
2.4 Fatigue failure process of an AM Ti-6Al-4V lattice. Adapted from [90]. 22
2.5 Fatigue failure mode of TPMS structures tested at 0.9 (high) and 0.75 (low) of the yield strength. Adapted from [49]. 23
2.6 Measurement of an internal surface by XCT. Adapted from [113]. . . . 26

2.7 Examples of (A) strut thickness variation, waviness, cross-section irregularity, (B) nodal misalignment, and (C) unconnected strut. Adapted from [7, 121]. 28
2.8 Examples of a keyhole pore, a gas pore, and a lack-of-fusion pore. Adapted from [146, 144]. 32
2.9 Numerical simulations of residual stress accumulation along the build direction. Adapted from [162]. 35
2.10 Electron backscatter diffraction (EBSD) map of an L-PBF 316L stainless steel lattice. Adapted from [181]. 37
2.11 Measured strut diameter of an AlSi10Mg lattice made by L-PBF as a function of the area-specific energy. Adapted from [186]. 39
2.12 Von mises stress distribution for subdivided filleted and conventionally filleted cells. Adapted from [202]. 45
2.13 An irregularly shaped component designed by direct patterning vs. conformal patterning. Adapted from [208]. 47
2.14 Topology optimized 3D cantilever without the consideration of printing orientation. Adapted from [226]. 49
2.15 A schematic illustration of the hierarchy levels of cubo-octet metamaterials. Adapted from [4]. 49
2.16 A schematic illustration of functional gradient design in terms of relative density, unit cell dimension, and unit cell type. Adapted from [237, 239, 240]. 51

3.1 (A) Geometries of the 2 tensile specimens used in this study. (B) Schematic illustrations of laser path along different consecutive layers and laser path along each cross-sectional plane. 60
3.2 (A) Engineering stress-strain curves of AM Ti-6Al-4V at a strain rate of 2×10^{-3} s^{-1}. (B) Elastic modulus, yield strength, ultimate tensile strength, and fracture strain of the 2 specimens under study. Error bars represent the standard deviation from 3 repetitions. 64
3.3 (A) Maximum applied stress vs. cycles to failure for the specimens manufactured in this work. Three measurements are performed per condition. (B) Correlation between scatter in fatigue life and maximum applied stress for different tested specimens. 65

3.4 (A) Schematic illustration of the positions at which the microstructural characterizations are performed in this work. (B-E) Cross sectional microstructure of the 2 specimens under study characterized by EBSD. (F) Average α lath thickness $\pm$ 1 standard deviation of the 2 specimens. 68

3.5 (A) Cross sectional EBSD map and orientation distribution function pole figure of the α lath microstructure of the $\varnothing$ 2.0 mm sample. (B) Texture index of the α lath microstructure of the 2 specimens under study. (C) Schematic illustration of $\beta \rightarrow \alpha$ transformation during the AM process of Ti-6Al-4V. (D) Cross sectional EBSD map and orientation distribution function pole figure of the reconstructed prior-β microstructure of the $\varnothing$ 2.0 mm sample. (E) Texture index and (F) grain size of the reconstructed prior-β microstructure of the 2 specimens. 71

3.6 Longitudinal EBSD map and orientation distribution function pole figure of the reconstructed prior-β microstructure of the (A) $\varnothing$ 1.3 mm sample and (B) $\varnothing$ 2.0 mm sample. (C) Texture index and (D) grain size of the reconstructed prior-β microstructure of the 2 samples. 72

3.7 (A) An example of the comparison between CAD design and computed tomography data. Red regions represent hills and blue regions represent pits. (B) Surface roughness (R_a) of the 2 specimens under study. Error bars represent the standard deviation from 3 repetitions. 74

3.8 (A) 3D rendered XCT images of a $\varnothing$ 2.0 mm sample and pores inside the sample. (B) Projection view of the porosity distribution along the build direction in the 2 specimens under study. (C) Fraction of porosity against the distance from sample surface. (D) $\sqrt{\text{Maximum Projection Area}}$, $\sqrt{A_{\text{p, max}}}$, and number of pores per unit volume of the 2 specimens. Error bars represent the standard deviation from 3 repetitions. (E) Sphericity vs. equivalent diameter of pores detected in this study. (F) $\sqrt{A_{\text{p, max}}}$ of lack-of-fusion pores as a function of the orientation relative to the loading direction. 77

3.9 (A) A segmented cross-sectional XCT slice of a $\varnothing$ 2.0 mm sample. (B) Proportions of average and minimal loading areas of the 2 specimens. (C) Corrected values of elastic modulus, yield strength, and ultimate tensile strength of the 2 specimens under study considering the effective loading area. Error bars represent the standard deviation from 3 specimens. . . 80

3.10 Summary of fatigue fracture behaviours including (A) fatigue crack initiation sites, (B) presence of multiple fatigue crack initiation sites, and (C) presence of porosity near the fatigue crack initiation sites for all the tested samples. 83
3.11 (A) Fatigue striations observed on the fracture surface of a ∅ 2.0 mm sample tested at σ_{max} of 600 MPa. The arrow shows where the striation spacing analysis is performed. (B) Image intensity vs. distance along the arrow shown in (A). Striation spacing is characterized by the distance between the 2 peaks. (C) Correlation between fatigue striation spacing and maximum applied stress for the 2 specimens under study. Shaded area represents 95% confidence interval from 5 repetitions. 85
3.12 (A) An example of the measurement of the distance from the initiation site. (B) Correlation between fatigue striation spacing and distance from the initiation site for the 2 specimens tested at 600 MPa. Error bars represent the standard deviation from 5 repetitions. 87
3.13 (A) An example of the measurement of the length of fatigue propagation path. (B) Estimated proportion of fatigue propagation cycles as a function of the maximum applied stress. 95% confidence interval from 5 repetitions is shown in shaded area. 88
3.14 (A) An example of the measurement of the projection area, A_p, of pore cluster near the fatigue crack initiation site. (B) $\sqrt{A_p}$ of the pore cluster for different tested specimens. ◯ represents the specimens without pore cluster near the initiation site. 90

4.1 (A) Geometries of the 7 tensile specimens used in this study. Schematic illustrations of (B) laser path along different consecutive layers and (C) laser path along each cross-sectional plane. 96
4.2 (A) Engineering stress-strain curves of AM Ti-6Al-4V at a strain rate of 2×10^{-3} s^{-1}. (B) Yield strength, ultimate tensile strength, and fracture strain vs. build orientation of the 7 specimens under study. Error bars represent the standard deviation from 3 repetitions. 102
4.3 (A) Cycles to failure vs. build orientation for the specimens manufactured in this work. Error bars represent the standard deviation from 3 repetitions. (B) Calculated map of scatter in fatigue life as a function of build orientation and maximum applied stress for the 7 specimens. . 103

4.4 (A-G) Longitudinal microstructure of the 7 specimens under study. (H) Average α lath thickness $\pm$ 1 standard deviation vs. build orientation of the 7 specimens. 103
4.5 Longitudinal EBSD maps of the α lath and the associated reconstructed prior-β microstructure of the 7 specimens under study. 105
4.6 (A) Contour pole figures of the α and prior-β microstructure of the 90° specimen. The texture rings confirm the $\beta \rightarrow \alpha$ transformation during the solidification process. (B) Texture index vs. build orientation for all the specimens. 106
4.7 (A) An example of the surface roughness (R_{a}) measurement on the 0° specimen. (B) Downward-facing and otherward-facing surface roughness (R_{a}) as a function of the build orientation. Error bars represent the standard deviation from 3 repetitions. 107
4.8 (A) 3D rendered XCT images of a 0° sample and pores inside the sample. (B) Projection view of the porosity distribution along the build direction in the 0°, 30°, and 90° samples. (C) Fraction of porosity against the polar angle. (D) Fraction of porosity against the distance from the sample surface. (E) Schematic illustration of the pore formation mechanisms. (F) $\sqrt{\text{Maximum Projection Area}}$, $A_{\mathrm{p,\ max}}$, and number of pores per unit volume as a function of the build orientation. 109
4.9 (A) A segmented cross-sectional XCT slice of a 0° sample. (B) Proportion of effective loading area $\pm$ 1 standard deviation vs. build orientation of the 7 specimens under study. (C) Corrected values of yield strength and ultimate tensile strength as a function of the build orientation. Error bars represent the standard deviation from 3 repetitions. 113
4.10 (A) Schematic illustration of the slip systems in Ti-6Al-4V. (B) Schmid factors of basal $\langle$a$\rangle$, prismatic $\langle$a$\rangle$, and pyramidal I $\langle$c+a$\rangle$ slip systems as a function of the build orientation. 115
4.11 Summary of fatigue crack initiation sites for the 7 specimens under study. 117
4.12 (A) Summary of presence of porosity near the fatigue crack initiation sites for all the tested samples. (B) $\sqrt{A_{\mathrm{p}}}$ of the pore cluster for the 60°, 75°, and 90° samples. 120
4.13 Fraction of grains with c-axes near-parallel (0°-10°) to the loading direction as a function of the build orientation. 122
4.14 (A) Geometrical details of the octet-truss lattice for the FEA simulation. (B) Boundary conditions used in the FEA simulation. 125

4.15 Schematic illustration of the primitive cell within the octet-truss lattice. 126
4.16 Comparison between the analytical solution and FEA calculation for the standard and optimized conditions. 131
4.17 Yield surface Φ of the octet-truss lattice defined by the analytical solution when (A) $\beta > 1$ and (B) $\beta < 1$. 134
4.18 (A) FEA calculation of the octet-truss lattice at $0.4\Sigma_z^Y$. (B) Maximum applied stress vs. cycles to failure for the lattice accounting for the orientation effect. 137

5.1 (A) Geometries of the BCC and FCC structures in this study. (B) Designed relative density as a function of the designed thickness-to-length ratio of the two types of structures under study. (C) Measured relative density vs. designed relative density for all the specimens. . . . 144
5.2 Engineering stress-strain curves of (A) BCC and (B) FCC structures measured at a strain rate of 10^{-3} s^{-1}. For different tested structures, plots of (C) elastic modulus vs. relative density and (D) yield strength vs. relative density. 147
5.3 (A) Maximum applied stress vs. cycles to failure for the metamaterials fabricated in this work. (B) Correlation between fatigue strength at 10^6 cycle as a function of relative density on a logarithm scale. 148
5.4 Deformation behaviour of the two types of specimens under monotonic loading at engineering strains of 15%. Note that the compression test for BCC2 lattice was stopped at an engineering strain of 2.5% since the collapse of the structure triggers the failure limit of the mechanical testing system. 150
5.5 Maximum strain vs. number of cycles for the BCC1 lattice tested at $0.6\Sigma^Y$ and associated in-situ observations on the deformation behaviour of the lattice using a digital camera. 151
5.6 Summary of the deformation behaviour of the BCC and FCC structures under cyclic loading. 155

6.1 (A) Geometries of the 5 Voronoi lattices in this study. (B) Schematic illustration of Voronoi cells and terms used in this work. (C) Contour plot of designed relative density as a function of designed strut thickness and number of Voronoi cells per mm^3 identifying the locations of structures V1-V5 studied. (D) Measured relative density vs. designed relative density for the 5 structures under study. 160

6.2 (A) Engineering stress-strain curves measured at a strain rate of 10^{-3} s^{-1}. For different tested lattices, plots of (B) elastic modulus vs. relative density and (C) yield strength vs. relative density. 167
6.3 (A) Maximum applied stress vs. cycles to failure for the lattices manufactured in this work. Three measurements are performed per condition before runout. (B) Correlation between fatigue strength at 10^6 cycle as a function of relative density on a logarithm scale. (C) Scatter in fatigue life for the lattices at different applied stresses. The scatter is given by the coefficient of variation of the fatigue life. 168
6.4 Surface quality characterization of different Voronoi structures. (A) shows an example of the edge profile extracted from a vertical strut of the V4 lattice using Image-J. (B) illustrates the surface roughness (R_a) of vertical, horizontal (upward-facing), and horizontal (downward-facing) struts as a function of the number of cells per mm^3. 170
6.5 (A) An example of the thickness map computed for the V4 lattice. (B) Example of strut thicknesses measured along 5 different struts in the V4 lattice. (C) Box plots showing the designed value, mean ± 1 standard deviation, and interquartile range. (D) Coefficient of variation of the strut thickness as a function of the designed value for the 5 structures under study. 172
6.6 (A) An example of a processing-induced porosity within the strut of V4 lattice. (B) Measured pore number density as a function of the designed strut thickness. (C) Measured maximum pore size as a function of the designed strut thickness. 174
6.7 (A) An example of the comparison between CAD design and computed tomography data. Red regions represent excess of material and blue regions represent lack of material. (B) Root mean square error (RMSE) of the geometrical deviation as a function of the designed strut thickness. 175
6.8 (A) An example of a unconnected strut after manufacturing. (B) Fraction of unconnected strut against the designed strut thickness for all Voronoi structures. (C) Probability of unconnectivity vs. orientation of strut relative to build plate. 177

6.9 Plot of the variation of maximum strain vs. number of accumulated fatigue cycles (R = 0.1, frequency = 30 Hz, maximum stress = 0.6 Σ_Y), and associated in-situ surface observations on the deformation behaviour of V4 lattice using digital camera. Note that no strut failure was observed at the surface before 35000 cycles (>90% of life) and the final collapse is associated with the initial strut failure. 179
6.10 Macroscopic observations on the initial strut failures of V3, V4, and V5 lattices at different maximum stresses confirming that they occur at around the same position within each structure. 180
6.11 FEA calculation of the V3, V4, and V5 lattices at different maximum stresses. 182
6.12 Macroscopic observations on the initial strut failure of V1 and V2 lattices at different maximum stresses confirming that they occur randomly within each structure. 183
6.13 FEA calculation of the V1 and V2 lattices at different maximum stresses. 184
6.14 Results of interrupted fatigue tests together with XCT for V4 lattice. (A) shows the variation of maximum strain vs. number of accumulated fatigue cycles until initial strut failure. (B) illustrates the associated variation in pore size vs. number of accumulated fatigue cycles. (C) shows the volume of V4 lattice before testing and after initial strut failure reconstructed from computed tomography. The initially failed strut was used for pore size and distribution analysis. (D) shows the fracture surface of the initially failed strut. 186
6.15 3D rendered XCT images of the V4 lattice during the interrupted fatigue tests ($R = 0.1$, frequency = 30 Hz, $\sigma_{\max} = 0.6\Sigma_Y$). 188
6.16 FEA calculation of the V4 lattice at $\sigma_{\max} = 0.6\Sigma_Y$. The loading condition of each failed strut is revealed to shed light on the failure process. . . . 191
6.17 (A) Maximum applied stress normalized with the yield strength against cycles to failure for the lattices manufactured in this work. (B) Correlation between normalized fatigue strength at 10^6 cycle and measured relative density for the Voronoi structures. 195

References

[1] D. Gu, X. Shi, R. Poprawe, D. L. Bourell, R. Setchi, J. Zhu, Material-structure-performance integrated laser-metal additive manufacturing, Science 372 (6545) (2021). doi:10.1126/science.abg1487.

[2] D. Zhang, D. Qiu, M. A. Gibson, Y. Zheng, H. L. Fraser, D. H. StJohn, M. A. Easton, Additive manufacturing of ultrafine-grained high-strength titanium alloys, Nature 576 (7785) (2019) 91–95. doi:10.1038/s41586-019-1783-1.
URL http://dx.doi.org/10.1038/s41586-019-1783-1

[3] T. DebRoy, H. L. Wei, J. S. Zuback, T. Mukherjee, J. W. Elmer, J. O. Milewski, A. M. Beese, A. Wilson-Heid, A. De, W. Zhang, Additive manufacturing of metallic components – Process, structure and properties, Progress in Materials Science 92 (2018) 112–224. doi:10.1016/j.pmatsci.2017.10.001.

[4] X. Zheng, H. Lee, T. H. Weisgraber, M. Shusteff, J. DeOtte, E. B. Duoss, J. D. Kuntz, M. M. Biener, Q. Ge, J. A. Jackson, S. O. Kucheyev, N. X. Fang, C. M. Spadaccini, Ultralight, ultrastiff mechanical metamaterials, Science 344 (6190) (2014) 1373–1377. doi:10.1126/science.1252291.

[5] M. S. Pham, C. Liu, I. Todd, J. Lertthanasarn, Damage-tolerant architected materials inspired by crystal microstructure, Nature 565 (7739) (2019) 305–311. doi:10.1038/s41586-018-0850-3.
URL http://dx.doi.org/10.1038/s41586-018-0850-3

[6] P. Kürnsteiner, M. B. Wilms, A. Weisheit, B. Gault, E. A. Jägle, D. Raabe, High-strength Damascus steel by additive manufacturing, Nature 582 (7813) (2020) 515–519. doi:10.1038/s41586-020-2409-3.
URL http://dx.doi.org/10.1038/s41586-020-2409-3

[7] D. Barba, E. Alabort, R. C. Reed, Synthetic bone: Design by additive manufacturing, Acta Biomaterialia 97 (2019) 637–656. doi:10.1016/j.actbio.2019.07.049.
URL https://doi.org/10.1016/j.actbio.2019.07.049

[8] Y. T. Tang, C. Panwisawas, J. N. Ghoussoub, Y. Gong, J. W. Clark, A. A. Németh, D. G. McCartney, R. C. Reed, Alloys-by-design: Application to new superalloys for additive manufacturing, Acta Materialia 202 (2021) 417–436.

doi:10.1016/j.actamat.2020.09.023.
URL https://doi.org/10.1016/j.actamat.2020.09.023

[9] N. T. Aboulkhair, M. Simonelli, L. Parry, I. Ashcroft, C. Tuck, R. Hague, 3D printing of Aluminium alloys: Additive Manufacturing of Aluminium alloys using selective laser melting, Progress in Materials Science 106 (August 2018) (2019) 100578. doi:10.1016/j.pmatsci.2019.100578.
URL https://doi.org/10.1016/j.pmatsci.2019.100578

[10] Alloyed, Automotive Headlights (2021).

[11] G. Aviation, GE9X Commercial Aircraft Engine (2018).

[12] Captiva, TirboLOX-l titainium lumbar cage (2018).

[13] Optisys, Additive Manufacturing transforms RF antenna design (2017).

[14] Alloyed, Rocket Nozzle (2021).

[15] Eplus3D, Metal 3D Printing Application - Heat Exchanger.

[16] T. Wohlers, History of AM 2023, Wohlers Report (2023) 1–61.
URL https://wohlersassociates.com/product/wr2023/

[17] J. S. Zhang, Y. T. Tang, R. Jin, A. Lui, P. S. Grant, E. Alabort, A. C. F. Cocks, R. C. Reed, On the size-dependent fatigue behaviour of laser powder bed fusion Ti-6Al-4V, Additive Manufacturing 79 (2024).
URL https://ssrn.com/abstract=4366193

[18] M. McGregor, S. Patel, S. McLachlin, Mihaela Vlasea, Architectural bone parameters and the relationship to titanium lattice design for powder bed fusion additive manufacturing, Additive Manufacturing 47 (April) (2021) 102273. arXiv:2105.07945, doi:10.1016/j.addma.2021.102273.
URL https://doi.org/10.1016/j.addma.2021.102273

[19] S. Liu, Y. C. Shin, Additive manufacturing of Ti6Al4V alloy: A review, Materials and Design 164 (2019) 107552. doi:10.1016/j.matdes.2018.107552.
URL https://doi.org/10.1016/j.matdes.2018.107552

[20] J. Tong, C. R. Bowen, J. Persson, A. Plummer, Mechanical properties of titanium-based Ti–6Al–4V alloys manufactured by powder bed additive manufacture, Materials Science and Technology (United Kingdom) 33 (2) (2017) 138–148. doi:10.1080/02670836.2016.1172787.

[21] X. Liu, P. K. Chu, C. Ding, Surface modification of titanium, titanium alloys, and related materials for biomedical applications, Materials Science and Engineering R: Reports 47 (3-4) (2004) 49–121. doi:10.1016/j.mser.2004.11.001.

[22] C. Cui, B. M. Hu, L. Zhao, S. Liu, Titanium alloy production technology, market prospects and industry development, Materials and Design 32 (3) (2011) 1684–1691. doi:10.1016/j.matdes.2010.09.011.

[23] R. W. Schutz, H. B. Watkins, Recent developments in titanium alloy application in the energy industry, Materials Science and Engineering: A 243 (1-2) (1998) 305–315. doi:10.1016/s0921-5093(97)00819-8.

[24] H. Fujii, K. Takahashi, Y. Yamashita, Application of titanium and its alloys for automobile parts, Nippon Steel Technical Report (88) (2003) 70–75. doi:10.1051/matecconf/202032102003.

[25] I. Gurrappa, Characterization of titanium alloy Ti-6Al-4V for chemical, marine and industrial applications, Materials Characterization 51 (2-3) (2003) 131–139. doi:10.1016/j.matchar.2003.10.006.

[26] I. V. Gorynin, Titanium alloys for marine application, Materials Science and Engineering: A 263 (2) (1999) 112–116. doi:10.1016/s0921-5093(98)01180-0.

[27] A. R. Prasad, K. Ramji, G. Datta, An Experimental Study of Wire EDM on Ti-6Al-4V Alloy, Procedia Materials Science 5 (2014) 2567–2576. doi:10.1016/j.mspro.2014.07.517.

[28] C. de Formanoir, A. Brulard, S. Vivès, G. Martin, F. Prima, S. Michotte, E. Rivière, A. Dolimont, S. Godet, A strategy to improve the work-hardening behavior of Ti–6Al–4V parts produced by additive manufacturing, Materials Research Letters 5 (3) (2017) 201–208. doi:10.1080/21663831.2016.1245681.
URL https://doi.org/10.1080/21663831.2016.1245681

[29] R. K. Gupta, V. A. Kumar, C. Mathew, G. S. Rao, Strain hardening of Titanium alloy Ti6Al4V sheets with prior heat treatment and cold working, Materials Science and Engineering: A 662 (2016) 537–550. doi:10.1016/j.msea.2016.03.094.
URL http://dx.doi.org/10.1016/j.msea.2016.03.094

[30] H. Guleryuz, H. Cimenoglu, Oxidation of Ti-6Al-4V alloy, Journal of Alloys and Compounds 472 (1-2) (2009) 241–246. doi:10.1016/j.jallcom.2008.04.024.

[31] R. Huang, M. Riddle, D. Graziano, J. Warren, S. Das, S. Nimbalkar, J. Cresko, E. Masanet, Energy and emissions saving potential of additive manufacturing: the case of lightweight aircraft components, Journal of Cleaner Production 135 (2016) 1559–1570. doi:10.1016/j.jclepro.2015.04.109.

[32] L. Thijs, F. Verhaeghe, T. Craeghs, J. V. Humbeeck, J. P. Kruth, A study of the microstructural evolution during selective laser melting of Ti-6Al-4V, Acta Materialia 58 (9) (2010) 3303–3312. doi:10.1016/j.actamat.2010.02.004.
URL http://dx.doi.org/10.1016/j.actamat.2010.02.004

[33] Y. Hu, H. Chen, X. Jia, X. Liang, J. Lei, Heat treatment of titanium manufactured by selective laser melting: Microstructure and tensile properties, Journal of Materials Research and Technology 18 (2022) 245–254. doi:10.1016/j.jmrt.2022.02.106.
URL https://doi.org/10.1016/j.jmrt.2022.02.106

[34] S. A. Etesami, B. Fotovvati, E. Asadi, Heat treatment of Ti-6Al-4V alloy manufactured by laser-based powder-bed fusion: Process, microstructures, and mechanical properties correlations, Journal of Alloys and Compounds 895 (2022) 162618. doi:10.1016/j.jallcom.2021.162618.
URL https://doi.org/10.1016/j.jallcom.2021.162618

[35] D. Herzog, V. Seyda, E. Wycisk, C. Emmelmann, Additive manufacturing of metals, Acta Materialia 117 (2016) 371–392. doi:10.1016/j.actamat.2016.07.019.
URL http://dx.doi.org/10.1016/j.actamat.2016.07.019

[36] N. A. Fleck, V. S. Deshpande, M. F. Ashby, Micro-architectured materials: Past, present and future, Proceedings of the Royal Society A: Mathematical, Physical and Engineering Sciences 466 (2121) (2010) 2495–2516. doi:10.1098/rspa.2010.0215.

[37] X. Xia, C. M. Spadaccini, J. R. Greer, Responsive materials architected in space and time, Nature Reviews Materials 7 (9) (2022) 683–701. doi:10.1038/s41578-022-00450-z.

[38] J. R. Greer, V. S. Deshpande, Three-dimensional architected materials and structures: Design, fabrication, and mechanical behavior, MRS Bulletin 44 (10) (2019) 750–757. doi:10.1557/mrs.2019.232.

[39] C. M. Portela, B. W. Edwards, D. Veysset, Y. Sun, K. A. Nelson, D. M. Kochmann, J. R. Greer, Supersonic impact resilience of nanoarchitected carbon, Nature Materials 20 (11) (2021) 1491–1497. doi:10.1038/s41563-021-01033-z.

[40] X. Ren, R. Das, P. Tran, T. D. Ngo, Y. M. Xie, Auxetic metamaterials and structures, Smart Materials and Structures 27 (023001) (2018). doi:10.11868/j.issn.1001-4381.2019.000391.

[41] T. Bückmann, M. Thiel, M. Kadic, R. Schittny, M. Wegener, An elasto-mechanical unfeelability cloak made of pentamode metamaterials, Nature Communications 5 (May) (2014) 1–6. doi:10.1038/ncomms5130.

[42] L. R. Meza, S. Das, J. R. Greer, Strong, lightweight, and recoverable three-dimensional ceramic nanolattices, Science 345 (6202) (2014) 1322–1326. doi:10.1126/science.1255908.

[43] M. Benedetti, A. du Plessis, R. O. Ritchie, M. Dallago, S. M. Razavi, F. Berto, Architected cellular materials: A review on their mechanical properties towards fatigue-tolerant design and fabrication, Materials Science and Engineering R: Reports 144 (January) (2021) 100606. doi:10.1016/j.mser.2021.100606.
URL https://doi.org/10.1016/j.mser.2021.100606

[44] T. Maconachie, M. Leary, B. Lozanovski, X. Zhang, M. Qian, O. Faruque, M. Brandt, SLM lattice structures: Properties, performance, applications and challenges, Materials and Design 183 (2019) 108137. doi:10.1016/j.matdes.2019.108137.
URL https://doi.org/10.1016/j.matdes.2019.108137

[45] O. Al-Ketan, R. Rowshan, R. K. Abu Al-Rub, Topology-mechanical property relationship of 3D printed strut, skeletal, and sheet based periodic metallic cellular materials, Additive Manufacturing 19 (2018) 167–183. doi:10.1016/j.addma.2017.12.006.
URL http://dx.doi.org/10.1016/j.addma.2017.12.006

[46] Z. Xiao, Y. Yang, R. Xiao, Y. Bai, C. Song, D. Wang, Evaluation of topology-optimized lattice structures manufactured via selective laser melting, Materials and Design 143 (2018) 27–37. doi:10.1016/j.matdes.2018.01.023.
URL https://doi.org/10.1016/j.matdes.2018.01.023

[47] V. S. Deshpande, N. A. Fleck, M. F. Ashby, Effective properties of the octet-truss lattice material, Journal of the Mechanics and Physics of Solids 49 (8) (2001) 1747–1769. doi:10.1016/S0022-5096(01)00010-2.

[48] S. J. Li, L. E. Murr, X. Y. Cheng, Z. B. Zhang, Y. L. Hao, R. Yang, F. Medina, R. B. Wicker, Compression fatigue behavior of Ti-6Al-4V mesh arrays fabricated by electron beam melting, Acta Materialia 60 (3) (2012) 793–802. doi:10.1016/j.actamat.2011.10.051.

[49] L. Yang, C. Yan, W. Cao, Z. Liu, B. Song, S. Wen, C. Zhang, Y. Shi, S. Yang, Compression–compression fatigue behaviour of gyroid-type triply periodic minimal surface porous structures fabricated by selective laser melting, Acta Materialia 181 (2019) 49–66. doi:10.1016/j.actamat.2019.09.042.
URL https://doi.org/10.1016/j.actamat.2019.09.042

[50] M. Banuta, I. Tarquini, Fatigue failure of a drive shaft, Journal of Failure Analysis and Prevention 12 (2) (2012) 139–144. doi:10.1007/s11668-012-9551-7.

[51] Y. Wang, C. Yu, L. Xing, K. Li, J. Chen, W. Liu, J. Ma, Z. Shen, Grain structure and texture of the SLM single track, Journal of Materials Processing Technology 281 (November 2019) (2020) 116591. doi:10.1016/j.jmatprotec.2020.116591.
URL https://doi.org/10.1016/j.jmatprotec.2020.116591

[52] B. Aksakal, Ö. S. Yildirim, H. Gul, Metallurgical failure analysis of various implant materials used in orthopedic applications, Journal of Failure Analysis and Prevention 4 (3) (2004) 17–23. doi:10.1361/15477020419794.

[53] S. Romano, A. Brückner-Foit, A. Brandão, J. Gumpinger, T. Ghidini, S. Beretta, Fatigue properties of AlSi10Mg obtained by additive manufacturing: Defect-based modelling and prediction of fatigue strength, Engineering Fracture Mechanics 187 (2018) 165–189. doi:10.1016/j.engfracmech.2017.11.002.
URL https://doi.org/10.1016/j.engfracmech.2017.11.002

[54] A. Yadollahi, N. Shamsaei, Additive manufacturing of fatigue resistant materials: Challenges and opportunities, International Journal of Fatigue 98 (2017) 14–31. doi:10.1016/j.ijfatigue.2017.01.001.
URL http://dx.doi.org/10.1016/j.ijfatigue.2017.01.001

[55] J. C. Stinville, M. A. Charpagne, A. Cervellon, S. Hemery, F. Wang, P. G. Callahan, V. Valle, T. M. Pollock, On the origins of fatigue strength in crystalline metallic materials, Science 377 (6610) (2022) 1065–1071. doi:10.1126/science.abn0392.

[56] C. M. Barr, T. Duong, D. C. Bufford, Z. Milne, A. Molkeri, N. M. Heckman, D. P. Adams, A. Srivastava, K. Hattar, M. J. Demkowicz, B. L. Boyce, Autonomous healing of fatigue cracks via cold welding, Nature 620 (7974) (2023) 552–556. doi:10.1038/s41586-023-06223-0.

[57] T. H. Becker, P. Kumar, U. Ramamurty, Fracture and fatigue in additively manufactured metals, Acta Materialia 219 (2021) 117240. doi:10.1016/j.actamat.2021.117240.
URL https://doi.org/10.1016/j.actamat.2021.117240

[58] P. Kumar, U. Ramamurty, High cycle fatigue in selective laser melted Ti-6Al-4V, Acta Materialia 194 (2020) 305–320. doi:10.1016/j.actamat.2020.05.041.
URL https://doi.org/10.1016/j.actamat.2020.05.041

[59] S. Beretta, S. Romano, A comparison of fatigue strength sensitivity to defects for materials manufactured by AM or traditional processes, International Journal of Fatigue 94 (2017) 178–191. doi:10.1016/j.ijfatigue.2016.06.020.
URL http://dx.doi.org/10.1016/j.ijfatigue.2016.06.020

[60] P. Li, D. H. Warner, A. Fatemi, N. Phan, Critical assessment of the fatigue performance of additively manufactured Ti-6Al-4V and perspective for future research, International Journal of Fatigue 85 (2016) 130–143. doi:10.1016/j.ijfatigue.2015.12.003.

[61] P. Edwards, M. Ramulu, Fatigue performance evaluation of selective laser melted Ti-6Al-4V, Materials Science and Engineering A 598 (2014) 327–337. doi:

10.1016/j.msea.2014.01.041.
URL http://dx.doi.org/10.1016/j.msea.2014.01.041

[62] V. D. Le, E. Pessard, F. Morel, S. Prigent, Fatigue behaviour of additively manufactured Ti-6Al-4V alloy: The role of defects on scatter and statistical size effect, International Journal of Fatigue 140 (June) (2020). doi:10.1016/j.ijfatigue.2020.105811.

[63] N. Hrabe, T. Gnäupel-Herold, T. Quinn, Fatigue properties of a titanium alloy (Ti–6Al–4V) fabricated via electron beam melting (EBM): Effects of internal defects and residual stress, International Journal of Fatigue 94 (2017) 202–210. doi:10.1016/j.ijfatigue.2016.04.022.
URL http://dx.doi.org/10.1016/j.ijfatigue.2016.04.022

[64] M. Nakatani, H. Masuo, Y. Tanaka, Y. Murakami, Effect of Surface Roughness on Fatigue Strength of Ti-6Al-4V Alloy Manufactured by Additive Manufacturing, Procedia Structural Integrity 19 (2019) 294–301. doi:10.1016/j.prostr.2019.12.032.
URL https://doi.org/10.1016/j.prostr.2019.12.032

[65] T. M. Mower, M. J. Long, Mechanical behavior of additive manufactured, powder-bed laser-fused materials, Materials Science and Engineering: A 651 (2016) 198–213. doi:10.1016/j.msea.2015.10.068.
URL http://dx.doi.org/10.1016/j.msea.2015.10.068

[66] B. Oberwinkler, M. Riedler, W. Eichlseder, Importance of local microstructure for damage tolerant light weight design of Ti-6Al-4V forgings, International Journal of Fatigue 32 (5) (2010) 808–814. doi:10.1016/j.ijfatigue.2009.06.021.
URL http://dx.doi.org/10.1016/j.ijfatigue.2009.06.021

[67] M. W. Wu, J. K. Chen, B. H. Lin, P. H. Chiang, M. K. Tsai, Compressive fatigue properties of additive-manufactured Ti-6Al-4V cellular material with different porosities, Materials Science and Engineering: A 790 (May) (2020) 139695. doi:10.1016/j.msea.2020.139695.
URL https://doi.org/10.1016/j.msea.2020.139695

[68] S. Zhao, S. J. Li, S. G. Wang, W. T. Hou, Y. Li, L. C. Zhang, Y. L. Hao, R. Yang, R. D. Misra, L. E. Murr, Compressive and fatigue behavior of functionally graded Ti-6Al-4V meshes fabricated by electron beam melting, Acta Materialia 150 (2018) 1–15. doi:10.1016/j.actamat.2018.02.060.

[69] Y. J. Liu, H. L. Wang, S. J. Li, S. G. Wang, W. J. Wang, W. T. Hou, Y. L. Hao, R. Yang, L. C. Zhang, Compressive and fatigue behavior of beta-type titanium porous structures fabricated by electron beam melting, Acta Materialia 126 (2017) 58–66. doi:10.1016/j.actamat.2016.12.052.

[70] B. Van Hooreweder, Y. Apers, K. Lietaert, J. P. Kruth, Improving the fatigue performance of porous metallic biomaterials produced by Selective Laser Melting, Acta Biomaterialia 47 (2017) 193–202. doi:10.1016/j.actbio.2016.10.005.
URL http://dx.doi.org/10.1016/j.actbio.2016.10.005

[71] S. Özbilen, D. Liebert, T. Beck, M. Bram, Fatigue behavior of highly porous titanium produced by powder metallurgy with temporary space holders, Materials Science Engineering C 60 (2016) 446–457. doi:10.1016/j.msec.2015.11.050.
URL http://dx.doi.org/10.1016/j.msec.2015.11.050

[72] S. Zhao, S. J. Li, W. T. Hou, Y. L. Hao, R. Yang, R. D. Misra, The influence of cell morphology on the compressive fatigue behavior of Ti-6Al-4V meshes fabricated by electron beam melting, Journal of the Mechanical Behavior of Biomedical Materials 59 (2016) 251–264. doi:10.1016/j.jmbbm.2016.01.034.

[73] M. Speirs, B. Van Hooreweder, J. Van Humbeeck, J. P. Kruth, Fatigue behaviour of NiTi shape memory alloy scaffolds produced by SLM, a unit cell design comparison, Journal of the Mechanical Behavior of Biomedical Materials 70 (January) (2017) 53–59. doi:10.1016/j.jmbbm.2017.01.016.
URL http://dx.doi.org/10.1016/j.jmbbm.2017.01.016

[74] S. M. Ahmadi, R. Hedayati, Y. Li, K. Lietaert, N. Tümer, A. Fatemi, C. D. Rans, B. Pouran, H. Weinans, A. A. Zadpoor, Fatigue performance of additively manufactured meta-biomaterials: The effects of topology and material type, Acta Biomaterialia 65 (2018) 292–304. doi:10.1016/j.actbio.2017.11.014.

[75] Y. J. Liu, D. C. Ren, S. J. Li, H. Wang, L. C. Zhang, T. B. Sercombe, Enhanced fatigue characteristics of a topology-optimized porous titanium structure produced by selective laser melting, Additive Manufacturing 32 (January) (2020). doi:10.1016/j.addma.2020.101060.

[76] N. Soro, N. Saintier, J. Merzeau, M. Veidt, M. S. Dargusch, Quasi-static and fatigue properties of graded Ti–6Al–4V lattices produced by Laser Powder Bed Fusion (LPBF), Additive Manufacturing 37 (October 2020) (2021) 101653. doi:10.1016/j.addma.2020.101653.
URL https://doi.org/10.1016/j.addma.2020.101653

[77] L. Bai, C. Gong, X. Chen, J. Zheng, L. Xin, Y. Xiong, X. Wu, M. Hu, K. Li, Y. Sun, Quasi-Static compressive responses and fatigue behaviour of Ti-6Al-4V graded lattice structures fabricated by laser powder bed fusion, Materials and Design 210 (2021) 110110. doi:10.1016/j.matdes.2021.110110.
URL https://doi.org/10.1016/j.matdes.2021.110110

[78] N. W. Hrabe, P. Heinl, B. Flinn, C. Körner, R. K. Bordia, Compression-compression fatigue of selective electron beam melted cellular titanium (Ti-6Al-4V)., Journal of biomedical materials research. Part B, Applied biomaterials 99 (2) (2011) 313–320. doi:10.1002/jbm.b.31901.

[79] S. Amin Yavari, S. M. Ahmadi, R. Wauthle, B. Pouran, J. Schrooten, H. Weinans, A. A. Zadpoor, Relationship between unit cell type and porosity and the fatigue behavior of selective laser melted meta-biomaterials, Journal of the Mechanical Behavior of Biomedical Materials 43 (2015) 91–100. doi:10.1016/j.jmbbm.2014.12.015.
URL http://dx.doi.org/10.1016/j.jmbbm.2014.12.015

[80] F. S. Bobbert, K. Lietaert, A. A. Eftekhari, B. Pouran, S. M. Ahmadi, H. Weinans, A. A. Zadpoor, Additively manufactured metallic porous biomaterials based on minimal surfaces: A unique combination of topological, mechanical, and mass transport properties, Acta Biomaterialia 53 (2017) 572–584. doi:10.1016/j.actbio.2017.02.024.
URL http://dx.doi.org/10.1016/j.actbio.2017.02.024

[81] A. Yánez, M. P. Fiorucci, A. Cuadrado, O. Martel, D. Monopoli, Surface roughness effects on the fatigue behaviour of gyroid cellular structures obtained by additive manufacturing, International Journal of Fatigue 138 (April) (2020) 105702. doi:10.1016/j.ijfatigue.2020.105702.
URL https://doi.org/10.1016/j.ijfatigue.2020.105702

[82] H. M. Kolken, A. F. Garcia, A. Du Plessis, C. Rans, M. J. Mirzaali, A. A. Zadpoor, Fatigue performance of auxetic meta-biomaterials, Acta Biomaterialia 126 (2021) 511–523. doi:10.1016/j.actbio.2021.03.015.
URL https://doi.org/10.1016/j.actbio.2021.03.015

[83] S. Kechagias, R. N. Oosterbeek, M. J. Munford, S. Ghouse, J. R. Jeffers, Controlling the mechanical behaviour of stochastic lattice structures: The key role of nodal connectivity, Additive Manufacturing 54 (December 2021) (2022) 102730. doi:10.1016/j.addma.2022.102730.
URL https://doi.org/10.1016/j.addma.2022.102730

[84] A. C. Jones, J. R. T. Jeffers, R. N. Oosterbeek, Frequency dependent fatigue behaviour of additively manufactured titanium lattices, Engineering Failure Analysis 152 (July) (2023) 107475. doi:10.1016/j.engfailanal.2023.107475.
URL https://doi.org/10.1016/j.engfailanal.2023.107475

[85] Z. Liu, H. Gong, J. Gao, Enhancement in the fatigue resistances of triply periodic surfaces-based scaffolds, International Journal of Mechanical Sciences 245 (January) (2023) 108119. doi:10.1016/j.ijmecsci.2023.108119.
URL https://doi.org/10.1016/j.ijmecsci.2023.108119

[86] Y. J. Liu, S. J. Li, H. L. Wang, W. T. Hou, Y. L. Hao, R. Yang, T. B. Sercombe, L. C. Zhang, Microstructure, defects and mechanical behavior of beta-type titanium porous structures manufactured by electron beam melting and selective laser melting, Acta Materialia 113 (2016) 56–67. doi:10.1016/j.actamat.2016.04.029.

[87] E. Santos, K. Osakada, M. Shiomi, Y. Kitamura, F. Abe, Microstructure and mechanical properties of pure titanium models fabricated by selective laser melting, Proceedings of the Institution of Mechanical Engineers, Part C: Journal of Mechanical Engineering Science 218 (7) (2004) 711–719. doi:10.11817/j.ysxb.1004.0609.2023-43850.

[88] Y. Okazaki, A. Ishino, Microstructures and Mechanical Properties of Laser-Sintered Commercially Pure Ti and Ti-6Al-4V, Materials 13 (609) (2020).

[89] E. G. Brodie, J. Richter, T. Wegener, A. Molotnikov, T. Niendorf, Influence of a remelt scan strategy on the microstructure and fatigue behaviour of additively manufactured biomedical Ti65Ta efficiently assessed using small scale specimens, International Journal of Fatigue 162 (January) (2022) 106944. doi:10.1016/j.ijfatigue.2022.106944.
URL https://doi.org/10.1016/j.ijfatigue.2022.106944

[90] M. W. Wu, J. K. Chen, B. H. Lin, P. H. Chiang, Improved fatigue endurance ratio of additive manufactured Ti-6Al-4V lattice by hot isostatic pressing, Materials and Design 134 (2017) 163–170. doi:10.1016/j.matdes.2017.08.048.
URL https://doi.org/10.1016/j.matdes.2017.08.048

[91] S. Amin Yavari, R. Wauthle, J. Van Der Stok, A. C. Riemslag, M. Janssen, M. Mulier, J. P. Kruth, J. Schrooten, H. Weinans, A. A. Zadpoor, Fatigue behavior of porous biomaterials manufactured using selective laser melting, Materials Science and Engineering C 33 (8) (2013) 4849–4858. doi:10.1016/j.msec.2013.08.006.
URL http://dx.doi.org/10.1016/j.msec.2013.08.006

[92] H. K. Rafi, N. V. Karthik, H. Gong, T. L. Starr, B. E. Stucker, Microstructures and mechanical properties of Ti6Al4V parts fabricated by selective laser melting and electron beam melting, Journal of Materials Engineering and Performance 22 (12) (2013) 3872–3883. doi:10.1007/s11665-013-0658-0.

[93] P. Kumar, R. Jayaraj, J. Suryawanshi, U. R. Satwik, J. McKinnell, U. Ramamurty, Fatigue strength of additively manufactured 316L austenitic stainless steel, Acta Materialia 199 (2020) 225–239. doi:10.1016/j.actamat.2020.08.033.
URL https://doi.org/10.1016/j.actamat.2020.08.033

[94] N. Macallister, T. H. Becker, Fatigue life estimation of additively manufactured Ti-6Al-4V: Sensitivity, scatter and defect description in Damage-tolerant models, Acta Materialia 237 (2022) 118189. doi:10.1016/j.actamat.2022.118189.
URL https://doi.org/10.1016/j.actamat.2022.118189

[95] B. Song, S. Dong, B. Zhang, H. Liao, C. Coddet, Effects of processing parameters on microstructure and mechanical property of selective laser melted Ti6Al4V, Materials and Design 35 (2012) 120–125. doi:10.1016/j.matdes.2011.09.051.
URL http://dx.doi.org/10.1016/j.matdes.2011.09.051

[96] L. Thijs, M. L. Montero Sistiaga, R. Wauthle, Q. Xie, J. P. Kruth, J. Van Humbeeck, Strong morphological and crystallographic texture and resulting yield strength anisotropy in selective laser melted tantalum, Acta Materialia 61 (12) (2013) 4657–4668. doi:10.1016/j.actamat.2013.04.036.
URL http://dx.doi.org/10.1016/j.actamat.2013.04.036

[97] J. S. Zhang, Y. T. Tang, R. Jin, A. Lui, P. S. Grant, E. Alabort, A. C. F. Cocks, R. C. Reed, On the size-dependent fatigue behaviour of laser powder bed fusion Ti-6Al-4V, Additive Manufacturing 79 (2024). doi:10.1016/j.addma.2023.103922.
URL https://ssrn.com/abstract=4366193

[98] B. E. Carroll, T. A. Palmer, A. M. Beese, Anisotropic tensile behavior of Ti-6Al-4V components fabricated with directed energy deposition additive manufacturing, Acta Materialia 87 (2015) 309–320. doi:10.1016/j.actamat.2014.12.054.
URL http://dx.doi.org/10.1016/j.actamat.2014.12.054

[99] N. Uçak, A. Çiçek, K. Aslantas, Machinability of 3D printed metallic materials fabricated by selective laser melting and electron beam melting: A review, Journal of Manufacturing Processes 80 (June) (2022) 414–457. doi:10.1016/j.jmapro.2022.06.023.
URL https://doi.org/10.1016/j.jmapro.2022.06.023

[100] A. Charles, A. Elkaseer, U. Paggi, L. Thijs, V. Hagenmeyer, S. Scholz, Down-facing surfaces in laser powder bed fusion of Ti6Al4V : Effect of dross formation on dimensional accuracy and surface texture, Additive Manufacturing 46 (February) (2021) 102148. doi:10.1016/j.addma.2021.102148.
URL https://doi.org/10.1016/j.addma.2021.102148

[101] A. Charles, M. Bayat, A. Elkaseer, L. Thijs, J. Henri, S. Scholz, Elucidation of dross formation in laser powder bed fusion at down-facing surfaces : Phenomenon-oriented multiphysics simulation and experimental validation, Additive Manufacturing 50 (December 2021) (2022) 102551. doi:10.1016/j.addma.2021.102551.
URL https://doi.org/10.1016/j.addma.2021.102551

[102] Z. Wang, Y. Zhang, S. Tan, L. Ding, A. Bernard, Support point determination for support structure design in additive manufacturing, Additive Manufacturing 47 (March) (2021) 102341. doi:10.1016/j.addma.2021.102341.
URL https://doi.org/10.1016/j.addma.2021.102341

[103] B. Ahuja, M. Karg, K. Y. Nagulin, M. Schmidt, Fabrication and characterization of high strength Al-Cu alloys processed using Laser Beam Melting in metal powder bed, Physics Procedia 56 (C) (2014) 135–146. doi:10.1016/j.phpro.2014.08.156.

[104] D. Koutny, D. Palousek, L. Pantelejev, C. Hoeller, R. Pichler, L. Tesicky, J. Kaiser, Influence of scanning strategies on processing of aluminum alloy EN AW 2618 using selective laser melting, Materials 11 (2) (2018). doi:10.3390/ma11020298.

[105] C. L. Smithson, T. Davis, T. W. Nelson, N. B. Crane, Effect of support structures and surface angles on near-surface porosity in laser powder bed fusion, Journal of Manufacturing Processes 94 (February) (2023) 328–337. doi:10.1016/j.jmapro.2023.03.065.
URL https://doi.org/10.1016/j.jmapro.2023.03.065

[106] A. Yánez, M. P. Fiorucci, A. Cuadrado, O. Martel, D. Monopoli, Surface roughness effects on the fatigue behaviour of gyroid cellular structures obtained by additive manufacturing, International Journal of Fatigue 138 (April) (2020) 105702. doi:10.1016/j.ijfatigue.2020.105702.
URL https://doi.org/10.1016/j.ijfatigue.2020.105702

[107] S. Lee, B. Rasoolian, D. F. Silva, J. W. Pegues, N. Shamsaei, Surface roughness parameter and modeling for fatigue behavior of additive manufactured parts: A non-destructive data-driven approach, Additive Manufacturing 46 (June) (2021) 102094. doi:10.1016/j.addma.2021.102094.
URL https://doi.org/10.1016/j.addma.2021.102094

[108] H. Masuo, Y. Tanaka, S. Morokoshi, H. Yagura, T. Uchida, Y. Yamamoto, Y. Murakami, Influence of defects, surface roughness and HIP on the fatigue strength of Ti-6Al-4V manufactured by additive manufacturing, International Journal of Fatigue 117 (July) (2018) 163–179. doi:10.1016/j.ijfatigue.2018.07.020.
URL https://doi.org/10.1016/j.ijfatigue.2018.07.020

[109] M. Benedetti, C. Santus, Notch fatigue and crack growth resistance of Ti-6Al-4V ELI additively manufactured via selective laser melting: A critical distance approach to defect sensitivity, International Journal of Fatigue 121 (November 2018) (2019) 281–292. doi:10.1016/j.ijfatigue.2018.12.020.
URL https://doi.org/10.1016/j.ijfatigue.2018.12.020

[110] Y. Murakami, M. Endo, Effects of defects, inclusions and inhomogeneities on fatigue strength, International Journal of Fatigue 16 (3) (1994) 163–182. doi:10.1016/0142-1123(94)90001-9.

[111] D. Greitemeier, C. Dalle Donne, F. Syassen, J. Eufinger, T. Melz, Effect of surface roughness on fatigue performance of additive manufactured Ti–6Al–4V, Materials Science and Technology (United Kingdom) 32 (7) (2016) 629–634. doi:10.1179/1743284715Y.0000000053.

[112] S. Lee, J. W. Pegues, N. Shamsaei, Fatigue behavior and modeling for additive manufactured 304L stainless steel: The effect of surface roughness, International Journal of Fatigue 141 (July) (2020). doi:10.1016/j.ijfatigue.2020.105856.

[113] A. Thompson, N. Senin, I. Maskery, L. Körner, S. Lawes, R. Leach, Internal surface measurement of metal powder bed fusion parts, Additive Manufacturing 20 (January) (2018) 126–133. doi:10.1016/j.addma.2018.01.003.
URL https://doi.org/10.1016/j.addma.2018.01.003

[114] A. Townsend, N. Senin, L. Blunt, R. K. Leach, J. S. Taylor, Surface texture metrology for metal additive manufacturing: a review, Precision Engineering 46 (2016) 34–47. doi:10.1016/j.precisioneng.2016.06.001.
URL http://dx.doi.org/10.1016/j.precisioneng.2016.06.001

[115] A. Thompson, I. Maskery, R. K. Leach, X-ray computed tomography for additive manufacturing: A review, Measurement Science and Technology 27 (7) (2016). doi:10.1088/0957-0233/27/7/072001.

[116] J. Gockel, L. Sheridan, B. Koerper, B. Whip, The influence of additive manufacturing processing parameters on surface roughness and fatigue life, International Journal of Fatigue 124 (March) (2019) 380–388. doi:10.1016/j.ijfatigue.2019.03.025.
URL https://doi.org/10.1016/j.ijfatigue.2019.03.025

[117] J. P. Kruth, M. Bartscher, S. Carmignato, R. Schmitt, L. De Chiffre, A. Weckenmann, Computed tomography for dimensional metrology, CIRP Annals - Manufacturing Technology 60 (2) (2011) 821–842. doi:10.1016/j.cirp.2011.05.006.
URL http://dx.doi.org/10.1016/j.cirp.2011.05.006

[118] R. Ullah, J. Lian, J. Akmal, J. Wu, E. Niemi, Prediction and validation of melt pool dimensions and geometric distortions of additively manufactured AlSi10Mg, International Journal of Advanced Manufacturing Technology 126 (7-8) (2023) 3593–3613. doi:10.1007/s00170-023-11264-w.
URL https://doi.org/10.1007/s00170-023-11264-w

[119] M. Tang, P. C. Pistorius, J. L. Beuth, Prediction of lack-of-fusion porosity for powder bed fusion, Additive Manufacturing 14 (2017) 39–48. doi:10.1016/j.addma.2016.12.001.
URL http://dx.doi.org/10.1016/j.addma.2016.12.001

[120] C. Qiu, S. Yue, N. J. Adkins, M. Ward, H. Hassanin, P. D. Lee, P. J. Withers, M. M. Attallah, Influence of processing conditions on strut structure and compressive properties of cellular lattice structures fabricated by selective laser melting, Materials Science and Engineering: A 638 (2015) 228–231. doi:10.1016/j.msea.2015.04.074.

[121] D. Melancon, Z. S. Bagheri, R. B. Johnston, L. Liu, M. Tanzer, D. Pasini, Mechanical characterization of structurally porous biomaterials built via additive manufacturing: experiments, predictive models, and design maps for load-bearing bone replacement implants, Acta Biomaterialia 63 (2017) 350–368. doi:10.1016/

j.actbio.2017.09.013.
URL https://doi.org/10.1016/j.actbio.2017.09.013

[122] S. Murchio, M. Dallago, F. Zanini, S. Carmignato, G. Zappini, F. Berto, D. Maniglio, M. Benedetti, Additively manufactured Ti–6Al–4V thin struts via laser powder bed fusion: Effect of building orientation on geometrical accuracy and mechanical properties, Journal of the Mechanical Behavior of Biomedical Materials 119 (March) (2021). doi:10.1016/j.jmbbm.2021.104495.

[123] E. Hernández-Nava, C. J. Smith, F. Derguti, S. Tammas-Williams, F. Leonard, P. J. Withers, I. Todd, R. Goodall, The effect of defects on the mechanical response of Ti-6Al-4V cubic lattice structures fabricated by electron beam melting, Acta Materialia 108 (2016) 279–292. doi:10.1016/j.actamat.2016.02.029.

[124] A. Sombatmai, V. Uthaisangsuk, S. Wongwises, P. Promoppatum, Multiscale investigation of the influence of geometrical imperfections, porosity, and size-dependent features on mechanical behavior of additively manufactured Ti-6Al-4V lattice struts, Materials and Design 209 (2021) 109985. doi:10.1016/j.matdes.2021.109985.
URL https://doi.org/10.1016/j.matdes.2021.109985

[125] H. D. Carlton, N. A. Volkoff-Shoemaker, M. C. Messner, N. R. Barton, M. Kumar, Incorporating defects into model predictions of metal lattice-structured materials, Materials Science and Engineering: A 832 (2022) 142427. doi:10.1016/j.msea.2021.142427.
URL https://doi.org/10.1016/j.msea.2021.142427

[126] A. Jam, A. du Plessis, C. Lora, S. Raghavendra, M. Pellizzari, M. Benedetti, Manufacturability of lattice structures fabricated by laser powder bed fusion: A novel biomedical application of the beta Ti-21S alloy, Additive Manufacturing 50 (December 2021) (2022) 102556. doi:10.1016/j.addma.2021.102556.
URL https://doi.org/10.1016/j.addma.2021.102556

[127] Z. S. Bagheri, D. Melancon, L. Liu, R. B. Johnston, D. Pasini, Compensation strategy to reduce geometry and mechanics mismatches in porous biomaterials built with Selective Laser Melting, Journal of the Mechanical Behavior of Biomedical Materials 70 (2017) 17–27. doi:10.1016/j.jmbbm.2016.04.041.
URL http://dx.doi.org/10.1016/j.jmbbm.2016.04.041

[128] C. Yan, L. Hao, A. Hussein, P. Young, D. Raymont, Advanced lightweight 316L stainless steel cellular lattice structures fabricated via selective laser melting, Materials and Design 55 (2014) 533–541. doi:10.1016/j.matdes.2013.10.027.
URL http://dx.doi.org/10.1016/j.matdes.2013.10.027

[129] R. Gümrük, R. A. Mines, S. Karadeniz, Static mechanical behaviours of stainless steel micro-lattice structures under different loading conditions, Materials Science and Engineering: A 586 (2013) 392–406. doi:10.1016/j.msea.2013.07.070.

[130] M. Leary, M. Mazur, J. Elambasseril, M. McMillan, T. Chirent, Y. Sun, M. Qian, M. Easton, M. Brandt, Selective laser melting (SLM) of AlSi12Mg lattice structures, Materials and Design 98 (2016) 344–357. doi:10.1016/j.matdes.2016.02.127.
URL http://dx.doi.org/10.1016/j.matdes.2016.02.127

[131] D. Li, R. Qin, B. Chen, J. Zhou, Analysis of mechanical properties of lattice structures with stochastic geometric defects in additive manufacturing, Materials Science and Engineering: A 822 (June) (2021) 141666. doi:10.1016/j.msea.2021.141666.
URL https://doi.org/10.1016/j.msea.2021.141666

[132] X. Cao, Y. Jiang, T. Zhao, P. Wang, Y. Wang, Z. Chen, Y. Li, D. Xiao, D. Fang, Compression experiment and numerical evaluation on mechanical responses of the lattice structures with stochastic geometric defects originated from additive-manufacturing, Composites Part B: Engineering 194 (March) (2020) 108030. doi:10.1016/j.compositesb.2020.108030.
URL https://doi.org/10.1016/j.compositesb.2020.108030

[133] M. Dallago, B. Winiarski, F. Zanini, S. Carmignato, M. Benedetti, On the effect of geometrical imperfections and defects on the fatigue strength of cellular lattice structures additively manufactured via Selective Laser Melting, International Journal of Fatigue 124 (November 2018) (2019) 348–360. doi:10.1016/j.ijfatigue.2019.03.019.
URL https://doi.org/10.1016/j.ijfatigue.2019.03.019

[134] U. Hossain, S. Ghouse, K. Nai, J. R. Jeffers, Mechanical and morphological properties of additively manufactured SS316L and Ti6Al4V micro-struts as a function of build angle, Additive Manufacturing 46 (August 2020) (2021) 102050. doi:10.1016/j.addma.2021.102050.
URL https://doi.org/10.1016/j.addma.2021.102050

[135] C. Chen, T. J. Lu, N. A. Fleck, Effect of imperfections on the yielding of two-dimensional foams, Journal of the Mechanics and Physics of Solids 47 (11) (1999) 2235–2272. doi:10.1016/S0022-5096(99)00030-7.

[136] X. P. Tan, Y. J. Tan, C. S. Chow, S. B. Tor, W. Y. Yeong, Metallic powder-bed based 3D printing of cellular scaffolds for orthopaedic implants: A state-of-the-art review on manufacturing, topological design, mechanical properties and biocompatibility, Materials Science and Engineering C 76 (2017) 1328–1343. doi:10.1016/j.msec.2017.02.094.
URL http://dx.doi.org/10.1016/j.msec.2017.02.094

[137] L. Liu, P. Kamm, F. García-Moreno, J. Banhart, D. Pasini, Elastic and failure response of imperfect three-dimensional metallic lattices: the role of geometric defects induced by Selective Laser Melting, Journal of the Mechanics and Physics

of Solids 107 (2017) 160–184. doi:10.1016/j.jmps.2017.07.003.
URL http://dx.doi.org/10.1016/j.jmps.2017.07.003

[138] D. Mahmoud, K. S. Al-Rubaie, M. A. Elbestawi, The influence of selective laser melting defects on the fatigue properties of Ti6Al4V porosity graded gyroids for bone implants, International Journal of Mechanical Sciences 193 (September 2020) (2021). doi:10.1016/j.ijmecsci.2020.106180.

[139] Y. Amani, S. Dancette, P. Delroisse, A. Simar, E. Maire, Compression behavior of lattice structures produced by selective laser melting: X-ray tomography based experimental and finite element approaches, Acta Materialia 159 (2018) 395–407. doi:10.1016/j.actamat.2018.08.030.
URL http://dx.doi.org/10.1016/j.actamat.2018.08.030

[140] W. Frieden Templeton, S. Hinnebusch, S. T. Strayer, A. C. To, C. Pistorius, S. P. Narra, A mechanistic explanation of shrinkage porosity in laser powder bed fusion additive manufacturing, Acta Materialia 266 (December 2023) (2023) 119632. doi:10.1016/j.actamat.2023.119632.
URL https://doi.org/10.1016/j.actamat.2023.119632

[141] S. A. Khairallah, A. T. Anderson, A. Rubenchik, W. E. King, Laser powder-bed fusion additive manufacturing: Physics of complex melt flow and formation mechanisms of pores, spatter, and denudation zones, Acta Materialia 108 (2016) 36–45. doi:10.1016/j.actamat.2016.02.014.
URL http://dx.doi.org/10.1016/j.actamat.2016.02.014

[142] W. E. King, H. D. Barth, V. M. Castillo, G. F. Gallegos, J. W. Gibbs, D. E. Hahn, C. Kamath, A. M. Rubenchik, Observation of keyhole-mode laser melting in laser powder-bed fusion additive manufacturing, Journal of Materials Processing Technology 214 (12) (2014) 2915–2925. doi:10.1016/j.jmatprotec.2014.06.005.
URL http://dx.doi.org/10.1016/j.jmatprotec.2014.06.005

[143] R. Rai, J. W. Elmer, T. A. Palmer, T. Debroy, Heat transfer and fluid flow during keyhole mode laser welding of tantalum, Ti-6Al-4V, 304L stainless steel and vanadium, Journal of Physics D: Applied Physics 40 (18) (2007) 5753–5766. doi:10.1088/0022-3727/40/18/037.

[144] F. H. Kim, S. P. Moylan, E. J. Garboczi, J. A. Slotwinski, Investigation of pore structure in cobalt chrome additively manufactured parts using X-ray computed tomography and three-dimensional image analysis, Additive Manufacturing 17 (2017) 23–38. doi:10.1016/j.addma.2017.06.011.
URL https://doi.org/10.1016/j.addma.2017.06.011

[145] R. Snell, S. Tammas-Williams, L. Chechik, A. Lyle, E. Hernández-Nava, C. Boig, G. Panoutsos, I. Todd, Methods for Rapid Pore Classification in Metal Additive Manufacturing, Jom 72 (1) (2020) 101–109. doi:10.1007/s11837-019-03761-9.

[146] H. Galarraga, D. A. Lados, R. R. Dehoff, M. M. Kirka, P. Nandwana, Effects of the microstructure and porosity on properties of Ti-6Al-4V ELI alloy fabricated by electron beam melting (EBM), Additive Manufacturing 10 (2016) 47–57. doi:10.1016/j.addma.2016.02.003.
URL http://dx.doi.org/10.1016/j.addma.2016.02.003

[147] A. du Plessis, Effects of process parameters on porosity in laser powder bed fusion revealed by X-ray tomography, Additive Manufacturing 30 (June) (2019) 100871. doi:10.1016/j.addma.2019.100871.
URL https://doi.org/10.1016/j.addma.2019.100871

[148] J. P. Oliveira, A. D. LaLonde, J. Ma, Processing parameters in laser powder bed fusion metal additive manufacturing, Materials and Design 193 (2020) 1–12. doi:10.1016/j.matdes.2020.108762.

[149] C. L. Druzgalski, A. Ashby, G. Guss, W. E. King, T. T. Roehling, M. J. Matthews, Process optimization of complex geometries using feed forward control for laser powder bed fusion additive manufacturing, Additive Manufacturing 34 (March) (2020) 101169. doi:10.1016/j.addma.2020.101169.
URL https://doi.org/10.1016/j.addma.2020.101169

[150] A. Leicht, U. Klement, E. Hryha, Effect of build geometry on the microstructural development of 316L parts produced by additive manufacturing, Materials Characterization 143 (January) (2018) 137–143. doi:10.1016/j.matchar.2018.04.040.
URL https://doi.org/10.1016/j.matchar.2018.04.040

[151] A. Çelik, E. Tekoğlu, E. Yasa, M. Sönmez, Contact-Free Support Structures for the Direct Metal Laser Melting Process, Materials 15 (11) (2022). doi:10.3390/ma15113765.

[152] C. N. Kelly, J. Francovich, S. Julmi, D. Safranski, R. E. Guldberg, H. J. Maier, K. Gall, Fatigue behavior of As-built selective laser melted titanium scaffolds with sheet-based gyroid microarchitecture for bone tissue engineering, Acta Biomaterialia 94 (2019) 610–626. doi:10.1016/j.actbio.2019.05.046.
URL https://doi.org/10.1016/j.actbio.2019.05.046

[153] M. Dallago, S. Raghavendra, V. Luchin, G. Zappini, D. Pasini, M. Benedetti, The role of node fillet, unit-cell size and strut orientation on the fatigue strength of Ti-6Al-4V lattice materials additively manufactured via laser powder bed fusion, International Journal of Fatigue 142 (September 2020) (2021) 105946. doi:10.1016/j.ijfatigue.2020.105946.
URL http://dx.doi.org/10.1016/j.ijfatigue.2020.105946

[154] S. Tammas-Williams, P. J. Withers, I. Todd, P. B. Prangnell, The Influence of Porosity on Fatigue Crack Initiation in Additively Manufactured Titanium Components, Scientific Reports 7 (1) (2017) 1–13. doi:10.1038/

s41598-017-06504-5.
URL http://dx.doi.org/10.1038/s41598-017-06504-5

[155] R. Biswal, A. K. Syed, X. Zhang, Assessment of the effect of isolated porosity defects on the fatigue performance of additive manufactured titanium alloy, Additive Manufacturing 23 (July) (2018) 433–442. doi:10.1016/j.addma.2018.08.024.
URL https://doi.org/10.1016/j.addma.2018.08.024

[156] L. Boniotti, S. Beretta, L. Patriarca, L. Rigoni, S. Foletti, Experimental and numerical investigation on compressive fatigue strength of lattice structures of AlSi7Mg manufactured by SLM, International Journal of Fatigue 128 (June) (2019) 105181. doi:10.1016/j.ijfatigue.2019.06.041.
URL https://doi.org/10.1016/j.ijfatigue.2019.06.041

[157] G. K. Lewis, E. Schlienger, Practical considerations and capabilities for laser assisted direct metal deposition, Materials and Design 21 (2000) 417–423.

[158] J. L. Bartlett, X. Li, An overview of residual stresses in metal powder bed fusion, Additive Manufacturing 27 (January) (2019) 131–149. doi:10.1016/j.addma.2019.02.020.
URL https://doi.org/10.1016/j.addma.2019.02.020

[159] J. L. Bartlett, B. P. Croom, J. Burdick, D. Henkel, X. Li, Revealing mechanisms of residual stress development in additive manufacturing via digital image correlation, Additive Manufacturing 22 (March) (2018) 1–12. doi:10.1016/j.addma.2018.04.025.

[160] C. Li, Z. Y. Liu, X. Y. Fang, Y. B. Guo, Residual Stress in Metal Additive Manufacturing, Procedia CIRP 71 (March) (2018) 348–353. doi:10.1016/j.procir.2018.05.039.

[161] E. R. Denlinger, M. Gouge, J. Irwin, P. Michaleris, Thermomechanical model development and in situ experimental validation of the Laser Powder-Bed Fusion process, Additive Manufacturing 16 (2017) 73–80. doi:10.1016/j.addma.2017.05.001.
URL http://dx.doi.org/10.1016/j.addma.2017.05.001

[162] C. Li, Z. Y. Liu, X. Y. Fang, Y. B. Guo, On the Simulation Scalability of Predicting Residual Stress and Distortion in Selective Laser Melting, Journal of Manufacturing Science and Engineering, Transactions of the ASME 140 (4) (2018) 1–10. doi:10.1115/1.4038893.

[163] I. Yadroitsava, S. Grewar, D. Hattingh, I. Yadroitsev, Residual Stress in SLM Ti6Al4V Alloy Specimens, in: Light Metals Technology 2015, Vol. 828 of Materials Science Forum, Trans Tech Publications Ltd, 2015, pp. 305–310. doi:10.4028/www.scientific.net/MSF.828-829.305.

[164] P. Mercelis, J. Kruth, Residual stresses in selective laser sintering and selective laser melting, Rapid Prototyping Journal 12 (5) (2006) 254–265. doi:10.1108/13552540610707013.
URL https://doi.org/10.1108/13552540610707013

[165] M. Shiomi, K. Osakada, K. Nakamura, T. Yamashita, F. Abe, Residual stress within metallic model made by selective laser melting process, CIRP Annals - Manufacturing Technology 53 (1) (2004) 195–198. doi:10.1016/S0007-8506(07)60677-5.

[166] D. D. Gu, W. Meiners, K. Wissenbach, R. Poprawe, Laser additive manufacturing of metallic components: Materials, processes and mechanisms, International Materials Reviews 57 (3) (2012) 133–164. doi:10.1179/1743280411Y.0000000014.

[167] G. Vastola, G. Zhang, Q. X. Pei, Y. W. Zhang, Controlling of residual stress in additive manufacturing of Ti6Al4V by finite element modeling, Additive Manufacturing 12 (2016) 231–239. doi:10.1016/j.addma.2016.05.010.
URL http://dx.doi.org/10.1016/j.addma.2016.05.010

[168] X. Zhao, A. Iyer, P. Promoppatum, S. C. Yao, Numerical modeling of the thermal behavior and residual stress in the direct metal laser sintering process of titanium alloy products, Additive Manufacturing 14 (2017) 126–136. doi:10.1016/j.addma.2016.10.005.
URL http://dx.doi.org/10.1016/j.addma.2016.10.005

[169] P. Prabhakar, W. J. Sames, R. Dehoff, S. S. Babu, Computational modeling of residual stress formation during the electron beam melting process for Inconel 718, Additive Manufacturing 7 (2015) 83–91. doi:10.1016/j.addma.2015.03.003.
URL http://dx.doi.org/10.1016/j.addma.2015.03.003

[170] T. Vilaro, C. Colin, J. D. Bartout, As-fabricated and heat-treated microstructures of the Ti-6Al-4V alloy processed by selective laser melting, Metallurgical and Materials Transactions A: Physical Metallurgy and Materials Science 42 (10) (2011) 3190–3199. doi:10.1007/s11661-011-0731-y.

[171] L. Cheng, X. Liang, J. Bai, Q. Chen, J. Lemon, A. To, On utilizing topology optimization to design support structure to prevent residual stress induced build failure in laser powder bed metal additive manufacturing, Additive Manufacturing 27 (March) (2019) 290–304. doi:10.1016/j.addma.2019.03.001.
URL https://doi.org/10.1016/j.addma.2019.03.001

[172] A. Hussein, L. Hao, C. Yan, R. Everson, P. Young, Advanced lattice support structures for metal additive manufacturing, Journal of Materials Processing Technology 213 (7) (2013) 1019–1026. doi:10.1016/j.jmatprotec.2013.01.020.
URL http://dx.doi.org/10.1016/j.jmatprotec.2013.01.020

[173] J. V. Gordon, C. V. Haden, H. F. Nied, R. P. Vinci, D. G. Harlow, Fatigue crack growth anisotropy, texture and residual stress in austenitic steel made by wire and arc additive manufacturing, Materials Science and Engineering: A 724 (December 2017) (2018) 431–438. doi:10.1016/j.msea.2018.03.075.
URL https://doi.org/10.1016/j.msea.2018.03.075

[174] A. Riemer, S. Leuders, M. Thöne, H. A. Richard, T. Tröster, T. Niendorf, On the fatigue crack growth behavior in 316L stainless steel manufactured by selective laser melting, Engineering Fracture Mechanics 120 (2014) 15–25. doi:10.1016/j.engfracmech.2014.03.008.

[175] H. Zhang, M. Xu, Z. Liu, C. Li, P. Kumar, Z. Liu, Y. Zhang, Microstructure, surface quality, residual stress, fatigue behavior and damage mechanisms of selective laser melted 304L stainless steel considering building direction, Additive Manufacturing 46 (March) (2021) 102147. doi:10.1016/j.addma.2021.102147.
URL https://doi.org/10.1016/j.addma.2021.102147

[176] S. Leuders, M. Thöne, A. Riemer, T. Niendorf, T. Tröster, H. A. Richard, H. J. Maier, On the mechanical behaviour of titanium alloy TiAl6V4 manufactured by selective laser melting: Fatigue resistance and crack growth performance, International Journal of Fatigue 48 (2013) 300–307. doi:10.1016/j.ijfatigue.2012.11.011.
URL http://dx.doi.org/10.1016/j.ijfatigue.2012.11.011

[177] T. Mukherjee, W. Zhang, T. DebRoy, An improved prediction of residual stresses and distortion in additive manufacturing, Computational Materials Science 126 (2017) 360–372. doi:10.1016/j.commatsci.2016.10.003.
URL http://dx.doi.org/10.1016/j.commatsci.2016.10.003

[178] V. Cain, L. Thijs, J. Van Humbeeck, B. Van Hooreweder, R. Knutsen, Crack propagation and fracture toughness of Ti6Al4V alloy produced by selective laser melting, Additive Manufacturing 5 (2015) 68–76. doi:10.1016/j.addma.2014.12.006.
URL http://dx.doi.org/10.1016/j.addma.2014.12.006

[179] S.-g. Chen, H.-j. Gao, Y.-d. Zhang, Q. Wu, Z.-h. Gao, X. Zhou, Review on residual stresses in metal additive manufacturing: formation mechanisms, parameter dependencies, prediction and control approaches, Journal of Materials Research and Technology 17 (2022) 2950–2974. doi:10.1016/j.jmrt.2022.02.054.
URL https://doi.org/10.1016/j.jmrt.2022.02.054

[180] S. A. David, J. M. Vitek, Correlation between solidification parameters and weld microstructures, International Materials Reviews 34 (1) (1989) 213–245. doi:10.1179/imr.1989.34.1.213.
URL https://doi.org/10.1179/imr.1989.34.1.213

[181] T. Tancogne-Dejean, A. B. Spierings, D. Mohr, Additively-manufactured metallic micro-lattice materials for high specific energy absorption under static and dynamic loading, Acta Materialia 116 (2016) 14–28. doi:10.1016/j.actamat.2016.05.054.
URL http://dx.doi.org/10.1016/j.actamat.2016.05.054

[182] T. Niendorf, F. Brenne, M. Schaper, Lattice structures manufactured by SLM: On the effect of geometrical dimensions on microstructure evolution during processing, Metallurgical and Materials Transactions B: Process Metallurgy and Materials Processing Science 45 (4) (2014) 1181–1185. doi:10.1007/s11663-014-0086-z.

[183] S. Ghouse, R. N. Oosterbeek, A. T. Mehmood, F. Vecchiato, D. Dye, J. R. Jeffers, Vacuum heat treatments of titanium porous structures, Additive Manufacturing 47 (April) (2021) 102262. doi:10.1016/j.addma.2021.102262.
URL https://doi.org/10.1016/j.addma.2021.102262

[184] L. Yang, S. Wu, C. Yan, P. Chen, L. Zhang, C. Han, C. Cai, S. Wen, Y. Zhou, Y. Shi, Fatigue properties of Ti-6Al-4V Gyroid graded lattice structures fabricated by laser powder bed fusion with lateral loading, Additive Manufacturing 46 (March) (2021) 102214. doi:10.1016/j.addma.2021.102214.
URL https://doi.org/10.1016/j.addma.2021.102214

[185] S. Ghouse, S. Babu, K. Nai, P. A. Hooper, J. R. Jeffers, The influence of laser parameters, scanning strategies and material on the fatigue strength of a stochastic porous structure, Additive Manufacturing 22 (May) (2018) 290–301. doi:10.1016/j.addma.2018.05.024.

[186] A. Großmann, J. Gosmann, C. Mittelstedt, Lightweight lattice structures in selective laser melting: Design, fabrication and mechanical properties, Materials Science and Engineering: A 766 (September) (2019) 138356. doi:10.1016/j.msea.2019.138356.
URL https://doi.org/10.1016/j.msea.2019.138356

[187] J. C. Fox, S. P. Moylan, B. M. Lane, Effect of Process Parameters on the Surface Roughness of Overhanging Structures in Laser Powder Bed Fusion Additive Manufacturing, Procedia CIRP 45 (2016) 131–134. doi:10.1016/j.procir.2016.02.347.
URL http://dx.doi.org/10.1016/j.procir.2016.02.347

[188] R. Vrána, J. Jaroš, D. Koutný, J. Nosek, T. Zikmund, J. Kaiser, D. Paloušek, Contour laser strategy and its benefits for lattice structure manufacturing by selective laser melting technology, Journal of Manufacturing Processes 74 (November 2021) (2022) 640–657. doi:10.1016/j.jmapro.2021.12.006.

[189] A. du Plessis, N. Razavi, F. Berto, The effects of microporosity in struts of gyroid lattice structures produced by laser powder bed fusion, Materials and Design 194

(2020) 108899. doi:10.1016/j.matdes.2020.108899.
URL https://doi.org/10.1016/j.matdes.2020.108899

[190] K. Karami, A. Blok, L. Weber, S. M. Ahmadi, R. Petrov, K. Nikolic, E. V. Borisov, S. Leeflang, C. Ayas, A. A. Zadpoor, M. Mehdipour, E. Reinton, V. A. Popovich, Continuous and pulsed selective laser melting of Ti6Al4V lattice structures: Effect of post-processing on microstructural anisotropy and fatigue behaviour, Additive Manufacturing 36 (July) (2020) 101433. doi:10.1016/j.addma.2020.101433.
URL http://dx.doi.org/10.1016/j.addma.2020.101433

[191] R. N. Oosterbeek, G. Sirbu, S. Hansal, K. Nai, J. R. Jeffers, Effect of chemical–electrochemical surface treatment on the roughness and fatigue performance of porous titanium lattice structures, Additive Manufacturing 78 (March) (2023) 103896. doi:10.1016/j.addma.2023.103896.
URL https://doi.org/10.1016/j.addma.2023.103896

[192] B. Van Hooreweder, Y. Apers, K. Lietaert, J. P. Kruth, Improving the fatigue performance of porous metallic biomaterials produced by Selective Laser Melting, Acta Biomaterialia 47 (2017) 193–202. doi:10.1016/j.actbio.2016.10.005.
URL http://dx.doi.org/10.1016/j.actbio.2016.10.005

[193] N. E. Uzan, S. Ramati, R. Shneck, N. Frage, O. Yeheskel, On the effect of shot-peening on fatigue resistance of AlSi10Mg specimens fabricated by additive manufacturing using selective laser melting (AM-SLM), Additive Manufacturing 21 (September 2017) (2018) 458–464. doi:10.1016/j.addma.2018.03.030.
URL https://doi.org/10.1016/j.addma.2018.03.030

[194] L. Hackel, J. R. Rankin, A. Rubenchik, W. E. King, M. Matthews, Laser peening: A tool for additive manufacturing post-processing, Additive Manufacturing 24 (May) (2018) 67–75. doi:10.1016/j.addma.2018.09.013.
URL https://doi.org/10.1016/j.addma.2018.09.013

[195] S. M. Ahmadi, R. Kumar, E. V. Borisov, R. Petrov, S. Leeflang, Y. Li, N. Tümer, R. Huizenga, C. Ayas, A. A. Zadpoor, V. A. Popovich, From microstructural design to surface engineering: A tailored approach for improving fatigue life of additively manufactured meta-biomaterials, Acta Biomaterialia 83 (2019) 153–166. doi:10.1016/j.actbio.2018.10.043.

[196] G. Meyer, J. Musekamp, F. Göbel, F. Gardian, C. Mittelstedt, Manufacturability investigation of inclined AlSi10Mg lattice struts by means of selective laser melting, Manufacturing Letters 31 (2022) 101–105. doi:10.1016/j.mfglet.2021.08.002.
URL https://doi.org/10.1016/j.mfglet.2021.08.002

[197] J. Noronha, M. Leary, M. Qian, E. Kyriakou, M. Brandt, Geometrical parameters and mechanical properties of Ti6Al4V hollow-walled lattices, Materials Science

and Engineering: A 840 (October 2021) (2022) 142667. doi:10.1016/j.msea.2022.142667.
URL https://doi.org/10.1016/j.msea.2022.142667

[198] X. Z. Zhang, H. P. Tang, J. Wang, L. Jia, Y. X. Fan, M. Leary, M. Qian, Additive manufacturing of intricate lattice materials: Ensuring robust strut additive continuity to realize the design potential, Additive Manufacturing 58 (July) (2022) 103022. doi:10.1016/j.addma.2022.103022.
URL https://doi.org/10.1016/j.addma.2022.103022

[199] R. M. Latture, R. X. Rodriguez, L. R. Holmes, F. W. Zok, Effects of nodal fillets and external boundaries on compressive response of an octet truss, Acta Materialia 149 (2018) 78–87. doi:10.1016/j.actamat.2017.12.060.
URL http://dx.doi.org/10.1016/j.actamat.2017.12.060

[200] S. Ren, Y. Chen, T. Liu, X. Qu, Effect of Build Orientation on Mechanical Properties and Microstructure of Ti-6Al-4V Manufactured by Selective Laser Melting, Metallurgical and Materials Transactions A: Physical Metallurgy and Materials Science 50 (9) (2019) 4388–4409. doi:10.1007/s11661-019-05322-w.
URL https://doi.org/10.1007/s11661-019-05322-w

[201] L. Yang, Y. Li, Y. Chen, C. Yan, B. Liu, Y. Shi, Topologically optimized lattice structures with superior fatigue performance, International Journal of Fatigue 165 (August) (2022) 107188. doi:10.1016/j.ijfatigue.2022.107188.
URL https://doi.org/10.1016/j.ijfatigue.2022.107188

[202] G. Savio, A. Curtarello, S. Rosso, R. Meneghello, G. Concheri, Homogenization driven design of lightweight structures for additive manufacturing, International Journal on Interactive Design and Manufacturing 13 (1) (2019) 263–276. doi:10.1007/s12008-019-00543-0.
URL https://doi.org/10.1007/s12008-019-00543-0

[203] S. Raghavendra, M. Dallago, F. Zanini, S. Carmignato, F. Berto, M. Benedetti, A probabilistic average strain energy density approach to assess the fatigue strength of additively manufactured cellular lattice materials, International Journal of Fatigue 172 (March) (2023) 107601. doi:10.1016/j.ijfatigue.2023.107601.
URL https://doi.org/10.1016/j.ijfatigue.2023.107601

[204] M. Dallago, S. Raghavendra, V. Fontanari, M. Benedetti, Stress concentration factors for planar square cell lattices with filleted junctions, Material Design and Processing Communications 2 (2) (2020) 1–8. doi:10.1002/mdp2.98.

[205] G. Savio, R. Meneghello, G. Concheri, Geometric modeling of lattice structures for additive manufacturing, Rapid Prototyping Journal 24 (2) (2018) 351–360. doi:10.1108/RPJ-07-2016-0122.
URL https://doi.org/10.1108/RPJ-07-2016-0122

[206] M. Zhao, F. Liu, G. Fu, D. Z. Zhang, T. Zhang, H. Zhou, Improved mechanical properties and energy absorption of BCC lattice structures with triply periodic minimal surfaces fabricated by SLM, Materials 11 (12) (2018). doi:10.3390/ma11122411.

[207] S. Wang, J. Wang, Y. Xu, W. Zhang, J. Zhu, Compressive behavior and energy absorption of polymeric lattice structures made by additive manufacturing, Frontiers of Mechanical Engineering 15 (2) (2020) 319–327. doi:10.1007/s11465-019-0549-7.

[208] W. Tao, DESIGN OF LATTICE STRUCTURE FOR ADDITIVE MANUFACTURING, Proceedings of ISFA2016 2016 International Symposium on Flexible Automation (2016) 1–3.

[209] C. Pan, Y. Han, J. Lu, Design and optimization of lattice structures: A review, Applied Sciences (Switzerland) 10 (18) (2020) 1–36. doi:10.3390/APP10186374.

[210] C. Liu, M. Pham, Spatially Programmable Architected Materials Inspired by The Metallurgical Phase Engineering, Advanced Materials 2305846 (2023) 1–8. doi:10.1002/adma.202305846.

[211] J. Nguyen, S. I. Park, D. W. Rosen, L. Folgar, J. Williams, Conformal lattice structure design and fabrication, 23rd Annual International Solid Freeform Fabrication Symposium - An Additive Manufacturing Conference, SFF 2012 (2012) 138–161.

[212] S. Xu, J. Shen, S. Zhou, X. Huang, Y. M. Xie, Design of lattice structures with controlled anisotropy, Materials and Design 93 (2016) 443–447. doi:10.1016/j.matdes.2016.01.007.
URL http://dx.doi.org/10.1016/j.matdes.2016.01.007

[213] D. Li, W. Liao, N. Dai, Y. M. Xie, Anisotropic design and optimization of conformal gradient lattice structures, CAD Computer Aided Design 119 (2020) 102787. doi:10.1016/j.cad.2019.102787.
URL https://doi.org/10.1016/j.cad.2019.102787

[214] J. Fu, J. Ding, L. Zhang, S. Qu, X. Song, M. W. Fu, Development of conformal shell lattices via laser powder bed fusion and unraveling their mechanical responses via modeling and experiments, Additive Manufacturing 62 (January) (2023). doi:10.1016/j.addma.2023.103406.

[215] J. Liu, A. T. Gaynor, S. Chen, Z. Kang, K. Suresh, A. Takezawa, L. Li, J. Kato, J. Tang, C. C. Wang, L. Cheng, X. Liang, A. C. To, Current and future trends in topology optimization for additive manufacturing, Structural and Multidisciplinary Optimization 57 (6) (2018) 2457–2483. doi:10.1007/s00158-018-1994-3.

[216] A. du Plessis, C. Broeckhoven, I. Yadroitsava, I. Yadroitsev, C. H. Hands, R. Kunju, D. Bhate, Beautiful and Functional: A Review of Biomimetic Design in Additive Manufacturing, Additive Manufacturing 27 (March) (2019) 408–427. doi:10.1016/j.addma.2019.03.033.
URL https://doi.org/10.1016/j.addma.2019.03.033

[217] A. M. Vilardell, A. Takezawa, A. du Plessis, N. Takata, P. Krakhmalev, M. Kobashi, I. Yadroitsava, I. Yadroitsev, Topology optimization and characterization of Ti6Al4V ELI cellular lattice structures by laser powder bed fusion for biomedical applications, Materials Science and Engineering: A 766 (August) (2019) 138330. doi:10.1016/j.msea.2019.138330.
URL https://doi.org/10.1016/j.msea.2019.138330

[218] X. Wang, S. Xu, S. Zhou, W. Xu, M. Leary, P. Choong, M. Qian, M. Brandt, Y. M. Xie, Topological design and additive manufacturing of porous metals for bone scaffolds and orthopaedic implants: A review, Biomaterials 83 (2016) 127–141. doi:10.1016/j.biomaterials.2016.01.012.
URL http://dx.doi.org/10.1016/j.biomaterials.2016.01.012

[219] D. Brackett, I. Ashcroft, R. Hague, Topology optimization for additive manufacturing, Proceedings of the Solid Freeform Fabrication Symposium, Austin, TX (2011) 348–362.

[220] M. Leary, L. Merli, F. Torti, M. Mazur, M. Brandt, Optimal topology for additive manufacture: A method for enabling additive manufacture of support-free optimal structures, Materials and Design 63 (2014) 678–690. doi:10.1016/j.matdes.2014.06.015.
URL http://dx.doi.org/10.1016/j.matdes.2014.06.015

[221] A. T. Gaynor, J. K. Guest, Topology optimization considering overhang constraints: Eliminating sacrificial support material in additive manufacturing through design, Structural and Multidisciplinary Optimization 54 (5) (2016) 1157–1172. doi:10.1007/s00158-016-1551-x.
URL http://dx.doi.org/10.1007/s00158-016-1551-x

[222] K. Hu, S. Jin, C. C. Wang, Support slimming for single material based additive manufacturing, CAD Computer Aided Design 65 (2015) 1–10. doi:10.1016/j.cad.2015.03.001.
URL http://dx.doi.org/10.1016/j.cad.2015.03.001

[223] M. Langelaar, Topology optimization of 3D self-supporting structures for additive manufacturing, Additive Manufacturing 12 (2016) 60–70. doi:10.1016/j.addma.2016.06.010.
URL http://dx.doi.org/10.1016/j.addma.2016.06.010

[224] X. Qian, Undercut and overhang angle control in topology optimization: A density gradient based integral approach, International Journal for Numerical Methods in Engineering 111 (3) (2017) 247–272. doi:https://doi.org/10.1002/nme.5461.
URL https://doi.org/10.1002/nme.5461

[225] J. Wu, C. C. Wang, X. Zhang, R. Westermann, Self-supporting rhombic infill structures for additive manufacturing, CAD Computer Aided Design 80 (2016) 32–42. doi:10.1016/j.cad.2016.07.006.
URL http://dx.doi.org/10.1016/j.cad.2016.07.006

[226] Y. Mass, O. Amir, Topology optimization for additive manufacturing: Accounting for overhang limitations using a virtual skeleton, Additive Manufacturing 18 (2017) 58–73. doi:10.1016/j.addma.2017.08.001.
URL https://doi.org/10.1016/j.addma.2017.08.001

[227] A. Ajdari, B. H. Jahromi, J. Papadopoulos, H. Nayeb-Hashemi, A. Vaziri, Hierarchical honeycombs with tailorable properties, International Journal of Solids and Structures 49 (11-12) (2012) 1413–1419. doi:10.1016/j.ijsolstr.2012.02.029.
URL http://dx.doi.org/10.1016/j.ijsolstr.2012.02.029

[228] S. Banerjee, On the mechanical properties of hierarchical lattices, Mechanics of Materials 72 (2014) 19–32. doi:10.1016/j.mechmat.2014.01.009.
URL http://dx.doi.org/10.1016/j.mechmat.2014.01.009

[229] R. Oftadeh, B. Haghpanah, D. Vella, A. Boudaoud, A. Vaziri, Optimal fractal-like hierarchical honeycombs, Physical Review Letters 113 (10) (2014) 1–5. doi:10.1103/PhysRevLett.113.104301.

[230] H. L. Fan, F. N. Jin, D. N. Fang, Mechanical properties of hierarchical cellular materials. Part I: Analysis, Composites Science and Technology 68 (15-16) (2008) 3380–3387. doi:10.1016/j.compscitech.2008.09.022.
URL http://dx.doi.org/10.1016/j.compscitech.2008.09.022

[231] H. Fan, Y. Luo, F. Yang, W. Li, Approaching perfect energy absorption through structural hierarchy, International Journal of Engineering Science 130 (2018) 12–32. doi:10.1016/j.ijengsci.2018.05.005.
URL https://doi.org/10.1016/j.ijengsci.2018.05.005

[232] L. R. Meza, A. J. Zelhofer, N. Clarke, A. J. Mateos, D. M. Kochmann, J. R. Greer, Resilient 3D hierarchical architected metamaterials, Proceedings of the National Academy of Sciences of the United States of America 112 (37) (2015) 11502–11507. doi:10.1073/pnas.1509120112.

[233] Y. Sha, L. Jiani, C. Haoyu, R. O. Ritchie, X. Jun, Design and strengthening mechanisms in hierarchical architected materials processed using additive manu-

facturing, International Journal of Mechanical Sciences 149 (July) (2018) 150–163. doi:10.1016/j.ijmecsci.2018.09.038.

[234] S. Yin, H. Chen, J. Li, T. X. Yu, J. Xu, Effects of architecture level on mechanical properties of hierarchical lattice materials, International Journal of Mechanical Sciences 157-158 (37) (2019) 282–292. doi:10.1016/j.ijmecsci.2019.04.051.

[235] L. Musenich, A. Stagni, F. Libonati, Design of hierarchical lattice structures attainable by additive manufacturing techniques, IOP Conference Series: Materials Science and Engineering 1275 (1) (2023) 012003. doi:10.1088/1757-899x/1275/1/012003.

[236] J. Parthasarathy, B. Starly, S. Raman, A design for the additive manufacture of functionally graded porous structures with tailored mechanical properties for biomedical applications, Journal of Manufacturing Processes 13 (2) (2011) 160–170. doi:10.1016/j.jmapro.2011.01.004.

[237] J. Plocher, A. Panesar, Effect of density and unit cell size grading on the stiffness and energy absorption of short fibre-reinforced functionally graded lattice structures, Additive Manufacturing 33 (February) (2020). doi:10.1016/j.addma.2020.101171.

[238] S. Y. Choy, C. N. Sun, K. F. Leong, J. Wei, Compressive properties of functionally graded lattice structures manufactured by selective laser melting, Materials and Design 131 (March) (2017) 112–120. doi:10.1016/j.matdes.2017.06.006.

[239] F. Liu, Z. Mao, P. Zhang, D. Z. Zhang, J. Jiang, Z. Ma, Functionally graded porous scaffolds in multiple patterns: New design method, physical and mechanical properties, Materials and Design 160 (2018) 849–860. doi:10.1016/j.matdes.2018.09.053.

[240] I. Maskery, A. O. Aremu, L. Parry, R. D. Wildman, C. J. Tuck, I. A. Ashcroft, Corrigendum to "Effective design and simulation of surface-based lattice structures featuring volume fraction and cell type grading" (Materials Design (2018) 155 (220–232), (S026412751830443X) (10.1016/j.matdes.2018.05.058)), Materials and Design 160 (2018) 106–107. doi:10.1016/j.matdes.2018.09.007.

[241] D. S. Al-Saedi, S. H. Masood, M. Faizan-Ur-Rab, A. Alomarah, P. Ponnusamy, Mechanical properties and energy absorption capability of functionally graded F2BCC lattice fabricated by SLM, Materials and Design 144 (2018) 32–44. doi:10.1016/j.matdes.2018.01.059.

[242] H. Montazerian, M. G. Mohamed, M. M. Montazeri, S. Kheiri, A. S. Milani, K. Kim, M. Hoorfar, Permeability and mechanical properties of gradient porous PDMS scaffolds fabricated by 3D-printed sacrificial templates designed with minimal surfaces, Acta Biomaterialia 96 (2019) 149–160. doi:10.1016/j.actbio.

2019.06.040.
URL https://doi.org/10.1016/j.actbio.2019.06.040

[243] L. Y. Chen, S. X. Liang, Y. Liu, L. C. Zhang, Additive manufacturing of metallic lattice structures: Unconstrained design, accurate fabrication, fascinated performances, and challenges, Materials Science and Engineering R: Reports 146 (August) (2021) 100648. doi:10.1016/j.mser.2021.100648.
URL https://doi.org/10.1016/j.mser.2021.100648

[244] J. Wang, A. Panesar, Machine learning based lattice generation method derived from topology optimisation, Additive Manufacturing 60 (September) (2022). doi:10.1016/j.addma.2022.103238.

[245] N. Després, E. Cyr, P. Setoodeh, M. Mohammadi, Deep Learning and Design for Additive Manufacturing: A Framework for Microlattice Architecture, Jom 72 (6) (2020) 2408–2418. doi:10.1007/s11837-020-04131-6.

[246] H. T. Kollmann, D. W. Abueidda, S. Koric, E. Guleryuz, N. A. Sobh, Deep learning for topology optimization of 2D metamaterials, Materials and Design 196 (2020). doi:10.1016/j.matdes.2020.109098.

[247] C. Wu, J. Luo, J. Zhong, Y. Xu, B. Wan, W. Huang, J. Fang, G. P. Steven, G. Sun, Q. Li, Topology optimisation for design and additive manufacturing of functionally graded lattice structures using derivative-aware machine learning algorithms, Additive Manufacturing 78 (May) (2023). doi:10.1016/j.addma.2023.103833.

[248] A. P. Garland, B. C. White, S. C. Jensen, B. L. Boyce, Pragmatic generative optimization of novel structural lattice metamaterials with machine learning, Materials and Design 203 (2021) 11–19. doi:10.1016/j.matdes.2021.109632.

[249] H. Hassanin, Y. Alkendi, M. Elsayed, K. Essa, Y. Zweiri, Controlling the Properties of Additively Manufactured Cellular Structures Using Machine Learning Approaches, Advanced Engineering Materials 22 (3) (2020) 1901338. doi:https://doi.org/10.1002/adem.201901338.
URL https://doi.org/10.1002/adem.201901338

[250] A. Challapalli, D. Patel, G. Li, Inverse machine learning framework for optimizing lightweight metamaterials, Materials and Design 208 (2021). doi:10.1016/j.matdes.2021.109937.

[251] L. Zheng, S. Kumar, D. M. Kochmann, Data-driven topology optimization of spinodoid metamaterials with seamlessly tunable anisotropy, Computer Methods in Applied Mechanics and Engineering 383 (2021) 113894. arXiv:2012.15744, doi:10.1016/j.cma.2021.113894.
URL https://doi.org/10.1016/j.cma.2021.113894

[252] D. Barba, C. Alabort, Y. T. Tang, M. J. Viscasillas, R. C. Reed, E. Alabort, On the size and orientation effect in additive manufactured Ti-6Al-4V, Materials and Design 186 (2020) 108235. doi:10.1016/j.matdes.2019.108235.
URL https://doi.org/10.1016/j.matdes.2019.108235

[253] A. Carpinteri, A. Spagnoli, S. Vantadori, Size effect in S-N curves: A fractal approach to finite-life fatigue strength, International Journal of Fatigue 31 (5) (2009) 927–933. doi:10.1016/j.ijfatigue.2008.10.001.
URL http://dx.doi.org/10.1016/j.ijfatigue.2008.10.001

[254] D. El Khoukhi, F. Morel, N. Saintier, D. Bellett, P. Osmond, V. D. Le, Probabilistic modeling of the size effect and scatter in High Cycle Fatigue using a Monte-Carlo approach: Role of the defect population in cast aluminum alloys, International Journal of Fatigue 147 (January) (2021) 106177. doi:10.1016/j.ijfatigue.2021.106177.
URL https://doi.org/10.1016/j.ijfatigue.2021.106177

[255] T. Tomaszewski, Modelling of critical defect distributions for estimating the size effect of selective laser melted 316L stainless steel, International Journal of Fatigue 167 (PA) (2023) 107378. doi:10.1016/j.ijfatigue.2022.107378.
URL https://doi.org/10.1016/j.ijfatigue.2022.107378

[256] Y. Zhai, H. Galarraga, D. A. Lados, Microstructure, static properties, and fatigue crack growth mechanisms in Ti-6Al-4V fabricated by additive manufacturing: LENS and EBM, Engineering Failure Analysis 69 (2016) 3–14. doi:10.1016/j.engfailanal.2016.05.036.
URL http://dx.doi.org/10.1016/j.engfailanal.2016.05.036

[257] J. Pegues, M. Roach, R. Scott Williamson, N. Shamsaei, Surface roughness effects on the fatigue strength of additively manufactured Ti-6Al-4V, International Journal of Fatigue 116 (April) (2018) 543–552. doi:10.1016/j.ijfatigue.2018.07.013.
URL https://doi.org/10.1016/j.ijfatigue.2018.07.013

[258] S. M. Razavi, B. Van Hooreweder, F. Berto, Effect of build thickness and geometry on quasi-static and fatigue behavior of Ti-6Al-4V produced by Electron Beam Melting, Additive Manufacturing 36 (November 2019) (2020) 101426. doi:10.1016/j.addma.2020.101426.
URL https://doi.org/10.1016/j.addma.2020.101426

[259] S. Ghods, R. Schur, A. Montelione, R. Schleusener, D. D. Arola, M. Ramulu, Importance of Build Design Parameters to the Fatigue Strength of Ti6Al4V in Electron Beam Melting Additive Manufacturing, Materials 15 (16) (2022). doi:10.3390/ma15165617.

[260] Z. Dong, X. Zhang, W. Shi, H. Zhou, H. Lei, J. Liang, Study of size effect on microstructure and mechanical properties of AlSi10Mg samples made by selective laser melting, Materials 11 (12) (2018). doi:10.3390/ma11122463.

[261] E. Hernández-Nava, C. J. Smith, F. Derguti, S. Tammas-Williams, F. Léonard, P. J. Withers, I. Todd, R. Goodall, The effect of density and feature size on mechanical properties of isostructural metallic foams produced by additive manufacturing, Acta Materialia 85 (2015) 387–395. doi:10.1016/j.actamat.2014.10.058.

[262] ASTM E8, ASTM E8/E8M standard test methods for tension testing of metallic materials 1, Annual Book of ASTM Standards 4 (C) (2010) 1–27. doi:10.1520/E0008.

[263] E. Maire, P. J. Withers, E. Maire, P. J. Withers, Quantitative X-ray tomography, International Materials Reviews 59 (1) (2014) 1–43. doi:10.1179/1743280413Y.0000000023.

[264] N. Otsu, A Threshold Selection Method from Gray-Level Histograms, IEEE TRANSACTIONS ON SYSTREMS, MAN, AND CYBERNETICS 9 (1) (1979) 62–66.

[265] D. El Khoukhi, F. Morel, N. Saintier, D. Bellett, P. Osmond, V. D. Le, J. Adrien, Experimental investigation of the size effect in high cycle fatigue: Role of the defect population in cast aluminium alloys, International Journal of Fatigue 129 (May) (2019) 105222. doi:10.1016/j.ijfatigue.2019.105222.
URL https://doi.org/10.1016/j.ijfatigue.2019.105222

[266] J. W. Pegues, S. Shao, N. Shamsaei, N. Sanaei, A. Fatemi, D. H. Warner, P. Li, N. Phan, Fatigue of additive manufactured Ti-6Al-4V, Part I: The effects of powder feedstock, manufacturing, and post-process conditions on the resulting microstructure and defects, International Journal of Fatigue 132 (November 2019) (2020). doi:10.1016/j.ijfatigue.2019.105358.

[267] X. Tan, Y. Kok, Y. J. Tan, G. Vastola, Q. X. Pei, G. Zhang, Y. W. Zhang, S. B. Tor, K. F. Leong, C. K. Chua, An experimental and simulation study on build thickness dependent microstructure for electron beam melted Ti-6Al-4V, Journal of Alloys and Compounds 646 (2015) 303–309. doi:10.1016/j.jallcom.2015.05.178.
URL http://dx.doi.org/10.1016/j.jallcom.2015.05.178

[268] N. T. Aboulkhair, N. M. Everitt, I. Ashcroft, C. Tuck, Reducing porosity in AlSi10Mg parts processed by selective laser melting, Additive Manufacturing 1 (2014) 77–86. doi:10.1016/j.addma.2014.08.001.
URL http://dx.doi.org/10.1016/j.addma.2014.08.001

[269] R. Hielscher, H. Schaeben, A novel pole figure inversion method: Specification of the MTEX algorithm, Journal of Applied Crystallography 41 (6) (2008) 1024–1037. doi:10.1107/S0021889808030112.

[270] C. Leyens, M. Peters, Titanium and titanium alloys, 2003. doi:10.1007/978-3-319-69743-7_7.

[271] N. Raghavan, R. Dehoff, S. Pannala, S. Simunovic, M. Kirka, J. Turner, N. Carlson, S. S. Babu, Numerical modeling of heat-transfer and the influence of process parameters on tailoring the grain morphology of IN718 in electron beam additive manufacturing, Acta Materialia 112 (2016) 303–314. doi:10.1016/j.actamat.2016.03.063.

[272] H. Beladi, Q. Chao, G. S. Rohrer, Variant selection and intervariant crystallographic planes distribution in martensite in a Ti-6Al-4V alloy, Acta Materialia 80 (2014) 478–489. doi:10.1016/j.actamat.2014.06.064.
URL http://dx.doi.org/10.1016/j.actamat.2014.06.064

[273] K. Yamanaka, W. Saito, M. Mori, H. Matsumoto, A. Chiba, Preparation of weak-textured commercially pure titanium by electron beam melting, Additive Manufacturing 8 (2015) 105–109. doi:10.1016/j.addma.2015.09.007.
URL http://dx.doi.org/10.1016/j.addma.2015.09.007

[274] X. P. Li, J. Van Humbeeck, J. P. Kruth, Selective laser melting of weak-textured commercially pure titanium with high strength and ductility: A study from laser power perspective, Materials and Design 116 (2017) 352–358. doi:10.1016/j.matdes.2016.12.019.

[275] I. Ghamarian, B. Hayes, P. Samimi, B. A. Welk, H. L. Fraser, P. C. Collins, Developing a phenomenological equation to predict yield strength from composition and microstructure in β processed Ti-6Al-4V, Materials Science and Engineering A 660 (2016) 172–180. doi:10.1016/j.msea.2016.02.052.
URL http://dx.doi.org/10.1016/j.msea.2016.02.052

[276] K. Kempen, B. Vrancken, S. Buls, L. Thijs, J. Van Humbeeck, J. P. Kruth, Selective Laser Melting of Crack-Free High Density M2 High Speed Steel Parts by Baseplate Preheating, Journal of Manufacturing Science and Engineering, Transactions of the ASME 136 (6) (2014) 1–6. doi:10.1115/1.4028513.

[277] O. Poncelet, M. Marteleur, C. van der Rest, O. Rigo, J. Adrien, S. Dancette, P. J. Jacques, A. Simar, Critical assessment of the impact of process parameters on vertical roughness and hardness of thin walls of AlSi10Mg processed by laser powder bed fusion, Additive Manufacturing 38 (December 2020) (2021) 101801. doi:10.1016/j.addma.2020.101801.
URL https://doi.org/10.1016/j.addma.2020.101801

[278] J. Damon, S. Dietrich, F. Vollert, J. Gibmeier, V. Schulze, Process dependent porosity and the in fl uence of shot peening on porosity morphology regarding selective laser melted AlSi10Mg parts, Additive Manufacturing 20 (2018) 77–89. doi:10.1016/j.addma.2018.01.001.
URL https://doi.org/10.1016/j.addma.2018.01.001

[279] A. D. Plessis, S. G. le Roux, Standardized X-ray tomography testing of additively manufactured parts : A round robin test, Additive Manufacturing 24 (2018) 125–136. doi:10.1016/j.addma.2018.09.014.
URL https://doi.org/10.1016/j.addma.2018.09.014

[280] A. D. Plessis, D. Glaser, S. Africa, N. R. Mathe, S. Africa, Pore closure effect of laser shock peening of additively manufactured AlSi10Mg, 3D Printing and Additive Manufacturing 6 (5) (2019) 245–252. doi:10.1089/3dp.2019.0064.

[281] I. Tsukrov, M. Kachanov, Stress concentrations and microfracturing patterns in a brittle-elastic solid with interacting pores of diverse shapes, International Journal of Solids and Structures 34 (22) (1997) 2887–2904. doi:10.1016/S0020-7683(96)00202-8.
URL http://dx.doi.org/10.1016/S0020-7683(96)00202-8

[282] H. Gong, K. Rafi, H. Gu, T. Starr, B. Stucker, Analysis of defect generation in Ti-6Al-4V parts made using powder bed fusion additive manufacturing processes, Additive Manufacturing 1 (2014) 87–98. doi:10.1016/j.addma.2014.08.002.
URL http://dx.doi.org/10.1016/j.addma.2014.08.002

[283] G. Kasperovich, J. Haubrich, J. Gussone, G. Requena, Correlation between porosity and processing parameters in TiAl6V4 produced by selective laser melting, Materials and Design 105 (2016) 160–170. doi:10.1016/j.matdes.2016.05.070.
URL http://dx.doi.org/10.1016/j.matdes.2016.05.070

[284] A. Nouri, A. Rohani Shirvan, Y. Li, C. Wen, Additive manufacturing of metallic and polymeric load-bearing biomaterials using laser powder bed fusion: A review, Journal of Materials Science and Technology 94 (2021) 196–215. doi:10.1016/j.jmst.2021.03.058.
URL https://doi.org/10.1016/j.jmst.2021.03.058

[285] E. O. Olakanmi, R. F. Cochrane, K. W. Dalgarno, A review on selective laser sintering/melting (SLS/SLM) of aluminium alloy powders: Processing, microstructure, and properties, Progress in Materials Science 74 (2015) 401–477. doi:10.1016/j.pmatsci.2015.03.002.
URL http://dx.doi.org/10.1016/j.pmatsci.2015.03.002

[286] B. Vayssette, N. Saintier, C. Brugger, M. El May, E. Pessard, Numerical modelling of surface roughness effect on the fatigue behavior of Ti-6Al-4V obtained by

additive manufacturing, International Journal of Fatigue 123 (February) (2019) 180–195. doi:10.1016/j.ijfatigue.2019.02.014.
URL https://doi.org/10.1016/j.ijfatigue.2019.02.014

[287] G. Lütjering, Influence of processing on microstructure and mechanical properties of ($\alpha + \beta$) titanium alloys, Materials Science and Engineering A 243 (1-2) (1998) 32–45. doi:10.1016/s0921-5093(97)00778-8.

[288] A. Fatemi, R. Molaei, S. Sharifimehr, N. Shamsaei, N. Phan, Torsional fatigue behavior of wrought and additive manufactured Ti-6Al-4V by powder bed fusion including surface finish effect, International Journal of Fatigue 99 (2017) 187–201. doi:10.1016/j.ijfatigue.2017.03.002.
URL http://dx.doi.org/10.1016/j.ijfatigue.2017.03.002

[289] P. Kumar, U. Ramamurty, Microstructural optimization through heat treatment for enhancing the fracture toughness and fatigue crack growth resistance of selective laser melted Ti–6Al–4V alloy, Acta Materialia 169 (2019) 45–59. doi:10.1016/j.actamat.2019.03.003.
URL https://doi.org/10.1016/j.actamat.2019.03.003

[290] Y. Li, K. Lietaert, W. Li, X. Y. Zhang, M. A. Leeflang, J. Zhou, A. A. Zadpoor, Corrosion fatigue behavior of additively manufactured biodegradable porous iron, Corrosion Science 156 (April) (2019) 106–116. doi:10.1016/j.corsci.2019.05.003.

[291] U. Karr, B. Schönbauer, M. Fitzka, E. Tamura, Y. Sandaiji, S. Murakami, H. Mayer, Inclusion initiated fracture under cyclic torsion very high cycle fatigue at different load ratios, International Journal of Fatigue 122 (November 2018) (2019) 199–207. doi:10.1016/j.ijfatigue.2019.01.015.
URL https://doi.org/10.1016/j.ijfatigue.2019.01.015

[292] S. C. Wu, Z. Song, G. Z. Kang, Y. N. Hu, Y. N. Fu, The Kitagawa-Takahashi fatigue diagram to hybrid welded AA7050 joints via synchrotron X-ray tomography, International Journal of Fatigue 125 (March) (2019) 210–221. doi:10.1016/j.ijfatigue.2019.04.002.

[293] Z. Xu, W. Wen, T. Zhai, Effects of pore position in depth on stress/strain concentration and fatigue crack initiation, Metallurgical and Materials Transactions A: Physical Metallurgy and Materials Science 43 (8) (2012) 2763–2770. doi:10.1007/s11661-011-0947-x.

[294] A. J. Sterling, B. Torries, N. Shamsaei, S. M. Thompson, D. W. Seely, Fatigue behavior and failure mechanisms of direct laser deposited Ti-6Al-4V, Materials Science and Engineering A 655 (2016) 100–112. doi:10.1016/j.msea.2015.12.026.
URL http://dx.doi.org/10.1016/j.msea.2015.12.026

[295] W. Chi, G. Li, W. Wang, C. Sun, Interior initiation and early growth of very high cycle fatigue crack in an additively manufactured Ti-alloy, International Journal of Fatigue 160 (October 2021) (2022) 106862. doi:10.1016/j.ijfatigue.2022.106862.
URL https://doi.org/10.1016/j.ijfatigue.2022.106862

[296] J. Nafar Dastgerdi, O. Jaberi, H. Remes, P. Lehto, H. Hosseini Toudeshky, J. Kuva, Fatigue damage process of additively manufactured 316 L steel using X-ray computed tomography imaging, Additive Manufacturing 70 (January) (2023) 103559. doi:10.1016/j.addma.2023.103559.
URL https://doi.org/10.1016/j.addma.2023.103559

[297] A. Polasik, The Role of Microstructure on High Cycle Fatigue Lifetime Variability in Ti-6Al-4V DISSERTATION Presented in Partial Fulfillment of the Requirements for the Degree Doctor of Philosophy in the Graduate School of The Ohio State University By Alison Polasik, Ph.D. thesis (2014).

[298] M. T. Hasib, H. E. Ostergaard, Q. Liu, X. Li, J. J. Kruzic, Tensile and fatigue crack growth behavior of commercially pure titanium produced by laser powder bed fusion additive manufacturing, Additive Manufacturing 45 (May) (2021) 102027. doi:10.1016/j.addma.2021.102027.
URL https://doi.org/10.1016/j.addma.2021.102027

[299] H. Galarraga, R. J. Warren, D. A. Lados, R. R. Dehoff, M. M. Kirka, Fatigue crack growth mechanisms at the microstructure scale in as-fabricated and heat treated Ti-6Al-4V ELI manufactured by electron beam melting (EBM), Engineering Fracture Mechanics 176 (2017) 263–280. doi:10.1016/j.engfracmech.2017.03.024.
URL http://dx.doi.org/10.1016/j.engfracmech.2017.03.024

[300] Z. H. Jiao, R. D. Xu, H. C. Yu, X. R. Wu, Evaluation on Tensile and Fatigue Crack Growth Performances of Ti6Al4V Alloy Produced by Selective Laser Melting, Procedia Structural Integrity 7 (2017) 124–132. doi:10.1016/j.prostr.2017.11.069.

[301] K. F. Walker, Q. Liu, M. Brandt, Evaluation of fatigue crack propagation behaviour in Ti-6Al-4V manufactured by selective laser melting, International Journal of Fatigue 104 (2017) 302–308. doi:10.1016/j.ijfatigue.2017.07.014.
URL http://dx.doi.org/10.1016/j.ijfatigue.2017.07.014

[302] R. Molaei, A. Fatemi, N. Phan, Significance of hot isostatic pressing (HIP) on multiaxial deformation and fatigue behaviors of additive manufactured Ti-6Al-4V including build orientation and surface roughness effects, International Journal of Fatigue 117 (April) (2018) 352–370. doi:10.1016/j.ijfatigue.2018.07.035.
URL https://doi.org/10.1016/j.ijfatigue.2018.07.035

[303] G. Qian, Y. Li, D. S. Paolino, A. Tridello, F. Berto, Y. Hong, Very-high-cycle fatigue behavior of Ti-6Al-4V manufactured by selective laser melting: Effect of build orientation, International Journal of Fatigue 136 (March) (2020) 105628. doi:10.1016/j.ijfatigue.2020.105628.
URL https://doi.org/10.1016/j.ijfatigue.2020.105628

[304] G. Nicoletto, Anisotropic high cycle fatigue behavior of Ti–6Al–4V obtained by powder bed laser fusion, International Journal of Fatigue 94 (2017) 255–262. doi:10.1016/j.ijfatigue.2016.04.032.

[305] W. Sun, Y. Ma, W. Huang, W. Zhang, X. Qian, Effects of build direction on tensile and fatigue performance of selective laser melting Ti6Al4V titanium alloy, International Journal of Fatigue 130 (June 2019) (2020). doi:10.1016/j.ijfatigue.2019.105260.

[306] A. Cutolo, C. Elangeswaran, G. K. Muralidharan, B. Van Hooreweder, On the role of building orientation and surface post-processes on the fatigue life of Ti-6Al-4V coupons manufactured by laser powder bed fusion, Materials Science and Engineering: A 840 (January) (2022) 142747. doi:10.1016/j.msea.2022.142747.
URL https://doi.org/10.1016/j.msea.2022.142747

[307] Z. Zou, M. Simonelli, J. Katrib, G. Dimitrakis, R. Hague, Microstructure and tensile properties of additive manufactured Ti-6Al-4V with refined prior-β grain structure obtained by rapid heat treatment, Materials Science and Engineering: A 814 (November 2020) (2021) 141271. doi:10.1016/j.msea.2021.141271.
URL https://doi.org/10.1016/j.msea.2021.141271

[308] MTEX, MTEX 5.8.2 toolbox (2022).

[309] F. Niessen, T. Nyyssönen, A. A. Gazder, R. Hielscher, Parent grain reconstruction from partially or fully transformed microstructures in MTEX, Journal of Applied Crystallography 55 (2022) 180–194. arXiv:2104.14603, doi:10.1107/S1600576721011560.

[310] U. Paggi, L. Thijs, B. V. Hooreweder, Implementation of contactless supports for industrially relevant additively manufactured parts in metal, Additive Manufacturing Letters 3 (June) (2022) 100095. doi:10.1016/j.addlet.2022.100095.
URL https://doi.org/10.1016/j.addlet.2022.100095

[311] S. Hémery, A. Nait-Ali, P. Villechaise, Combination of in-situ SEM tensile test and FFT-based crystal elasticity simulations of Ti-6Al-4V for an improved description of the onset of plastic slip, Mechanics of Materials 109 (2017) 1–10. doi:10.1016/j.mechmat.2017.03.013.

[312] V. Hasija, S. Ghosh, M. J. Mills, D. S. Joseph, Deformation and creep modeling in polycrystalline Ti-6Al alloys, Acta Materialia 51 (15) (2003) 4533–4549. doi:10.1016/S1359-6454(03)00289-1.

[313] I. Bantounas, D. Dye, T. C. Lindley, The effect of grain orientation on fracture morphology during high-cycle fatigue of Ti-6Al-4V, Acta Materialia 57 (12) (2009) 3584–3595. doi:10.1016/j.actamat.2009.04.018.
URL http://dx.doi.org/10.1016/j.actamat.2009.04.018

[314] A. Moridi, A. G. Demir, L. Caprio, A. J. Hart, B. Previtali, B. M. Colosimo, Deformation and failure mechanisms of Ti–6Al–4V as built by selective laser melting, Materials Science and Engineering A 768 (July) (2019). doi:10.1016/j.msea.2019.138456.

[315] R. Zhao, C. Chen, W. Wang, T. Cao, S. Shuai, S. Xu, T. Hu, H. Liao, J. Wang, Z. Ren, On the role of volumetric energy density in the microstructure and mechanical properties of laser powder bed fusion Ti-6Al-4V alloy, Additive Manufacturing 51 (September 2021) (2022) 102605. doi:10.1016/j.addma.2022.102605.
URL https://doi.org/10.1016/j.addma.2022.102605

[316] J. C. Williams, R. G. Baggerly, N. E. Paton, Deformation behavior of HCP Ti-Al alloy single crystals, Metallurgical and Materials Transactions A: Physical Metallurgy and Materials Science 33 (13) (2002) 837–850. doi:10.1007/s11661-002-1016-2.

[317] F. Bridier, D. L. McDowell, P. Villechaise, J. Mendez, Crystal plasticity modeling of slip activity in Ti-6Al-4V under high cycle fatigue loading, International Journal of Plasticity 25 (6) (2009) 1066–1082. doi:10.1016/j.ijplas.2008.08.004.
URL http://dx.doi.org/10.1016/j.ijplas.2008.08.004

[318] T. Mukai, M. Yamanoi, H. Watanabe, K. Higashi, Ductility enhancement in AZ31 magnesium alloy by controlling its grain structure, Scripta Materialia 45 (1) (2001) 89–94. doi:10.1016/S1359-6462(01)00996-4.

[319] P. Jussila, Analytical solutions of the mechanical behaviour of rock with applications to a repository for spent nuclear fuel, no. October, 1997.

[320] F. Bridier, P. Villechaise, J. Mendez, Slip and fatigue crack formation processes in an α/β titanium alloy in relation to crystallographic texture on different scales, Acta Materialia 56 (15) (2008) 3951–3962. doi:10.1016/j.actamat.2008.04.036.

[321] D. Banerjee, J. C. Williams, Perspectives on Titanium Science and Technology, Acta Materialia 61 (3) (2013) 844–879. doi:10.1016/j.actamat.2012.10.043.
URL http://dx.doi.org/10.1016/j.actamat.2012.10.043

[322] A. N. Stroh, A theory of the fracture of metals, Vol. 6, 1957. doi:10.1080/00018735700101406.

[323] M. Hayes, Connexions between the moduli for anistropic elastic materials, Journal of Elasticity 2 (2) (1972) 135–141. doi:10.1007/BF00046063.

[324] K. S. Ravi Chandran, Duality of fatigue failures of materials caused by Poisson defect statistics of competing failure modes, Nature Materials 4 (4) (2005) 303–308. doi:10.1051/nmat1351.

[325] A. C. F. Cocks, Inelastic deformation of porous materials, Journal of the Mechanics and Physics of Solids 37 (6) (1989) 693–715.

[326] A. M. Makiyama, S. Vajjhala, L. J. Gibson, Analysis of crack growth in a 3D voronoi structure: A model for fatigue in low density trabecular bone, Journal of Biomechanical Engineering 124 (5) (2002) 512–520. doi:10.1115/1.1503792.

[327] M. Leary, Design of titanium implants for additive manufacturing, Elsevier Inc., 2018. doi:10.1016/B978-0-12-812456-7.00009-3.
URL http://dx.doi.org/10.1016/B978-0-12-812456-7.00009-3

[328] K. Ushijima, W. J. Cantwell, R. A. Mines, S. Tsopanos, M. Smith, An investigation into the compressive properties of stainless steel micro-lattice structures, Journal of Sandwich Structures and Materials 13 (3) (2011) 303–329. doi:10.1177/1099636210380997.

[329] L. J. Gibson, M. F. Ashby, Cellular Solids: Structure and Properties, 1997.

[330] M. Smith, Z. Guan, W. J. Cantwell, Finite element modelling of the compressive response of lattice structures manufactured using the selective laser melting technique, International Journal of Mechanical Sciences 67 (2013) 28–41. doi:10.1016/j.ijmecsci.2012.12.004.
URL http://dx.doi.org/10.1016/j.ijmecsci.2012.12.004

[331] L. Dong, V. Deshpande, H. Wadley, Mechanical response of Ti-6Al-4V octet-truss lattice structures, International Journal of Solids and Structures 60 (2015) 107–124. doi:10.1016/j.ijsolstr.2015.02.020.
URL http://dx.doi.org/10.1016/j.ijsolstr.2015.02.020

[332] Z. Liu, B. He, T. Lyu, Y. Zou, A Review on Additive Manufacturing of Titanium Alloys for Aerospace Applications: Directed Energy Deposition and Beyond Ti-6Al-4V, Jom 73 (6) (2021) 1804–1818. doi:10.1007/s11837-021-04670-6.
URL https://doi.org/10.1007/s11837-021-04670-6

[333] H. M. Kolken, A. F. Garcia, A. D. Plessis, A. Meynen, C. Rans, L. Scheys, M. J. Mirzaali, A. A. Zadpoor, Mechanisms of fatigue crack initiation and propagation in auxetic meta-biomaterials, Acta Biomaterialia 138 (2022) 398–409. doi:10.1016/j.actbio.2021.11.002.

[334] M. Zaiser, S. Zapperi, Disordered mechanical metamaterials, Nature Reviews Physics 5 (11) (2023) 679–688. doi:10.1038/s42254-023-00639-3.

[335] D. R. Reid, N. Pashine, J. M. Wozniak, H. M. Jaeger, A. J. Liu, S. R. Nagel, J. J. De Pablo, Auxetic metamaterials from disordered networks, Proceedings of the National Academy of Sciences of the United States of America 115 (7) (2018) E1384–E1390. arXiv:1710.02493, doi:10.1073/pnas.1717442115.

[336] M. Zaiser, F. Mill, A. Konstantinidis, K. E. Aifantis, Strain localization and strain propagation in collapsible solid foams, Materials Science and Engineering: A 567 (2013) 38–45. doi:10.1016/j.msea.2012.12.038.

[337] D. Tüzes, P. D. Ispánovity, M. Zaiser, Disorder is good for you: the influence of local disorder on strain localization and ductility of strain softening materials, International Journal of Fracture 205 (2) (2017) 139–150. arXiv:1604.01821, doi:10.1007/s10704-017-0187-1.

[338] S. Raghavendra, A. Molinari, A. Cao, C. Gao, F. Berto, G. Zappini, M. Benedetti, Quasi-static compression and compression–compression fatigue behavior of regular and irregular cellular biomaterials, Fatigue and Fracture of Engineering Materials and Structures 44 (5) (2021) 1178–1194. doi:10.1111/ffe.13422.

[339] J. S. Zhang, Y. T. Tang, Y. Deng, H. Liu, A. Lui, P. S. Grant, E. Alabort, R. C. Reed, A. C. F. Cocks, Orientation Matters : Assessing the Cyclic Deformation Behaviour of Laser Powder Bed Fusion Ti-6Al-4V, Manuscript Submitted to Additive Manufacturing (2024). doi:https://dx.doi.org/10.2139/ssrn.4769399.

[340] P. Qi, B. Li, T. Wang, L. Zhou, Z. Nie, Effect of heat treatment on microstructure and mechanical properties of alsi10mg alloy fabricated by selective laser melting, Materials Science Forum 1035 MSF (2021) 312–317. doi:10.4028/www.scientific.net/MSF.1035.312.

[341] T. Hildebrand, P. Rüegsegger, A new method for the model-independent assessment of thickness in three-dimensional images, Journal of Microscopy 185 (1) (1997) 67–75. doi:10.1046/j.1365-2818.1997.1340694.x.

[342] G. Escobar-Palafox, R. Gault, K. Ridgway, Preliminary empirical models for predicting shrinkage, part geometry and metallurgical aspects of Ti-6Al-4V shaped metal deposition builds, IOP Conference Series: Materials Science and Engineering 26 (1) (2011). doi:10.1088/1757-899X/26/1/012002.

[343] X. Lu, X. Lin, M. Chiumenti, M. Cervera, Y. Hu, X. Ji, L. Ma, H. Yang, W. Huang, Residual stress and distortion of rectangular and S-shaped Ti-6Al-4V parts by Directed Energy Deposition: Modelling and experimental calibration, Additive Manufacturing 26 (August 2018) (2019) 166–179. doi:10.1016/j.addma.2019.02.001.
URL https://doi.org/10.1016/j.addma.2019.02.001

[344] E. Mirkoohi, D. E. Sievers, H. Garmestani, K. Chiang, S. Y. Liang, Three-dimensional semi-elliptical modeling of melt pool geometry considering hatch spacing and time spacing in metal additive manufacturing, Journal of Manufacturing Processes 45 (October 2018) (2019) 532–543. doi:10.1016/j.jmapro.2019.07.028.
URL https://doi.org/10.1016/j.jmapro.2019.07.028

[345] B. Lozanovski, M. Leary, P. Tran, D. Shidid, M. Qian, P. Choong, M. Brandt, Computational modelling of strut defects in SLM manufactured lattice structures, Materials and Design 171 (2019) 107671. doi:10.1016/j.matdes.2019.107671.
URL https://doi.org/10.1016/j.matdes.2019.107671

[346] M. R. Karamooz Ravari, M. Kadkhodaei, A Computationally Efficient Modeling Approach for Predicting Mechanical Behavior of Cellular Lattice Structures, Journal of Materials Engineering and Performance 24 (1) (2015) 245–252. doi:10.1007/s11665-014-1281-4.

[347] W. Ronan, V. S. Deshpande, N. A. Fleck, The tensile ductility of cellular Solids: The role of imperfections, International Journal of Solids and Structures 102-103 (2016) 200–213. doi:10.1016/j.ijsolstr.2016.10.004.
URL http://dx.doi.org/10.1016/j.ijsolstr.2016.10.004

[348] A. E. Simone, L. J. Gibson, The effects of cell face curvature and corrugations on the stiffness and strength of metallic foams, Acta Materialia 46 (11) (1998) 3929–3935. doi:10.1016/S1359-6454(98)00072-X.

[349] R. M. Latture, M. R. Begley, F. W. Zok, Defect Sensitivity of Truss Strength, Journal of the Mechanics and Physics of Solids 124 (2019) 489–504. doi:10.1016/j.jmps.2018.10.019.
URL https://doi.org/10.1016/j.jmps.2018.10.019

[350] X. E. Guo, L. J. Gibson, Behavior of intact and damaged honeycombs: A finite element study, International Journal of Mechanical Sciences 41 (1) (1999) 85–105. doi:10.1016/S0020-7403(98)00037-X.

[351] M. Gavazzoni, S. Foletti, D. Pasini, Cyclic response of 3D printed metamaterials with soft cellular architecture: The interplay between as-built defects, material and geometric non-linearity, Journal of the Mechanics and Physics of Solids 158 (September 2021) (2022) 104688. doi:10.1016/j.jmps.2021.104688.
URL https://doi.org/10.1016/j.jmps.2021.104688

[352] S. K. Maiti, M. F. Ashby, L. J. Gibson, Fracture toughness of brittle cellular solids, Scripta Metallurgica 18 (3) (1984) 213–217. doi:10.1016/0036-9748(84)90510-6.

[353] N. A. Fleck, X. M. Qiu, The damage tolerance of elastic-brittle, two-dimensional isotropic lattices, Journal of the Mechanics and Physics of Solids 55 (3) (2007) 562–588. doi:10.1016/j.jmps.2006.08.004.